THESE

présentée pour obtenir le grade de

Docteur de TELECOM ParisTech

Spécialité: Communication et Electronique

Hao Lin

Analyse et conception de systèmes multi-porteuses pour la transmission par courant porteur en ligne

Soutenue le 12 Novembre 2009 devant le jury composé de :

Président	M. J.C. Belfiore
Rapporteurs	M. M. Bellanger
	M. M.K. Renfors
Examinateurs	Mme. A. Hayar
	M. O. Isson
	M. P. Siohan

Equipe d'accueil: Orange Labs (WASA/CREM) à Rennes
Laboratoire universitaire: Eurécom, Sophia Antipolis
Ecole doctorale: Télécom ParisTech

Dissertation

In Partial Fulfillment of the Requirements
for the Degree of Doctor of Philosophy
from TELECOM ParisTech

Specialization: Communication and Electronics

Hao Lin

Analysis and design of multi-carrier systems for power line communications

Defended on November 12, 2009 in front of a jury composed of:

President:	Mr. J.C. Belfiore
Reporters:	Mr. M. Bellanger
	Mr. M.K. Renfors
Examiners:	Ms. A. Hayar
	Mr. O. Isson
	Mr. P. Siohan

This thesis takes place at France Telecom, Orange Labs (WASA/CREM), Rennes.

I would like to express my gratitude to all those who gave me the possibility to complete this thesis. I want to thank France Telecom Orange Labs (CREM team) and institute Eurecom for giving me this opportunity of doing this thesis in the first instance.

I am deeply indebted to my supervisor Dr. P. Siohan. His contagious enthusiasm and patience went a long way in bringing this work into its final form. From him, I learnt the value of rigor and motivation in research. He deserves equal credit for this work, if not more. The fact that he treats his Ph.D. students as equals, makes me consider him as a good friend rather than my supervisor. I want to thank my academic supervisor Ass. Prof. A. Hayar whose help, stimulating suggestions and encouragement helped me in all the time of research.

I also would like to thank my thesis committee, Prof. J.C. Belfiore, Prof. M. Bellanger, Prof. M. K. Renfors and Dr. O. Isson for reviewing my dissertation and for their constructive comments.

My colleagues from the CREM team of Orange Labs supported me in my research work. I want to thank them for all their help, support, interest and valuable hints. Especially I am obliged to Dr. M. Le Bot, Dr. A. Skrzypczak, Dr. C. Lélé, G. Ndo and Y. Dandach. I also want to thank my former team leader Mr. P. Gelpi, my current team leader Mr. J.C. Rault and our secretary Mrs. G. Le Gouallec for their great helps in difficult times.

Especially, I would like to give my special thanks to my wife Li Li whose patient love enabled me to complete this work.

January 2010
Hao Lin
Rennes, France

Contents

List of Figures

List of Tables

Abstract

This thesis aims at investigating an alternative MultiCarrier Modulation (MCM) scheme, named OFDM Offset QAM (OFDM/OQAM), in the Power Line Communications (PLC) context. The objective of this thesis is to illustrate the pros and cons of the OFDM/OQAM compared with the widely used OFDM scheme and further demonstrate the feasibility of using OFDM/OQAM in PLC. The main contributions of this thesis include: 1) PLC channel analysis: we analyze the PLC channel from an information theory point of view; 2) Analytical transmission model: we derive a theoretical transmission model for the OFDM/OQAM system over frequency selective channel; 3) Prototype filter design criteria discussion: different criteria of prototype filter design are discussed in this thesis for PLC; 4) Channel equalization methods: we present two channel equalization methods in this thesis and the efficiency of the presented methods is evaluated by simulations; 5) Capacity analysis: the transmission capacities of the OFDM and the OFDM/OQAM are analyzed/compared in this thesis and the fact that, under the most recent HomePlug AV specifications, the OFDM/OQAM system can, generally, provide higher capacity than the one of OFDM system is shown; 6) Flexibility: we point out two flexibilities in the PLC context, named modulation scheme flexibility and prototype filter flexibility, respectively. The modulation flexibility can be realized by a unified MCM transceiver and it can eventually solve the existing compatibility issue in the current PLC draft standard. The prototype filter flexibility can be used to provide better channel estimation performance.

Résumé

Le but de cette thèse est l'étude de la modulation multiporteuse OFDM Offset QAM (OFDM/OQAM), comme modulation alternative à l'OFDM, dans le contexte des communications par Courants Porteurs en Ligne (CPL). On s'est proposé dans le cadre de cette thèse d'illustrer les avantages et inconvénients de l'OFDM/OQAM par rapport à l'OFDM, très largement utilisé d'un point de vue pratique. Le but recherché est également de montrer la faisabilité en terme d'implémentation de l'OFDM/OQAM pour les CPL. Les principales contributions que nous avons apportées sont: 1) Une analyse des canaux CPL: nous analysons les canaux CPL d'un point de vue de la théorie d'information; 2) Une modélisation de la transmission: nous élaborons un modèle théorique de transmission pour un système OFDM/OQAM sur canal sélectif en fréquence; 3) Une discussion sur les critères de conception du filtre prototype: differents critères de conception du filtre prototype sont analysés dans cette thèse, pour les CPL; 4) Des méthodes d'égalisation: nous approfondissons deux méthodes d'égalisation et la robustesse des méthodes analysées est évaluée par simulations; 5) Une analyse de capacité: les capacités de transmission de l'OFDM et de l'OFDM/OQAM sont analysées et ensuite comparées. Il est en particulier montré que, compte tenu des spécifications HomePlugAV les plus récentes, l'OFDM/OQAM présente d'une manière générale une capacité plus importante que l'OFDM; 6) Une analyse sur la flexibilité: nous avons fait ressortir dans cette thèse deux notions importantes en terme de flexibilité: la flexibilité de la modulation et la flexibilité du prototype. La première peut être réalisée par un transrécepteur unifié pour les modulations multiporteuses. Ceci permet, en outre, de résoudre la problématique d'interopérabilité dans les spécifications actuelles pour les CPL. Enfin, le second type de flexibilité peut être exploité pour l'amélioration des performances en estimation de canal.

Acronyms

Here are the main acronyms used in this document. The meaning of an acronym is usually indicated once, when it first occurs in the text.

AC	Alternating Current
ASCET	Adaptive Sine/Cosine-Modulated Filter Bank equalizer for Trans-multiplexer
AR	AutoRegressive
AWGN	Additive White Gaussian Noise
BER	Bit Error Rate
BPL	Broadband Power Line
BPSK	Binary Phase Shift Keying
BS	Base Station
CA	Complex Additions
CCO	Coding Cut-Off
CE	Channel Estimation
CEPCA	Consumer Electronics Powerline Communication Alliance
CIR	Channel Impulse Response
CM	Complex Multiplications
CMFB	Cosine Modulated Filter Banks
CP	Cyclic Prefix
CSR	Complex Split-Radix
CTF	Channel Transfer Function
CTR2	Cooley-Tukey Radix-2
DCT	Discrete Cosine Transform
DMT	Discrete MultiTone
DSL	Digital Subscriber Line
DoF	Degree of Freedom
DST	Discrete Sine Transform
DWMT	Discrete Wavelet MultiTone
EGF	Extended Gaussian Function
EIC	Equalization with Interference Cancellation
EMC	Electromagnetic Compatibility
EMFB	Exponentially Modulated Filter Banks
EMI	Electromagnetic Interference
FBMC	Filter Bank MultiCarrier

FCT	Fast Cosine-like Transform
FFT	Fast Fourier Transform
FIR	Finite Impulse Response
FL	Frequency Localization
FMT	Filter MultiTone
FS	Frequency Selective
FST	Fast Sine-like Transform
GBIP	General Purpose Interface Bus
GI	Guard Interval
HPAV	HomePlug AV
HPF	High-Pass Filter
HS	Hermitian Symmetry
IAM	Interference Approximation Method
IEEE	Institute of Electrical and Electronics Engineers
ICI	Inter-Carrier Interference
IFCT	Inverse Fast Cosine-like Transform
IFFT	Inverse Fast Fourier Transform
IFST	Inverse Fast Sine-like Transform
IOTA	Isotropic Orthogonal Transform Algorithm
ISI	Inter-Symbol Interference
LB	Lower Bound
LE	Linear Equalizer
LOS	Line of Sight
LP-CMFB	Linear Phase-Cosine Modulated Filter Banks
LS	Least Square
LTI	Linear Time Invariant
MAC	Media Access Control
MCM	Multi-Carrier Modulation
MDF	Modified Doroslovački Filter
MDFT	Modified DFT
MEM	Maximum Entropy Method
MMSE	Minimum Mean Square Error
MFB	Modulated Filter Bank
MOE	Maximum Outside Energy
MWCβ	Maximum Weighted Combining $\beta_{\{0,I\}}$
NPR	Nearly Perfect Reconstruction
OFDM	Orthogonal Frequency Division Mutiplexing
OQAM	Offset Quadrature Amplitude Modulation
PAM	Pulse Amplitude Modulation
PDP	Power Delay Profile
PDS	Power Delay Spectrum
PF	Polyphase Filtering
PHY	Physical
PLC	Power Line Communications
POP	Pair of Pilots
PR	Perfect Reconstruction

PSD	Power Spectrum Density
QAM	Quadrature Amplitude Modulation
QPSK	Quadrature Phase-Shift Keying
RA	Real Additions
RI	Roll-off Interval
RM	Real Multiplications
RSR	Real Split-Radix
SER	Symbol Error Rate
SINR	Signal-to-Interference-plus-Noise Ratio
SIR	Signal-to-Interference Ratio
SNR	Signal-to-Noise Ratio
SRRC	Square Root Raised Cosine
TDMA	Time Division Multiple Access
TFL	Time Frequency Localization
TL	Time Localization
TMUX	Transmultiplexer
UPA	Universal Powerline Association
UWB	Ultra Wide Band
VDSL	Very high bit-rate Digital Subscriber Line
VNA	Vector Network Analysis
WAN	Wide Area Networks
WLAN	Wireless Local Area Networks
WOFDM	Wavelet Orthogonal Frequency Division Mutiplexing
WPAN	Wireless Personal Area Networks
ZF	Zero Forcing

Notations

The main notations used in this thesis are listed in below

x	scalar
$\|x\|$	norm of x
$(x)^*$	conjugate of x
$\mathbf{x}_{1\times N}$	row vector with size $1 \times N$
$\mathbf{x}_{N\times 1}$	column vector with size $N \times 1$
$\mathbf{X}_{N\times N}$	matrix with size $N \times N$
$\mathbf{X}_{(a:b)\times(c:d)}$	sub-matrix, i.e. taking row indices $\in [a, b]$ and column indices $\in [c, d]$
$\mathbf{X}_{\text{diag}}$	diagonal matrix with size specified in the context
$\mathbf{X}^T_{N\times N}$	transpose of $\mathbf{X}_{N\times N}$
$\mathbf{X}^H_{N\times N}$	transpose conjugate of $\mathbf{X}_{N\times N}$
$\mathbf{0}_{1\times N}$	zero row vector with size $1 \times N$
$\mathbf{0}_{N\times 1}$	zero column vector with size $N \times 1$
$\mathbf{0}_{N\times N}$	zero matrix with size $N \times N$
$\mathbf{I}_N$	identical matrix with size $N \times N$
$\mathbf{F}_M$	Fourier transform matrix with size $M \times M$, i.e., $[\mathbf{F}_M]_{m,k} = \frac{1}{\sqrt{M}} e^{-j\frac{2\pi mk}{M}}$
$\mathbf{F}^H_M$	inverse Fourier transform matrix with size $M \times M$, i.e., $[\mathbf{F}_M]_{m,k} = \frac{1}{\sqrt{M}} e^{j\frac{2\pi mk}{M}}$
$\mathbf{C}^{\text{I}}_N$	cosine-like type I transform matrix with size $N \times N$
$\mathbf{S}^{\text{I}}_N$	sine-like type I transform matrix with size $N \times N$
$\mathbf{C}^{\text{III}}_N$	cosine-like type III transform matrix with size $N \times N$
$\mathbf{S}^{\text{III}}_N$	sine-like type III transform matrix with size $N \times N$
$(\mathbf{C}^{\text{III}}_N)^T$	inverse cosine-like type III transform matrix with size $N \times N$
$(\mathbf{S}^{\text{III}}_N)^T$	sine-like type III transform matrix with size $N \times N$
W^{ml}	Fourier transform kernel factor ($W = e^{-j\frac{2\pi ml}{M}}$)
C^{ml}_{2N}	cosine-like transform kernel factor ($C^{ml}_{2N} = \cos\left(\frac{2\pi ml}{2N}\right)$)
S^{ml}_{2N}	sine-like transform kernel factor ($S^{ml}_{2N} = \sin\left(\frac{2\pi ml}{2N}\right)$)
$\tilde{C}^{ml}_{2N}$	modified cosine-like transform kernel factor ($\tilde{C}^{ml}_{2N} = \cos\left(\frac{\pi ml}{2N}\right)$)
$\tilde{S}^{ml}_{2N}$	modified sine-like transform kernel factor ($\tilde{S}^{ml}_{2N} = \sin\left(\frac{\pi ml}{2N}\right)$)
$\delta(t)$	Dirac delta function
$\delta_{n,m}$	Kronecker delta

M	number of carriers in both OFDM and OFDM/OQAM systems
T_s	sampling inteval
f_s	sampling frequency
T_0	useful OFDM symbol duration ($T_0 = MT_s$)
F_0	frequency spacing ($F_0T_0 = 1$)
τ_0	OFDM/OQAM system rate ($2\tau_0 = T_0$)
L_f	prototype filter length
D	causality delay factor ($D = L_f - 1$)
$\phi_{m,n}$	OFDM/OQAM phase term
$\mathrm{E}[a]$	expectation of random variable a
$\mathrm{Var}[a]$	variance of random variable a
$\mathbb{R}$	real field
$\mathbb{C}$	complex field
$\mathrm{Re}\{a\}$	real part of a
$\mathrm{Im}\{a\}$	imaginary part of a
j	$j^2 = -1$
$\mathbf{Re}_{N\times N}$	real-part-taken operation matrix with size $N \times N$
$\mathbf{Im}_{N\times N}$	imaginary-part-taken operation matrix with size $N \times N$
$[\mathbf{PS}]$	parallel to serial operation
$[\mathbf{SP}]$	serial to parallel operation
$U(z)$	Z-transform of $u[k]$
Γ	SNR gap ($\Gamma = \frac{1}{3}\left[\mathbf{Q}^{-1}(\frac{\mathrm{SER}}{4})\right]^2$)
σ_n^2	variance of additive white noise
σ_c^2	variance of OFDM entrance complex-valued symbol
σ_a^2	variance of OFDM/OQAM entrance real-valued symbol ($2\sigma_a^2 = \sigma_c^2$)
$[\cdot]_{\downarrow N}$	decimation (downsampling) with factor N
$[\cdot]_{\uparrow N}$	interpolation (upsampling) with factor N
$A_g[\tau, \mu]$	ambiguity function of the prototype filter $g[k]$ at phase-space (τ, μ)
$\lceil a \rceil$	the smallest integer that is larger than a
$\lfloor a \rfloor$	the largest integer that is smaller than a

Chapter 1

Résumé Français

L'intérêt pour des communications numériques réalisées par courant porteur en ligne a significativement augmenté récemment. La présence généralisée d'une infrastructure de distribution d'énergie rend ce médium particulièrement attractif pour l'introduction de nouveaux services. En effet sa couverture potentielle est supérieure à ce que l'on peut atteindre avec n'importe quelle autre alternative filaire ou sans fil. Cependant, en dépit de ce potentiel énorme, la transmission large bande sur des réseaux électriques est confrontée à plusieurs challenges. 1) Le canal électrique filaire constitue un milieu très hostile et très bruité qui est difficile à modéliser; 2) Le canal électrique filaire génère plusieurs challenges pour les concepteurs de modems. 3) L'absence de blindage des lignes électriques provoque des interférences électromagnétiques.

De nombreuses améliorations ont pu être apportées durant la dernière décennie pour trouver des solutions réalisables pour les différents challenges que nous venons de mentionner. Toutefois, de manière naturelle, la plupart des contributions sur ce sujet ont été publiées dans des journaux relatifs à l'électronique grand public, à la distribution d'énergie ou encore à l'électronique industrielle et seul un nombre plus restreint est apparu dans des revues plus spécialisées dans les systèmes de communication. Cette thèse vise à combler en partie cette lacune.

Dans cette thèse nous introduisons tout d'abord diverses caractérisations des canaux de transmission par courant porteur en ligne pour des réseaux électriques privatifs. Une première contribution de cette thèse réside dans leur analyse par des méthodes basées sur la théorie de l'information. Toutefois, l'axe principal de cette dissertation concerne l'étude d'un système avancé de multiplexage orthogonal en fréquence de type OFDM où les sous-porteuses sont modulées par une modulation d'amplitude en quadrature avec décalage (offset) temporel (OQAM). Ce système OFDM/OQAM a récemment été remis en pleine lumière en particulier du fait de ses caractéristiques de localisation temps-fréquence. Toutefois, l'étude analytique des performances en transmission de l'OFDM/OQAM dans des canaux non idéaux n'a pratiquement pas été abordée. Afin de remédier à cette situation, dans cette thèse, nous dérivons une analyse des performances théoriques de cette modulation dans le cas d'une transmission dans un canal sélectif en fréquence. En outre,

sur la base de cette dérivation, plusieurs autres contributions sont réalisées : recherche d'un critère approprié pour la conception du filtre prototype, détermination de méthodes d'égalisation et analyse de la capacité de transmission. Ces contributions nous donnent également un outil pour réaliser des comparaisons avec le système OFDM. Il en résulte la détermination d'un seuil de rapport signal à bruit (SNR) qui permet de décider d'un schéma vainqueur entre l'OFDM et l'OFDM/OQAM. Dans le même ordre d'idée, nous proposons donc un schéma complet de transmission multi-porteuse qui nous permet d'exploiter effectivement un gain de flexibilité de modulation. De plus, dans cette thèse, nous introduisons une flexibilité supplémentaire qu'il est également possible d'exploiter dans le cas de l'OFDM/OQAM. Cette flexibilité est liée à la commutation de filtre prototype qui peut apporter un gain très significatif pour ce qui est de l'estimation de canal.

1.1 Chapitre 2

Dans l'introduction générale, le chapitre 2 de cette thèse, nous rappelons l'évolution et les motivations qui ont favorisé l'avénement de la transmission par courant porteur en ligne: le PLC. Nous abordons ensuite les motivations plus précises en relation avec le sujet de thèse. La modélisation de canal et les techniques de modulation apparaissent comme deux enjeux essentiels auxquels on va s'intéresser plus particulièrement. Dans cette introduction nous indiquons aussi chapitre par chapitre comment nous abordons ces deux problèmes.

La modélisation du canal PLC a progressé significativement ces dernières années et continue de le faire. Les Orange Labs sur le site de Lannion ont en particulier été parmi les premiers à effectuer des mesures et à proposer des modèles pour des bandes élargies (jusqu'à 100 MHz) valables pour différents types d'habitations. Dans la thèse nous examinons ces modèles d'une façon inédite en nous appuyant sur des outils de théorie de l'information qui sont présentés dans le chapitre 4.

Toutefois les études sur les modulations constituent la partie essentielle de notre travail. L'introduction rappelle les différentes étapes technologiques qui ont marqué l'avénement des systèmes de modulation multiporteuses. Elle revient également sur le rôle fondateur de la théorie de Gabor en tant qu'outil mathématique de base pour la classification des différentes familles de solution. Dans cette thèse nous privilégions la modulation dite OFDM/OQAM car elle permet d'avoir une efficacité spectrale qui est en théorie maximum et qu'elle permet d'obtenir un signal à la fois bien localisé en temps et en fréquence. En contre partie de ces avantages sa seule limitation est de ne satisfaire la condition d'orthogonalité que dans le corps de réels. Par rapport à l'OFDM, modulation phare à l'heure actuelle, l'OFDM/OQAM ne transmet que des données non redondantes car elle n'a pas besoin de préfixe cyclique (CP). Cette absence de CP peut toutefois générer une interférence qui peut devenir critique lors de la transmission dans des canaux dispersifs en temps. Des solutions d'égalisations sont proposées pour faire face à ce problème.

Une étude sur la capacité respective des systèmes CP-OFDM et OFDM/OQAM montre ensuite que, de manière générale, il peut exister des situations où l'avantage peut revenir à l'un ou l'autre de ces systèmes. En effet, même si dans la pratique, avec les contraintes réglementaires et matérielles connues actuellement en PLC, l'OFDM/OQAM a l'avantage, on ne peut pas exclure que le contexte puisse évoluer dans le futur. Dans cette hypothèse, sur la base d'un noyau de transformation commun, nous proposons, un

système de modulation unifié incluant les 2 modulations, CP-OFDM et WOFDM, proposées par IEEE P1901 et aussi HS-OQAM, la variante bande de base de l'OFDM/OQAM, et pouvant commuter à chaque instant de l'un à l'autre de ces systèmes. Nous proposons également un second type de flexibilité qui consiste à commuter d'un filtre prototype à un autre suivant que l'on transmet un préambule ou des données utiles.

1.2 Chapitre 3

Dans le chapitre 3 nous présentons brièvement le contexte technologigue associé à la transmission par courant porteur en ligne (PLC, en anglais). Historiquement, le réseau électrique a servi pour la distribution d'énergie et nous montrons comment progressivement il s'est aussi développé en tant que système de communication. Cette évolution explique que pendant plusieurs années les études dans le domaine ont avant tout concerné la distribution d'énergie ainsi que l'électronique industrielle et l'électronique grand public. Les réseaux électriques étant en place, leur utilisation s'est ensuite élargie avec l'introduction des systèmes PLC. Les objectifs initiaux visaient au contrôle et à la commande à distance du réseau. Par la suite, le PLC s'est intéressé à la transmission d'information en tant que technique d'accès aux immeubles et habitations. A présent un des objectifs essentiels des PLC est de s'imposer en tant que système de transmission d'information au sein des habitations (in-home). Cet objectif répond à un besoin toujours croissant de haut débit et de qualité de service qui va de pair avec la multiplication des services de télécommunications (voIP, Internet, Télévision haute définition, jeux vidéo, etc.). Les PLC apparaissent donc aujourd'hui comme un nouveau domaine d'étude du point de vue des communications numériques. Plusieurs défis sont à relever, en particulier, en ce qui concerne, tout d'abord, la modélisation des canaux, des bruits et diverses interférences typiques du réseau électrique dans des bandes de fréquences qui tendent à s'élargir, et aussi pour ce qui concerne les méthodes de transmission robustes et à haut débit sur ce type de canaux, les architectures de réseaux et les protocoles de transmission. L'impact commercial des produits PLC est déjà significatif et va susciter pour l'avenir de nouvelles exigences auxquelles les techniques de communication numérique peuvent apporter de bonnes réponses. Dans l'état actuel, les systèmes se basent sur des spécifications proposées par des alliances d'industriels et se mettent aussi en, place par le biais du standard IEEE P1901.

La présente thèse va développer des aspects de recherche liés à la modélisation du canal PLC et surtout à l'aspect modulation qui, comme l'illustre la standard IEEE P1901, est un élément discriminant des solutions techniques en présence.

1.3 Chapitre 4

Le chapitre 4 fournit un bref état de l'art sur l'in-home PLC, la modélisation de canal et son analyse par une approche basée sur la théorie de l'information. Le canal PLC a longtemps été considéré comme un milieu de transmission extrêmement hostile et bruyant difficile à modéliser. Philipps, Zimmermann, d'une part et Dostert, d'autre part, dans deux articles de référence publiés respectivement à ISPLC'99 [96] et dans IEEE Trans. Commun. [139], ont été des pionniers dans ce domaine. Depuis, un grand nombre de contributions ont

été fondées en réalité sur leur modèle. Récemment, Tonello *et al.* ont ajouté quelques *a priori* concernant la connaissance statistique de ce modèle [93] pour obtenir un nouveau modèle sur lequel nous reviendrons. Un autre modèle de canal introduit dans ce chapitre est celui proposé par Tlich *et al.* [123]. Ce modèle réaliste est obtenu à partir d'un large ensemble de mesures réalisées dans un grand nombre d'habitations et soumis ensuite à un large éventail d'analyses statistiques.

Avec le modèle de Zimmermann, nous avons appris que le canal PLC est multi-trajet et que sa réponse en fréquence peut s'exprimer mathématiquement comme suit

$$H(f) = \sum_{i=1}^{N_P} g_i A(f, d_i) e^{-j2\pi f \tau_i}, \tag{1.1}$$

avec

$$A(f, d) = e^{-(a_0 + a_1 f^k)d}, \tag{1.2}$$

où N_P représente le nombre de trajets et $A(f, d)$ est le facteur d'atténuation dans le câble; g_i désigne le gain du i-ème trajet; τ_i représente le i-ème temps de parcours. Les deux paramètres a_0 et a_1 sont deux paramètres fixes ajustés en fonction des mesures. Dans [139], les auteurs proposent une technique qui en deux étapes permet d'obtenir ces paramètres.

Pour le modèle préconisé par Tonello, l'idée est de supposer que les réflecteurs se situent à des intervalles de distance finie, au maximum de $L_{\max}$, parcourus selon un processus de Poisson d'intensité Λ (m^{-1}). Avec ce modèle, le nombre de parcours suit une distribution de Poisson de moyenne $L_{\max}\Lambda$, tandis que les distances inter-trajectoire d'arrivée sont indépendantes et distribuées de façon exponentielle avec une moyenne de $1/\Lambda$.

Les gains de trajet g_i résultent d'un série de transmissions et des facteurs de réflexion. Par conséquent, ils peuvent être modélisés comme des variables complexes aléatoires indépendantes ayant une distribution d'amplitude log-normale et une phase uniforme dans $[0, 2\pi]$. Néanmoins, ils peuvent également être modélisés comme des valeurs réelles et uniformément réparties à l'intérieur de $[-1, 1]$ comme dans [139]. Les autres paramètres a_0, a_1, k sont supposés constants (k peut être fixé à 1). a_0 et a_1 peuvent être choisis en fonction du profil lié à la perte de trajet (path-loss). Ainsi, à partir du moment où les paramètres a_0, a_1, k sont connus, et supposant que $k = 1$, la réalisation de la réponse impulsionnelle du canal (CIR) peut se générer, pour une réalisation des paramètres aléatoires N_P, g_i, d_i, par [93]

$$\begin{aligned} h(t) &= A \sum_{i=1}^{N_P} g_i e^{-a_0 d_i} \frac{a_1 d_i + j2\pi(t - \frac{d_i}{v})}{(a_1 d_i)^2 + 4\pi^2 (t - \frac{d_i}{v})^2} \\ &\times \left(e^{j2\pi B_1 (\frac{d_i}{v}) - a_1 B_1 d_i} - e^{j2\pi B_2 (\frac{d_i}{v}) - a_1 B_2 d_i}\right). \end{aligned} \tag{1.3}$$

Ensuite, compte tenu des hypothèses précédentes, la perte de trajet moyenne peut se calculer sous forme close [93]

$$PL(f) = A^2 \frac{\Lambda}{3} \left(\frac{1 - e^{-\Lambda L_{\max}}}{2a_0 + 2a_1 f^k} \right) (1 - e^{-2L_{\max}(a_0 + a_1 f^k)}). \tag{1.4}$$

Par ailleurs, Tlich *et al.* ont proposé un modèle InHome PLC basé sur un large ensemble de mesures. Ces mesures ont été réalisées dans la gamme de fréquences allant de

30 KHz à 100 MHz et pour des environnements correspondant à des habitats différents (ancien / nouvel appartement / studio dans campagne / ville, etc.). Ensuite, les mesures ont été classées dans 9 catégories en fonction de la capacité de transmission qu'elles pouvaient permettre. Finalement, les auteurs ont fourni un générateur de canal InHome PLC réaliste qui est fréquemment utilisé dans cette thèse.

Dans une deuxième partie de ce chapitre nous utilisons ce générateur pour analyser les canaux in-home PLC avec des outils de théorie de l'information : la méthode de maximum d'entropie (MEM), basée sur le théorème de Burg, et l'estimation des degrés de liberté (DOF), basée sur un théorème de décomposition du signal en sous-espaces.

Avec le théorème de Burg, nous avons appris que le taux maximum d'entropie d'un processus stochastique avec pour variable h_i suit un processus auto-régressif (AR), i.e.,

$$h_i = -\sum_{k=1}^{N_r} a_k h_{i-k} + Z_i, \tag{1.5}$$

où les Z_i sont *i.i.d.* $\sim N(0, \sigma^2)$. Les paramètres $a_1, \cdots, a_{N_r}, \sigma^2$ peuvent être obtenus en résolvant les équations de Yule-Walker, i.e.,

$$\begin{aligned} R(0) &= -\sum_{k=1}^{N_r} a_k R(-k) + \sigma^2, \\ R(q) &= -\sum_{k=1}^{N_r} a_k R(q-k), \quad q = 1, \cdots, N_r. \end{aligned}$$

Dans la pratique, on peut toujours estimer les fonctions d'autocorrélation à partir des mesures, i.e., $\hat{R(q)}$. En conséquence, l'entropie estimée est donnée par

$$\hat{H}^{N_r} = \log(\pi e) + \int_{-1/2}^{1/2} \log \frac{\sigma^2}{|1 + \sum_{k=1}^{N_r} \hat{a}_k^{N_r} e^{-j2\pi k\tilde{\tau}}|^2} d\tilde{\tau}.$$

Cette entropie peut permettre des comparaisons entre les différentes classes de canal PLC. Par exemple, aux Figures 1.1(a) et 1.1(b), nous montrons que la classe 9 a une entropie relativement plus élevée que celle correspondant au canal de classe 3, ce qui implique que la classe 9 a une plus grande capacité de transmission.

Pour des échantillons de canal notés $\mathbf{c}$, la matrice de covariance de canal s'écrit

$$\mathbf{K}_{\mathbf{c}}^N = \frac{1}{N} \sum_{i=1}^{N} \mathbf{c}_i \mathbf{c}_i^H. \tag{1.6}$$

Ensuite, nous pouvons décomposer cette matrice en sous-espace de signal et sous-espace de bruit, i.e.,

$$\mathbf{K}_{\mathbf{c}}^N = \mathbf{U}_{\mathbf{c}} \mathbf{\Lambda}_{\mathbf{c}} \mathbf{U}_{\mathbf{c}}^H = \sum_{i=1}^{N} \lambda_i(\mathbf{c}) \psi_i(\mathbf{c}) \psi_i^H(\mathbf{c}), \quad \mathbf{U}_{\mathbf{c}}^H \mathbf{U}_{\mathbf{c}} = \mathbf{I}_N. \tag{1.7}$$

Le nombre de valeurs propres significatives, N, représente le degré de liberté (DoF) [136]. L'analyse des DoF montre que N n'augmente pas linéairement en fonction de

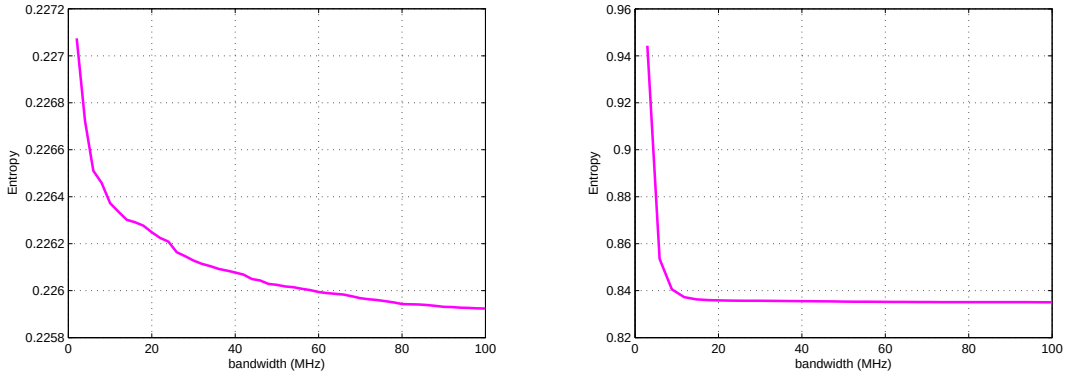

(a) class 3 (b) class 9

Figure 1.1: Entropie estimée pour : (a), (b)

la largeur de bande, voir Figure 1.2. En outre, nous observons qu'il existe un seuil de saturation et que ce seuil se produit plus tôt dans la classe de canal 9 cas que dans celle de classe 3. Par conséquent, on peut en déduire que les canaux de classe plus élevée pourraient être plus appropriés à une transmission par un système multi-bande.

Un article en relation avec ce chapitre a été publié à ISPLC09.

- H. Lin, A. Hayar and P. Siohan, "An information theoretical analysis on indoor PLC channel characterizations," *ISPLC '09*, Dresden, Germany, Mar. 2009.

1.4 Chapitre 5

Le chapitre précédent a montré que le canal PLC était multi-trajet et donc sélectif en fréquence. Pour lutter contre la sélectivité en fréquence, l'une des solutions possibles est d'utiliser une modulation multi-porteuse (MCM). De fait pour la transmission PLC en large bande, la MCM a été adoptée en normalisation [1]. La question qui s'est ensuite posée est : "Quel système MCM doit être utilisé dans la norme". Deux systèmes de MCM, nommés OFDM / DMT et Wavelet OFDM, et soutenus respectivement par HPAV et Panasonic, ont été retenus dans le projet de norme. Cette thèse présente un schéma alternatif, appelé OFDM/OQAM, et se concentre sur l'analyse de l'OFDM/OQAM par rapport à l'OFDM.

Dans ce chapitre, nous introduisons quelques outils mathématiques qui peuvent nous aider à mieux comprendre l'OFDM/OQAM d'un point de vue de la théorie de Gabor. Nous présentons tout d'abord la modulation OFDM/DMT, y compris ses avantages et ses inconvénients, ainsi que l'OFDM filtré (Windowed OFDM) proposé par HPAV. Ensuite, nous présentons l'OFDM/OQAM, du point de vue des principes de base, de la structure de réalisation et des différentes possibilités offertes pour le choix de son filtre prototype.

Dans le contexte PLC, où la transmission s'effectue préférentiellement en bande de base, nous introduisons une variante de l'OFDM/OQAM, intitulée HS-OQAM, utilisant une forme spécifique de symétrie hermitienne (HS). L'objectif est de conserver telle quelle la structure de l'OFDM/OQAM conventionnel et d'introduire certaines contraintes sur les

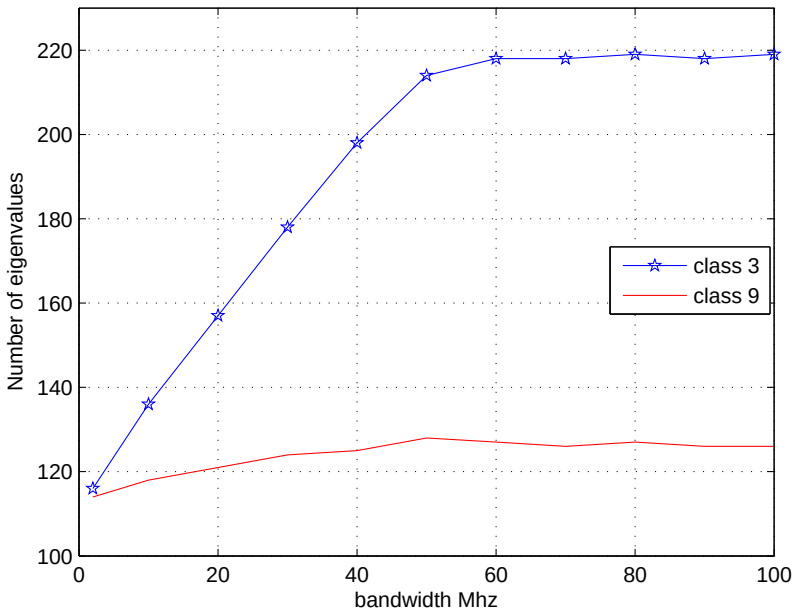

Figure 1.2: Evolution du nombre de valeurs propres pour les différentes classes de canaux.

symboles d'entrée afin obtenir un signal modulé à valeur réelle. Nous montrons également le lien entre le système HS-OQAM et le système de bancs de filtres en cosinus à phase linéaire (LP-CMFB). En fin de compte, nous indiquons quelles sont les motivations, pour utiliser dans le contexte PLC, le système HS-OQAM au lieu de l'OFDM. Nous ne donnons qu'un court aperçu concernant la solution Wavelet OFDM qui ne constitue pas une composante essentielle de la thèse[1].

La modulation multitone discrète (DMT) correspond au système de Gabor[2] le plus simple que l'on puisse imaginer. Au cours des deux dernières décennies, la DMT a été étudiée, dans plusieurs publications, pour la transmission dans des canaux multi-trajet. Les avantages théoriques de la DMT ont été démontrés dans un article pionnier de Kalet [73] publié il y a vingt ans. La DMT est la modulation phare pour la transmission Digital Subscriber Loops (DSL), et les références [31] et [119] en donnent d'excellentes descriptions. La DMT est un système de modulation équivalent à l'OFDM et possède donc les mêmes mérites. De fait elle a été retenue par l'alliance HomePlug AV pour la transmission PLC [5]. Toutefois, les inconvénients de l'OFDM/DMT ont également été remarqués par de nombreux chercheurs.

Une première limitation de la DMT est la nécessité, afin de contrecarrer l'interférence créée par le canal, de transmettre des éléments de signal, éventuellement nuls, sous forme d'un intervalle dit de garde. Dans [5], l'intervalle de garde proposé est une duplication de la partie du symbole OFDM et correspond donc au préfixe cyclique (CP) initialement

[1] Au chapitre 8, nous montrons néanmoins comment ce schéma de modulation peut s'intégrer dans une structure de modulateur (et démodulateur) unifiée.

[2] Le système de Gabor peut s'exprimer mathématiquement comme suit: $g_{m,n}(t) = g(t - nT_0)e^{j2\pi mF_0 t}$ avec deux paramètres T_0 et F_0 [54].

proposé par Peled et Ruiz [94]. Dans le reste de cette thèse, l'intervalle de garde de l'OFDM/DMT correspond au CP. Un second inconvénient du DMT/OFDM est que pour des applications à haut débit, comme le PLC, afin de ne pas interférer avec d'autres applications parallèles existantes, telles que des radios amateurs, la question du masque de protection est prépondérante pour la modulation. Ainsi, l'OFDM, du fait de sa mise en forme rectangulaire, a une mauvaise localisation en fréquence et ne peut pas satisfaire simplement un masque fréquentiel contraignant. La solution proposée par HPAV est de filtrer le symbole OFDM par une fenêtre ce qui conduit à un OFDM dit fenêtré (Windowed OFDM). Cette méthode de filtrage permet d'améliorer le spectre du signal à la fois dans les bords extrêmes et également à proximité des encoches (notches) imposées par la régulation. Toutefois, la localisation en fréquence n'est toujours pas très bonne. L'explication a déjà été donnée, dans le cadre de la théorie de Gabor par le théorème de Balian-Low qui montre que, pour les systèmes de Gabor à densité critique[3], nous ne pouvons pas avoir en même temps une orthogonalité en complexe et une bonne localisation temps-fréquence.

Une première alternative, est fournie avec la modulation MultiTone filtrée (FMT) introduite par Cherubini *et al.* [30]. La FMT correspond essentiellement à un système de Gabor sur-échantillonné. Ce sur-échantillonnage augmente le nombre de degrés de liberté et permet ainsi d'avoir une fonction de mise en forme bien localisée en temps et fréquence. En contre-partie, le suréchantillonnage, pour une durée temps symbole donnée identique pour les systèmes DMT et FMT, va multiplier dans le cas de la FMT l'écart inter-porteuse par le facteur de sur-échantillonnage et réduire d'autant l'efficacité spectrale théorique de la FMT. Puisque dans cette thèse, nous nous concentrerons uniquement sur les systèmes à densité (ou de manière équivalente échantillonnage) critique, nous ne reviendrons pas sur les systèmes de Gabor sur-échantillonnés. Les lecteurs intéressés par ce sujet peuvent se référer à [29, 15, 20, 16, 38, 113].

Par ailleurs, un autre schéma de modulation basé sur le système de Gabor, appelé O-QAM, a été proposé en 1981 par Hirosaki en 1981 [66]. Dans [66], O-QAM signifie orthogonally multiplexed QAM. L'acronyme OFDM/OQAM est introduit pour la première fois dans [52] où le terme OQAM retrouve sa signification d'origine Offset-QAM. Dans chaque cas le principe reste le même et correspond à celui introduit longtemps auparavant par Saltbzerg [109]. Toutefois ce n'est qu'à partir de l'article [52] que l'OFDM/OQAM est apparu, technologiquement parlant, comme une alternative crédible à l'OFDM. Cette référence montre en effet que, même dans le cas d'une densité critique (i.e. à efficacité spectrale maximum), l'OFDM/OQAM peut fournir un signal bien localisé en temps et fréquence. Cela peut sembler un brin miraculeux dans la mesure où on s'affranchit de la régle édictée par le théorème de Balian-Low. En réalité, l'article [52] est le premier à montrer que ce n'est pas exactement le cas car pour l'OFDM/OQAM la condition d'orthogonalité ne s'appliquant pas dans le corps des complexes mais dans celui des réels

Une autre étape importante a consisté avec Siohan *et al.* à revisiter l'OFDM/OQAM dans le cadre de la théorie des bancs de filtres et à fournir des schémas d'implémentations efficaces, à base de FFTs, pour un modulateur/démodulateur OFDM/OQAM causal [115].

Puisque l'OFDM/OQAM peut utiliser des filtres prototypes bien localisés et en même temps permet d'atteindre une efficacité spectrale maximum, il a paru naturel, lors de la conférence ISPLC 2007, de le proposer pour la transmission PLC [117]. Dans cet article

[3] Atteignant en théorie l'efficacité spectrale maximum.

les auteurs ont fourni des résultats expérimentaux qui montrent que l'OFDM/OQAM est robuste aux interférences à bande étroite et rentre aisément dans le masque de spécification de HPAV. En parallèle, Lélé *et al.* a presenté, dans le cadre de cette même conférence, des méthodes d'estimation de canal pour l'OFDM/OQAM montrant que l'OFDM/OQAM était plus performant que le CP-OFDM/DMT dans le contexte PLC. Cependant, à la différence du Windowed OFDM et du WOFDM, l'OFDM/OQAM ne correspond pas naturellement à un schéma de transmission en bande de base et fournit un signal à valeur complexe.

En s'inspirant des conditions imposées aux symboles injectés en entrée de la DMT, nous pouvons de la même façon présenter les conditions de symétrie hermitienne (HS) pour les symboles en entrée de l'OFDM/OQAM conventionnel (sans en changer la structure du système, i.e., gardant la même taille de FFT et la même largeur de bande). Ceci nous conduit à un système intitulé HS-OQAM qui peut s'appliquer directement pour le PLC en bande de base.

Pour des symboles de donnée de durée T_0 et un espacement en fréquence $F_0 = 1/T_0$, le signal OFDM/OQAM à temps discret s'obtient pour une période d'échantillonnage T_s, telle que $T_0 = MT_s$, par

$$s[k] = \sum_{m=0}^{M-1} \sum_{n \in \mathcal{Z}} a_{m,n} \underbrace{g[k - nN] e^{j\frac{2\pi}{M} m\left(k - \frac{D}{2}\right)} e^{j\phi_{m,n}}}_{g_{m,n}[k]}. \tag{1.8}$$

La variante HS-OQAM se déduit de l'OFDM/OQAM conventionnel, en introduisant pour $m = 1, \cdots, N-1$, des contraintes HS données par

$$a_{0,n} = a_{N,n} = 0;$$

et

$$a_{m,n} = a_{M-m,n} (-1)^{D-N-n} e^{-j2\phi_0}. \tag{1.9}$$

M est le nombre total de porteuses; g est le filtre prototype; $D = L_g - 1$ et L_g est la longueur du filtre g; $N = M/2$ est le décalage (offset) en temps discret; $\phi_{m,n}$ est un terme de phase additionel qui peut s'exprimer par $\frac{\pi}{2}(n+m) + \phi_0$, ϕ_0 peut être choisi arbitrairement; Les symboles transmis $a_{m,n}$ sont à valeur réelle. Ils peuvent être obtenus à partir d'une constellation 2^{2K}-QAM, en prenant les parties réelles et imaginaires de ces symboles à valeur complexe. Ensuite, dans ce chapitre, nous montrons qu'il existe un lien entre HS-OQAM et les bancs de filtres à phase linéaire modulés en cosinus, i.e., le système HS-OQAM peut être vu comme une version de transmultiplexeur duale du banc de filtres LP-CMFB.

Dans ce chapitre, nous donnons aussi une brève présentation de notre ensemble initial de filtres prototypes, c-a-d, le filtre prototype en racine de cosinus surélevé (SRRC), le prototype dit Isotropic Orthogonal Transform Algorithm (IOTA), et des filtres prototypes optimisés directement en temps discret selon les critères de localisation temps-fréquence (TFL) et de sélectivité fréquentielle (FS). Pour les filtres prototypes SRRC et FS, en plus de la longueur, L_g, et du nombre de porteuses, M, le paramètre de facteur de retombée, noté r (ou ρ), est aussi à prendre en compte.

Nous avons publié un article de conférence en relation avec ce chapitre.

- H. Lin and P. Siohan, "OFDM/OQAM with hermitian symmetry: Design and performance for baseband communications," *ICC '08*, Beijing, China, May 2008.

1.5 Chapitre 6

Ce chapitre est dédié à l'étude d'un modèle théorique pour la transmission OFDM/OQAM dans un canal non idéal. Si le canal de transmission est multi-trajet et invariant dans le temps, le signal démodulé à la position (m_0, n_0) peut s'écrire

$$\begin{aligned} y_{m_0,n_0} &= \underbrace{\sum_{l=0}^{L_h-1} c_l A_g[-l,0] e^{-j\frac{2\pi m_0 l}{M}}}_{\text{distorsion : } \alpha_{m_0}} a_{m_0,n_0} + \underbrace{\left(\begin{array}{l} \sum_{(p^0,q^0)} a_{m_0+p,n_0+q} e^{j\frac{\pi}{2}(p+q+pq)} e^{j\pi p n_0} \\ \cdot \underbrace{\sum_{l=0}^{L_h-1} c_l A_g[-qN-l, pF_0] e^{-j\frac{\pi(2m_0+p)l}{M}}}_{H_{m_0}^{(p,q)}} \end{array} \right)}_{\text{ISI+ICI : } J_{m_0,n_0}} \\ &= \alpha_{m_0} a_{m_0,n_0} + \underbrace{J_{m_0,n_0}|_{(p=0,q\neq 0)}}_{\text{ISI}} + \underbrace{J_{m_0,n_0}|_{(p\neq 0)}}_{\text{ICI}}, \end{aligned} \tag{1.10}$$

où les coefficients c_l correspondent à la réponse impulsionnelle d'un canal comprenant L_h trajets. $A_g(\tau,\nu)$, fonction d'ambiguité du filtre prototype g, a pour expression en temps continu :

$$A_g(\tau,\nu) = \int_{-\infty}^{\infty} g(t+\frac{\tau}{2}) g^*(t-\frac{\tau}{2}) e^{j2\pi\nu t}\, dt. \tag{1.11}$$

Son expression en temps-discret est donnée par $A_g[l,k] = A_g(lT_s, kF_0)$. (p,q) sont deux entiers qui ne peuvent être nuls simultanément. Il est ensuite possible de calculer la puissance d'interférence : l'interférence inter-symboles (ISI) et l'interférence entre porteuses (ICI), i.e.,

$$\begin{aligned} P_{\text{ISI+ICI}}^{\text{demod}}(m_0) &= \mathrm{E}\left[|J_{m_0,n_0}|^2\right] \\ &= \sum_{(p^0,q^0)} \sum_{(p'^0,q'^0)} \mathrm{E}\left[a_{m_0+p,n_0+q} a_{m_0+p',n_0+q'}\right] \\ &\times\ e^{j\frac{\pi}{2}(p+q+pq)} e^{j\pi p n_0} e^{-j\frac{\pi}{2}(p'+q'+p'q')} e^{-j\pi p' n_0} H_{m_0,n_0}^{(p,q)} H_{m_0}^{(p',q')} \\ &= \sigma_a^2 \sum_{(p^0,q^0)} \left| H_{m_0}^{(p,q)} \right|^2. \end{aligned} \tag{1.12}$$

Il faut noter cependant que (6.12) correspond à l'expression de la puissance d'interférence après démodulation et de fait nous la notons avec l'exposant $^{\text{demod}}$. Avant détection, il est également nécessaire d'effectuer les opérations de "prise de partie réelle" et d'égalisation.

En considérant simplement la prise de partie réelle, i.e., pas d'égaliseur, l'interférence est donnée par $I_{m_0,n_0} = \mathrm{Re}\{J_{m_0,n_0}\}$. Par conséquent, sa puissance s'écrit

$$P_{\text{ISI+ICI}}^{\mathrm{Re}\{\text{demod}\}}(m_0) = \mathrm{E}\left[|I_{m_0}|^2\right] = \sigma_a^2 \sum_{(p^0,q^0)} \left| \mathrm{Re}\{ e^{j\frac{\pi}{2}(p+q+pq)} H_{m_0}^{(p,q)} \} \right|^2. \tag{1.13}$$

De fait, les expressions de l'ISI et de l'ICI sont données par

$$P_{\text{ISI}}^{\mathrm{Re}\{\text{demod}\}}(m_0) = \sigma_a^2 \sum_{q\neq 0} \left| \mathrm{Re}\{ e^{j\frac{\pi}{2}q} H_{m_0}^{(0,q)} \} \right|^2, \tag{1.14}$$

et

$$P_{\mathrm{ICI}}^{\mathrm{Re}\{\mathrm{demod}\}}(m_0) = \sigma_a^2 \sum_{(p\neq 0, q\in\mathcal{Z})} \left|\mathrm{Re}\{e^{j\frac{\pi}{2}(p+q+pq)} H_{m_0}^{(p,q)}\}\right|^2. \tag{1.15}$$

Finalement, le rapport Signal-à -Interférence (SIR), pour la sous-porteuse m_0 s'écrit

$$\mathrm{SIR}_{m_0}^{\mathrm{Re}\{\mathrm{demod}\}} = \frac{|\mathrm{Re}\{\alpha_{m_0}\}|^2}{P_{\mathrm{ISI+ICI}}^{\mathrm{Re}\{\mathrm{demod}\}}(m_0)}. \tag{1.16}$$

De manière évidente, on peut également exprimer séparément les rapports signal à interférence inter-symboles et signal à interférence inter-porteuses en fonction de notre objectif d'analyse.

Supposons à présent qu'un simple égaliseur à un coefficient (également dit à un tap) de type zéro-forcing (ZF) est utilisé à la réception, i.e., placé entre les opérations de démodulation et de prise de partie réelle. De ce fait, la puissance de l'interférence à l'entrée du détecteur de la m_0-ième sous -porteuse s'écrit

$$P_{\mathrm{ISI}}^{\mathrm{Re}\{\mathrm{ZF}\}}(m_0) = \sigma_a^2 \sum_{q\neq 0} \left|\mathrm{Re}\{\frac{e^{j\frac{\pi}{2}q} H_{m_0}^{(0,q)}}{H_{m_0}}\}\right|^2, \tag{1.17}$$

et

$$P_{\mathrm{ICI}}^{\mathrm{Re}\{\mathrm{ZF}\}}(m_0) = \sigma_a^2 \sum_{(p\neq 0, q\in\mathcal{Z})} \left|\mathrm{Re}\{\frac{e^{j\frac{\pi}{2}(p+q+pq)} H_{m_0}^{(p,q)}}{H_{m_0}}\}\right|^2, \tag{1.18}$$

où H_{m_0} est le coefficient de l'égaliseur pour la sous-porteuse m_0 et peut se calculer par

$$H_{m_0} = \sum_{l=0}^{L_h-1} c_l e^{-j\frac{2\pi l m_0}{M}}. \tag{1.19}$$

Le rapport Signal-à-Interférence-Plus-Bruit (SINR) pour la sous-porteuse m_0 après l'opération "prise de partie réelle" s'écrit

$$\mathrm{SINR}_{m_0} = \frac{\left|\mathrm{Re}\{\frac{\alpha_{m_0}}{H_{m_0}}\}\right|^2 \sigma_a^2}{P_{\mathrm{ISI+ICI}}^{\mathrm{Re}\{\mathrm{ZF}\}}(m_0) + \frac{\sigma_n^2}{2|\mathrm{Re}\{H_{m_0}\}|^2}}. \tag{1.20}$$

Le calcul théorique du SINR peut nous fournir l'expression du taux d'erreur binaire (BER)

$$P_b = \frac{1}{M} \sum_{m_0=0}^{M-1} P_b^{\mathrm{fselect}}(m_0), \tag{1.21}$$

avec un BER par sous-porteuse pour une constellation 2^{2K}-QAM (codage de Gray), donné par

$$\begin{aligned} P_b(m_0) &\approx \frac{2^K-1}{2^K\cdot K}\mathrm{erfc}\left(\sqrt{\frac{3}{2}\cdot\frac{\mathrm{SINR}_{m_0}}{2^{2K}-1}}\right) \\ &+ \frac{2^K-2}{2^K\cdot K}\mathrm{erfc}\left(3\sqrt{\frac{3}{2}\cdot\frac{\mathrm{SINR}_{m_0}}{2^{2K}-1}}\right). \end{aligned} \tag{1.22}$$

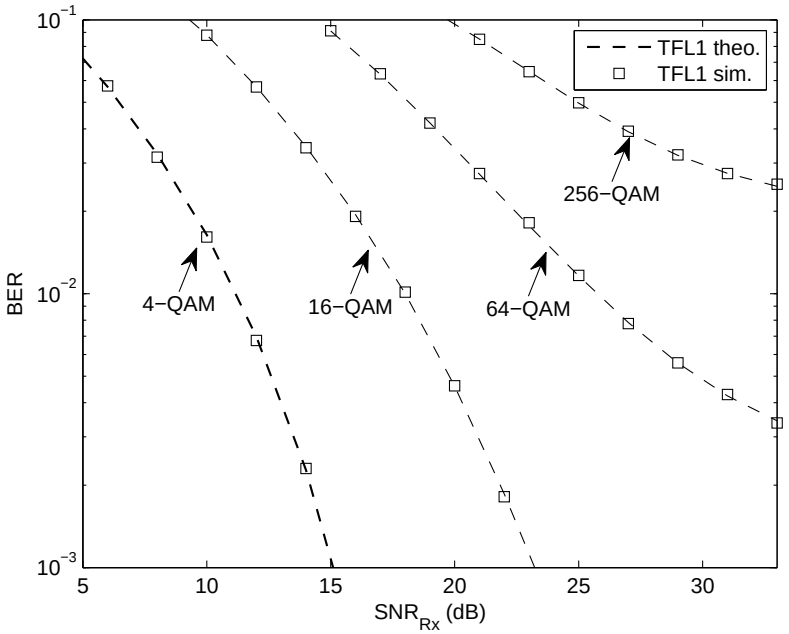

Figure 1.3: Comparaison des taux d'erreur bit : théorie vs. simulation pour le canal de Ma [87] avec $L_f = M = 128$.

La validité de l'approximation proposée pour le calcul théorique de la probabilité d'erreur est illustrée à la Figure 1.3 par une comparaison avec les résultats de la simulation du système de transmission. Le filtre prototype utilisé pour cette validation est le filtre dit TFL1 obtenu pour $L_f = M = 128$.

Cette démonstration montre explicitement l'impact de l'interférence sur la performance en transmission. En fait, cet impact est directement lié au filtre prototype retenu. De fait, dans ce chapitre, nous comparons les différents filtres prototypes de notre ensemble initial afin de déterminer un bon critère de design pour la transmission OFDM/OQAM sur un modèle théorique de canal PLC [87]. Dans un premier essai, nous supposons que nos filtres prototypes sont courts tels que $L_f = M$ avec $M = 128$ et nous utilisons la constellation 64-QAM. Les résultats sont reportés aux Figures 1.4 et 1.5. Ils montrent que le critère TFL conduit à la plus faible puissance d'interférence, ce qui se traduit par une meilleure performance en termes de taux d'erreur binaire. Par principe le critère TFL est approprié pour produire des filtres courts car ceux ci doivent être bien localisés en temps. De plus, comme la localisation fréquentielle est également prise en compte, le résultat est acceptable dans le domaine fréquentiel.

A contrario, le critère FS, qui ne s'intéresse qu'à la caractéristique de sélectivité fréquentielle, et ne prend pas en compte l'aspect temporel, n'est pas approprié pour, produire des filtres protoypes courts et de bonne qualité. Ceci peut se vérifier en reprenant l'ensemble de comparaison précédent mais en augmentant cette fois la longueur du filtre prototype qui est à présent donnée par $L_f = 4M$ pour tous les filtres à l'exception de celui optimisé selon le critère TFL. Les résultats sont donnés aux Figures 1.6 et 1.7. Les

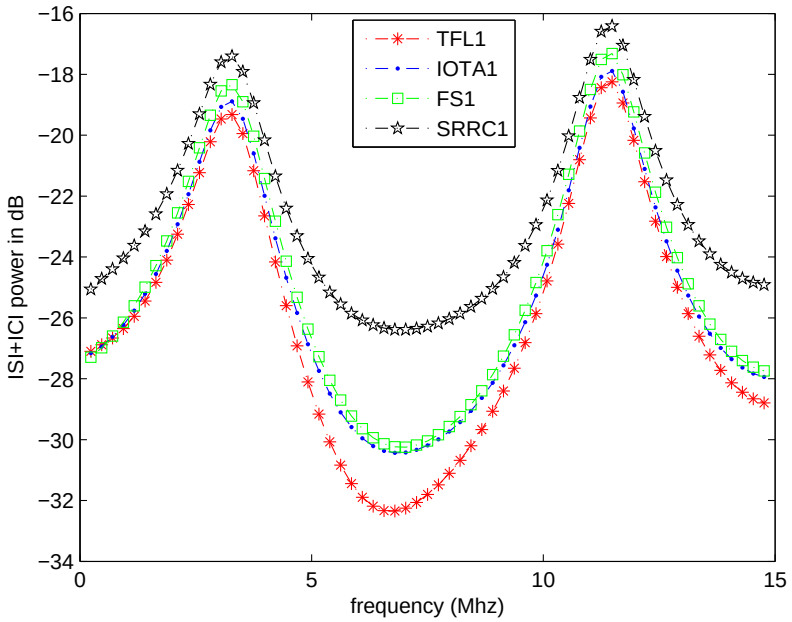

Figure 1.4: Comparaison de l'interférence pour une longueur de filtre $L_f = M = 128$ (Canal de Ma [87]).

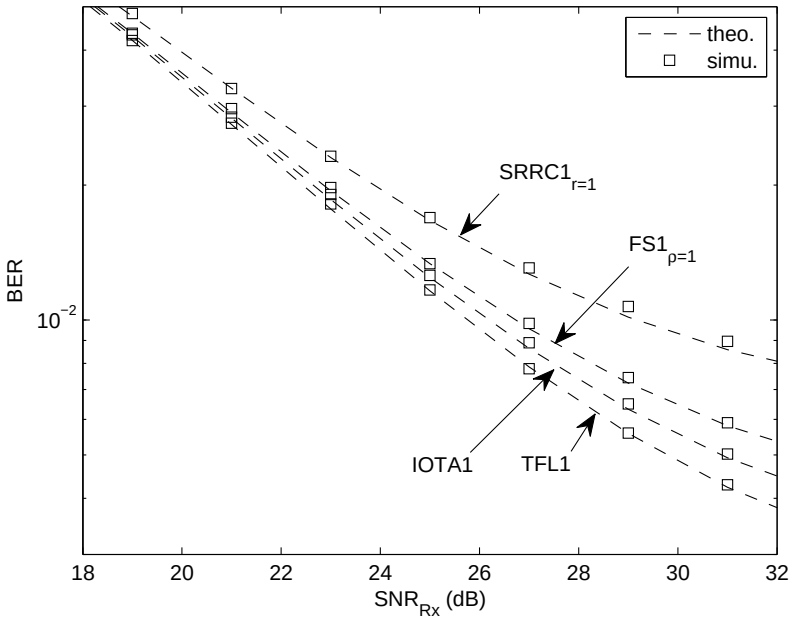

Figure 1.5: Comparaison des taux d'erreur bit en 64-QAM pour une longueur de filtre $L_f = M = 128$ (Canal de Ma [87]).

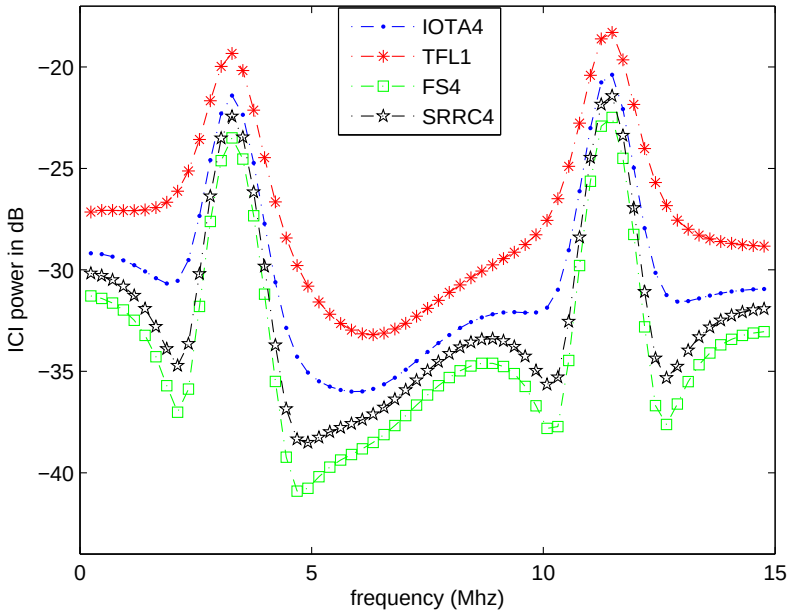

Figure 1.6: Comparaison de l'interférence entre porteuses pour pour une longueur de filtre $L_f = 4M$ avec $M = 128$ (Canal de Ma [87]).

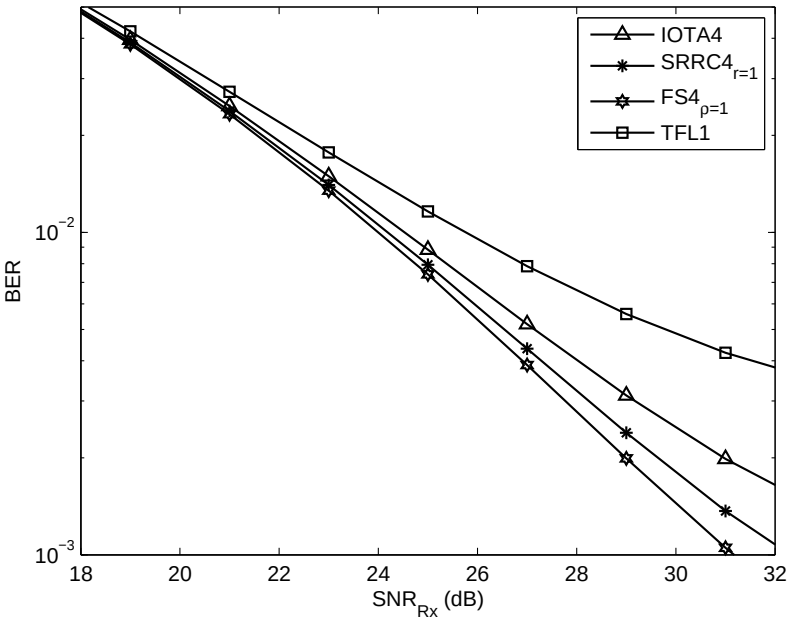

Figure 1.7: Comparaison des taux d'erreur bit en 64-QAM pour une longueur de filtre $L_f = 4M$ avec $M = 128$ (Canal de Ma [87]).

simulations montrent que le critère FS peut très bien fonctionner à condition que le filtre prototype puisse être choisi de longueur suffisante.

Les filtres prototypes conçus selon les critères TFL et FS ont en commun la propriété d'être à reconstruction parfaite (PR). Par suite, la question que l'on peut se poser est : que se passe-t-il si on relâche la contrainte d'orthogonalité ? De cette façon nous pouvons bénéficier de plus de degrés de liberté dans leur conception. Ceci nous amène à introduire un autre type de critère où l'on recherche un filtre sélectif en fréquence (FS) mais vérifiant simplement une contrainte de reconstruction presque parfaite (NPR). Dans ce chapitre, deux différentes méthodes de design sont choisies qui satisfont ce nouveau critère.

La première nous conduit à un filtre prototype appelé prototype Rossi [108] et la seconde fournit le prototype dit Mirab en liaison avec la référence [90]. La comparaison des performances entre les filtres prototypes Mirab, Rossi, FS, SRRC prototype donne le résultat reporté à la Figure 1.8. Il montre que le prototype Mirab peut fournir la meilleure performance mais aussi que le gain est très faible par rapport aux prototypes Rossi ou FS. Seule la différence de ces 3 prototypes par rapport à SRRC est un peu significative.

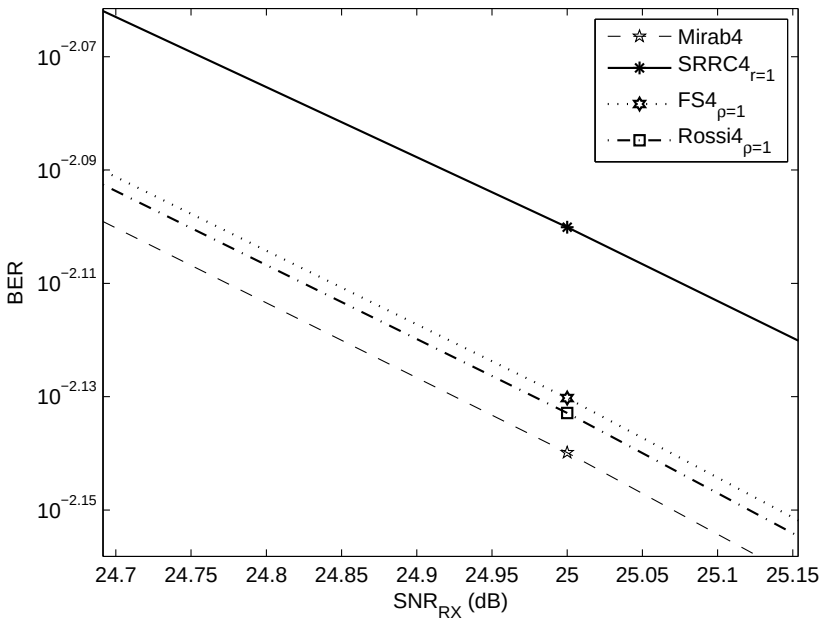

Figure 1.8: Comparaison des taux d'erreur bit en 64-QAM pour une longueur de filtre $L_f = 4M$ avec $M = 128$ (Canal de Ma [87]).

Les articles publiés, ou soumis, en relation avec ce chapitre sont :

- H. Lin and P. Siohan, "HS-OQAM PLC: Long Prototype Filter or Equalizer?," *WSPLC '09*, Udine, Italy, Oct. 2009.

- H. Lin and P. Siohan, "Long Prototype Filter or Complex Equalizer? When OFDM/OQAM Meets Frequency Selective Fading," *soumis*, 2009.

1.6 Chapitre 7

Dans ce chapitre, nous proposons deux méthodes d'égalisation de l'OFDM/OQAM en complément de la technique ZF à un coefficient utilisée dans le chapitre précédent. En réalité, l'égalisation par sous-porteuse du système OFDM/OQAM a déjà été discutée il y a bien longtemps par Hirosaki dans deux de ses articles [65, 66]. Cependant, cette méthode est relativement complexe à mettre en œuvre du fait du réalignement imposé aux composantes en phase et en quadrature [65]. Plus tard, Qin et Bellanger ont proposé une égalisation adaptative par porteuse utilisant soit un échantillonage à fréquence critique ou à la fréquence double [102]. Par ailleurs, Nedic *et al.*, dans [91], a aussi introduit une égalisation adaptative par porteuse pour l'OFDM/OQAM, mais la complexité demeure encore relativement élevée.

En outre, quelques références (e.g. [126, 67, 134]) proposent une égalisation avec un filtre FIR minimisant l'erreur quadratique moyenne (MMSE) par porteuse en OFDM/OQAM. Le problème de complexité demeure encore avec la nécessité d'inverser une matrice de canal non diagonale.

De manière différente, dans ce chapitre nous proposons, avec notre première méthode, d'utiliser un égaliseur adaptatif dit point-wise initialement proposé pour un transmultiplexeur basé sur un système de banc de filtres en sinus et cosinus (ASCET) [69]. Nous proposons de modifier cet égaliseur pour l'adapter au système OFDM/OQAM. Nous montrons que les coefficients de l'égaliseur ASCET vont dépendre du terme de phase du système OFDM/OQAM :

$$\phi_{m,n} \text{ dans } [52] \begin{cases} c_{0m} = -\frac{1}{2}\left(\frac{\eta_{-1m}-\eta_{1m}}{2} - j\left(\eta_{0m} - \frac{\eta_{-1m}+\eta_{1m}}{2}\right)\right) \\ c_{1m} = \frac{\eta_{-1m}+\eta_{1m}}{2} \\ c_{2m} = -\frac{1}{2}\left(\frac{\eta_{-1m}-\eta_{1m}}{2} + j\left(\eta_{0m} - \frac{\eta_{-1m}+\eta_{1m}}{2}\right)\right) \end{cases} \tag{1.23}$$

et

$$\phi_{m,n} \text{ dans } [115] \begin{cases} c_{0m} = \mp\frac{1}{2}\left(\frac{\eta_{-1m}-\eta_{1m}}{2} - j\left(\eta_{0m} - \frac{\eta_{-1m}+\eta_{1m}}{2}\right)\right) \\ c_{1m} = \frac{\eta_{-1m}+\eta_{1m}}{2} \\ c_{2m} = \mp\frac{1}{2}\left(\frac{\eta_{-1m}-\eta_{1m}}{2} + j\left(\eta_{0m} - \frac{\eta_{-1m}+\eta_{1m}}{2}\right)\right) \end{cases} \tag{1.24}$$

où, dans (1.24), le signe - s'applique aux porteuses paires et le + aux porteuses impaires. En outre, nous présentons également les performances théoriques de l'OFDM/OQAM avec l'égaliseur ASCET.

La deuxième méthode d'égalisation proposée est nommée égalisation avec annulation d'interférences (EIC). Cette méthode tire parti de la connaissance que nous avons de l'expression de l'interférence. Pourquoi ne pas utiliser un expression approchée et retirer directement le terme d'interférence afin de l'annuler ? Les expressions mathématiques de l'égaliseur consistent à obtenir dans une première étape les estimées des symboles reçus

$$\hat{a}^{(1)}_{m_0,n_0} = \text{HD}\left[\text{Re}\left\{\frac{y_{m_0,n_0}}{H_{m_0}}\right\}\right], \tag{1.25}$$

où HD[·] représente une décision dure et H_{m_0} est le coefficient ZF déduit de l'estimation de canal. Dans une seconde étape, l'estimation des symboles s'affine en retirant le terme

d'interférence estimée

$$\hat{a}^{(2)}_{m_0,n_0} = \mathrm{Re}\left\{ \frac{y_{m_0,n_0} - \hat{J}_{m_0,n_0}}{\sum_{l=0}^{L_h-1} c_l A_g[-l,0] e^{-j\frac{2\pi m_0 l}{M}}} \right\}. \tag{1.26}$$

Toutefois, un calcul direct de $\hat{J}_{m_0,n_0}$ conduit à une complexité opératoire de l'ordre de M^2 pour chaque position temps-fréquence (m_0, n_0) avec M qui sera généralement très grand. Dans la sous-section à venir, nous discutons de l'implémentation de l'égaliseur EIC et de la complexité qui en résulte au final. Pour que l'égaliseur EIC ait du sens cette implémentation doit être efficace. Dans ce chapitre, nous introduisons trois éléments qui contribuent à réduire significativement sa complexité.

- Tout d'abord avec un filtre prototype bien localisé en temps et fréquence, la sommation dans (7.26) peut être limitée à un voisinage de petite taille autour de (m_0, n_0).
- Deuxièmement, $\hat{J}_{m_0,n_0}$ peut se calculer par des FFTs dont la complexité peut être réduite en tenant compte des propriétés de symétrie de la fonction d'ambiguité.
- Troisièmement, puisque le retard introduit par le canal est significativement moindre que T_0 (en temps discret, cela signifie que la longueur du canal, notée L_h, est simplement une fraction de M), la complexité opératoire peut être réduite avec des algorithmes de FFT élaguées (cf. [88, 116]).

Ensuite, nous présentons une comparaison entre deux options très intéressantes, l'une utilise le filtre prototype court optimisé selon le critère TFL sous la contrainte PR (TFL1) en combinaison avec l'égaliseur ASCET ou EIC, l'autre se base sur le filtre prototype sélectif en fréquence satisfaisant approximativement la condition PR (NPR), i.e., Rossi4$_{\rho=1}$ avec l'égaliseur ZF à un tap.

Les résultats sont présentés à la Figure 1.9, où il apparaît nettement que lorsque l'égaliseur le plus simple (le ZF) est utilisé le filtre prototype TFL1 donne une performance inférieure à celle du filtre Rossi4$_{\rho=1}$. Cependant, quand, avec le filtre TFL1, nous utilisons l'égaliseur ASCET au lieu du ZF, nous aboutissons, pour un BER de 10^{-2}, à une performance comparable à celle obtenue par la combinaison Rossi4$_{\rho=1}$ avec égaliseur ZF. De la même manière, l'application de l'égaliseur κ-EIC pour $\kappa = 1$ nous permet au final d'obtenir une performance supérieure à celle correspondant aux deux cas précédents. La comparaison en termes de complexité opératoire et de latence entre les combinaisons filtre Rossi4 avec ZF, filtre TFL1 avec égaliseur ASCET et aussi κ-EIC est présentée dans le tableau 1.1. La complexité est comparée par le nombre d'opérations réelles, i.e., multiplications (RM) et additions (RA), en supposant que multiplications et additions en complexe, CM et CA, sont telles que 1CM=4RM+2RA et 1CA=2RA.

Les articles publiés et soumis en relation avec ce chapitre sont :

- H. Lin, C. Lélé and P. Siohan, "Equalization with Interference Cancellation for Hermitian Symmetric OFDM/OQAM systems," *ISPLC '08*, Jeju Island, South Korea, Apr. 2008.
- H. Lin and P. Siohan, "HS-OQAM PLC: Long Prototype Filter or Equalizer?," *WSPLC '09*, Udine, Italy, Oct. 2009.

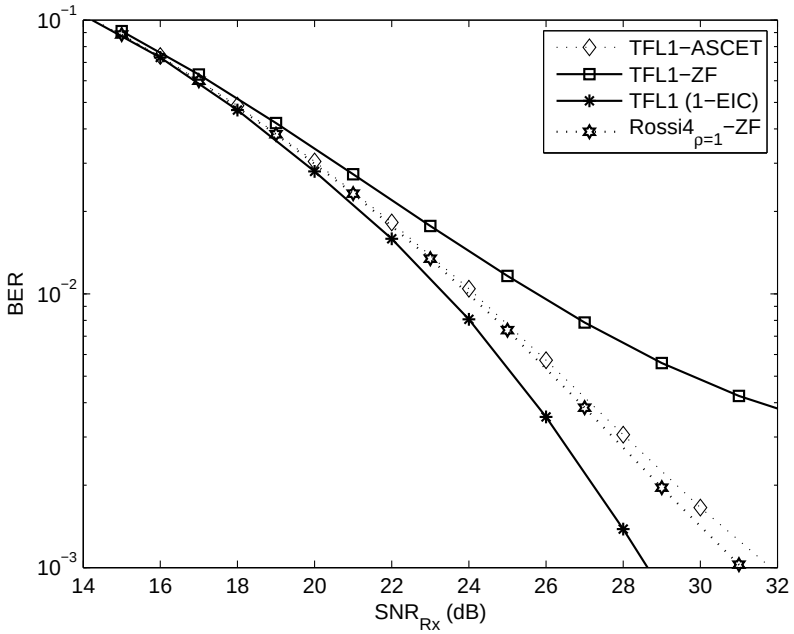

Figure 1.9: Comparaison des taux d'erreur bit en 64-QAM pour une longueur de filtre $L_f = 4M$ avec $M = 128$ (Canal de Ma [87]).

Table 1.1: Comparison complexité et latence (pour $M = 128$).

	TFL1-ASCET			Rossi4-ZF			TFL1-EIC ($\kappa = 1$)		
	Polyphase	Egaliseur		Polyphase	Egaliseur		Polyphase	Egaliseur	
		online	periodic		online	periodic		online	periodic
RM	1024	762	1260	4096	252	0	1024	2520	7648
RA	512	633	1260	3584	126	0	512	2268	13952
Latence	$2\tau_0$			$8\tau_0$			$(2+\kappa)\tau_0 = 3\tau_0$		

- H. Lin, P. Siohan, P. Tanguy and J-P. Javaudin "An analysis of EIC for OFDM/OQAM systems," *Journal of Communications (JCM)*, vol. 4, no. 1, pp. 52-60, Feb., 2008.
- H. Lin and P. Siohan, "Capacity analysis for PLC with different multi-carrier modulations," *IEEE Trans. on Power Delivery*, Vol. 25, no. 1, pp. 113-124, Jan. 2010.
- H. Lin and P. Siohan, "Long Prototype Filter or Complex Equalizer? When OFDM/OQAM Meets Frequency Selective Fading," *submitted*, 2009.

1.7 Chapitre 8

La flexibilité joue un rôle primordial dans les communications modernes. La modulation multiporteuse est un très bon exemple avec l'opération d'allocation de ressource (bit loading), qui rend flexible le nombre de bits transmis sur chaque porteuse utile en fonction de l'environnement de transmission. En général, la flexibilité offerte par le bit loading apporte un gain significatif par rapport à une choix uniforme des constellations de modu-

lation. Dans ce chapitre, nous montrons deux autres types de flexibilité qui peuvent être exploitées dans le cas des PLC. Le premier correspond à une flexibilité de modulation multiporteuse. Comme son nom l'indique, le gain attendu provient d'une combinaison intégrant différents schémas de modulations multiporteuses envisageables en PLC. En réalité, chaque schéma de modulation, que ce soit DMT ou HS-OQAM etc., a ses avantages et inconvénients. Dans l'absolu, il n'existe pas de schéma qui puisse être tout le temps le meilleur quelle que soit le canal et les contraintes systèmes. Par conséquent, si nous pouvons trouver une modulateur qui possède tous les avantages déjà existants et dans le même temps évite leurs inconvénients, au bout du compte ce modulateur sera le meilleur.

Dans ce chapitre, nous proposons un modulateur multiporteuse (MCM) unifié de ce type et un algorithme pour son implémentation. Comme ce modulateur peut générer HS-OQAM, DMT et aussi WOFDM, un mode de sélection approprié permet d'obtenir un gain dû à cette flexibilité.

Nous analysons tout d'abord la capacité de transmission des modulations HS-OQAM et DMT. Une comparaison similaire pourrait également être réalisée entre DMT et WOFDM. Les expressions analytiques de la capacité pour HS-OQAM sont données par

$$R_{\text{OQAM-ZF}} = F_0 \sum_{m=0}^{M_u-1} \log_2 \left(1 + \frac{\text{SINR}_m^{\text{OQAM-ZF}}}{\Gamma}\right), \tag{1.27}$$

et

$$R_{\text{OQAM-ASCET}} = F_0 \sum_{m=0}^{M_u-1} \log_2 \left(1 + \frac{\text{SINR}_m^{\text{OQAM-ASCET}}}{\Gamma}\right), \tag{1.28}$$

où le calcul du SINR par sous-porteuse est presenté au chapitre précédent et où M_u correspond au nombre de porteuses utiles, m désigne la m-ième porteuse utile. Γ est le "SNR gap" qui est utilisé pour mesure l'écart d'un système par rapport à la capacité de Shannon. En l'absence de codage de canal, et omettant tous les dégradations non prédictibles liées au canal, ce gap dépend uniquement du taux d'erreur symbole (SER), i.e., $\Gamma = \frac{1}{3}\left[\mathbf{Q}^{-1}(\frac{\text{SER}}{4})\right]^2$ [33, 59]. Il faut noter que, bien entendu, la capacité du système HS-OQAM dépend de la méthode d'égalisation utilisée en réception.

Pour le système DMT, en se basant sur les références [112, 92], la capacité peut s'écrire

$$R_{\text{DMT}} = \frac{M}{M + L_{\text{cp}}} F_0 \sum_{m=0}^{M_u-1} \log_2 \left(1 + \frac{\text{SINR}_m^{\text{DMT}}}{\Gamma}\right),$$

où l'expression du SINR par sous-porteuse est approximée par [112, 92]

$$\text{SINR}_m^{\text{DMT}} \approx \frac{|H_m|^2 \sigma_c^2}{\sigma_n^2 + N_{\text{ISI+ICI}}(m)}. \tag{1.29}$$

avec

$$N_{\text{ISI+ICI}}(m) = 2\sigma_c^2 \sum_{l=L_{\text{cp}}+1}^{L_h-1} \left| \sum_{i=l}^{L_h-1} c_i e^{-j\frac{2\pi}{M} im} \right|^2, \tag{1.30}$$

où σ_c^2 et σ_n^2 correspondent respectivement à la variance des symboles complexes, $c_{m,n}$, en entrée de la DMT et au bruit additif gaussien; c est la CIR de longueur L_h; L_{cp} est la

Table 1.2: Tableau des SNR_{Tx} seuils pour la spécification HomePlug AV.

SNR_{Tx} seuil (dB)	classe 2	classe 3	classe 4	classe 5	classe 6	classe 7	classe 8	classe 9
HS-OQAM-ZF	79	73.5	72	67	65	63	60.2	60
HS-OQAM-ASCET	83	78	75.6	71	69	66	63.5	63

longueur du CP. On notera que quand la longueur du CP est supérieure à celle du retard lié au canal, le symbole d'approximation de l'équation (1.29) se transforme en égalité.

De ce fait, à travers la comparaison de la capacité de transmission des systèmes HS-OQAM et DMT, nous pouvons trouver une valeur seuil de SNR afin de décider quel est le schéma qui offre la plus grande capacité. Ensuite, en se référant à ces SNR_{Tx} seuils en transmission, nous sommes capables de décider quelle est la modulation la plus appropriée pour un canal PLC donné.

Les seuils de SNR_{Tx} dépendent aussi du filtre prototype utilisé pour le système HS-OQAM. Les seuils auxquels on fait référence dans ce chapitre ont été calculés pour le TFL1. L'utilisation d'un autre filtre prototype impliquera une modification des valeurs seuils de SNR_{Tx}. A titre d'exemple, nous avons évalué le SNR_{Tx} seuil dans le cas HS-OQAM vs. DMT pour la spécification HomePlug AV [5] dans laquelle, la taille de FFT est de 3072; la fréquence d'échantillonnage de 75 MHz; la longueur du CP pour la DMT est de 417 échantillons, et le SER cible est fixé à 10^{-3}. Pour cette simple comparaison, nous n'avons pas introduit d'encoches à des fréquences particulières [5] et le bruit de fond est supposé être additif, blanc et gaussien. Les SNR_{Tx} seuils sont donnés au Tableau 1.2, pour des réponses en fréquence correspondant aux modèles de canaux réalistes de chacune des classes décrite dans l'annexe 10.1. A partir de cette table, nous pouvons décider quand il est préférable de choisir soit la DMT pour les valeurs supérieures au seuil, soit HS-OQAM, dans le cas inverse.

Ensuite, nous examinons comment réaliser en pratique la commutation entre systèmes de modulation. Nous introduisons un système MCM unifié émetteur-récepteur qui va permettre d'obtenir le gain de flexibilité. La recherche d'une structure unifiée n'est pas seulement motivée par l'aspect capacité en transmission PLC, elle peut aussi servir, par exemple, pour la future norme ITU G.hn, qui vise à réaliser un système de transmission filaire unifié dans l'environnement in-door, applicable aux lignes téléphoniques, câbles coaxiaux et lignes électriques [53]. Dans ce contexte, où nous sommes confrontés à différentes conditions de transmission du fait de la grande diversité des canaux, la flexibilité offerte par une structure de transrécepteur multiporteuse unifiée peut être d'un grand intérêt.

De plus, dans la récente version draft de la norme PLC IEEE P1901 [1], la contreverse entre les différents schémas de modulation candidats s'est traduite par la proposition d'un schéma contenant une double couche physique (dual-PHY). De ce point de vue, une structure de transrécepteur unifiée pourrait constituer une réponse satisfaisante. En résumé, les avantages de la structure unifiée sont 1) De permettre l'obtention du gain de flexibilité que nous venons de mentionner; 2) De dépasser la contreverse provoquée par l'introduction de 2 couches physiques totalement distinctes dans la norme IEEE P1901, qui se traduit par un partage de la ressource en transmission par des équipements d'usagers utilisant deux systèmes différents (OFDM et WOFDM)[4]. Dans le cas de la structure

[4]La solution apportée par la norme consiste à utiliser un protocole entre couches physiques (IPP), qui de fait est similaire au principe d'accès TDMA et sert les 2 systèmes séparément par tranches temporelles,

MCM unifiée, l'émetteur est libre de choisir entre les 3 systèmes (OFDM, WOFDM ou HS-OQAM) et le récepteur peut détecter le système utilisé par un signal d'information qui lui est transmis. En outre, pour être réellement attractif, le transrécepteur unifié doit offrir un certain nombre d'avantages: 1) Disposer d'un schéma d'implémentation aisément réalisable; 2) Posséder une structure d'implémenttation régulière; 3) Avoir une grande flexibilité, e.g., en s'adaptant facilement à toute transformation à base de puissance de 2; 4) Présenter un faible coût du point de vue de la complexité opératoire.

Le modulateur MCM unifié est représenté aux Figures 1.10 et 1.11. Globalement, on note que la structure est composée de trois parties: le pré-traitement (PRP), le noyau de transformation et le post-traitement (POP).

Pour les parties PRP et POP, le contenu de chaque bloc dépend du schéma de modulation sélectionné. Pour le noyau de transformation, nous pouvons le choisir soit basé FFT (Fig. 1.10) ou basé sur une transformée rapide en cosinus/sinus de type I (FCT/FST-I), cf. Fig. 1.11. L'avantage d'utiliser un noyau FCT/FST-I est de réduire la complexité opératoire et aussi d'aboutir à une solution qui s'implémente aisément en hardware. Une règle de sélection envisageable consiste à se référer à la table des SNR seuils (cf. Tab. 1.2). L'opérateur peut par un signal dit de sélection de modulation (ModSel) réaliser le choix de son schéma MCM désiré. Les détails de chaque bloc PRP ou POP est fourni dans le corps principal de ce texte de thèse. Le démodulateur MCM unifié a une structure duale de celle du modulateur.

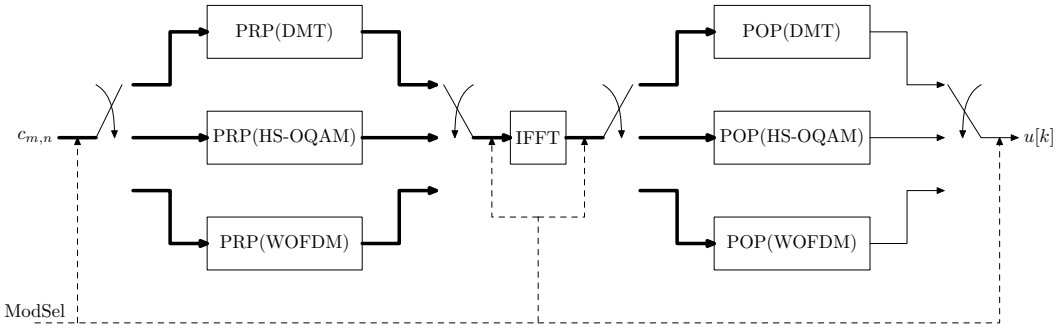

Figure 1.10: Modulateur MCM unifié avec noyau FFT.

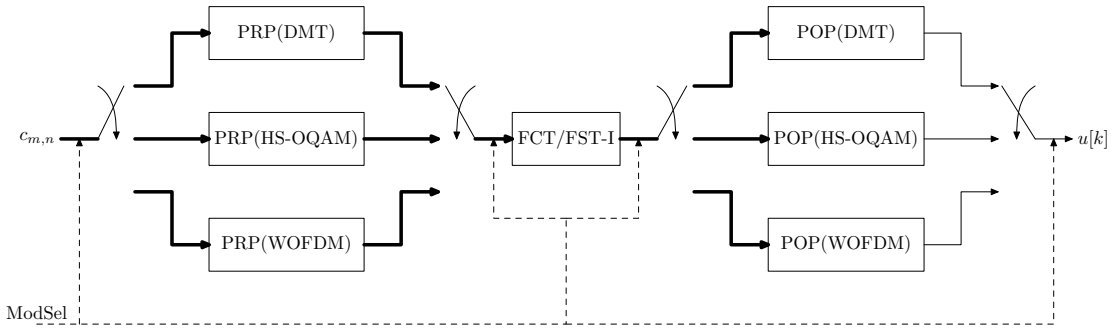

Figure 1.11: Modulateur MCM unifié avec noyau FCT/FST-I.

cf. [58].

Dans la suite, nous reportons les gains en performance obtenus quand le transrécepteur MCM unifié est utilisé au lieu de transrécepteurs conventionnels non flexibles. Nous simulons le cas d'une comparaison entre le transrécepteur unifié vs. le seul modulateur HS-OQAM et vs. le seul modulateur DMT. Dans nos simulations le transrécepteur unifié est implémenté sur la base d'un noyau FCT/FST-I.

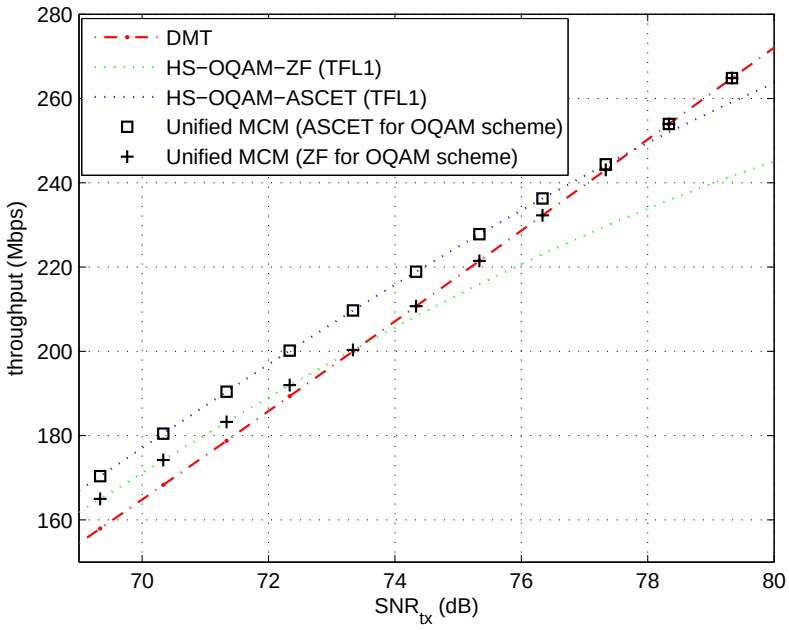

Figure 1.12: Comparaison des débits pour le canal de classe 3 : DMT vs. HS-OQAM vs. transrécepteur MCM unifié.

Si le canal de transmission n'est pas idéal, le récepteur a besoin d'un égaliseur pour compenser la distorsion introduite par le canal et annuler ainsi l'interférence. Par conséquent, l'égaliseur peut être intégré dans le bloc POP. Dans nos simulations l'égaliseur sera le ZF à 1 coefficient pour la DMT et soit l'égaliseur ZF ou ASCET pour HS-OQAM. Les modèles de canaux PLC correspondent aux modèles réalistes des classes 3, 5 et 9. L'estimation de canal et la synchronisation sont toujours supposées être réalisées parfaitement. Le filtre prototype pour la modulation HS-OQAM est le Rossi4$_{\rho=1}$. Les paramètres en transmission sont en relation avec la spécification HPAV, i.e. taille de FFT: 3072; le CP pour la DMT: 417; La fréquence d'échantillonnage : 75 MHz. Pour le transrécepteur unifié la règle de sélection entre les schémas DMT et HS-OQAM est décidée à partir de la table 1.2. Les résultats sont reportés aux Figures 1.12-1.14. Nous observons qu'avec le système MCM unifié nous nous situons toujours au pic de la capacité. Ce gain correspond donc au "gain de flexibilité de modulation" que nous avons introduit.

Une deuxième possibilité de flexibilité provient des différentes possibilités de choix du filtre prototype pour le système OFDM/OQAM. Cet autre aspect de la flexibilité peut être très utile pour le processus d'estimation de canal. En fait, nous pouvons trouver un facteur décisif du point de vue de l'estimation de canal pour le système OFDM/OQAM. Ce facteur dépend fortement du filtre prototype. Par conséquent, l'obtention d'une bonne

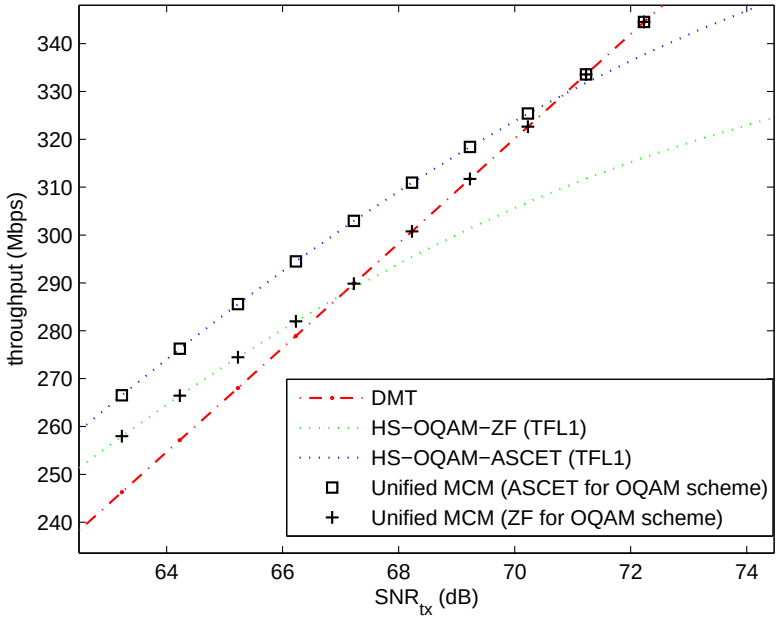

Figure 1.13: Comparaison des débits pour le canal de classe 5 : DMT vs. HS-OQAM vs. transrécepteur MCM unifié.

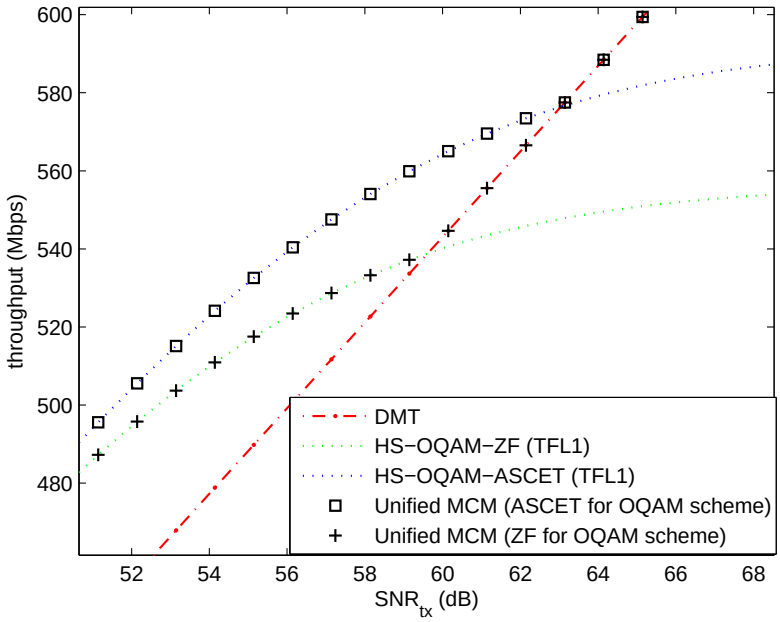

Figure 1.14: Comparaison des débits pour le canal de classe 9 : DMT vs. HS-OQAM vs. transrécepteur MCM unifié.

estimation de canal repose sur le fait de trouver un filtre prototype qui soit conçu en tenant compte de ce facteur décisif.

La méthode d'estimation de canal (CE) par préambule pour le système OFDM/OQAM a été présentée dans [83], où il apparaît que la méthode dite d'approximation de l'interférence (IAM) permet d'obtenir de très bonnes performances. L'idée est de trouver une structure de préambule particulière à l'émetteur de façon à accroître virtuellement la puissance du pilote à la réception. Cette sorte de pilote est appelé pseudo-pilote [83]. En présence d'un terme de bruit b_{m_0,n_0}, plus le pseudo-pilote est puissant plus la méthode de CE fonctionne bien :

$$\hat{H}^c_{m_0} \approx H^c_{m_0} + \frac{b_{m_0,n_0}}{\underbrace{p_{m_0,n_0} + jp^{(i)}_{m_0,n_0}}_{\tilde{p}_{m_0,n_0}}}, \tag{1.31}$$

où $H^c_{m_0}$ est le coefficient de canal pour la porteuse d'indice m_0; $\tilde{p}_{m_0,n_0}$ est le pseudo-pilote à la position (m_0, n_0); b_{m_0,n_0} est est le bruit de fond à cette même position.

Dans ce chapitre, nous nous concentrons sur une structure de préambule IAM particulière nommée IAM de type 1 (IAM1) [83]. La structure IAM1 est telle que $p_{m,0} = p_{m,2} = 0$ et $p_{4k,1} = p_{4k+1,1} = 1$; $p_{4k+2,1} = p_{4k+3,1} = -1$ avec $k = 0, \cdots, \frac{M}{4} - 1$ (cf. Fig. 1.15). De

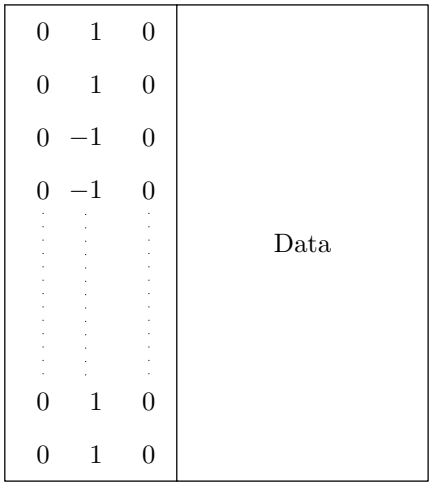

Figure 1.15: Structure de préambule IAM1.

cette manière, le pseudo-pilote d'indice fréquentiel m situé au milieu du préambule s'écrit [83]

$$\tilde{p}_{m,1} \approx p_{m,1} + j(2p_{m+1,1} \langle g \rangle^{m,1}_{m+1,1}). \tag{1.32}$$

En notant $| \langle g \rangle^{m,1}_{m+1,1} | = \beta_0$, on peut voir que la puissance du pseudo-pilote est donnée par

$$\mathrm{E}[|b_{m,1}|^2] = 2\sigma_a^2(1 + 4\beta_0^2), \tag{1.33}$$

et que la puissance de bruit résultante pour le CE s'écrit $\frac{\sigma_n^2}{2\sigma_a^2(1+4\beta_0^2)}$ où σ_n^2 est la variance du bruit. Ainsi la dépendance de la puissance du bruit par rapport à la valeur du paramètre β_0 apparaît clairement. Plus β_0 sera élevé meilleure devrait être l'estimation de canal. Une analyse un peu plus détaillée nous montre que le facteur β_0 est relié à la mesure de

localisation temporelle (TL) du filtre prototype, noté $g[k]$. Ainsi, est-ce que cela signifie simplement qu'en maximisant la mesure TL de $g[k]$, nous obtiendrons le meilleur filtre pour l'estimation de canal ? La réponse est négative. Nous observons en effet que si nous améliorons la mesure TL de $g[k]$, nous perdons en même temps du point de vue de la mesure de localisation fréquentielle (FL). De ce fait, la technique d'approximation par la méthode IAM ne sera plus valide. Nous introduisons donc un autre paramètre, noté β_I, pour contrôler la mesure FL de $g[k]$. Au final, un bon filtre prototype pour l'estimation de canal par préambule doit prendre en compte β_0 et β_I. Dans ce chapitre, nous présentons une variante de la séquence discrète de Doroslovački [44], appelé filtre de Doroslovački modifié (MDF), que nous utilisons ensuite pour la partie transmission du préambule du système OFDM/OQAM. Pour optimiser les coefficients du MDF, nous introduisons également deux critères de synthèse. Le premier critère s'intitule critère du Maximum Outside Energy (MOE) et le second est nommé critère du Maximum Weighted Combining $\beta_{\{0,I\}}$ (MWCβ). Les résultats de simulation sont reportés à la Figure 1.16 où nous comparons, dans le cas du canal PLC théorique introduit dans [87], la méthode proposée initialement dans [83] avec cette nouvelle méthode. On notera que, dans cette représentation graphique, la mesure du SNR (noté E_b/N_0) ne prend en compte pour le signal que l'énergie par bit utile. Le gain de flexibilité provient ici du fait que l'on commute entre le prototype MDF, qui est optimisé pour la partie CE par préambule, et le prototype TFL1 pour la partie transmission des donnés utiles. On notera que pour les 2 critères nous améliorons significativement les performances par rapport à l'OFDM/OQAM non flexible et aussi bien entendu par rapport au CP-OFDM. Nos résultats, quasi identiques pour les 2 critères, se situent entre les bornes de l'estimation parfaite fournies par le CP-OFDM (LB CP-OFDM) et par l'OFDM/OQAM (LB OQAM-TFL1).

Les articles publiés ou soumis en relation avec ce chapitre sont

- H. Lin and P. Siohan, "Transmission Capacity for Indoor PLC: A comparison between DMT and HS-OQAM," *ISPLC '09*, Dresden, Germany, Mar. 2009.
- H. Lin and P. Siohan, "A Unified Structure for Multi-Carrier Modulations in Power-Line Communications," *Globecom '09*, Hawaii, USA, Nov. 2009.
- H. Lin and P. Siohan, "Modulation Diversity in Wideband In-Home PLC," *WSPLC '09*, Udine, Italy, Oct. 2009.
- H. Lin and P. Siohan, "Capacity analysis for PLC with different multi-carrier modulations," *IEEE Trans. on Power Delivery*, Vol. 25, no. 1, pp. 113-124, Jan. 2010.
- H. Lin and P. Siohan, "Robust channel estimation for OFDM/OQAM," *IEEE Communications Letters*, Vol. 13, no. 10, pp. 724-726, Oct. 2009.
- H. Lin and P. Siohan, "Modulation flexibility in PLC: A Unified MCM Transceiver Design and Implementation" *revised in* 2009.

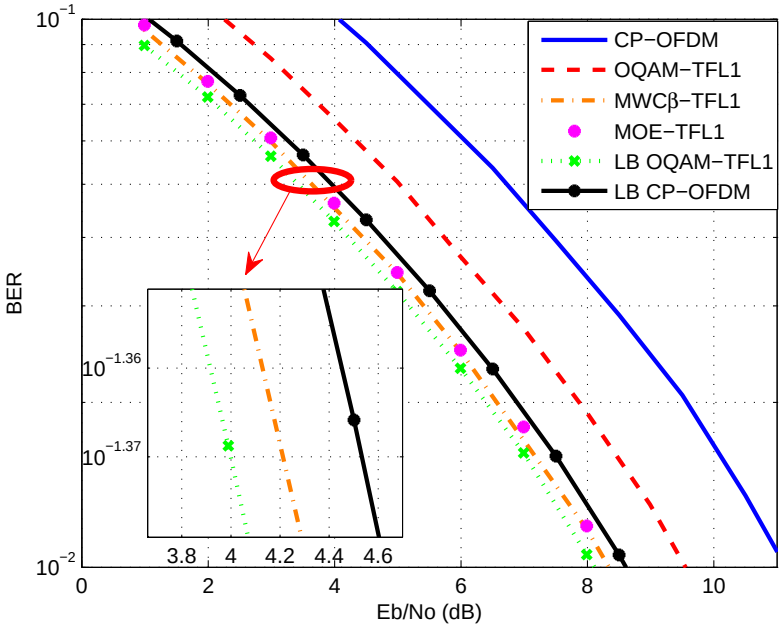

Figure 1.16: Résultats en BER vs. E_b/N_0 pour une transmission QPSK avec estimation de canal (modèle de Ma [87]) par préambule.

Chapter 2

Introduction

Digital communication over power line is an old idea that dates back to the early 1920s, when the first patents were filed in this area [45]. Since then, utility companies around the world have successfully used this technology for remote metering and control. These applications, however, require only very low bit rates. More recently, there has been a growing interest in the possibility of exploiting the power grid to provide broadband data transmissions. The attractive feature of this idea is the presence of a vast infrastructure in place for power distribution, and the penetration of the service could be much higher than any other wired or wireless alternative. Thus, the resulting possible applications involve enormous area, e.g. voice, video and internet, etc..

Despite of the enormous potential, meanwhile, the consideration of broadband transmission over power line networks faces many challenges. This is mainly due to the fact that some technical problems still remain to be solved: 1) power line channel is a very harsh and noisy medium that is extremely difficult to be modelled. 2) power line channel creates the challenges for modem designer, i.e. how to properly choose the modulation, coding and detection schemes. 3) the crucial issue of electromagnetic interference due to the unshielded nature of power line cables. Solving the aforementioned problems can further make a huge step in modern communication system.

Although, a dramatic improvement has been made, over a recent decade, for finding the feasible solutions in some of the above challenges, as a matter of fact, most contributions on this topic are published in transactions on consumer electronics, power delivery, industry applications, and industrial electronics, whereas very few papers on power line communications have appeared in publications of the Communications Society, which usually fosters technical innovation in the area of communications systems. Moreover, the power line channel poses unique challenges in modem design, channel modelling, medium access, and many other aspects of communications architecture. Many of these challenges have only been partially addressed and solved to date. Actually, most efforts in this area have focused on channel modelling and the realization of working products; but with very few exceptions, a solid communications approach is still lacking. Thus, this thesis focuses the attentions particularly on the communication area. We spend most of the pages on

the multi-carrier modulation scheme for the communications over power line networks.

As a matter of fact, the multi-carrier modulation idea can be traced back to 1957. At that time, the bandwidth efficiency issue was firstly addressed by Doelz *et al.* [43] with their proposed solution called Kineplex system. However the complexity issue was not yet considered in Kineplex system until Weinstein and Ebert proposed the use of Fast Fourier Transforms as well as guard interval in frequency division multiplexing system [137]. This celebrate proposal, actually, gave rise to a revolution in digital communication area. Up to now, the OFDM (Orthogonal Frequency Division Multiplexing) scheme has been applied in almost every applications no matter what wireless or wired communications. OFDM, actually, is a particular form of multi-carrier transmission and is suited for frequency selective channels and high data rates. This technique permits to map each symbols onto the orthogonal carriers, which leads to a very simple receiver. However, since the communication technologies are always innovative, recently, many attentions have been paid on searching for some novel alternative multi-carrier schemes. Because, many researchers as well as engineers have noticed that the time-frequency localization feature of the pulse shape function is sometimes of great importance, whereas, OFDM does not have this feature. Another reason of looking for novel multi-carrier schemes other than OFDM is from the spectrum efficiency point of view. Then, we have to mention a celebrate paper "Theory of Communication" written by Dennis Gabor who was the first one looking at the time-frequency analysis on communication signal. However, at that time, this pioneer paper absorbed few attentions in digital communications domain and during a long time his paper remained to be un-referenced and rarely researched [50].

It is only recently that, Gabor theory and analysis have been highlighted by many researchers and referenced by the innovational papers, wherein people found that multi-carrier system could be considered as a form of Gabor system and then many properties can be verified and derived using Gabor analysis [50]. That means, as well, that OFDM belongs to the Gabor system. Later after, Balian and Low mathematically proved, in their papers [10] and [86], that a Gabor system cannot be possible to have good time-frequency feature, full spectrum efficiency and orthogonality, simultaneously. This result frustrated many researchers and engineers, since a good alternative multi-carrier scheme seems to be a miracle. Otherwise said, OFDM might be the only solution. Since then, the research interest was separated into two different directions: one direction tends to find a scheme that relaxes the spectrum efficiency to get the rest of the features and this eventually leads to a so-called Filter MultiTone (FMT) idea [30]. In the other direction, people still stuck into finding a way that can obtain all of the above three features even though it seems to be impossible until an OFDM/OQAM idea was presented in [52]. This idea, indeed, made a meaningful breakthrough in the sense of solving a supposed unsolvable problem. Actually, this technique has been introduced long ago by Chang [28] and Salzberg [109] but their papers had not been very much noticed at that time. After the paper of [52] being published, a large number of works have been done based on this technique [18, 19, 131, 95, 115] and the OFDM/OQAM scheme, also named Filter Bank MultiCarrier (FBMC), has been seriously considered in the radio context [3, 4, 14]. On the other hand, although more and more papers have been published concerning the OFDM/OQAM idea, most of them are concentrating on the multiplexing structure design and the feasible prototype filter design. The issue of a theoretical analysis on OFDM/OQAM system over a non-ideal channel with additive noise has rarely been addressed. Moreover, many necessary

receiver technologies are still lacking, such as channel estimation and equalization. In this thesis, we try to fill this gap.

A large number of pages of this thesis are concerned with the study of the OFDM/OQAM system including its analysis and design. An analytical performance is derived, which permits us to have a theoretical way for calculating error rate as well as the attainable throughput. This derivation made a great contribution on the study of OFDM/OQAM system. Based on this derivation, a corresponding PLC oriented analysis was presented in ISPLC'09 and ultimately was selected to be the winner of "Best Paper Award". Furthermore, this theoretical derivation can be utilized to separately analyze inter-carrier interference (ICI) and inter-symbol interference (ISI). This eventually highlights a proper prototype filter design criterion tendency. On the other hand, in this thesis, we investigate an appropriate solution by jointly considering prototype filter design and equalization methods, in terms of the system performance as well as the system complexity and latency. In addition, the flexibility is highly pronounced in this thesis in order to have more gains in transmission in PLC. We present two flexibilities, i.e., "modulation scheme flexibility" and "prototype filter flexibility". These novel ideas have not been considered in multi-carrier communications based PLC yet and they can ultimately result in some remarkable achievements. The topic of power line channel modelling and channel characteristic analysis, however, will be briefly touched with a small amount of pages.

The second chapter addresses a short historical introduction of power line communications. The idea of using power line network to transmit data was proposed long time ago and at that time the applications were remote voltage monitoring and remote meter readings. Since recently, power line channel was proposed to be a transmission medium for broadband communications. However, the feasibility of broadband PLC highly depends upon the solvability of PLC challenges. This chapter gives an overview of the possible challenges for broadband PLC; the structures of PLC access network and in-home network; the advantages of using in-home PLC over the other existing solutions; the IEEE P1901 working group.

The third chapter summarizes a short state of art on in-home PLC channel modelling and presents an information theoretic way for channel characteristic analysis. Power line channel has been regarded as an extremely hostile and noisy medium that is difficult to be modelled until Philipps, Zimmermann and Dostert presented their celebrate papers in ISPLC'99 [96] and IEEE Trans. Commun. journal [139], independently. Since then, a large number of contributions were actually based on this model. Tonello *et al.* added some *a priori* statistical knowledge onto this model [93] to get a new model that, as well, is reported in this chapter. Another channel model, introduced in this chapter, is the one proposed by Tlich *et al.* [123]. This model is obtained by fostering a bunch of realistic in-home PLC channel measurements then statistically analyzing them. The second part of this chapter concerns an information theoretical analysis on in-home PLC channel measurements using Maximum Entropy Method (MEM) and Degree of Freedom (DoF) conception.

The fourth chapter concentrates on an introduction of the existing multi-carrier modulation techniques. Among them, OFDM/OQAM is the target technique of this thesis. Therefore, we spend most of the pages on it, including its principle and its adaptation in PLC transmission with its variant named Hermitian Symmetric OFDM/OQAM (HS-OQAM). Other modulation schemes, introduced in this chapter, include OFDM and

Wavelet OFDM. Further, since OFDM is considered as a competitive solution against OFDM/OQAM, the advantages as well as disadvantages are well studied and discoursed in this chapter.

The fifth chapter highlights an analytical discussion for OFDM/OQAM transmission over PLC channels. We derive a mathematical expression of the interference and, based on that, we are able to decide a proper prototype filter design criterion. Furthermore, the trade-off between performance and complexity is also discussed.

The sixth chapter presents the possible equalization solutions for OFDM/OQAM system. Two equalization methods are presented therein, the first one is an extended pointwise FIR sub-carrier equalizer and the second one is a decision feedback-like equalizer. The main theme of this chapter is all around one question that when OFDM/OQAM modulation faces in-home PLC channel, shall we use long prototype filter or complex equalization?

The seventh chapter discourses two novel flexibilities in PLC, named modulation scheme flexibility and prototype filter flexibility, that we can expect to exploit in PLC. The modulation scheme flexibility can be obtained by introducing a unified transceiver, by which we can arbitrarily switch from one modulation scheme to another. The selection rule as well as the efficient implementation of this unified transceiver are given in this chapter. The prototype filter flexibility can be exploited by separately filtering preamble and payload with different prototype filters. Thus, the flexibility gain can be significant in channel estimation comparison.

Inside the Orange Labs, this research work is included in the so-called "Research Objects" entitled "Access Technologies" and "Home Networking". This work also contributed to the PLC work package of the European OMEGA FP7 project.

Chapter 3

Broadband Transmission over Power Line Networks

3.1 A Brief Overview of PLC

These years, the terminology of Power Line Communications (PLC) has become a hot topic in communication area. More and more tracks, concerning this topic, have emerged in several well known international electrical engineering conferences. As well, some international symposiums have been created, for the subject particularly on PLC (e.g. International Symposium on Power Line Communications and Its Applications (ISPLC)), and are getting maturer over the past decade. All these phenomenons illustrate one fact that PLC has been re-considered as a future transmission medium for high-rate data communications.

The idea of using power lines to support data communications is not new at all, i.e. the first applications of communications over power lines can be traced back to over 100 years ago [45]. That time, the transmissions over power lines were used for the remote voltage monitoring in telegraph systems and remote meter readings. Nowadays, due to the competition from the other existing solutions as well as the ubiquity feature of power line networks, the target applications of PLC are involved in broadband Internet Access, indoor wired local area networks (LANs) for residential and business premises, in-vehicle data communications and smart grid applications (advanced metering and control, real-time energy pricing, peak shaving, mains monitoring, distributed energy generation, etc.).

The convenience and inexpensiveness of this "no new wire" medium is the highlighted advantage for PLC suggestion. Over this medium, electrical distribution grids are additionally used as a transmission medium for the transfer of various telecommunications services, which realizes the reduction of cost and expenditure in the realization of new telecommunications networks. High- or middle-voltage power supply networks could be used to bridge a longer distance to avoid building an extra communications network. Low-voltage supply networks are available worldwide in a very large number of households

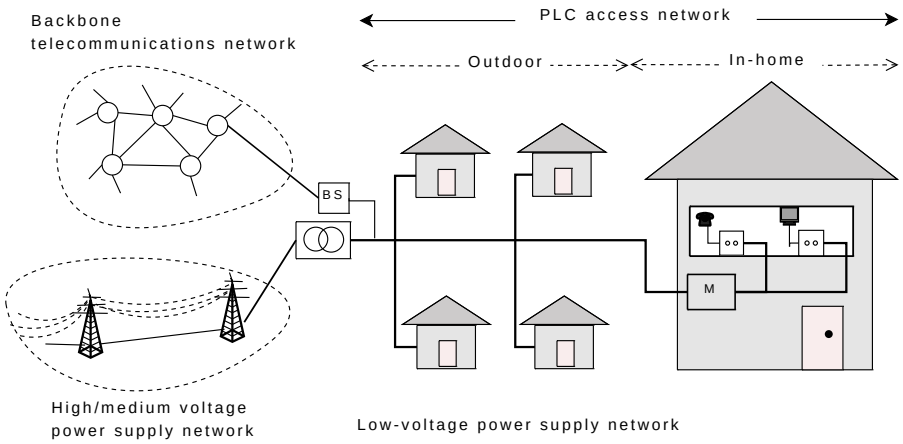

Figure 3.1: Structure of a PLC access network [68] (M: Meter Unit).

and can also be used for the realization of PLC access networks to provide the so-called telecommunications *last mile*. PLC can also be applied within buildings or houses, where an internal electrical installation is used for the realization of in-home PLC networks.

On the other hand, the feasibility of PLC was questionable, in the past, due to several problems: power line medium was regarded as a harsh and hostile transmission medium that is very difficult to model; frequency selective fading demands sophisticated technologies; various forms of noise (background white/colored, impulsive noise periodic/aperiodic, narrowband interference) require some special cares on signal processing. Additional challenges are due to the fact that power line cables are often unshielded and thus become both a source and a victim of electromagnetic interference (EMI) to/from the other existence communication solutions. Another afflicting worry is that power line cables are shared medium. Thus, they cannot provide a dedicated link between transmitter and subscriber. Actually, power line cables connect a low-voltage transformer to a set of individual homes or a set of dwelling units, without isolating each unit. Since power line medium is shared with a set of users, the signals generated by one user may interfere with the others that appear in the same circuit.

The above-mentioned challenges caused skepticism about the feasibility of broadband communications over power lines in the past time and there was a period of age that PLC was unfortunately dived into a frozen situation. But today, since significant improvements in the aspect of technologies, as well as in the proposals targeting the above challenges, have been made, the feasibility of PLC is re-considered and the prospect of PLC seems to be quite bright. Furthermore, in June 2005, the IEEE P1901 Standards PLC working group was created and this group is entering a crucial phase for accelerating an international technological standard of PLC. Thus, soon after, PLC may become a strong competitive solution to the other existing ones.

PLC can be classified as its functionality into Access and In-home. The former can be concerned with the transmission of broadband content on the medium- and low-voltage power lines that feed homes. The latter is concerned with enabling low-voltage wiring in in-home structures to carry digital content. As shown in Fig. 3.1, the low-voltage supply

networks consist of a transformer unit and a number of power supply cables linking the end users, which are connected to the network over Meter units (M, Fig. 3.1). A power line transmission system applied to a low-voltage network uses it as a medium for the realization of PLC access networks. In this way, the low-voltage networks can be used for the realization of the so called *last mile* networks.

The low-voltage supply networks are connected to medium- and high-voltage networks via a transformer unit, see Fig. 3.1. The PLC access networks are connected to the backbone Wide Area Networks (WAN) via a Base/master Station (BS) usually placed within the transformer unit. Many utilities supplying electrical power have their own telecommunications networks linking their transformer units and they can be used as backbone network. If this is not the case, the transformer units can be connected to a conventional telecommunications network.

The PLC subscribers are connected to the network via a PLC modem placed in the electrical power Meter unit (M, Fig. 3.1) or connected to any socket in the internal electrical network. In the first case, the subscribers within a house or a building are generally connected to the PLC modem using another communications technology (e.g. DSL, WLAN). In the second case, the internal electrical installation is used as a transmission medium that leads to the so-called *in-home PLC solution*.

3.2 In-home PLC

3.2.1 Structure and Possible Applications

Basically, the structure of an in-home PLC network is not much different from the PLC access systems using low-voltage supply networks. There can also be a BS that controls an in-home PLC network, and probably connects it to the outdoor area (Fig. 3.2). The BS can be placed with the meter unit, or in any other suitable place in the in-home PLC network. All devices of an in-home PLC network are connected via PLC modems, such as the subscribers of a PLC access network. The modems are connected directly to the wall power supply sockets, which are available in the whole house/flat. Thus, different devices can be connected to the in-home PLC network wherever wall sockets are available.

In-home PLC systems use internal electrical infrastructure as transmission medium. It makes possible the realization of PLC local networks within houses, which connect some typical devices existing in private homes that can be generally classified into four categories (Fig. 3.3):

- Home applications/Health/Safety (e.g. refrigerator, micro-wave oven, massage chair and security alarm etc.).
- Information and Communications (e.g. telephone, computer, etc.).
- Digital entertainment (e.g. digital TV, DVD recorder, home-theater, TV game, etc.).
- Document/Imaging (e.g. printer, scanner, digital camera, etc.).

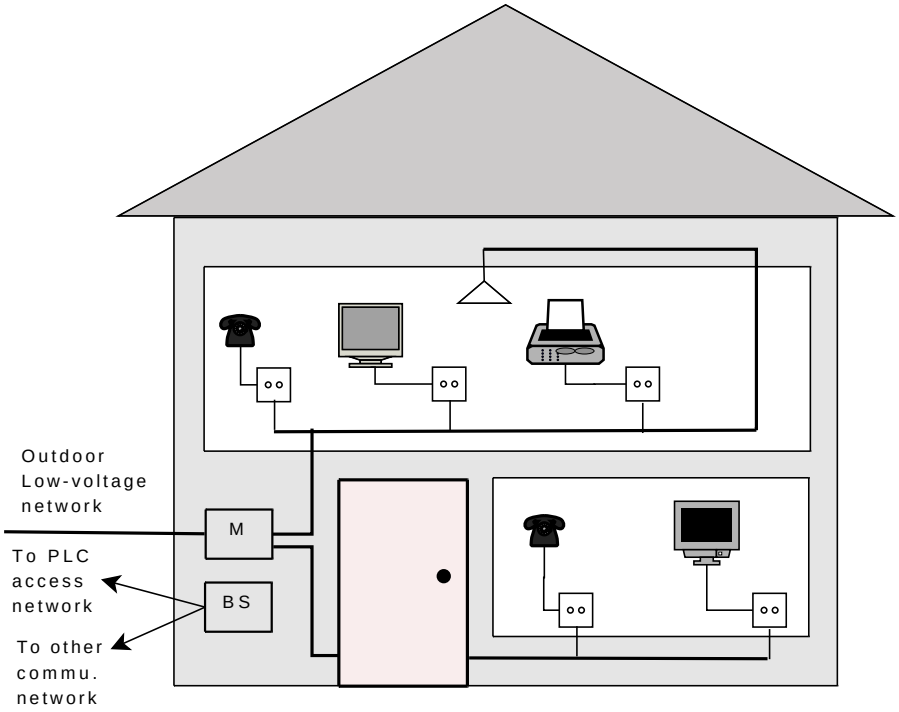

Figure 3.2: Structure of a PLC in-home network [68].

Figure 3.3: Extend the product value chain by PLC [76].

3.2.2 Why In-home PLC?

One question might be posed from the very beginning is that since there are already many solutions for in-home communications, why do we still need in-home PLC?

Actually, the merits of PLC are as follows [76]: It contributes to low power consumption; It can be applied for the use of energy control and monitoring; It enables energy saving; It reduces the wiring and lightens the transportation system (vehicles, aircrafts etc.). In other words, PLC is more "green". Indeed, PLC provides a green ubiquitous concept, economical realization and installation.

For in-home communications, PLC has also some other advantages. Actually, in-home powerline is the most pervasive medium (i.e. multiple outlets are already in every room). Moreover, we do not need new wires, as the whole home is networked. Every "networkable" device is connected to a power outlet, so many devices become potential target for added value service.

On the other hand, comparing the other existing in-home communication solutions (e.g. wired: Ethernet, HomePNA, coax; or wireless: HomeRF, bluetooth, UWB and Wi-Fi), in-home PLC also has its advantages over the others. For instance, for wired solutions, Ethernet needs new wire installation and its each node must be connected to the Ethernet and it requires hub/router; In HomePNA solution, there are not many phone plugs within a home. In coax case, it is a lack of ubiquity of cable outlets inside a home and the compatibility with existing services (e.g. TV, modems). For wireless solutions, such as UWB and Bluetooth, they have a transmission distance limitation. In WiFi/802.11n case, due to potential obstacles, sometimes the signal cannot penetrate (e.g. corner or communications between first and second floor).

3.3 IEEE P1901

IEEE P1901 ("IEEE P1901 Draft Standard for Broadband over Power Line Networks: Medium Access Control and Physical Layer Specifications") is an IEEE draft standard for broadband over power line networks defining medium access control and physical layer specifications. The P1901 baseline was approved with more than 85% of positive votes during the meeting held in Kyoto, Japan, 16-19 December 2008 [1]. The baseline adopted in December 2008 includes three separate options for PHY and MAC. The third option, which was added in order to get a successful confirmation vote in Kyoto, is compatible with G.hn/G.9960, which is another home networking standard being developed by ITU-T for operation over power lines, phone lines and coaxial cables.

IEEE P1901 aims at developing specifications for high speed (>100 Mbps at the physical layer) communication devices via alternating current electric power lines. The standard will use transmission frequencies below 30 MHz (optional band up to 60 MHz). The aim is to define MAC and PHY layer specifications for all classes of Broadband Power Line (BPL) devices. Many companies and standard bodies are participating in the developing IEEE P1901 standard including HomePlug Powerline Alliance, Universal Powerline Association (UPA) and Consumer Electronics Powerline Communication Alliance (CEPCA). HomePlug Powerline Alliance and Panasonic (CEPCA member) have proposed within the IEEE P1901 working group to converge towards a common MAC layer supporting both HPAV and Panasonic (i.e. HD-PLC) PLC PHYs. HomePlug Panasonic proposals have been

selected as Technology Baseline in the access, in-home and Coexistence clusters of P1901 working group, all other proposals (among them UPA/DS2 proposal) being rejected.

This proposal would ensure the coexistence between HomePlug and Panasonic technologies. Nevertheless, the inter-PHY protocol that would allow the coexistence between HPAV version (OFDM) and Panasonic version (wavelet OFDM) is yet to be finalized.

The following table is provided by [39] summarizing the main differences between Panasonic [55] and HPAV [6, 5].

Table 3.1: Comparison of the PHY parameters of P1901 actors.

	Panasonic	HPAV
Modulation	Wavelet OFDM	windowed OFDM
Channel coding	RS-CC; LDPC	Turbo code
Mapping	PAM 2-32	QAM 2-1024
FFT size	512 (extendable to 2048)	3072
Sampling frequency	62.5 MHz	75 MHz
Frequency band	4-28 MHz (2-28 MHz optional)	2-28 MHz
Guard Interval (μs)	No	5.56, 7.56, 47.12
Symbol length (μs)	8.192	40.96+GI
PHY rate (Mbps)	190	200
Notches	Programmable	Programmable

Note that this table cannot be considered as a scientific comparison. It only gives the specifications as defined independently by the manufacturers and does not provide sufficient details concerning the technologies. This thesis, developed in the following chapters, provides an in depth analysis of a Filter Bank MultiCarrier (FBMC) of the OFDM/OQAM type. In comparison of HPAV, it illustrates some advantages of FBMC modulation, i.e., no CP, better frequency localization and flexibility.

Chapter 4

PLC Channel Characterization and Modelling

Power line is considered as a very hostile medium that is extremely difficult to be modelled. Especially, in the use of broadband communications, the channel modelling method was a conspicuous lack in the past time. To realize the idea of transmission over power line, the call-for technology was announced and a very timing and effective international symposium, international symposium on power-line communications and its applications (ISPLC), was created in 1997. This symposium gathers many PLC engineers and researchers all over the world every year for exchanging the novel ideas as well as the contributions on PLC.

It was in 1999 that two celebrate papers, [96] and [138], were presented simultaneously, but independently, at ISPLC symposium reporting new results on PLC channel modelling in the high frequency range case. One paper was written by Zimmermann and Dostert and the other one was written by Philipps. Both papers revealed a fact that the power line channel also has a multi-path behavior due to the impedance mismatching. Furthermore, the parameter-based mathematical expression of the channel transfer function was individually given in these two papers. Coincidentally, the presented mathematical expressions of these two different papers were surprisingly similar. However, the difference is that in Zimmermann's model there was an additional attenuation term which did not exist in Philipps' model, whereas this term could be eventually factored out from the weight term of Philipps' model. Since then, the Zimmermann's model has been considered as a fundamental PLC channel model that illustrates the PLC medium more precisely than Philipps' model [139] but both of these papers have become two highly cited references in the later channel modelling research (e.g. more than 90% citation rate in the subsequent-published ISPLC papers on channel modelling).

In this chapter, we aim to introduce three PLC channel models. The first one is, of course, the fundamental Zimmermann's model. The second one is an in-home PLC analytical model proposed by Tonello *et al.* [93]. This model is, in general, based on the

fundamental one appending to it some reasonable statistical properties. Thus, it makes the fundamental model more analytical. The third model introduced in this chapter is a purely measurements dependent model [123, 121]. This model is obtained directly by analyzing the collected measurements and it classifies the in-home PLC channels into 9 classes. The classification depends on the power line circuit topology and on realistic living environments [122]. Therefore, this last model is considered as a fairly realistic in-home PLC model that truly captures the realistic channel features.

In the second part of this chapter, we introduce a novel channel characteristic analysis idea from an information theory point of view. The analysis is carried out on the realistic channel models [123, 121] and some new interesting facts are unveiled in this part.

4.1 Channel Measurement Sounder

In the aforementioned models, one may find that the first thing of great importance is how to get the measurements. Recently, Orange Labs in Lannion has managed to foster the in-home wideband PLC measurements. The wideband propagation measurements are undertaken in the 30 KHz - 100 MHz band in various in-home channel environments (country and urban, new and old buildings, apartments and houses) as shown in Tab. 4.1.

Table 4.1: Distribution of transfer functions by site.

Site number	Site information	Number of transfer functions
1	House - Urban	19
2	New house - Urban	13
3	Recently restored apartment - Urban	12
4	Recent house - Urban	28
5	Recent house - Urban	34
6	Recent house - Country	22
7	Old house - Country	16

There are, in total, seven measurement sites and a total of 144 transfer functions. For each site, the transfer functions are measured between a principal outlet (most probable to receive a PLC module) and all other outlets in the home (except improbable outlets such as refrigerator ones...). Channel Transfer Function (CTF) measurements are carried out in the frequency domain, by means of a Vector Network Analyser (VNA), as shown in the block diagram of Fig. 4.1.

The coupler box plugged in the AC wall outlet behaves like a High-Pass Filter (HPF), with the 3 dB cutoff at 30 KHz. The probing signal passes through the coupler and the AC power line network and exits through a similar coupler plugged in a different outlet. A direct coupler to coupler connection is used to calibrate the test setup. Two over-voltage limiting devices with -10 dB and -6 dB losses, respectively, are used in front of the entry port of the VNA 8753ES and its exit port, which can serve as an entry port, to protect it from over-voltages produced by the impulsive noises of the AC power line. A computer is connected to the VNA through a General Purpose Interface Bus (GPIB). This allows the

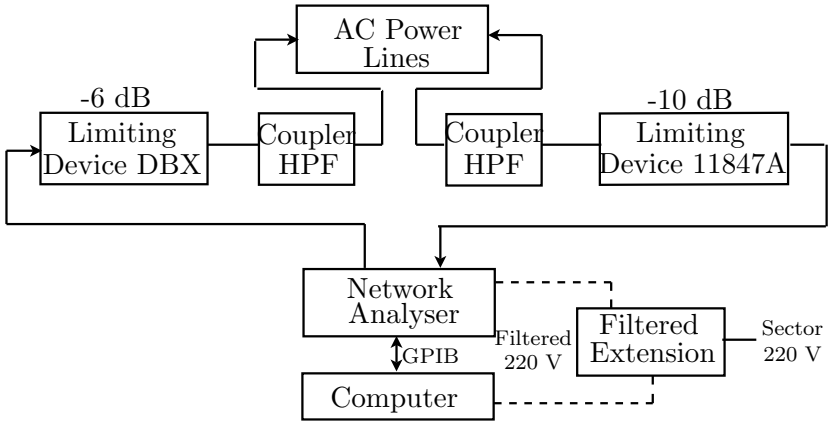

Figure 4.1: Powerline channel measurement system.

computer to record data and control the VNA using the INTUILINK software [2]. The VNA and the computer are isolated from the power line network using a filtered extension. This extension is systematically connected to an outlet not likely to be connected to a PLC modem, such as washing machine outlet. These precautions are taken in order to minimize the influence of the measurement devices on the measured transfer functions.

4.2 Channel Transfer Function Modelling

After showing the measurement sounder, we next talk about the topic of CTF modelling. In what follows, we aim at introducing three models, they are: Zimmermann's fundamental model [138, 139], Tonello's analytical model [93], and the realistic model proposed by Tlich *et al.* from Orange Labs in Lannion [123, 121].

4.2.1 Zimmermann's Model

Signal Multi-path Propagation

A fundamental theoretical PLC channel model was originally proposed by Zimmermann and Dostert [139] considering that the signal propagation does not take place along a direct Line-Of-Sight (LOS) path between transmitter and receiver, but additional echoes must be taken into account. A simple example in describing the mutipath phenomenon is depicted in Fig. 4.2 where only one bridge is assumed to be implemented. The link has one branch and consists of the segments (1), (2) and (3) with the lengths l_1, l_2, l_3 and the characteristic impedance Z_{L1}, Z_{L2}, Z_{L3}.

Let us assume that A and C are matched, i.e. $Z_A = Z_{L1}$ and $Z_C = Z_{L2}$. The remaining points for reflections are B and D, with the reflection factors denoted as r_{1B}, r_{3D}, r_{3B}, and the transmission factors denoted as t_{1B}, t_{3B}. With these assumptions, an infinite number of propagation paths is possible in principle, due to multiple reflection as illustrated in Tab. 4.2. Each path i has a weighting factor g_i, representing the product of the reflection and transmission factors along the path with amplitude being less or equal to one, i.e.

$$|g_i| \leq 1. \tag{4.1}$$

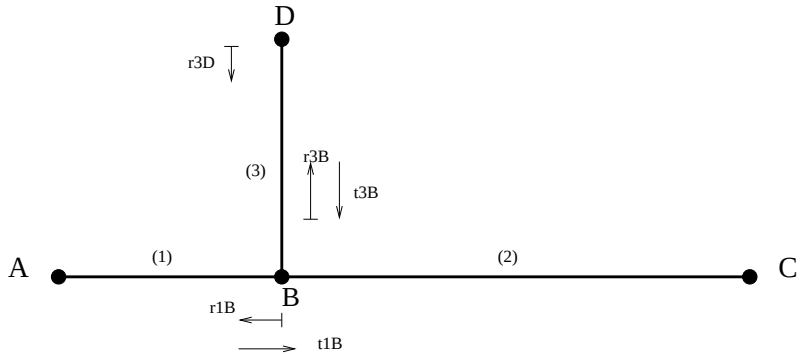

Figure 4.2: Multi-path signal propagation; cable with one bridge [139].

Table 4.2: Signal propagation paths.

Path No.	Way of the signal path	length of path d_i
1	$A \rightarrow B \rightarrow C$	$l_1 + l_2$
2	$A \rightarrow B \rightarrow D \rightarrow B \rightarrow C$	$l_1 + 2l_3 + l_2$
$\vdots$	$\vdots$	$\vdots$
N	$A \rightarrow B(\rightarrow D \rightarrow B)^{N_P-1} \rightarrow C$	$l_1 + 2(N_P - 1)l_3 + l_2$

Each weighting factor g_i corresponds to a path length d_i (see Tab. 4.2) which further relates to the delay of a path τ_i as

$$\tau_i = \frac{d_i\sqrt{\epsilon_r}}{v_0} = \frac{d_i}{v}. \tag{4.2}$$

It can be calculated from the dielectric constant ϵ_r of the insulating material, the speed of light v_0. Further, the losses of cables cause a global attenuation $A(f, d)$ increasing with length and frequency. Taking into account all of these factors, the PLC channel frequency transfer function model yields

$$H(f) = \sum_{i=1}^{N_P} g_i A(f, d_i) e^{-j2\pi f\tau_i}. \tag{4.3}$$

The cable losses derivations in [139] further gives the formula of attenuation factor in the form

$$A(f, d) = e^{-(a_0+a_1 f^k)d}, \tag{4.4}$$

where two parameters a_0 and a_1 should be properly chosen to fit the measurements. Ultimately, it leads to a complete CTF model as

$$H(f) = \sum_{i=1}^{N_P} \underbrace{|g_i(f)|e^{\phi_{g_i}(f)}}_{\substack{\text{weighting}\\ \text{factor}}} \underbrace{e^{-(a_0+a_1 f^k)d_i}}_{\substack{\text{attenuation}\\ \text{portion}}} \underbrace{e^{-j2\pi f\tau_i}}_{\substack{\text{delay}\\ \text{portion}}}, \tag{4.5}$$

or

$$H(f) = \sum_{i=1}^{N_P} \underbrace{g_i}_{\substack{\text{weighting} \\ \text{factor}}} \underbrace{e^{-(a_0+a_1 f^k)d_i}}_{\substack{\text{attenuation} \\ \text{portion}}} \underbrace{e^{-j2\pi f\tau_i}}_{\substack{\text{delay} \\ \text{portion}}}. \tag{4.6}$$

The CTF model (4.6) is a further simplified one assuming the weighting factors g_i are only real-valued.

Parametric Fitting

Next, we intend to show how to estimate the parameters for this parametric CTF model. A two-step strategy was mentioned in [139]. In the first step, the attenuation coefficients are determined from the attenuation profile using a single-path model, e.g. $N_P = 1$ in (4.6) as

$$|A(f,d)| = |e^{-(a_0+a_1 f^k)d}|, \tag{4.7}$$

where the parameter k stands for the degree of decrease of the path loss as the frequency increases. It is set to be one in [139]. Further, the parameters a_0, a_1 are chosen to fit the measured attenuation profile as in [139, Fig. 3] for a specified distance d.

In the second step, the number N_P, position d_i of the significant paths are derived from the impulse response by a simple peak detection approach using (4.2). The amplitude can be estimated in time domain. Let us digitize (4.6) to

$$H[m] = \sum_{i=1}^{N_P} g_i e^{-(a_0+a_1(m\triangle f)^k)d_i} e^{-j2\pi m\triangle f\tau_i}, \tag{4.8}$$

where $\triangle f$ is frequency spacing. Therefore, the CIR can be obtained by discrete inverse Fourier transform in the form

$$h[n] = \sum_{m} \sum_{i=1}^{N_P} g_i e^{-(a_0+a_1(m\triangle f)^k)d_i} e^{-j2\pi m\triangle f(\tau_i - n\triangle t)}, \tag{4.9}$$

where $\triangle t$ is the time resolution. Assume that the time resolution and peak detection are fine enough, so we can expect that the i-th estimated sampled peak approximately approaches the real one, i.e.

$$\left\lfloor \frac{\hat{\tau}_i}{\triangle t} \right\rfloor \cdot \triangle t \simeq \hat{\tau}_i \simeq \tau_i. \tag{4.10}$$

where $\lfloor a \rfloor$ means to take the greatest integer smaller than a. Then (4.9) leads to

$$h\left[\left\lfloor \frac{\hat{\tau}_j}{\triangle t} \right\rfloor\right] = \sum_{i=1}^{N_P} g_i \underbrace{\sum_{m} e^{-(a_0+a_1(m\triangle f)^k)d_i} e^{-j2\pi m\triangle f(\tau_i - \left\lfloor \frac{\hat{\tau}_j}{\triangle t} \right\rfloor \triangle t)}}_{B_{d_i,\tau_i,\left\lfloor \frac{\hat{\tau}_j}{\triangle t} \right\rfloor} \Longrightarrow B_{\tau_i,\left\lfloor \frac{\hat{\tau}_j}{\triangle t} \right\rfloor}}. \tag{4.11}$$

The solution becomes straightforward if we write (4.11) in matrix form as

$$\underbrace{\begin{bmatrix} \hat{g_1} & \cdots & \hat{g_L} \end{bmatrix}}_{\hat{\mathbf{g}}} \underbrace{\begin{bmatrix} B_{\hat{\tau_1},\lfloor \frac{\hat{\tau_1}}{\triangle t} \rfloor} & \cdots & B_{\hat{\tau_1},\lfloor \frac{\hat{\tau_L}}{\triangle t} \rfloor} \\ \vdots & \ddots & \vdots \\ B_{\hat{\tau_L},\lfloor \frac{\hat{\tau_1}}{\triangle t} \rfloor} & \cdots & B_{\hat{\tau_L},\lfloor \frac{\hat{\tau_L}}{\triangle t} \rfloor} \end{bmatrix}}_{\mathbf{B}} = \underbrace{\begin{bmatrix} h\left[\left\lfloor \frac{\hat{\tau_1}}{\triangle t} \right\rfloor\right] & \cdots & h\left[\left\lfloor \frac{\hat{\tau_L}}{\triangle t} \right\rfloor\right] \end{bmatrix}}_{\mathbf{h}}$$

The estimated amplitude yields

$$\hat{\mathbf{g}} = \mathbf{h}\mathbf{B}^{-1}. \tag{4.12}$$

4.2.2 Tonello's Analytical Model

We presented the Zimmermann model, which is a parametric model, with all the parameters estimated from the measurements. In order to obtain a statistical model, in [93], the authors proposed to add some statistical properties to the conventional Zimmermann model. The starting CTF model is again the Zimmermann based model in band pass conception as

$$H(f) = A\sum_{i=1}^{N_P} g_i e^{-j\frac{2\pi d_i}{v}f} e^{-(a_0+a_1 f^k)d_i}, \quad 0 \le B_1 \le f \le B_2, \tag{4.13}$$

where the parameter A allows adding an attenuation to the frequency response.

The idea is to assume that the reflectors are placed over a finite distance interval and are located according to a Poisson arrival process with intensity Λ (m^{-1}). The maximum network length is equal to $L_{\max}$. With this model the number of paths has a Poisson distribution with mean $L_{\max}\Lambda$, while the inter-arrival path distances are independent and exponentially distributed with mean $1/\Lambda$.

The path gains g_i are the product of several transmission and reflection factors, therefore, they are plausibly modelled as independent complex random variables with an amplitude that is log-normal distributed and with uniform phase in $[0, 2\pi]$. Nevertheless, they can also be modelled as real-valued and uniformly distributed within $[-1, 1]$, as in [139]. The other parameters a_0, a_1, k are assumed to be constant (k can remain to be one). a_0 and a_1 can be chosen to adapt the channel path loss profile.

Thus, as long as we get the parameters (a_0, a_1, k, assume $k = 1$), the CIR realization can be generated (corresponding to a realization of the random parameters N_P, g_i, d_i) as [93]

$$\begin{aligned} h(t) &= A\sum_{i=1}^{N_P} g_i e^{-a_0 d_i} \frac{a_1 d_i + j2\pi(t - \frac{d_i}{v})}{(a_1 d_i)^2 + 4\pi^2(t - \frac{d_i}{v})^2} \\ &\times \left(e^{j2\pi B_1(\frac{d_i}{v}) - a_1 B_1 d_i} - e^{j2\pi B_2(\frac{d_i}{v}) - a_1 B_2 d_i}\right). \end{aligned} \tag{4.14}$$

Next, under the consideration that the path gains are independent and uniformly distributed in $[-1, 1]$, and the path delays are drawn from a Poisson arrival process, i.e. the inter-arrival path delays are independent and exponentially distributed with mean $1/\Lambda$, the average path loss model can be calculated in closed form [93]

$$PL(f) = A^2 \frac{\Lambda}{3}\left(\frac{1 - e^{-\Lambda L_{\max}}}{2a_0 + 2a_1 f^k}\right)(1 - e^{-2L_{\max}(a_0 + a_1 f^k)}). \tag{4.15}$$

The freedom in choosing the parameters can provide channels with different statistics. The approach presented in [93] is to first fix the maximum path length and path arrival rate to a certain reasonable value. Then, the parameter k is fixed which mostly determines the shape (concavity) of the average path loss and the path loss slope at high frequencies. Then, the remaining parameters a_0, a_1 are obtained from the desired path loss at zero frequency and at the stop frequency. For example, if we normalize the channel average path loss at zero frequency, the parameter a_0 can be chosen to satisfy the relation

$$\sqrt{\frac{\Lambda}{3}\left(\frac{1-e^{-\Lambda L_{\max}}}{2a_0}\right)(1-e^{-2L_{\max}a_0})} = 1. \tag{4.16}$$

Then, from the measurements, the factor A can be chosen to obtain the desired average path loss at zero frequency.

4.2.3 Tlich *et al.* realistic CTF Modelling

The above two CTF modelling approaches are based on a theoretical channel model (4.6). On the other hand, in [121], the authors presented a novel PLC CTF modelling which does not commence with the theoretical Zimmermann model, but is totally based on the realistic channel measurements introduced in the Sec. 4.1. The measurements of PLC CTF by site can be distinguished into two categories [121]:

- PLC CTF where the Tx and Rx outlets are in the same electrical circuit.
- PLC CTF where the Tx and Rx outlets belong to different electrical circuit.

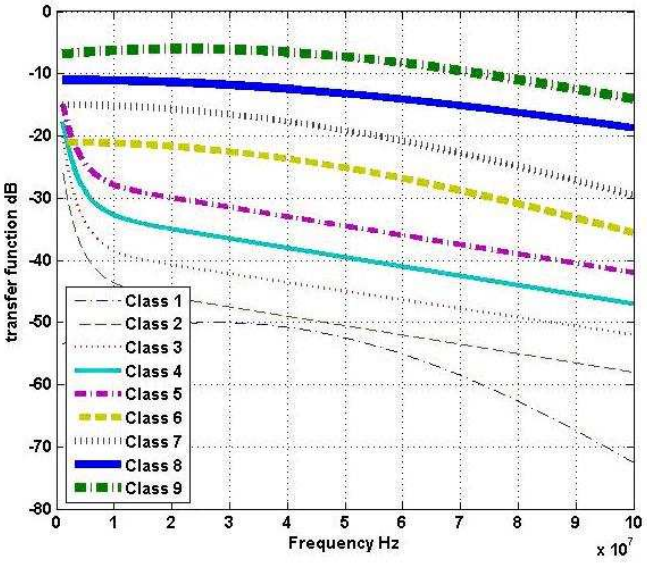

Figure 4.3: Average attenuation for the nine classes of PLC in-home channels [121].

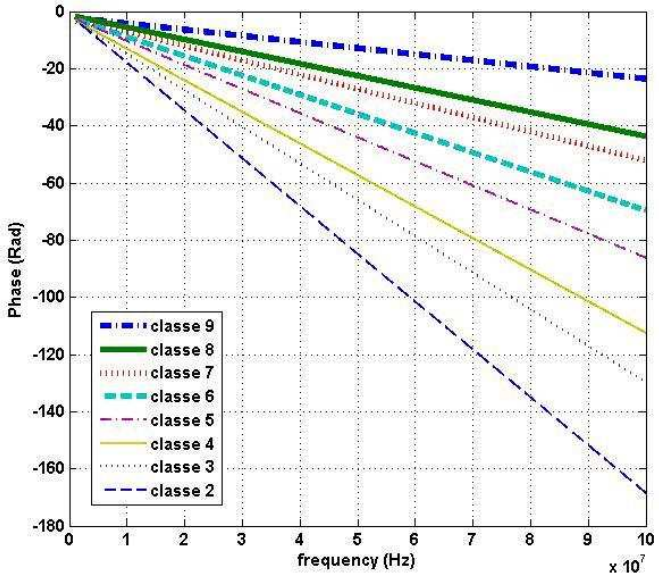

Figure 4.4: Average phase for the nine classes of PLC in-home channels [121].

Furthermore, as stated in [121], the PLC measurements can be classified into 9 classes in terms of their capacities. The relation between channel classification and circuit category is that Classes 1 to 6 are composed of different electrical circuit channels only. Class 7 is composed of an equal mixture of same and different circuits channels. Class 9 and 8 composed of the same circuits channels only. The idea of the CTF modelling is based on the channel classifications and also depends on the circuit categories. As revealed in [121], the measurements of the same class have almost the same statistical behaviors. Figs. 4.3 and 4.4 show the calculated average CTF attenuation and phase for each class.

The peak and notch width distributions are obtained from the measurements and shown in Figs. 4.5, 4.6 for different circuit categories. The distribution can be seen as the Rayleigh distribution defined as

$$f(x) = \frac{x e^{\frac{-x^2}{2\sigma^2}}}{\sigma^2}, \quad \text{with,} \quad \sigma^2 = \frac{1}{2N_o}\sum_{i=1}^{N_o} x_i^2, \tag{4.17}$$

where N_o is the number of observations, and x_i is the width in frequency of the peak or notch of the observation i. Finally, it is concluded that in the same circuit case, $\sigma = 7.1685e6$ and in the different circuit case, $\sigma = 4.6341e6$.

Next, the height in amplitude of a peak or notch is also calculated statistically and its distribution is depicted in Figs. 4.7 and 4.8 depending on the circuit categories. The authors conclude that the heights distribution is close to the triangular distribution defined by

$$f(x) = \begin{cases} \frac{2(b-x)}{(b-a)^2}, & a \le x \le b \\ 0, & \text{else} \end{cases}$$

where a and b are the minimal peak-height and maximal peak-height. Ultimately, when the Tx and Rx outlets are in the same circuit, [121] shows that $a = 2$ dB and $b = 30$ dB,

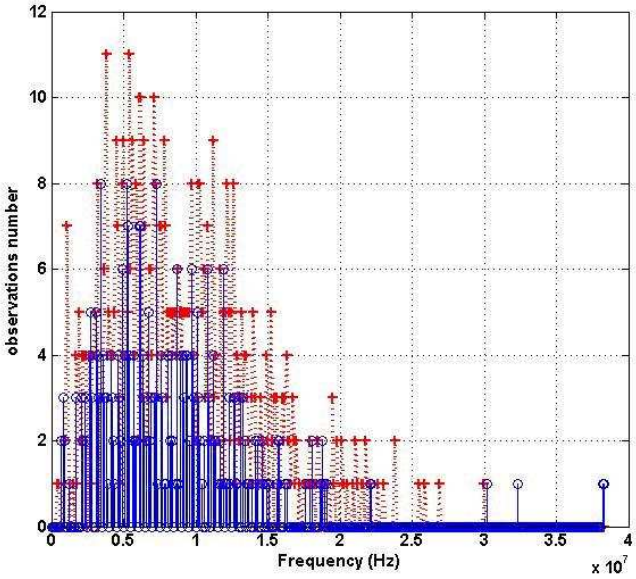

Figure 4.5: Peak and notch widths distribution: same electrical circuits [121].

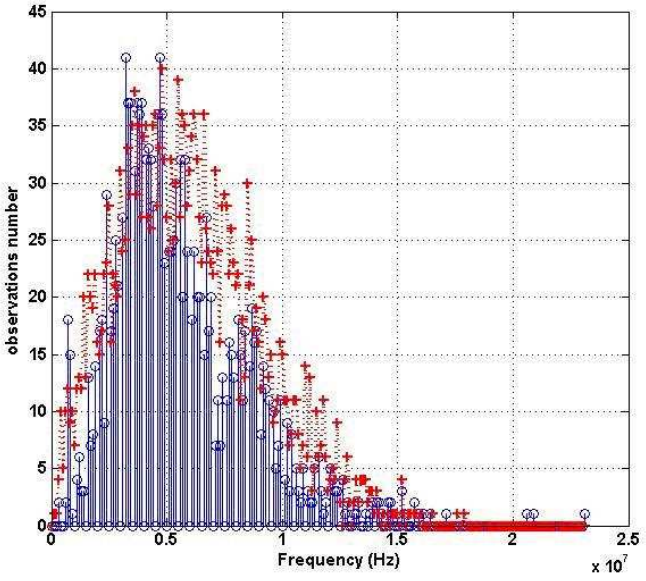

Figure 4.6: Peak and notch widths distribution: different electrical circuits [121].

whilst, in the different circuit case, $a = 2$ dB and $b = 35$ dB.

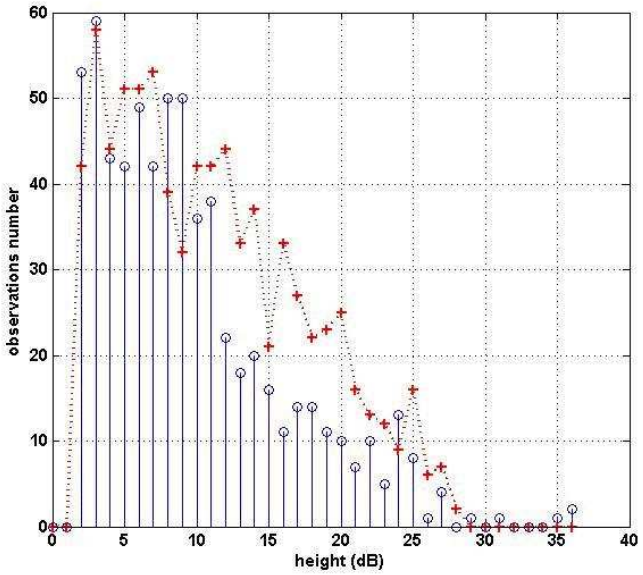

Figure 4.7: Peak and notch heights distribution: same electrical circuits [121].

Finally, the number of peaks and notches is calculated for different circuit categories. It shows a Gaussian distribution tendency as depicted in Figs. 4.9 and 4.10 defined as

$$f(x) = \frac{1}{\sqrt{2\pi\sigma^2}} \exp\left[\frac{(x-\mu)^2}{2\sigma^2}\right]. \tag{4.18}$$

In the same circuit case, the mean and variance are equal to $\mu = 11.4828$ and $\sigma^2 = 11.83$, respectively; In the case of different circuits, they are $\mu = 17.1848$ and $\sigma^2 = 6.8116$. Generally speaking, the channel frequency response of the same electrical circuit case present fewer notches and more peaks than the different electrical circuit case. This is partially related to the fact that a different electrical circuit means that the signal has to pass through the meter and probably the electrical components inside the Meter increase the attenuation.

The CTF modelling involves, for the selected channel class, the generation of the average features, attenuation and phase, together with its specific features, peaks and notches of each channel realization.

In this thesis, all the simulations or the performance analysis are based on the Zimmermann's theoretical model and on the realistic in-home PLC models and generators. Illustrations of the magnitude and phase responses for the channel classes 2 to 9 are presented in the appendix 10.1. As to the Tonello's analytical model, it has been reported that it ultimately has a very similar behavior as the class 2-5 realistic in-home PLC model [121].

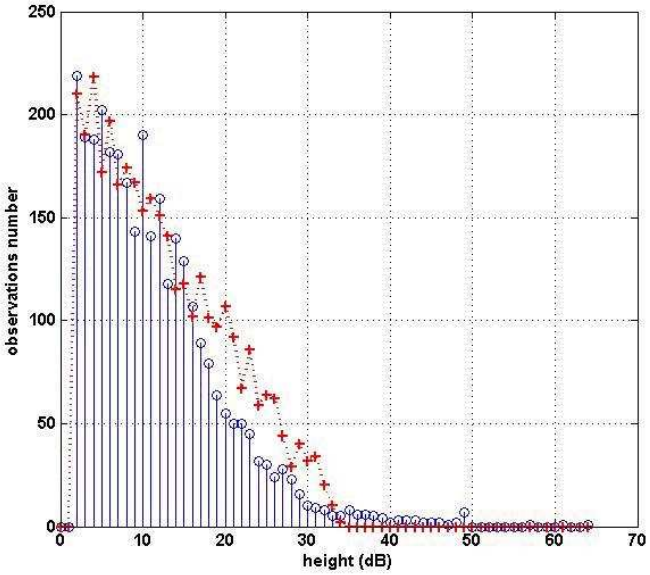

Figure 4.8: Peak and notch heights distribution: different electrical circuits [121].

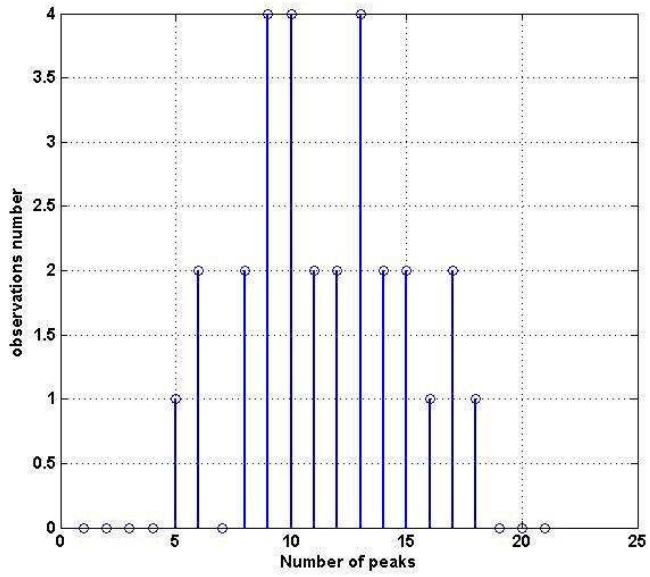

Figure 4.9: Number of peak and notch distribution: same electrical circuits [121].

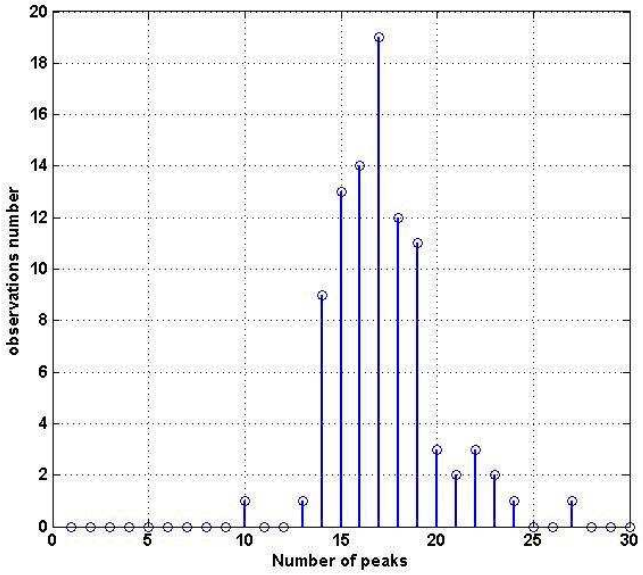

Figure 4.10: Number of peak and notch distribution: different electrical circuits [121].

4.3 In-home PLC Channel Characterization analysis

In this section, we discourse the analysis of power line channel characterization. The analysis is based on the realistic in-home PLC channel "pseudo-measurements" that are actually obtained by the channel model generator [121]. This generator can provide variant in-home PLC channel realizations with a given class number as well as the target frequency range.

Although, extensive characterizations of power line channels have been reported (e.g. [97, 42, 49, 100] and the references therein), however, we highlight an information theoretical idea. The mathematical tools for realizing this idea are Maximum Entropy Method (MEM) and Degree of Freedom (DoF) analyzing.

4.3.1 Maximum Entropy Method Analysis

The principle of Maximum Entropy Method (MEM) was originally presented by Burg to analyze the signal spectrum based on its second-order statistics [24]. Later, this approach was further dually-applied to model a wireless channel supposing that the covariance channel knowledge is available [41]. Actually, when the modelling is based on measurements, the estimate of the covariance channel knowledge is always assumed to be available. Here, we aim at taking advantage of this method to investigate the in-home PLC channel characteristics. Let $\{h_i\}_{i\in\mathbf{Z}}$ be the sequence of samples at frequencies $i\triangle f$, $\triangle f$ is the frequency resolution[1], of the channel frequency response and then, the spectral autocorrelation func-

[1]We should mention that in this thesis the upper case H, usually, denotes the frequency domain channel coefficient. However in this particular section we temporally denote h as the frequency response because the upper case letter H has another use.

tion is defined as

$$R(k) = \mathrm{E}[h_i h_{i+k}^*], \quad k = 0, \cdots, N_r, \quad \text{for all} \quad i \tag{4.19}$$

where $\mathrm{E}[\cdot]$ denotes expectation; the superscript * stands for conjugate. According to Burg's theorem [36], the maximum entropy of a random process fits the N_r-th order Autoregressive (AR) model with its form as

$$h_i = -\sum_{k=1}^{N_r} a_k h_{i-k} + Z_i, \tag{4.20}$$

where the Z_i are *i.i.d.* $\sim N(0, \sigma^2)$ and $a_1, \cdots, a_{N_r}$, σ^2 are chosen to satisfy (4.19). The coefficients $a_1, \cdots, a_{N_r}, \sigma^2$ can be obtained by solving the Yule-Walker equations

$$\begin{aligned} R(0) &= -\sum_{k=1}^{N_r} a_k R(-k) + \sigma^2, \\ R(q) &= -\sum_{k=1}^{N_r} a_k R(q-k), \quad q = 1, \cdots, N_r. \end{aligned}$$

The power delay spectrum (PDS) of the N_r-th order AR process (4.20) yields

$$P(\tilde{\tau}) = \frac{\sigma^2}{|1 + \sum_{k=1}^{N_r} a_k e^{-j2\pi k\tilde{\tau}}|^2}, \tag{4.21}$$

where $\tilde{\tau} = \frac{\tau}{T_s}$ is the normalized delay and τ is the delay in seconds; T_s is the sample duration in time. In practice, the spectral autocorrelation function is estimated from a finite set of N_r frequency measurements, e.g. $[h_1^l, \cdots, h_{N_r}^l]$ over a bandwidth of $N_r \triangle f$ (l is the l-th channel realization). A sampled estimated autocorrelation function yields [101]

$$\hat{R}^{N_r}(k) = \frac{1}{LN_r} \sum_{l=1}^{L} \sum_{i=1}^{N_r - k} h_i^l (h_{i+k}^l)^*, \quad k \geq 0,$$

where L is the number of channel realizations. For a given N_r, we estimated the autocorrelation function $\hat{R}_r^N(k)$, the coefficients $\hat{a}_k^{N_r}$ and the PDS $\hat{P}_r^N(\tau)$. As a consequence, the estimated entropy is given by

$$\hat{H}^{N_r} = \log(\pi e) + \int_{-1/2}^{1/2} \log \frac{\sigma^2}{|1 + \sum_{k=1}^{N_r} \hat{a}_k^{N_r} e^{-j2\pi k\tilde{\tau}}|^2} d\tilde{\tau}.$$

The roots of (4.21) determine the number of significant clusters. However, in practice, some existing roots may not be significant and they are unnecessary to model. The analysis on $\hat{H}^{N_r}$ w.r.t. N_r may demonstrate this.

For analyzing data, we chose the pseudo-measurements of class 3, 6 and 9 realistic in-home PLC channel realizations [121]. The estimated entropy and PDS for the class 3 and 9 are depicted in Fig. 4.11(a) and Fig. 4.11(b). In each class, the estimated entropy

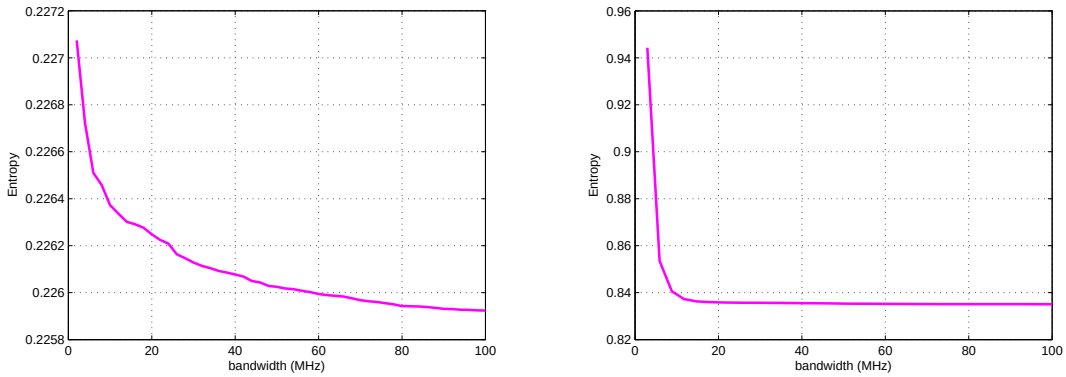

(a) class 3 (b) class 9

Figure 4.11: Estimated entropy for: (a), (b).

is plotted versus an ascending bandwidth up to 100 MHz[2]. The estimated entropy of class 9 is higher than the one of class 3. This is consistent with the channel classification rule, i.e. large class channel has higher channel capacity. Furthermore, we remark that, in the class 3 case, in narrowband region (say, $1 - 30$ MHz)[3], the entropy does not rapidly descend when we increase the bandwidth. However, for the class 9 case, the entropy slope appears to be quite steep in this region. That means, by augmenting the bandwidth in the narrowband region, the class 9 gains much more information about the channel knowledge than the class 3. But if we move to the wideband region (i.e., beyond 30 MHz), the entropy of the class 3 keeps descending, although again, it descends slowly. The class 9 case, on the contrary, shows a flat floor tendency. For this situation, it seems that, in the wideband region, the class 9 cannot gain much information from the wideband but the class 3 still does.

This inference can be easily verified by checking the estimated PDSs as shown in Fig. 4.12 for class 3 and Fig. 4.13 for class 9 with different bandwidths. First we compare the PDS of class 3 in a fixed bandwidth (say, 50 MHz) with the one of class 9 in the same bandwidth. The comparison shows that class 3 has wider delay spread and weaker energy than class 9. Further, in the class 3 case, the channel energy is spread over a large number of paths. However, in the case of class 9, the channel energy concentrates on few paths. Next, remind of what we remarked in the entropy analysis that the class 9 channel cannot get much information from the wideband but class 3 does. This remark can be verified and further explained by the estimated PDSs. In class 3 case, in the narrowband region (e.g., 5 MHz), the PDS does not have a well described shape. When we increase the bandwidth from 5 to 30 MHz or even higher, the PDS shape is effectively refined. On the other hand, in class 9 case, when we augment the bandwidth from 5 to 30 MHz, its PDS already results in a pretty definite shape. If we further increase the

[2]The realistic in-home PLC channel generator can provide variant channel realizations of a given class number and a given target bandwidth [121].

[3]Here, we abuse the term of narrowband to stand for the frequency range up to 30 MHz. This range, however, is normally considered as broadband/wideband for PLC. In this chapter, we call it narrowband is because it is narrower compared with the frequency range up to 100 MHz.

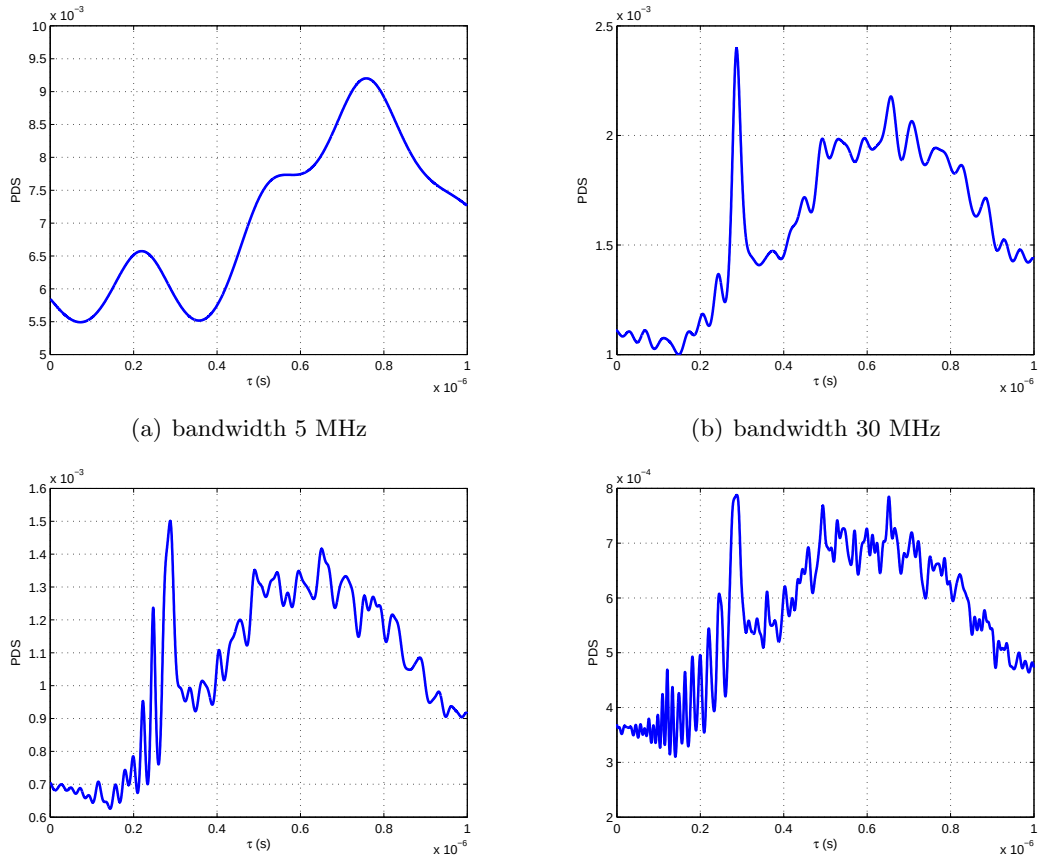

(a) bandwidth 5 MHz

(b) bandwidth 30 MHz

(c) bandwidth 50 MHz

(d) bandwidth 100 MHz

Figure 4.12: Estimated PDS for class 3 with bands: (a), (b), (c), (d).

bandwidth, the PDS shape does not change much. The entropy analysis tells us that, for class 9 channel, further increasing bandwidth in wideband range cannot provide much information about the channel knowledge. Therefore, the situation that PDS of class 9 in wideband does not change much becomes understandable. Ultimately, we can say that the PLC channels have the following characterization that the small class channel, like class 3, has longer delay spread, more selectivity in frequency and weaker channel energy but the large class channel, like class 9, has shorter delay spread and flatter attenuation appears in frequency. As long as we get this conclusion, the links among the above analysis tend to be clear. Because of that class 3 channel behaves more selective in frequency, so it usually needs more samples to describe the channel behavior. However, class 9 channel has flatter frequency behavior, therefore, it is logical that a smaller class number of frequency samples might be enough to model the channel. Note that the class 6 channel behaves somewhere in between the class 3 and 9 channels (see Fig. 4.14).

On the other hand, for the channel behaving like class 9, we suggest to use multi-band system instead of a single wideband. Thus, we can gain more capacity from the bands. The multi-band evaluation will be discussed later on.

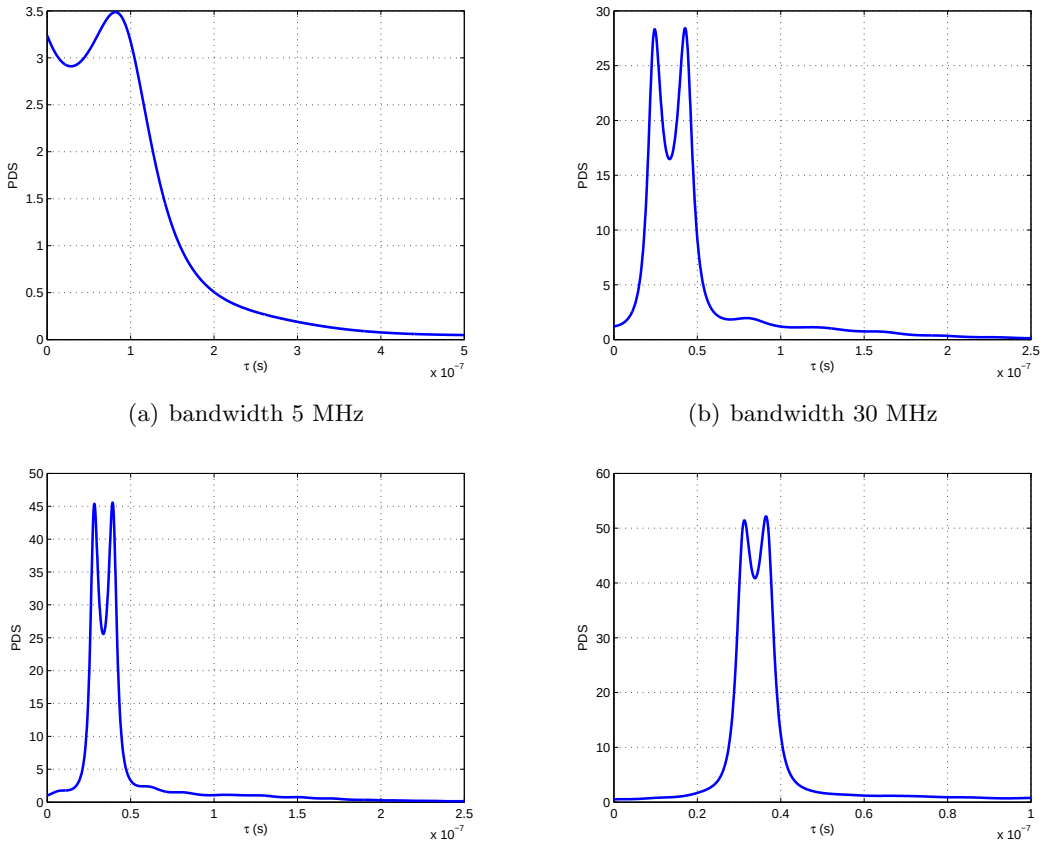

(a) bandwidth 5 MHz

(b) bandwidth 30 MHz

(c) bandwidth 50 MHz

(d) bandwidth 100 MHz

Figure 4.13: Estimated PDS for class 9 with bands: (a), (b), (c), (d).

4.3.2 Degree of Freedom analysis for In-home PLC channel

In the preceding section, we investigated the in-home PLC channel characteristics using a MEM approach. It confirms the results presented in [121] showing that the small class number channel class possesses the longer delay spread and suffers worse frequency selectivity than the large class number channel. Moreover, we remark that the channel of larger class number might be more appropriate for multi-band system. In this section, we further verify this remark by investigating the degree of freedom (DoF) for the different channel classes. Our approach, to do so, is based on the analysis of the channel subspace and the eigendecomposition of the covariance matrix, $\mathbf{K_c}$, of the samples of channel time response, which can be obtained by applying the inverse Fourier transform to the samples of the observed channel process $[h(0), \cdots, h((N_r - 1)\delta_f)]^T$, where the superscript ^{T} stands for the transpose operation, in the frequency domain [23]. The covariance matrix of measured channel samples, $\mathbf{c}$, is written as

$$\mathbf{K_c} = \mathrm{E}\left[\mathbf{c}\mathbf{c}^H\right] = \mathrm{E}\left[\mathbf{g}\mathbf{g}^H\right] + \sigma_n^2\mathbf{I}_N, \tag{4.22}$$

where $\mathbf{g}$ is a vector of samples of the noise-free channel process, and $\mathbf{I}_N$ is the $N \times N$ identity matrix; The superscript ^{H} denotes paraconjugate operation. Assume that the noiseless

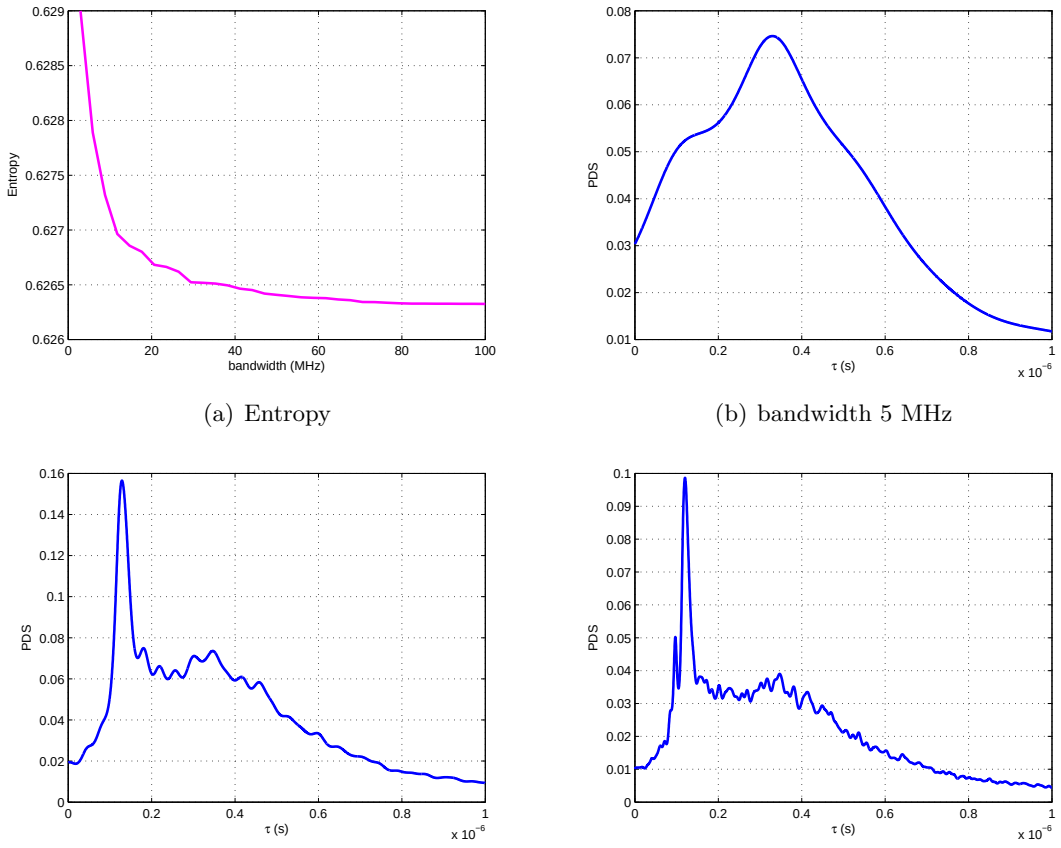

(a) Entropy

(b) bandwidth 5 MHz

(c) bandwidth 30 MHz

(d) bandwidth 100 MHz

Figure 4.14: Class 6: Estimated entropy (a) and Estimated PDS (b), (c), (d).

channel has length p, then the maximum-likelihood covariance matrix estimate computed from N_r statistically independent channel observations with length N_r and $p < N_r$ yields [9]

$$\mathbf{K}_{\mathbf{c}}^{N_r} = \frac{1}{N_r} \sum_{i=1}^{N_r} \mathbf{c}_i \mathbf{c}_i^H. \tag{4.23}$$

The covariance matrix is Hermitian positive definite. Thus, a unitary matrix $\mathbf{U_c}$ exists such that the Karhunen-Loéve (KL) expansion gives

$$\mathbf{K}_{\mathbf{c}}^{N_r} = \mathbf{U_c} \mathbf{\Lambda_c} \mathbf{U}_{\mathbf{c}}^H = \sum_{i=1}^{N_r} \lambda_i(\mathbf{c}) \psi_i(\mathbf{c}) \psi_i^H(\mathbf{c}), \quad \mathbf{U}_{\mathbf{c}}^H \mathbf{U_c} = \mathbf{I}_{N_r}, \tag{4.24}$$

where $\lambda_1(\mathbf{c}) \geq \lambda_2(\mathbf{c}) \geq \cdots \geq \lambda_{N_r}(\mathbf{c})$, $\psi_i(\mathbf{c})$ is the i-th column of $\mathbf{U_c}$; $\lambda_i(\mathbf{c})$ and $\psi_i(\mathbf{c})$ are the i-th eigenvalues and eigenvectors of $\mathbf{K}_{\mathbf{c}}^{N_r}$, respectively. Decomposing (4.23) into

principal and noise components yields [101]

$$\begin{aligned}
&\mathbf{U}_{s,\mathbf{c}} = [\psi_1(\mathbf{c}), \cdots, \psi_L(\mathbf{c})], \\
&\lambda_1(\mathbf{c}) \geq \cdots \geq \lambda_L(\mathbf{c}), \\
&\mathbf{U}_{n,\mathbf{c}} = [\psi_{L+1}(\mathbf{c}), \cdots, \psi_{N_r}(\mathbf{c})], \\
&\lambda_{L+1}(\mathbf{c}) \geq \cdots \geq \lambda_{N_r}(\mathbf{c}),
\end{aligned}$$

where $\mathbf{U}_{s,\mathbf{c}} \perp \mathbf{U}_{n,\mathbf{c}}$. $\mathbf{U}_{s,\mathbf{c}}$ defines the subspace containing both signal and noise components, whereas $\mathbf{U}_{n,\mathbf{c}}$ denotes the noise only subspace. L is the number of significant eigenvalues which also represents the channel DoFs [136], in the sense that any set of observations can be characterized by a set of approximately L independent random variables which excite L modes (their corresponding eigenvectors).

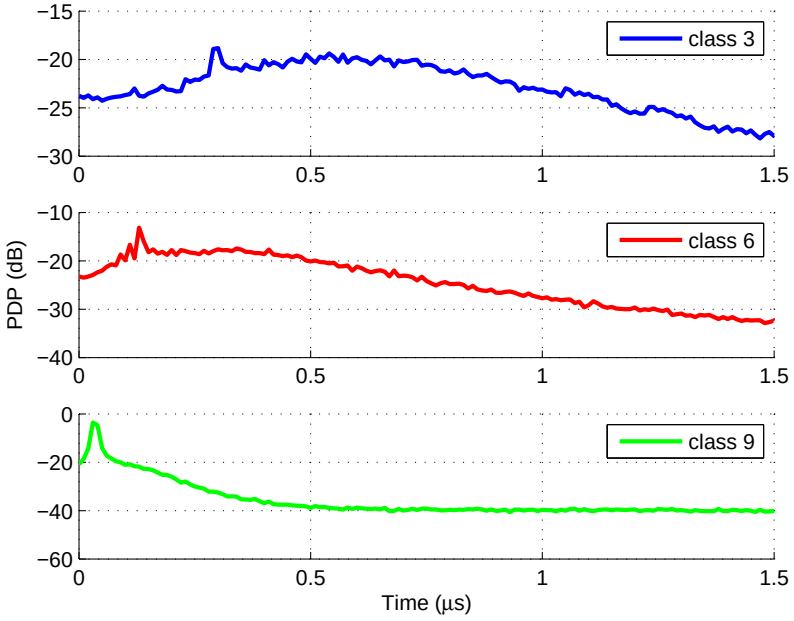

Figure 4.15: Power Delay Profile in three different class channels.

Let us now present the simulation results we get for a frequency resolution equal to 100 KHz/sample. We first see the Power Delay Profile (PDP) curves which are depicted in Fig. 4.15. It confirms our viewpoint presented in the preceding section. In Figs. 4.16, 4.17 and 4.18, we plot, for different classes, the fraction of the captured energy for M_r considered eigenvalues defined by $E_{M_r} = \sum_{i=1}^{M_r} \lambda_i(\mathbf{c}) / \sum_{i=1}^{N_r} \lambda_i(\mathbf{c})$, where N_r is the total number of eigenvalues. We observe that, for class 3 and 6, the majority of the channel energy (say, 90%), in narrower bandwidth case, is confined in a small number of significant eigenvalues; whereas in the wide bandwidth case, the channel energy is spread over a large number of the eigenvalues. However, this situation is a bit different for large class number (e.g. class 9). In Fig. 4.18, the solid curves represent the bandwidth less than 50 MHz while the ones beyond 50 MHz are plotted in dash lines. We find that when the bandwidth is less than 50 MHz, the curves have a similar ordering as in class 3 and 6 cases. However,

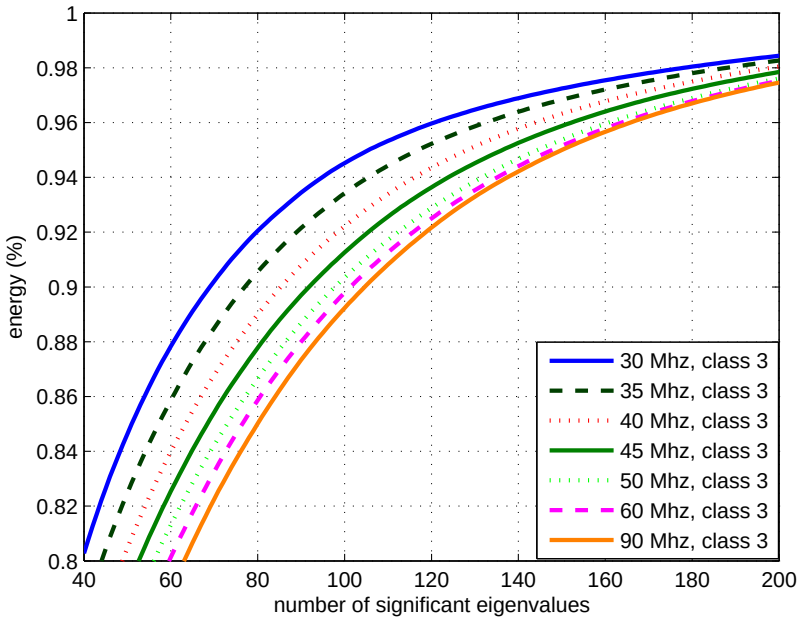

Figure 4.16: Fraction of the captured energy versus the number of significant eigenvalues in class 3 case.

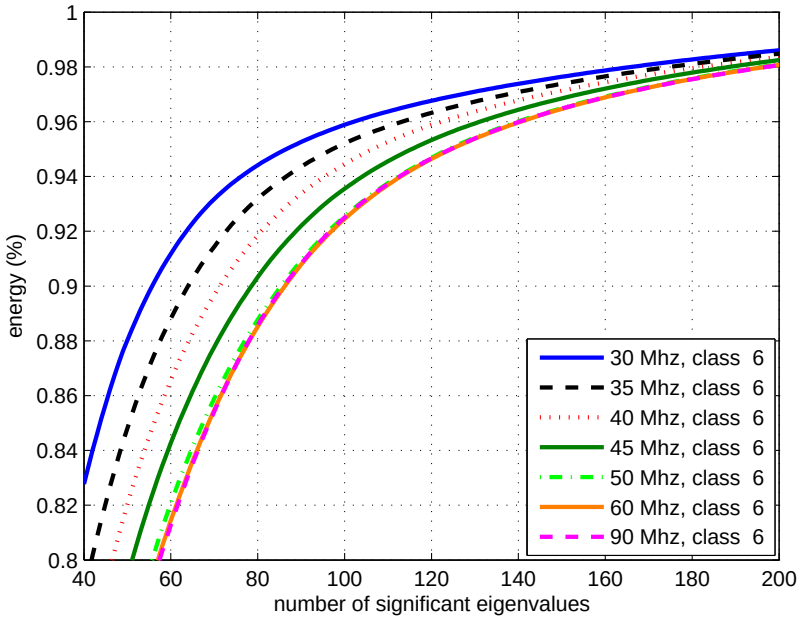

Figure 4.17: Fraction of the captured energy versus the number of significant eigenvalues in class 6 case.

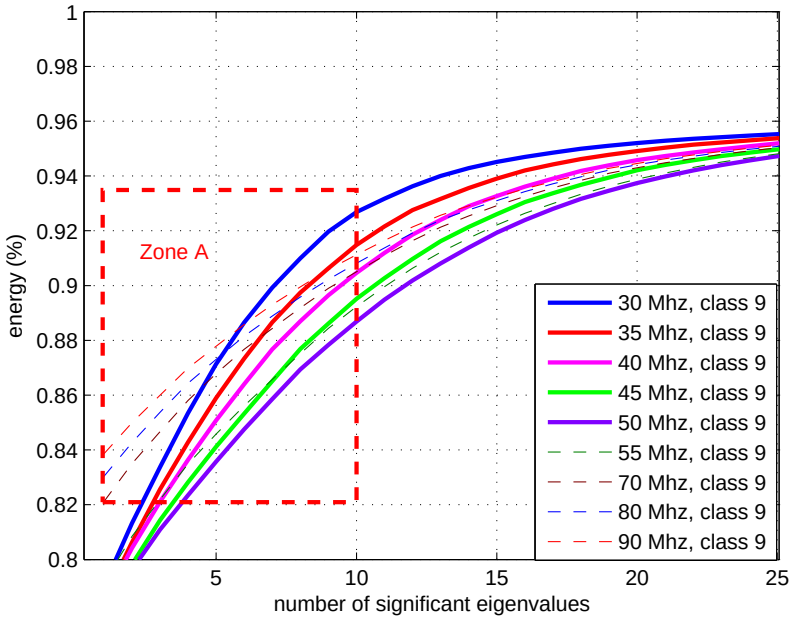

Figure 4.18: Fraction of the captured energy versus the number of significant eigenvalues in class 9 case.

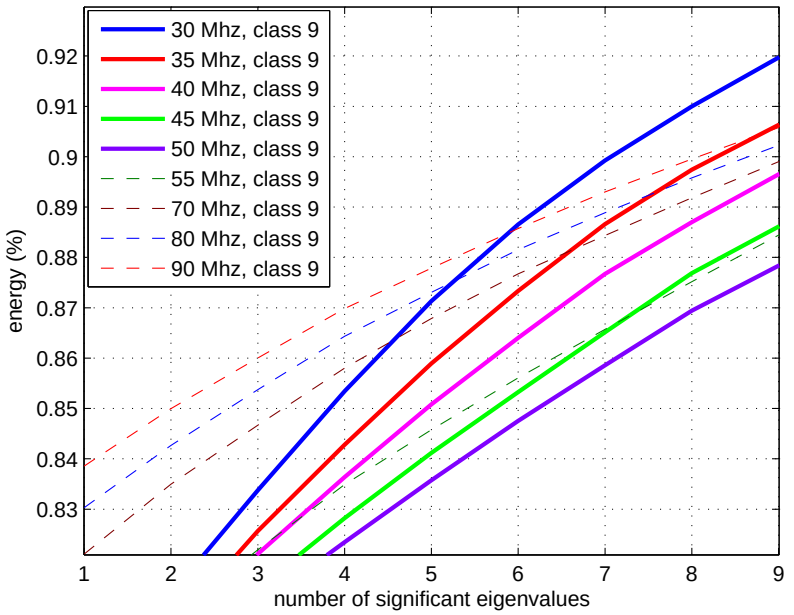

Figure 4.19: A zoomed version of Fig. 4.18.

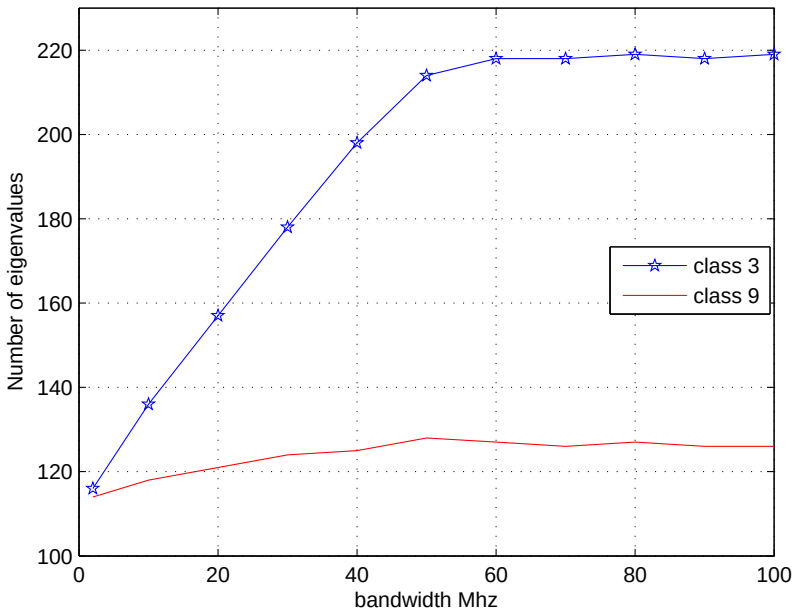

Figure 4.20: Evolution number of the eigenvalue for variant class case.

when the bandwidth is beyond 50 MHz, the curves are displaying by an opposite order. Furthermore, for class 9, the majority of the channel energy concentrates on the very beginning number of eigenvalues, e.g., the first 5 eigenvalues contain almost 84% channel energy for all bandwidth cases. If we further zoom in the zone A (see, Fig. 4.19), it seems that the first extracted DoFs, with smaller bandwidth cases, have the smaller energy compared to the others extracted with larger bandwidth.

Fig. 4.20, plotted for 95% captured energy, shows that the number of significant eigenvalues increases with the channel bandwidth. We see that, for class 3, the increase is linear until bandwidth is less than 50 MHz, where a saturation effect begins to occur. This critical bandwidth can be actually seen as the threshold, below which, the signal bandwidth does not effectively provide sufficient resolution to resolve all eigenvalues, or the complete number of multi-path components. Beyond this threshold, on the other hand, the channel is degenerated in the sense that all the paths can be resolved. Therefore, it will be not necessary to continue enlarging the bandwidth. It is obvious that class 9 begins to saturate at a pretty smaller bandwidth threshold (around 20 MHz) and the number of DoFs for class 9 is much less than that of class 3. Thus, this can prove our remark that for larger class number, multi-band system is more appropriate.

4.3.3 Multi-band Evaluation

Previously, we remarked that the larger class number PLC channel is more appropriate for multi-band system based on the entropy analysis. Then, in Sec.4.3.2, the subspace analysis gave us an evidence that the number of DoFs for the larger class number is much less than the smaller class number and, with increasing the bandwidth, the DoF cannot

be significantly increased for the larger class number. The conclusions of the previous two sections are actually consistent with each other. Finally, in this section, we numerically evaluate our remark. For the sake of simplicity, we still choose these three classes, i.e. class 3, 6 and 9 for comparison. In what follows, we calculate the channel capacity using multi-band and wideband for each class. The capacity calculation is based on Shannon's capacity formula and for the same reference noise and power spectral density (PSD) emission mask [121]. The calculation parameters are: Carrier width ($\triangle f = 100$ KHz); Transmitted PSD ($P_t = -50$ dBm/Hz); White noise PSD ($P_n = -140$ dBm/Hz); Number of the carriers N_r is subject to the bandwidth (i.e. wideband: $1-90$ MHz; multi-band: $1-30$, $30-60$, $60-90$ MHz). The capacity C formula for one measurement is given by

$$C = \Delta f \sum_{i=1}^{N_r} \log_2 \left(1 + \frac{P_t \cdot |h_i|^2}{P_n}\right) \text{(bit/s)} \tag{4.25}$$

The results are layout in the Table 4.3, where the capacity is averaged over a large set of measurements. The results proved our remark, i.e. the capacity improvements for class 9, 6 and 3, using multi-band instead of wideband, are 5.7, 4.6 and 3.3 Mbits/s, respectively. This improvement can also be called multi-band gain. It is worth noting that the above validation was done using a database coming from a simulator and not real measurements. Indeed, the multi-band gain is very small because the inputs samples are not coming from a real measurements but from channel model which doesn't take into account the underlaying correlation of UWB taps at large bandwidth.

Table 4.3: Capacity comparison.

Capacity (Gbits/s)	class 9	class 6	class 3
C_{1-30}	0.8371	0.6952	0.5329
C_{30-60}	0.8548	0.6873	0.4931
C_{60-90}	0.8245	0.6335	0.4459
C_{1-90}	2.5107	2.0115	1.4686

4.4 Summary and Conclusion

In the first part of the chapter, we presented a fundamental theoretical PLC CTF model and its parametric modelling. Next we introduced an analytical modelling based on the theoretical CTF model adding some statistical assumption. Finally, we ended by showing a measurement analysis based on a realistic CTF modelling which is totally independent of the theoretical model. In the second part of this chapter, we analyzed the in-home PLC channel characterizations w.r.t. different channel classes. The MEM based analysis portrays that the small class channels have longer delay spread, worse frequency selectivity and weaker channel energy. Furthermore, the estimated entropy of this group of channels descends slowly when we increase the bandwidth. Therefore, for modelling this group of channels, we usually need more samples, alternatively, wider band can provide more refined channel modelling. On the other hand, the large class channels have shorter delay spread and flatter attenuation in frequency that relates to their estimated entropies that

descend rapidly in the narrowband range, but, almost remain flat in the wideband range. After that, the DoF analysis further confirmed what we deduced in the MEM analysis. Moreover, we remark that the significant eigenvalue energy is spread over the frequency band. But, there exists a saturation threshold for each channel class case. The small class channel has a threshold which happens in wider frequency band and the large class channel has a threshold which happens in pretty narrow frequency band. It reveals that the large class channel might be more suitable for multi-band systems. The multi-band was evaluated right after the analysis, wherein, we gave a simple example, e.g. capacity comparison, which shows that large class channels have more multi-band gains.

However, for the transmission view point, the main feature of the PLC channel, which has been illustrated in several studies [96, 139, 121, 93] and analyzed again in this chapter, is its multi-path behavior. Consequently, Multi-carrier Modulations (MCMs), here again, appear as the most appropriate transmission means.

Chapter 5

Gabor Systems and MCM Schemes

The multi-path behavior or, equivalently, the frequency selective feature of the PLC channel has been recalled and analyzed in the previous chapter. To fight against frequency selectivity, one of the possible solutions is to use Multi-Carrier Modulation (MCM). In PLC, as a matter of fact, it has been decided to adopt MCMs at the physical layer for the future BPL standard [1]. Now, the question is "which MCM scheme should be used in the standard". Two MCM schemes, named OFDM/DMT and Wavelet OFDM, have been elected in the draft standard proposed by HPAV and Panasonic, respectively, targeting to the USA/European and Asian markets. This thesis presents an alternative scheme called OFDM/OQAM and focuses on the analysis of OFDM/OQAM compared with OFDM.

In this chapter, we first give some mathematical tools that can help us to better understand OFDM/OQAM scheme from a Gabor theory point of view. Next, we present the OFDM/DMT modulation including its advantages and disadvantages as well as the proposed windowing process by HPAV in PLC. Then, we pay more attention on the presentation of OFDM/OQAM including the basic idea, its structure and the initial set of prototype filters used in this thesis. After that, we unveil the Hermitian Symmetry condition for OFDM/OQAM (HS-OQAM) to make the conventional OFDM/OQAM system to fit to baseband communications. The goal is to keep the conventional OFDM/OQAM system structure to be unchanged and add some conditions on the entry symbols to eventually get a real-valued modulated signal. Furthermore, we show a link between HS-OQAM system and the Linear Phase Cosine Modulated Filter Bank (LP-CMFB) system. In the end, the motivation of using HS-OQAM system instead of OFDM in PLC is discussed. As to the Wavelet OFDM, we only give a brief introduction since it is not the main scope of this thesis.

5.1 Preliminary

5.1.1 Vector spaces

A fundamental notion is that of **vectors** which in turn define vector spaces.

Definition 5.1.1.1 *Vector.*

A **vector** *of K^n is a n-uple x (also noted $\vec{x}$ or $\mathbf{x}$) of elements of the field K (e.g., $\mathbb{R}$ or $\mathbb{C}$):*

$$x = \begin{pmatrix} x_1 \\ \vdots \\ x_i \\ \vdots \\ x_n \end{pmatrix} \tag{5.1}$$

Definition 5.1.1.2 *Vector space.*

A set of vectors E is a **vector space** *on the field K if it is supplemented with an internal addition operation and an external product operation on $E \times K$ such that $(E, +)$ is a group, i.e., for all vectors $x, y, x \in E$*

- *$x + y \in E$ (E is closed under vector addition),*
- *$(x + y) + z = x + (y + z)$ (associative law of vector addition),*
- *$x + y = y + x$ (commutative law of vector addition),*
- *There exists a unique $0_E \in E$ such that $x + 0_E = x$ (zero vector),*
- *There exists a unique '$\Leftrightarrow x$' such that $x+ \Leftrightarrow x = 0_E$ (existence of additive inverses)*

.

Definition 5.1.1.3 *Inner product and Hilbert space.*

A **inner product** *(or* **dot product** *or* **scalar product***) is a symmetric*[1] *positive definite*[2] *bilinear*[3] *form from $E \times E$ to $K : x, y \mapsto \langle x, y \rangle$ such that:*

- *$\langle x, y \rangle = \langle y, x \rangle$ for all x and y in E (commutativity),*
- *$\langle \lambda x + \mu y, z \rangle = \lambda \langle x, z \rangle + \mu \langle y, z \rangle$ (bilinearity),*
- *$\langle x, x \rangle > 0$ if $x \neq 0_E$ (positive definiteness)*

Two vectors x and y such that $\langle x, y \rangle = 0$ are said to be **orthogonal**.

The inner product induces a **norm** *noted $\|x\|$ such that*

$$\|x\|^2 = \langle x, x \rangle.$$

[1] $f : E \times E \to F$ is said to be **symmetric** if $f(x, y) = f(y, x)$ for all $x, y \in E \times E$.

[2] $f : E \to F$ is said to be **positive definite** if and only if $f(x, x) > 0$ for any $x \in E$ such that $x \neq 0_E$.

[3] $f : E \times E \to G$ is said to be **bilinear** if $h_y : E \to F$ such that $h_y = f(x, y)$ is linear for all $y \in E$ and $k_x : E \to F$ such that $k_x = f(x, y)$ is linear for all $x \in E$.

E added with the inner product is said to be a **pre-Hilbert** *space. If E added with the induced norm is complete*[4] *then E is said to be a* **Hilbert space**.

Example Let $\mathcal{L}^2(\mathbb{R})$ be the space of square integrable functions defined by:

$$\mathcal{L}^2(\mathbb{R}) = \left\{ f : \mathbb{R} \mapsto \mathbb{C} \Big| \int_{-\infty}^{+\infty} |f(t)|^2 dt < +\infty \right\}, \tag{5.2}$$

where $\mathbb{R}$ and $\mathbb{C}$ are real and complex fields, respectively. The operation defined by

$$\langle f, g \rangle_{\mathcal{L}^2(\mathbb{R}),\mathbb{C}} = \int_{-\infty}^{+\infty} f^*(t) g(t) dt \tag{5.3}$$

is an inner product in $\mathcal{L}^2(\mathbb{R})$, where $f^*(t)$ is complex conjugate of $f(t)$. Thus, $\mathcal{L}^2(\mathbb{R})$ added with this inner product is a Hilbert space. Equivalently, the operation defined by

$$\langle f, g \rangle_{\mathcal{L}^2(\mathbb{R}),\mathbb{R}} = \mathrm{Re}\Big\{ \int_{-\infty}^{+\infty} f^*(t) g(t) dt \Big\} \tag{5.4}$$

is an euclidian inner product and $\mathcal{L}^2(\mathbb{R})$ with this inner product is also a Hilbert space. In both cases, the norm of the function is defined as

$$\|f\|_{\mathcal{L}^2(\mathbb{R})} = \sqrt{\int_{-\infty}^{+\infty} |f(t)|^2 dt}. \tag{5.5}$$

Another frequently used Hilbert space is shown as follows.

Example Let $\ell^2(\mathbb{Z})$ be the space of square summable sequences defined by:

$$\ell^2(\mathbb{Z}) = \left\{ x : \mathbb{Z} \mapsto \mathbb{C} \Big| \sum_{k=-\infty}^{+\infty} |x[k]|^2 < +\infty \right\}, \tag{5.6}$$

where $\mathbb{Z}$ is integer field. The operation defined as

$$\langle x, y \rangle_{\ell^2(\mathbb{Z}),\mathbb{C}} = \sum_{k=-\infty}^{+\infty} x^*[k] y[k] \tag{5.7}$$

is an inner product and $\ell^2(\mathbb{Z})$ with this inner product in a Hilbert space. Equivalently, the operation defined as

$$\langle x, y \rangle_{\ell^2(\mathbb{Z}),\mathbb{R}} = \mathrm{Re}\Big\{ \sum_{k=-\infty}^{+\infty} x^*[k] y[k] \Big\} \tag{5.8}$$

is an Euclidian inner product and $\ell^2(\mathbb{Z})$ with this inner product is also a Hilbert space. In both cases, the norm of the function is defined as:

$$\|x\|_{\ell^2(\mathbb{Z})} = \sqrt{\sum_{k=-\infty}^{+\infty} |x[k]|^2}. \tag{5.9}$$

[4] A set $(E, \| \cdot \|)$ is said to be **complete** whenever any Cauchy series converges within this set, i.e., $\forall \varepsilon > 0$, $\exists n$ such that $\forall p, q \geq n$, $\|x_p - x_q\| < \varepsilon$.

5.1.2 Bases and frames

Definition 5.1.2.1 *Basis.*

Let $\mathcal{H}$ be a separable Hilbert space (e.g. $\mathcal{L}^2(\mathbb{R})$) equipped with inner product $\langle f, g\rangle$ and norm $\|f\| = \sqrt{\langle f, f\rangle}$. A sequence $\{e_n\}_{n\in\mathcal{Z}}$ is a **basis** *for $\mathcal{H}$ if for all $f \in \mathcal{H}$ there exist* **unique** *scalars c_n dependent on f such that*

$$f = \sum c_n e_n. \tag{5.10}$$

A basis is called *unconditional* if the series expansion is convergent to f in the norm independently of the specific order of the sequence $\{e_n\}$. A basis is bounded if $0 < \inf \|e_n\| \leq \sup \|e_n\| < \infty$.

Definition 5.1.2.2 *Orthonormal basis.*

A basis $\{e_n\} \subseteq \mathcal{H}$ is an **orthonormal basis** *if and only if:*

- $\langle e_n, e_m\rangle = \delta_{n,m}$[5],
- $\forall f \in \mathcal{H},\ f = \sum_{n\in\mathcal{Z}} \langle f, e_n\rangle e_n$.

The square summability of coefficients is guaranteed by the Parseval's formula for orthonormal bases, which reads $\|f\|^2 = \sum_n |\langle f, e_n\rangle|^2$ for all $f \in \mathcal{H}$.

Remark 5.1.2.1 *In the consideration of Hilbert space $\mathcal{H}$, an orthonormal basis is equivalent to a* **Hilbertian basis**.

Definition 5.1.2.3 *A basis $\{f_n\}$ is called* **Riesz basis**, *if there always exists a* **biorthogonal family** *$\{\check{f}_n\}$, satisfying $\langle f_k, \check{f}_n\rangle = \delta_{k,n}$ which generates l^2-coefficients $c_n = \langle f, \check{f}_n\rangle$ for all $f \in \mathcal{H}$.*

Definition 5.1.2.4 *Frame.*

A sequence $\{f_n\}$ in $\mathcal{H}$ is a **frame** *for $\mathcal{H}$ if there exist constants $0 < A \leq B < +\infty$, such that [46]*

$$A\|f\|^2 \leq \sum_n \|\langle f, f_n\rangle\|^2 \leq B\|f\|^2 \qquad \forall f \in \mathcal{H}. \tag{5.11}$$

Valid constants A, B are called *frame bounds*. The frame is *tight* if $A = B$, and it is *exact* if it is no longer a frame when any one of its elements is removed. A sequence that satisfies the upper frame bound (and which may or may not satisfy the lower frame bound) is called a *Bessel sequence*.

Property 5.1.2.1 *Every frame $\{f_n\}$ in $\mathcal{H}$ provides a series representation of arbitrary elements $f \in \mathcal{H}$, i.e. there exists a sequence of square summable coefficients c_n so that $f = \sum_n c_n f_n$. If the frame is not exact then these expansion coefficients will not be unique. However, there is always at least one computable, canonical choice.*

[5] Here $\delta_{n,m}$ denotes the Kronecker delta.

Property 5.1.2.2 *If $\{f_n\}$ in $\mathcal{H}$ forms a frame, then there always exists a dual frame $\{\check{f}_n\}$ with $\frac{1}{B}$ and $\frac{1}{A}$ being its frame bounds, such that*

$$\forall f \in \mathcal{H} \quad f = \sum_n \langle f, f_n \rangle \check{f}_n = \sum_n \langle f, \check{f}_n \rangle f_n \tag{5.12}$$

Remark 5.1.2.2 *Any Riesz basis for $\mathcal{H}$is a frame, and conversely a frame is a Riesz basis if and only if it is exact.*

Remark 5.1.2.3 *If a frame is tight, i.e., $A = B = 1$, then the frame is automatically an orthonormal basis and an orthonormal basis must be a tight frame [40].*

5.1.3 Gabor systems, Gabor frames and Density

Dennis Gabor introduced in 1946 in his "Theory of Communication" a method to represent a one-dimensional signal in two dimensions, with time and frequency as coordinates [54]. Gabor's research in communication theory was driven by the question how to represent locally as good as possible by a finite number of data the information of a signal which is given *a priori* through uncountable many function values $g(t)$. Gabor proposed to expand a function g into a series of elementary functions $\{g_{m,n}\}$, which are constructed from a single building block by translation and modulation.

Definition 5.1.3.1 *Given $g \in \mathcal{L}^2(\mathbb{R})$ and fixed $T_0, F_0 > 0$, the Gabor system corresponding to g, T_0 and F_0 verifies [54]*

$$\forall t \in \mathbb{R}, \quad g_{m,n}(t) = g(t - nT_0)e^{j2\pi mF_0 t}. \tag{5.13}$$

The function g is called prototype function, and the functions $g_{m,n}$ are the functions translated from the prototype function with parameters T_0 and F_0. Gabor systems are sometimes referred to as Weyl-Heisenberg systems.

Definition 5.1.3.2 *A Gabor system that forms a frame for $\mathcal{L}^2(\mathbb{R})$ is called a Gabor frame.*

Definition 5.1.3.3 *We define the density of a Gabor system as $\rho_G = \frac{1}{T_0 F_0}$.*

Proposition 5.1.3.1 *A Gabor system $\{g_{m,n}\}_{m,n\in\mathbb{Z}}$ can be a frame only when $\rho_G \geq 1$, can be an exact frame only when $\rho_G = 1$, and must be incomplete if $\rho_G < 1$ [104, 40, 103].*

5.1.4 Gabor System and Balian-Low Theorem

The Balian-Low Theorem (BLT) is a key result in time-frequency analysis. It was originally stated by Balian [10] and, independently, by Low [86].

Theorem 5.1 *If a Gabor system $\{g_{m,n}\}_{m,n\in\mathbb{Z}}$ with density $\rho_G = 1$ forms an orthonormal basis for $\mathcal{L}^2(\mathbb{R})$ then*

$$\left(\int_{-\infty}^{\infty} |tg(t)|^2 dt\right)\left(\int_{-\infty}^{\infty} |\gamma\hat{g}(\gamma)|^2 d\gamma\right) = +\infty, \tag{5.14}$$

where $\hat{g}(\gamma) = \int_{-\infty}^{\infty} g(t)e^{-j2\pi\gamma t}dt$ is the Fourier transform of g. The BLT was later extended from orthonormal bases to exact frames [40].

Proposition 5.1.4.1 *BLT gives the relation between Gabor density and signal localization [50] as: $\rho_G > 1$, frames with excellent time-frequency localization properties exist (a particular example are frames with Gaussian g with appropriate density); $\rho_G = 1$, frames and orthonormal bases are possible, but without good time-frequency localization; $\rho_G < 1$, Gabor system is incomplete.*

In practice, Gabor systems may be used for signal decomposition and reconstitution, e.g. for sub-band coding, or, conversely for signal synthesis followed by signal analysis, e.g. for a transmission purpose. In the first case, a Gabor frame ($\rho_{\mathrm{G}} \geq 1$) has to be used to perfectly reconstruct the signal. At the contrary, in the second case, the condition to recover the transmitted information is to use a Gabor family for which the set $g_{m,n}$ satisfies a linear independence condition, i.e. corresponds to Riesz bases with ($\rho_{\mathrm{G}} \leq 1$).

Therefore, for Gabor-based MCMs, as in [78], we can distinguish between the 3 following cases:

- Undercritical time-frequency lattice ($\rho_{\mathrm{G}} < 1$) for which incomplete Riesz bases using well localized prototype functions exist.
- Critical time-frequency lattice ($\rho_{\mathrm{G}} = 1$) for which complete Gabor bases exist but necessarily lead to bad time-frequency localization feature.
- Overcritical time-frequency lattice ($\rho_{\mathrm{G}} > 1$) for which Riesz basis do not exist and if frames may exist they do not permit to recover the information from the received signal.

5.1.5 Time-frequency Localization

The lower limits of signal simultaneous localization in time and frequency are given by the uncertainty relations. The existence of these limits is a consequence of the fact that the signal and it Fourier spectrum are not mutually independent functions. For the continuous time signals, a well-known uncertainty relation is the one shown by Gabor [54]. It gives the lower bound for the product of the ordinary second moments in time and frequency. Signals that reach this uncertainty limit have the best joint localization and, in Gabor's case, are Gaussian functions. This limit was extended for discrete time signals by Ishii and Furukawa [70] with the constraints that the signal spectrum is real-valued and zero at the angular frequency $\omega = \pi$. Later, Calvez and Vilbé [25] further extended this work to a more relaxed constraint of complex-valued signal spectrum with zero at the angular frequency $\omega = \pi$. However, this relation is not, in general, valid for all finite-energy discrete time signals. In [44], Doroslovački presented a modified second moment in time and frequency to derive the Gabor uncertainty limit to finite-energy discrete time signal without the frequency constraint.

Modified Localization Factor

Based on Doroslovački's definitions, a measure of the time-frequency localization for a discrete-time sequence $x[k]$ is given by

$$\xi_{\mathrm{mod}} = \frac{1}{4\pi\sqrt{m_2 M_2}}, \tag{5.15}$$

where m_2 is the modified second moment in time and reads

$$m_2(x) = \frac{1}{\|x\|^2} \sum_{k\in\mathbb{Z}} \left(k - \frac{1}{2} - T(x)\right)^2 \left|\frac{x[k] + e^{j2\pi F(x)} x[k-1]}{2}\right|^2, \tag{5.16}$$

and M_2 is the modified second moment in frequency with the expressions as

$$M_2(x) = \frac{1}{(2\pi)^2\|x\|^2} \sum_{k\in\mathbb{Z}} |x[k] - e^{j2\pi F(x)} x[k-1]|^2, \tag{5.17}$$

where $F(x)$, the gravity center in frequency, reads

$$F(x) = \frac{1}{2\pi} \frac{\mathrm{Im}\{\sum_{k\in\mathbb{Z}} x[k]x^*[k-1]\}}{\mathrm{Re}\{\sum_{k\in\mathbb{Z}} x[k]x^*[k-1]\}}, \tag{5.18}$$

and $T(x)$, the gravity center in time, reads

$$T(x) = \frac{\sum_{k\in\mathbb{Z}} (k-1/2)|x[k] + e^{j2\pi F(x)x[k-1]}|^2}{\sum_{k\in\mathbb{Z}} |x[k] + e^{j2\pi F(x)x[k-1]}|^2} \tag{5.19}$$

Theorem 5.2 *The time-frequency localization of a discrete time signal is bounded in* $0 \leq \xi_{mod} \leq 1$.

The equality holds when the discrete function is an optimal function proposed by Doroslovački, we call it Doro function. This function attains the uncertainty limit but it is not in general an orthogonal function [113]. We will re-discuss this function in the later chapters.

5.1.6 An Overview of MCMs from Gabor Theory to PLC

Discrete MultiTone (DMT) modulation, seen as a very basic member in Gabor systems, has been studied for non-flat channels in a number of publications over the past decades. The theoretical advantages of DMT were demonstrated in the pioneering paper by Kalet [73] twenty years ago. DMT has been widely used in Digital Subscriber Lines (DSL), and excellent descriptions of this can be found in [31] and [119]. Since DMT retains all the merits of OFDM modulation, it has been proposed as a suitable modulation for PLC [5]. However, the drawbacks of OFDM/DMT have also been noticed by many researchers. In the first, in order to counteract the interference, DMT needs to append some redundancy with the so-called guard interval, e.g. in [5], the proposed guard interval is a duplication of the part of the OFDM symbol and therefore it has been named cyclic prefix (CP). This idea was originally proposed by Peled and Ruiz [94]. In the rest of this thesis, the guard interval of OFDM/DMT is identical to CP, unless indicated otherwise. The second drawback is that for broadband applications like PLC, the protection mask issue is fairly strict for the modulation itself in order not to interfere with other parallel existing applications such as radio amateurs. However, OFDM cannot very much fit into this mask due to the poor frequency localization of rectangular pulse shaping. One solution proposed by HPAV is to filter the OFDM symbol by a window and then it leads to a so-called windowed OFDM or windowed DMT system. This filtering method can refine the symbol spectrum on the border side and the notch positions. However, the frequency localization is still not very

good. The explanation has already been given in Gabor theory and Balian-Low theorem, i.e. for the critical sampled Gabor system, we cannot have both orthogonality and good time-frequency localization feature (refer to Theorem 5.1 and Proposition 5.1.4.1).

To overcome this drawback, Cherubini *et al.* proposed a Filter MultiTone (FMT) instead of DMT [30]. It is essentially an over-sampled Gabor system ($\rho_{\mathrm{G}} < 1$), i.e. it corresponds to a transmultiplexer with under-critical time-frequency lattice ($T_0F_0 > 1$) [78]. Following the guide of Proposition 5.1.4.1, FMT relaxes the Gabor density to have more degrees of freedom to generate a pulse shaping with good localization features. Although FMT fixed the pulse shaping localization problem of DMT, it still suffers from the spectrum leakage issue due to the carrier separation. The spectral loss directly links to the sampling factor of FMT. Since, in this thesis, we will only focus on the transmultiplexer with critical time-frequency lattice, the under-critical case is out of the scope. The readers who are interested in this topic can refer to the related references [29, 15, 20, 16, 38, 113].

As we stated at the beginning of this section, the classical OFDM system based on ordinary quadrature amplitude modulation (OFDM/QAM) prohibits time-frequency well-localized basis functions in the case of critical Gabor density where spectral efficiency is maximal [52]. In Gabor theory this phenomenon is known as Balian-Low theorem [10, 86, 40]. Two approaches to circumvent this problem: The first one, cf. [30], is to generate an orthonormal basis (tight frames) that retains perfectly orthogonality with undercritical grid (i.e., over-sampling). The second one, cf. [78], is to generate a non-orthonormal basis but a bi-orthogonal basis functions under the condition of undercritical grid. However, both methods result in a significant loss in spectral efficiency, which is undesirable in high-data-rate applications.

Besides, another Gabor system based modulation, the so-called O-QAM, was proposed by Hirosaki in 1981 [66], where O-QAM meant Orthogonally multiplexed QAM, Hirosaki was also the first to introduce a DFT processing in the O-QAM or, equivalently, OFDM/OQAM modulation scheme. Note, however, that a digital implementation based on polyphase networks and DFT has already been proposed in [13, 21]. Later the acronym OFDM/OQAM was introduced at first in [52] where OQAM had recovered its initial meaning of Offset-QAM. This principle has been introduced long ago [28] and [109], but it is more recently [52] that OFDM/OQAM has been presented as a viable alternative to OFDM. In [52], it has been pointed out that OFDM/OQAM allows time-frequency well-localized pulse shaping filters even in critical Gabor density case (i.e. maximum spectral efficiency). It sounds like a miracle since it breaks the rule of Balian-Low theorem. The key idea behind is to change the orthogonality condition from complex-valued field to real-valued field (discussed more in detail in the forth-coming sections). After that, Siohan *et al.* revealed the relation between OFDM/OQAM and filter bank theory and further gave an efficient implementation of causal OFDM/OQAM systems using FFTs [115]. Since OFDM/OQAM can have well-localized pulse shaping filters and it retains maximum spectral efficiency, it was therefore introduced in PLC domain by Skrzypczak *et al.* at ISPLC conference in 2007 [117], wherein the authors gave some experimental results to show that OFDM/OQAM is fairly robust to narrowband noise and very much fits into the PLC mask. Meanwhile, Lélé *et al.* presented some channel estimation methods for OFDM/OQAM at that conference [83] to further give a proof of OFDM/OQAM outperforming CP-OFDM/DMT in the PLC context. However, at that moment, OFDM/OQAM cannot be directly utilized in practical PLC transmission with the reason that, for base-

band communications, the modulated signal has preferably to be real-valued which is not the case for conventional OFDM/OQAM modulation. Inspired by DMT entries conditions, we intend to present the Hermitian Symmetry (HS) constraints on the entry symbols of the conventional OFDM/OQAM system (without changing the structure of OFDM/OQAM system, i.e., keeping the same FFT size and bandwidth) leading then to a HS-OQAM system such that it can be practically applied in PLC.

In addition to DMT and HS-OQAM, Koga *et al.* presented a non-Gabor system based modulation called wavelet OFDM (WOFDM) in ISPLC conference 2003 [77]. This modulation is based on the cosine modulated filter banks (CMFB) [130]. There are several common features between WOFDM and HS-OQAM that are discoursed in the forth-coming chapters. Since WOFDM is not the key attention of this thesis, a brief introduction is given in this thesis and we mainly focus our attention on HS-OQAM and CP-OFDM/DMT.

5.2 DMT modulation

DMT modulation was firstly introduced in the DSL context [31, 119]. It actually inherits all the features of OFDM modulation. Hence, the two main advantages of DMT are: 1) efficient implementation by FFTs; 2) simple equalization at the receiver. Owing to these benefits, DMT has been proposed recently to PLC [5]. In this section, we first show the relation between DMT and Gabor system. Then we discuss its main disadvantages and advantages. We end this section with an introduction of the proposed DMT system in HPAV.

5.2.1 Links between DMT system with Gabor system

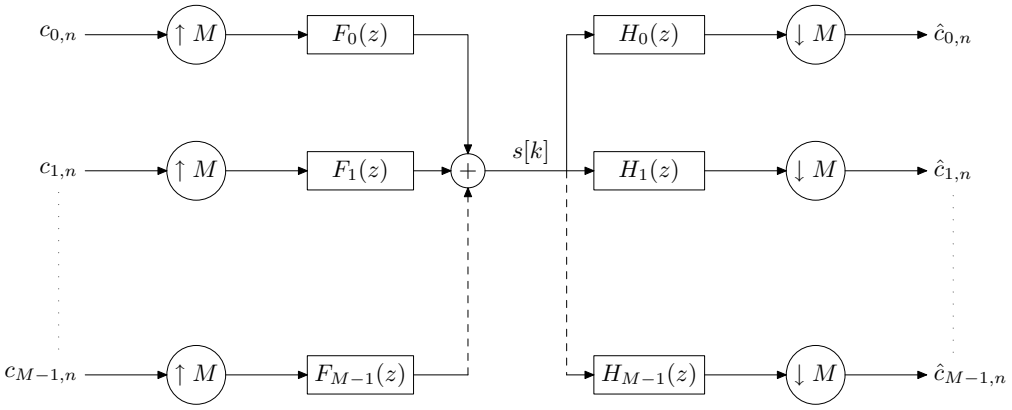

Figure 5.1: Baseband representation of DMT system.

Since DMT system belongs to the Gabor family, so the transmission structure can be expressed as in Fig. 5.1 which is a typical filter bank based transmultiplexer (TMUX) structure assuming M number of total carriers. The complex-valued entrance symbols $c_{m,n}$ are obtained from 2^{2K}-QAM constellations with $m \in \{0, \cdots, M-1\}$ standing for the sub-carrier index (or sub-channel index) and $n \in \mathbb{Z}$ denoting time index. The discrete

baseband modulated DMT signal can be formulated as

$$s[k] = \sqrt{\frac{1}{M}} \sum_{m=0}^{M-1} \sum_{n \in \mathbb{Z}} c_{m,n} \Pi[k - nT_0] e^{j2\pi m F_0 (k - \frac{D}{2})}, \tag{5.20}$$

where F_0 is the carrier spacing equaling to $F_0 = 1/M$. T_0 is the symbol duration with $T_0 = M$ (in samples). D is the delay for causality with $D = M - 1$. The Π function represents the rectangular filter with length M (M is assumed to be an even value):

$$\Pi[k] = \begin{cases} 1 & k \in [-\frac{M}{2}, \frac{M}{2}[\\ 0 & \text{otherwise.} \end{cases}$$

From (5.20), it is easy to find that the synthesis functions are actually Gabor functions because the basis function is composed of the translation in time and modulation in frequency, i.e.,

$$\Pi_{m,n}[k] = \sqrt{\frac{1}{M}} \Pi[k - nT_0] e^{j2\pi m F_0 (k - \frac{D}{2})}. \tag{5.21}$$

Further, the basis functions can form an orthonormal basis, i.e.,

$$\langle \Pi_{m,n}, \Pi_{p,q} \rangle = \sum_{k \in \mathbf{Z}} \Pi_{m,n}[k] \Pi^*_{p,q}[k] = \delta_{m,p} \delta_{n,q}. \tag{5.22}$$

where the superscript * stands for conjugate. Note that (5.22) is also usually considered as the orthogonality condition.

5.2.2 Bad-localized Rectangular filter

Remind that, in Sec. 5.1.4 for Gabor systems, there cannot exist any basis functions that have simultaneously orthogonality and good localization in time-frequency when Gabor density is equal to one (critical sampling) referencing to Proposition 5.1.4.1. Otherwise said, for the critically sampled DMT system (i.e. $T_0 F_0 = 1$) equipped with an orthogonal pulse shaping verifying (5.22), its pulse shaping filter cannot have good time-frequency localization feature. In Fig. 5.2, we show the frequency representation of the DMT. It is easy to see that its second lobe attenuation is only 13 dB lower than the main lobe.

Alternatively, we can also calculate its localization factor ξ_{mod} by (5.15) resulting, for $T_0 = M = 16$, in the value of 0.155 which is way too far from the upper bound, i.e., $0.155 \ll 1$. Further, the localization feature of a pulse filter can also be verified by its ambiguity function over a phase space [52, 63]. Let us define a sampled version of the ambiguity function of $g(t)$ as $A_g[l, k] = A_g(lT_0, kF_0)$ where $A_g(\tau, \mu)$ is given by

$$A_g(\tau, \mu) = \int_{-\infty}^{\infty} g(t - \frac{\tau}{2}) g^*(t + \frac{\tau}{2}) e^{j2\pi\mu t} dt.$$

This function gives an insight of the energy leakage of the given function over time and frequency axes. In Fig. 5.2, we depict the ambiguity function of the rectangular pulse with length $T_0 = M = 16$ for example. The ambiguity function shows that the energy is spreading more over frequency than time domain. This is not desirable in the case of transmission over the channel with narrowband noise nor in the case of frequency selective

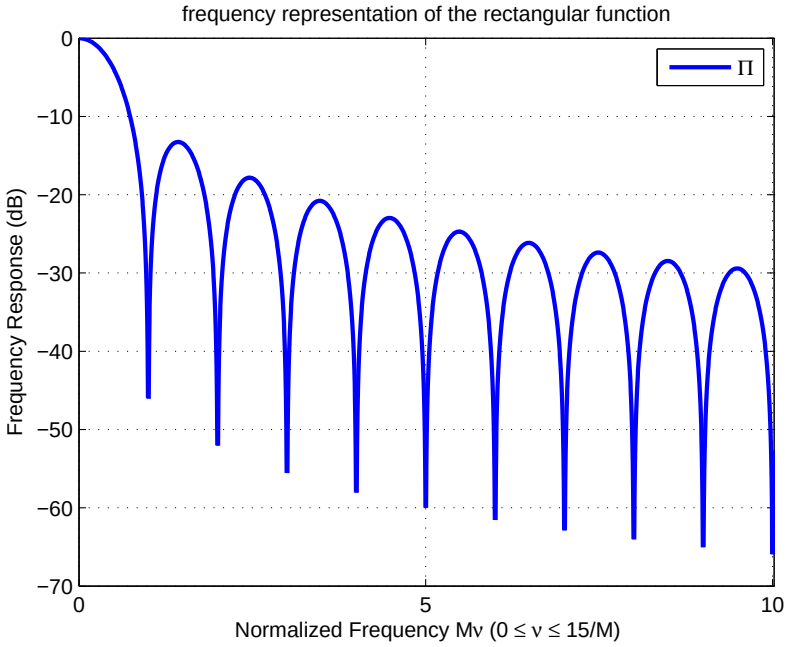

Figure 5.2: Frequency representation of the rectangular function.

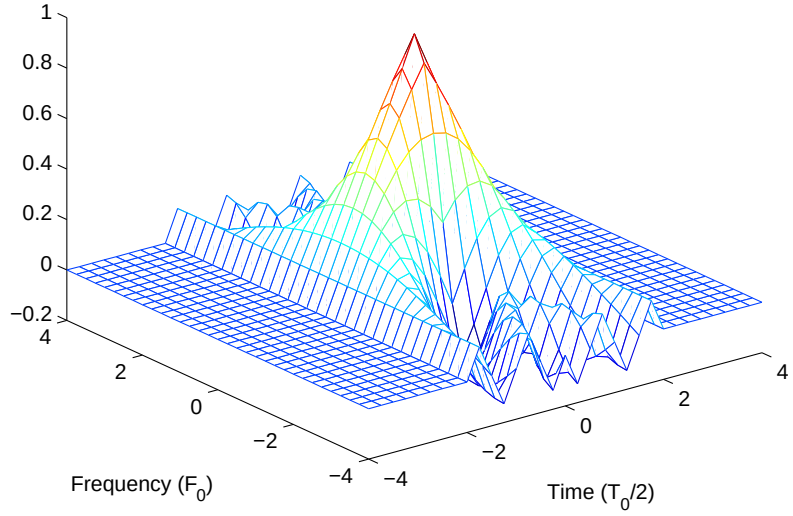

Figure 5.3: Ambiguity function of the rectangular pulse with length T_0 over the phase space.

channel. Because, then, the DMT with rectangular function is fairly sensitive to the narrowband noise [77, 117] or Inter-Carrier-Interference (ICI)[6].

5.2.3 Efficient Implementation and One-tap Equalization

In practice, DMT can be efficiently implemented by Fast Fourier Transforms (FFTs). Moreover, in order to eliminate the Inter-Symbol-Interference (ISI) and ICI, HPAV proposes to use a CP whose length is supposed to be longer than the channel impulse response (CIR) length. Fig. 5.4 depicts the system structure, where the n-th $M \times 1$ block symbols $\mathbf{c}_M(n)$ is first precoded by the IFFT matrix $\mathbf{F}_M^H$ with (m,k)-th entry $e^{j2\pi mk/M}/\sqrt{M}$, to yield the so-called "time-domain" block vector $\mathbf{s}_M(n) = \mathbf{F}_M^H \mathbf{c}_M(n)$. Then a CP of length L_{cp} is inserted between each $\mathbf{s}_M(n)$. The entries of the resulting redundant block, say $\mathbf{s}_{\text{cp}}(n)$, are finally sequentially sent through the channel. The total number of time-domain samples per transmitted block is, thus, $P = M + L_{\text{cp}}$. Consider the $M \times L_{\text{cp}}$ matrix $\bar{\mathbf{F}}_{\text{cp}}$ formed by the last L_{cp} columns of $\mathbf{F}_M$. Defining $\mathbf{F}_{\text{cp}} := [\bar{\mathbf{F}}_{\text{cp}}, \mathbf{F}_M]^H$ as the $P \times M$ matrix corresponding to the combined multicarrier modulation and CP insertion, the block of symbols to be transmitted can simply be expressed as $\mathbf{s}_{\text{cp}}(n) = \mathbf{F}_{\text{cp}} \mathbf{s}_M(n)$.

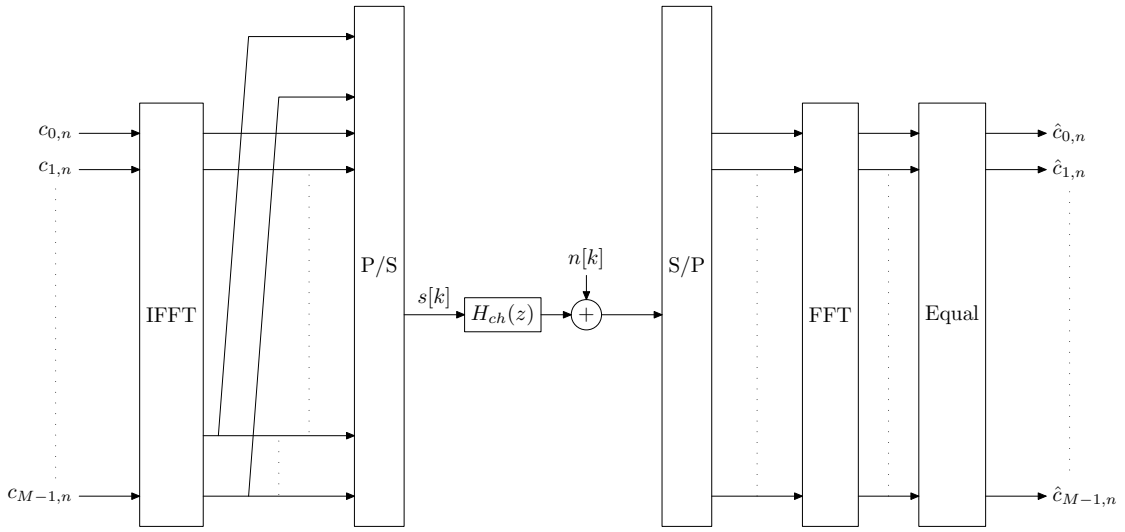

Figure 5.4: Efficient implementation of DMT with CP.

The frequency-selective channel can be modelled as a FIR filter with CIR column vector $\mathbf{h} := [c_0 \cdots c_{M-1}]^T$ and additive with Gaussian noise (AWGN). Then, the n-th received symbol block is given by

$$\mathbf{r}_P(n) = \mathbf{H}_0 \mathbf{F}_{\text{cp}} \mathbf{s}_M(n) + \mathbf{H}_1 \mathbf{F}_{\text{cp}} \mathbf{s}_M(n-1) + \mathbf{n}_P(n), \tag{5.23}$$

[6] Although ICI, in the case of perfect synchronization without Doppler shift, can be eliminated by CP addition, it leads to a throughput loss, which will be further discussed in chapter 4 and chapter 6.

where the $P \times P$ matrix $\mathbf{H}_0$ is defined as

$$\mathbf{H}_0 = \begin{bmatrix} c_0 & 0 & 0 & \cdots & 0 \\ \vdots & c_0 & 0 & \cdots & 0 \\ c_{L_h-1} & \cdots & \ddots & \cdots & \vdots \\ \vdots & \ddots & \cdots & \ddots & 0 \\ 0 & \cdots & c_{L_h-1} & \cdots & c_0 \end{bmatrix},$$

and $\mathbf{H}_1$ is the $P \times P$ upper triangular Toeplitz filtering matrix and is also considered as the ISI matrix, given by

$$\mathbf{H}_1 = \begin{bmatrix} 0 & \cdots & c_{L_h-1} & \cdots & c_1 \\ \vdots & \ddots & 0 & \cdots & \vdots \\ 0 & \cdots & \ddots & \cdots & c_{L_h-1} \\ \vdots & \vdots & \vdots & \ddots & \vdots \\ 0 & \cdots & 0 & \cdots & 0 \end{bmatrix}.$$

Then, the receiver first treats the received block by multiplying with a matrix filter $\mathbf{R}_{\text{cp}} := [\mathbf{0}_{M \times L_{\text{cp}}}, \mathbf{I}_M]$. If $L_{\text{cp}} \geq L_h$, we have $\mathbf{R}_{\text{cp}}\mathbf{H}_1 = \mathbf{0}_{M \times P}$. That way, the ISI can be perfectly eliminated. The next equalization of DMT relies on the well-known property that every circulant matrix can be diagonalized by post- (pre-) multiplication by (I)FFT matrices [135]. Indeed, after removing the CP at the receiver, (5.23) reduces to

$$\mathbf{r}_M(n) = \mathbf{C}_M(\mathbf{c})\mathbf{F}_M^H \mathbf{s}_M(n) + \mathbf{n}_M(n), \tag{5.24}$$

where $\mathbf{C}_M(\mathbf{c})$ is a $M \times M$ circulant matrix with first row

$$\mathbf{C}_M(\mathbf{c}) := \text{Circ}_M(c_0, 0 \cdots 0, c_{L_h-1} \cdots c_1). \tag{5.25}$$

Therefore, after demodulation with the FFT matrix, the "frequency domain" received signal is given by

$$\begin{aligned} \mathbf{x}_M(n) &= \mathbf{F}_M \mathbf{C}_M(\mathbf{c}) \mathbf{F}_M^H \mathbf{s}_M(n) + \mathbf{F}_M \mathbf{n}_M(n) \\ &= \text{diag}[H_0, \cdots, H_{M-1}]\mathbf{s}_M(n) + \mathbf{F}_M \mathbf{n}_M(n) \\ &= \mathbf{D}_M(\tilde{\mathbf{c}}_M)\mathbf{s}_M(n) + \tilde{\mathbf{n}}_M(n), \end{aligned} \tag{5.26}$$

where $\tilde{\mathbf{c}}_M = [H_0 \cdots H_{M-1}]^T = \sqrt{M}\mathbf{F}_M \mathbf{c}$ with H_k denoting the channel's transfer function on the k-th subcarrier. $\mathbf{D}_M(\tilde{\mathbf{h}}_M)$ standing for the $M \times M$ diagonal matrix with $\tilde{\mathbf{h}}_M$ on its diagonal.

Assuming, without loss of generality, that the symbols have variance $\sigma_s^2 = 1$ and additive white noise of variance σ_n^2. The one-tap equalizer yields, e.g. Zero-Forcing (ZF) and Minimum Mean Square Error (MMSE),

$$\mathbf{G}_{ZF} = \mathbf{D}_M(\text{pinv}[\tilde{\mathbf{c}}_M]), \quad \mathbf{G}_{MMSE} = \mathbf{D}_M(\tilde{\mathbf{c}}_M)^H (\sigma_n^2 \mathbf{I}_M + \mathbf{D}_M(\tilde{\mathbf{c}}_M)\mathbf{D}_M(\tilde{\mathbf{c}}_M)^H)^{-1},$$

where pinv$[\cdot]$ stands for the pseudo-inverse operation.

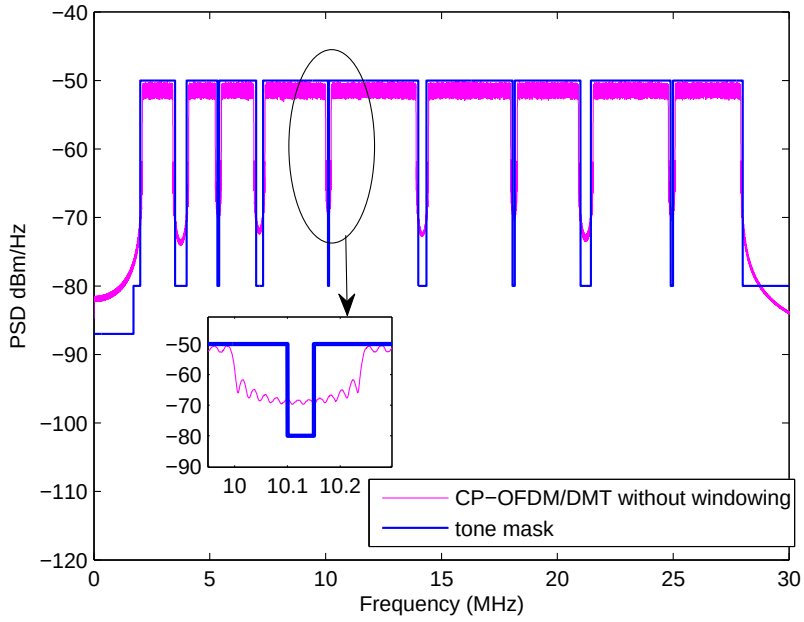

Figure 5.5: HomePlug AV Transmit Spectrum Mask.

5.2.4 Windowed OFDM in HPAV

For broadband in-home PLC, referencing to the HPAV specification [5], the OFDM/DMT has already been proposed as a suitable PHY layer modulation scheme. On the other hand, since the transmission bandwidth is defined to 30 MHz [5], a tone mask needs to be applied to protect the other parallel existing applications. A tone mask defines the set of tones that can be used in a given regulatory jurisdiction or a given application of the HPAV system. Certain tones need to be turned off to comply with the spectral mask requirements of the region or application. Thus, the tone mask can be seen as the first constraint for choosing an appropriate MCM scheme, i.e. the power spectral density (PSD) of the modulated signal using the chosen MCM scheme must fit to this tone mask.

The defined tone mask is portrayed in Fig. 5.5, where the parameters are the ones defined in HPAV [5], i.e. FFT size $M = 3072$, sampling frequency $f_s = 75$ MHz, there are 1155 carriers in the range from 1.8 MHz to 30 MHz. Of these, 917 carriers are used for transmitting the symbols and the rest carriers are switched off. In Fig. 5.5, the notch places represent the carriers that need to be turned off. The conventional CP-OFDM/DMT modulation cannot exactly fit into this mask (see, Fig. 5.5) neither in the notch places nor for the border area. A post-processing windowing operation is then proposed by HPAV [5], whereby, eventually, CP-OFDM modulation can fit into this mask. The windowing scheme is described in Fig. 5.7, where instead of conventional CP-OFDM/DMT, the CP length in Windowing CP-OFDM is equal to GI+RI with GI denoting the conventional CP length and the additional RI denoting the roll-off interval. After GI+RI addition, the OFDM symbol is filtered by a window filter which shapes only the border of each OFDM

symbol with a length of the RI as shown in Fig. 5.7.

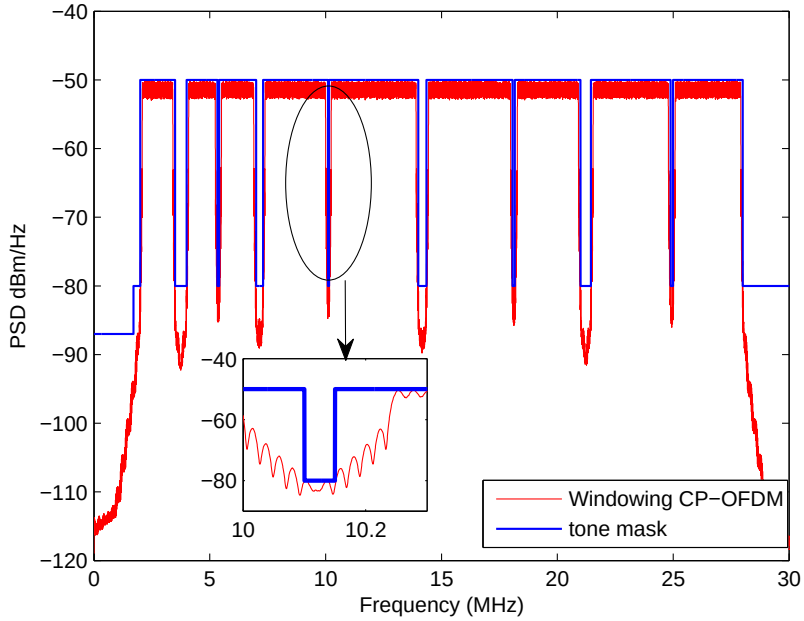

Figure 5.6: HomePlug AV Transmit Spectrum Mask.

This windowing operation will not affect the performance of the modulation and it permits the modulated signal PSD to exactly fit into the tone mask (see, Fig. 5.6). The en/de-windowing process at the receiver is described in the following (cf. Fig. 5.7) [22]:

- Map the transmit symbols onto the orthogonal carriers using IFFT;
- Append CP with length GI+RI;
- Filter the generated CP-OFDM symbol with a given window;
- Parallel to serial by overlapping the consecutive windowed-CP-OFDM symbols with an overlapping factor of RI;
- On the receiver side, serial to parallel conversions for each block size (FFT size+GI);
- Remove the first GI samples of each block;
- Move the first RI samples to the end for each block.

5.3 Wavelet OFDM modulation

Besides DMT modulations, Koga *et al.* proposed a WOFDM modulation for PLC [77] and a recent introduction of WOFDM for PLC was given by Galli *et al.*, in [57]. The original idea of WOFDM is evolved from the so-called discrete wavelet multi-tone (DWMT). The

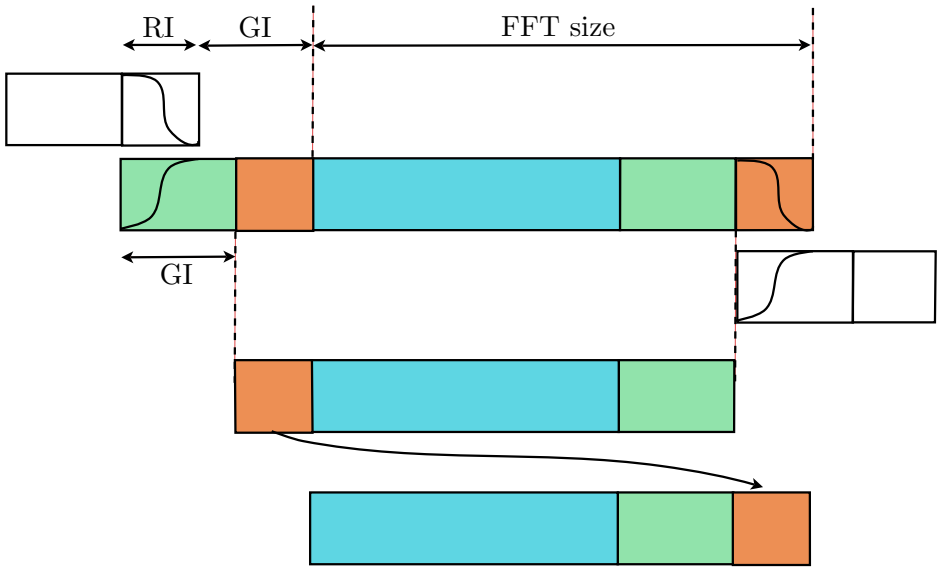

Figure 5.7: Window OFDM scheme.

utilization of DWMT was firstly presented in ADSL applications by Tzannes *et al.,* [129, 128] and a comparison between DMT and DWMT was originally made by Rizos *et al.,* in [105]. The general WOFDM system structure is depicted in Fig. 8.29. Compared with DMT and HS-OQAM, there are three main differences in WOFDM system, the first one is that each of the analysis/synthesis filter has a cosine expression, therefore, WOFDM is not a Gabor system based MCM. The second one is that, to have the same spectrum efficiency as the HS-OQAM system, WOFDM only needs half of carriers of the HS-OQAM case. Furthermore, entry symbols of WOFDM are multi-level Pulse Amplitude Modulation (PAM) and the synthesis filters of WOFDM are cosine modulated kernel based. Therefore, WOFDM can directly generate a real-valued baseband modulated signal without any HS constraints. The last one is that the analysis and synthesis filters of WOFDM do not have a linear phase property.

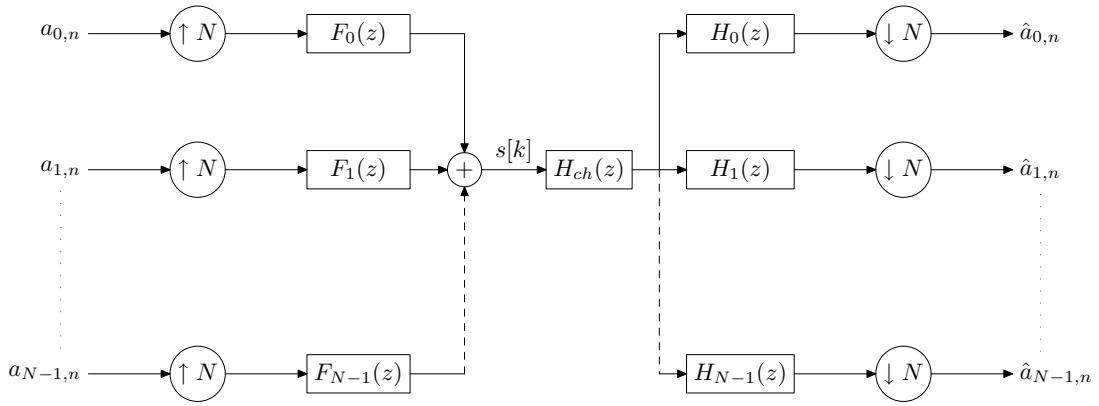

Figure 5.8: Baseband representation of WOFDM system.

The discrete-time modulated WOFDM signal yields [77, 71]

$$s[k] = \sum_{m=0}^{N-1} \sum_{n \in \mathbf{Z}} a_{m,n} f_m[k - nN], \tag{5.27}$$

with the synthesis filters

$$f_m[k] = 2p_0[k] \cos\left(\frac{\pi}{N}(m + 0.5)\left(k - \frac{L_f - 1}{2}\right) - \theta_m\right),$$

where $a_{m,n}$ are multi-level PAM symbols; $\theta_m = (-1)^m \frac{\pi}{4}$; $p_0[k]$ is the prototype filter and L_f is the length of $p_0[k]$, we can also simply set $D = L_f - 1$. Based on the descriptions in [129, 128, 105, 110, 77], the prototype filter length is written as $L_f = \tilde{b}N$ and the overlap factor $\tilde{b}$ is generally given by a even number [105, 110, 77]. To make it coherent with the HS-OQAM case, we can write the prototype filter length of WOFDM as $L_f = 2bN = bM$ ($M = 2N$) with b an arbitrary positive integer. Therefore, HS-OQAM and WOFDM can have a same prototype filter length. Moreover, in [84], we have shown that WOFDM and HS-OQAM share a same perfect reconstruction condition (5.37), so WOFDM and HS-OQAM can eventually share one prototype filter.

5.4 OFDM/OQAM modulation

In this section, we focus our attention on OFDM/OQAM modulation. This alternative MCM possesses several advantages for data transmission. It seems that OFDM/OQAM breaks the concept of Balian-Low theorem, i.e. it can have well-localized pulse shaping filter with a critical Gabor density. This section first briefly summarizes how come does this miracle become true for OFDM/OQAM. Then, we analyze the localization advantage for OFDM/OQAM compared with OFDM/DMT. Later, we introduce an HS version of OFDM/OQAM to PLC and its related features.

5.4.1 From Balian-Low to Offset-QAM

A Gabor function, that has both critical density and well-localization feature, has been proven to be in-exist until OFDM/OQAM was presented [28, 109]. A wise processing, offset QAM, permits to separately transmit the real and imaginary part of the ordinary complex-valued QAM symbols, cf. Fig. 5.9. The specificity of OQAM scheme is that considering two successive carriers, the time offset is introduced onto the imaginary part of the QAM symbols on one of the carriers, whereas it is introduced onto the real part of the symbols on the other one. The number of carriers is assumed to be even, and the continuous-time transmitted signal writes [17]

$$\begin{aligned} s(t) &= \sum_{n=-\infty}^{+\infty} \sum_{m=0}^{N-1} \left(c^{\Re}_{2m,n} g(t - nT_0)) + j c^{\Im}_{2m,n} g(t - T_0/2 - nT_0)\right) e^{j2\pi(2m)F_0 t} \\ &+ \left(j c^{\Im}_{2m+1,n} g(t - nT_0)) + c^{\Re}_{2m+1,n} g(t - T_0/2 - nT_0)\right) e^{j2\pi(2m+1)F_0 t}, \end{aligned} \tag{5.28}$$

where $N = M/2$ with M the number of subcarriers; T_0 is the signaling interval, $F_0 = 1/T_0$ the spacing between two successive carriers, $c^{\Re}_{m,n}$ and $c^{\Im}_{m,n}$ the real and imaginary

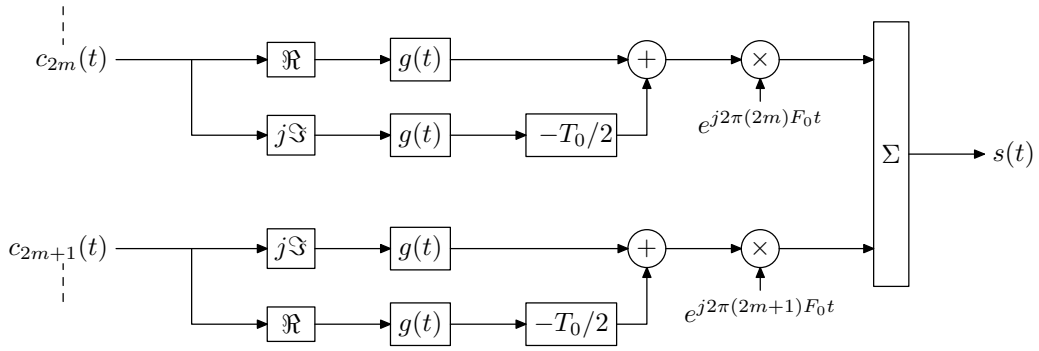

Figure 5.9: Modulator of analogue OFDM/OQAM.

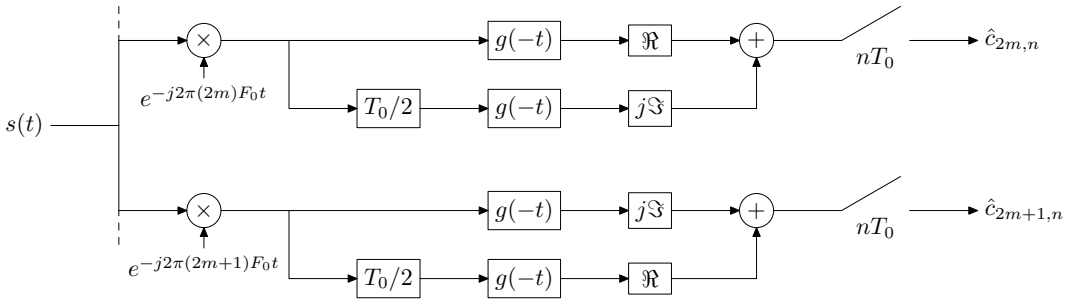

Figure 5.10: Demodulator of analogue OFDM/OQAM.

parts, respectively, of the QAM complex-valued symbols $c_{m,n}$, and $g(t)$ a symmetrical real-valued pulse shape. (5.28) corresponds to the structure in Fig. 5.9, wherein real and imaginary parts have staggered dispositions, that is why OQAM is sometimes also called staggered QAM. The difference between OFDM/QAM and OFDM/OQAM can be easily understood by phase-space analysis. In Fig. 5.11, the ordinary OFDM/QAM symbols are located at (mF_0, nT_0) point in phase-space grid. Then, for a critical transmission, we have $F_0T_0 = 1$. But, in case of OFDM/OQAM transmission, each real-valued transmitted symbol, i.e., either real or imaginary part of QAM symbol, is located at $(mF_0, nT_0/2)$. So that, OQAM system virtually increases the density to 2. But, actually, OFDM/OQAM has the same spectral efficiency as in OFDM without CP case, i.e., critical sampling, since transmitting real-valued symbols on a lattice with density 2 is equivalent to the transmission of complex-valued symbols on a lattice of density equal to 1. On the other hand, since the system separately transmits real and imaginary part of QAM symbols, the orthogonality constraint, for OFDM/OQAM, can be relaxed only considering the real-field. Therefore, it provides more degrees of freedom to obtain a well-localized prototype filter.

At the demodulation side, the symbols are estimated by

$$\hat{c}^{\Re}_{2m,n} = \mathrm{Re}\left\{\int_{-\infty}^{+\infty} g(t - nT_0)e^{-j2\pi(2m)F_0t}s(t)dt\right\} \tag{5.29}$$

$$\hat{c}^{\Im}_{2m,n} = \mathrm{Im}\left\{\int_{-\infty}^{+\infty} g(t - T_0/2 - nT_0)e^{-j2\pi(2m)F_0t}s(t)dt\right\} \tag{5.30}$$

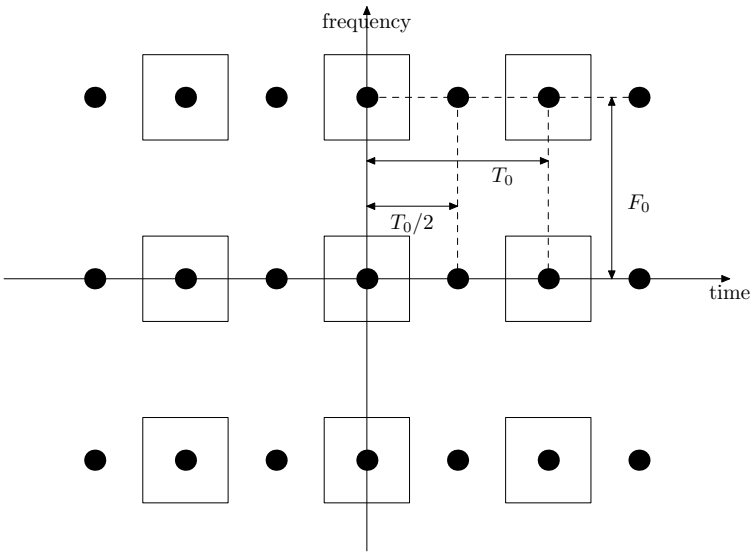

Figure 5.11: Phase space with different lattice points, circle: OFDM/OQAM, square: OFDM/QAM.

$$\hat{c}^{\mathrm{J}}_{2m+1,n} = \mathrm{Im}\left\{\int_{-\infty}^{+\infty} g(t-nT_0)e^{-j2\pi(2m+1)F_0 t}s(t)dt\right\} \tag{5.31}$$

$$\hat{c}^{\mathrm{R}}_{2m+1,n} = \mathrm{Re}\left\{\int_{-\infty}^{+\infty} g(t-T_0/2-nT_0)e^{-j2\pi(2m+1)F_0 t}s(t)dt\right\} \tag{5.32}$$

Eqs. (5.29)-(5.32) clearly explain the reason why we no longer need orthogonality constraint in complex-field.

5.4.2 Mathematical Formulation and PR conditions

Discrete-time OFDM/OQAM description

In above, we briefly introduced the idea of offset QAM for MCM which, when analyzed in a Gabor perspective, can be considered as a theoretical breakthrough [17]. The staggered structure of OQAM can be easily implemented as a certain pre-processing. The discrete-time OFDM/OQAM modulated signal reads

$$s[k] = \sum_{m=0}^{M-1}\sum_{n\in\mathcal{Z}} a_{m,n}\underbrace{g[k-nN]e^{j\frac{2\pi}{M}m\left(k-\frac{L_f-1}{2}\right)}e^{j\phi_{m,n}}}_{g_{m,n}[k]} \tag{5.33}$$

with

$$\text{with } \phi_{m,n} = \phi_0 + \frac{\pi}{2}(n+m) \pmod{\pi} \tag{5.34}$$

where L_f is the length of the filter g and as shown in [115] that the prototype filter length of OFDM/OQAM can be either an even or an odd integer, $N = M/2$ is the discrete-time offset. $\phi_{m,n}$ is an additional phase term in which ϕ_0 can be arbitrarily chosen. The transmitted symbols $a_{m,n}$ are real-valued. They are obtained from a 2^{2K}-QAM constellation, taking the real and imaginary parts of these complex-valued symbols.

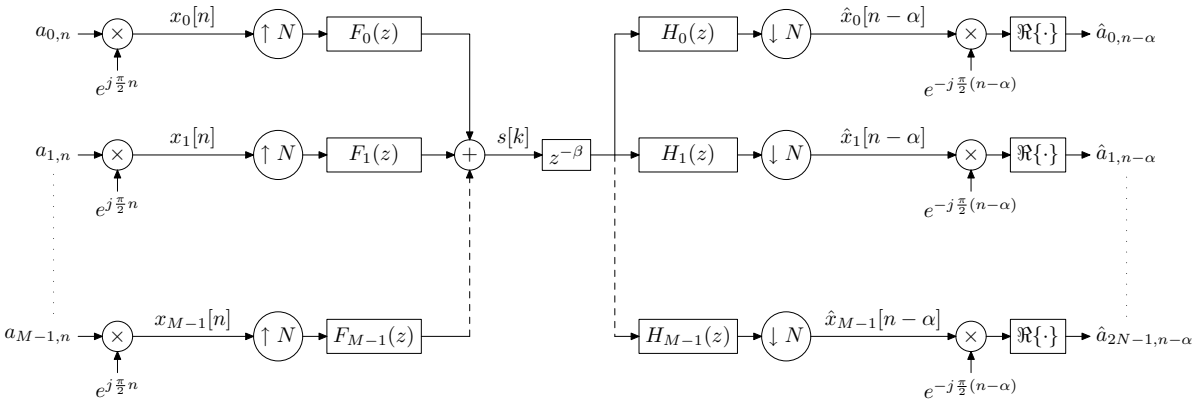

Figure 5.12: Discrete-time OFDM/OQAM system structure.

For two successive subcarriers, the time-offset N is introduced onto the real part for the first one and onto the imaginary part for the second one [52, 115, 17], so that M has to be even.

PR condition and Link with WOFDM

To make a parallel between OFDM and OFDM/OQAM, we place ourselves in the situation where both systems transmit the same quantity of information. This is the case if they have the same number of sub-carriers (M) together with a duration of N samples for the OQAM real data and $M = 2N$ for the QAM complex ones.

Based on the derivation of the modulated TMUX in [115] and assuming that the OFDM/OQAM prototype filter is of unit energy, the synthesis and analysis filter bank, for $m = 0, ..., M-1$, $k = 0, ..., L_f - 1$, are such that:

$$f_m[k] = g[k]e^{j\frac{2\pi}{M}m(k-\frac{L_f-1-N}{2})}, \tag{5.35}$$

$$h_m[k] = g[k]e^{j\frac{2\pi}{M}m(k-\frac{L_f-1+N}{2})} = f_m^*[L_f-1-k], \tag{5.36}$$

respectively. As shown in [115], in order to get a causal TMUX, as depicted in Fig. 5.12, leading to a delay of α symbols, L_f is expressed as $L_f - 1 = \alpha N - \beta$ with α and β two integers such that $\alpha > 0$ and $0 \leq \beta \leq N-1$ [115, 113]. If, as assumed in the rest of the thesis, the prototype filter $g[k]$, is real-valued and symmetrical, then $h_m[k] = f_m[k]$ for all m and k.

In the z domain, the prototype filter $G(z)$ can also be expressed as a function of its polyphase components $P_l(z)$ of order $2N$ [130]:

$$G(z) = \sum_{l=0}^{2N-1} z^{-l}P_l(z^{2N}) \quad \text{with} \quad P_l(z) = \sum_n g[l+2N]z^{-n}.$$

In [115], it is shown that, for OFDM/OQAM, one gets a perfect orthogonality if and only if for $0 \leq l \leq N-1$:

$$P_l(z)P_l(z^{-1}) + P_{l+N}(z)P_{l+N}(z^{-1}) = \frac{1}{N}, \forall z. \tag{5.37}$$

Thus, for OFDM/OQAM we recover a Perfect Reconstruction (PR) condition already known for CMFB [130] and Modified Discrete Fourier Transform (MDFT) filterbanks [74, 75]. As WOFDM, and also most of the practical implementations of (Discrete Wavelet MultiTone) DWMT systems [111], are based on CMFB, this also means that a prototype filter, providing perfect orthogonality for OFDM/OQAM, also leads to WOFDM and DWMT PR TMUXs.

5.4.3 TF-Localization Analysis for Different Prototype Filters

Previously, we discoursed the idea of "Offsetting" complex QAM processing that fakes an over-critical transmission. We also discoursed that, by OQAM processing, a good pulse shape filter, which provides both perfect reconstruction and well-localized TF feature, can be obtained. In this part, we intend to introduce some well-designed prototype filters particularly for OFDM/OQAM modulation.

SRRC Filter

The first introduced one is the elaborate Square Root Raised Cosine filter (SRRC). It is well known, in digital communication systems, that the combination of the transmit and receiver SRRC filters satisfies the Nyquist condition. Although the perfect Nyquist condition satisfaction requires SRRC filter to be continuous-time and with infinite length, the truncated discrete-time SRRC is still widely applied in digital communications. The frequency domain expression of SRRC filter is as below

$$R_C(\nu) = \begin{cases} \frac{1}{\sqrt{F_0}} & |\nu| \leq (1-r)\frac{F_0}{2}, \\ \frac{1}{\sqrt{F_0}} \cos\left(\frac{\pi}{2r}\left(\frac{|\nu|}{F_0} - \frac{1-r}{2}\right)\right) & (1-r)\frac{F_0}{2} < |\nu| \leq (1+r)\frac{F_0}{2}, \\ 0 & (1+r)\frac{F_0}{2} < |\nu|, \end{cases} \tag{5.38}$$

where $0 \leq r \leq 1$ is the roll-off factor. The temporal response SRRC filter in continuous-time reads

$$r_C(t) = \sqrt{F_0}\frac{4rF_0t\cos\left(\pi(1+r)F_0t\right) + \sin\left(\pi(1-r)F_0t\right)}{\left(1-(4rF_0t)^2\right)\pi F_0t}. \tag{5.39}$$

Compared with rectangular filter, SRRC has better frequency localization feature but with a cost of time localization loss. Fig. 5.13 depicts the comparison between SRRC vs. rectangular in time and frequency domain, with SRRC filter length $4M$ ($M = 64$ the number of carriers) and $r = 0.5$.

It is clear that the SRRC filter has a strong second lobe attenuation which implies a better localization in frequency domain. However, it losses a bit localization in time domain. The ambiguity function representation, depicted in Fig. 5.14, shows the energy leakage of SRRC filter. The energy of SRRC filter at the receiver is highly concentrated in frequency but a little leakage appears in time domain. Therefore, we can deduce that, for the transmissions using SRRC filters, the system suffers more from the interference in time (ISI) than from frequency domain (ICI), which implies that SRRC filter is the preferred one for the transmission where frequency selectivity is a predominant effect. The TF-localization level calculated by Eq. (5.15) results in $\xi_{\text{mod}} \simeq 0.75$.

EGF Filter

Actually, the key objective of the prototype filter design, in [52, 63], is to find a prototype filter that has good TF-localization[7] and orthogonality. With this objective in mind, a most straightforward way is to orthogonalize a well-localized non-orthogonal function then to truncate it with a desired length[8]. The EGF filter is such a filter and the orthogonalization method used leads to a function known as $z_{\lambda,\nu_0,\tau_0}(t)$ [114], such that

$$z_{\lambda,\nu_0,\tau_0}(t) = \frac{1}{2}\sum_{k=0}^{+\infty} d_{k,\lambda,\nu_0}\left[g_\lambda\left(t+\frac{k}{\nu_0}\right)+g_\lambda\left(t-\frac{k}{\nu_0}\right)\right]\sum_{l=0}^{+\infty} d_{l,1/\lambda,\tau_0}\cos\left(2\pi l\frac{t}{\tau_0}\right), \quad (5.40)$$

where d_{k,λ,ν_0} are real coefficients and g_λ is the Gaussian function: $g_\lambda(t) = (2\lambda)^{\frac{1}{4}}e^{-\pi\lambda t^2}$ with, λ the spreading parameter, a strictly positive real number; ν_0 and τ_0 are the time and frequency real parameters of the modulation system such that $\tau_0\nu_0 = \frac{1}{2}$ or with the previous notations $\tau_0 = \frac{T_0}{2}$ and $\nu_0 = F_0$. A particular λ (valued 1) leads to a special filter in the EGF family called Isotropic Orthogonal Transform Algorithm (IOTA). Le Floch *et al.*, in [52], gave an overview of the main features concerning IOTA, whereas the proofs of these different properties can be found in [7] or [8].

Fig. 5.15 portrays the comparison between IOTA filter vs. rectangular one in both time and frequency domain (IOTA filter has a length of $4M$ with $M = 64$). It is obvious to see that the IOTA filter has better frequency localization than the rectangular filter. Moreover, it has further a stronger second lobe attenuation than SRRC filter. The ambiguity representation is shown in Fig. 5.16, as its name indicates, the energy of the IOTA filter has an isotropic spreading over time and frequency axes.

IOTA filter is a particular case in EGF family, as we discoursed in Fig. 5.16, its spreading factor (in case of $\lambda = 1$) permits the EGF filter to have same degree of spreading over time and frequency. In this thesis, we will focus on this particular filter of the EGF family. The localization factor of IOTA with length $4M$ is equal to 0.977.

TFL Filter

The previous two discussed prototype filters, i.e., SRRC and IOTA, are both orthogonal in the sense of continuous-time. In digital communications systems, we normally use their digitized-truncated versions which lead to an orthogonality loss. As stated in [115], this orthogonality loss of SRRC is worse than that of IOTA with the same truncation length. The solution to avoid this orthogonality loss is that the filter design shall be carried out in discrete-time domain directly taking into account the orthogonality conditions.

Since we have the discrete-time orthogonal condition (5.37), the completely orthogonal discrete filter design is feasible. Pinchon *et al.* proposed two design criteria in [98] and

[7] Although, both papers emphasized the importance of localization features of prototype filter, the presented prototype filter design algorithms were not the same, i.e. in [52], the authors focused on an Isotropic Orthogonal Transform Algorithm (IOTA) and [63] presented a Hermite function derivation. However, the similarity of these two prototype filters are that the base function is invariant when applying the Fourier transform, i.e. isotropy. The details of the Hermite function can be found in [62].

[8] Same as for the SRRC filter, the truncation naturally leads to an orthogonality loss and the loss level depends upon the truncation length. However, the orthogonality loss of IOTA is less than the one of the SRRC filter (cf. [115]).

[99]. The first presented criterion is called Time-Frequency Localization (TFL) criterion which targets to maximize the TF-localization factor ξ_{mod} of (5.15) with the constraint of (5.37). The filter length can be defined to be a multiple of M as bM with positive integer b. Fig. 5.17 gives the comparison between TFL1 ($b = 1$) and the rectangular window. The ambiguity representation of TFL1 is given in Fig. 5.18, where we find that the TFL1 filter has better localization in time than in frequency. The TF-localization factor ξ_{mod} of TFL1 is 0.912 and for TFL4 ($b = 4$) is 0.980 with $M = 64$.

FS Filter

The second criterion, presented in [98] and [99], is related to minimizing the out-of-band energy. Using a normalized frequency, i.e., a sampling frequency equal to 1, the objective function for minimization writes

$$\min_{\{\text{parameters}\}} \frac{E(f_c)}{E(0)} \quad \text{with} \quad E(f_c) = \int_{f_c}^{\frac{1}{2}} |P(e^{j2\pi\nu u})|^2 d\nu, \tag{5.41}$$

where f_c is the cutoff frequency and has the expression as $f_c = (1+\rho)\frac{1}{2M}$. We note that the factor ρ can be also seen as a "roll-off" factor between $[0, 1]$ and "parameters" stands for the prototype filter coefficients or a set of variables related to them.

Minimizing the above objective function w.r.t. the orthogonal constraint (5.37) leads to a so-called Frequency Selective (FS) filter. As for the TFL filter, the filter length can be chosen to be bM. Fig. 5.19 shows the comparison between the FS4 ($b = 4$) with $\rho = 1$ vs. the rectangular window and the ambiguity representation Fig. 5.20 portrays that the FS filter has better frequency localization than time localization. Furthermore, the TF-localization factor ξ_{mod} of FS1 ($\rho = 1$) is 0.548 and for FS4 ($\rho = 1$) is 0.895 with $M = 64$ in above figures.

5.5 Hermitian Symmetric OFDM/OQAM for PLC

Wired communication systems, as e.g. PLC and DSL, often impose the transmission of real-valued baseband transmit signals. As the coefficients of the OFDM/OQAM synthesis filter bank are complex-valued, see (5.33), the transmit baseband OFDM/OQAM signal is also, in general, complex-valued. In this section, we intend to keep the conventional OFDM/OQAM system structure and add some conditions on the entry symbols such that we can get a real-valued modulated signal. The resulting system, we term it as HS-OQAM. Then, we show that there exists a link between HS-OQAM and LP-CMFB.

5.5.1 HS Constraints

As shown with (5.35), each synthesis filter is the frequency shift version of the prototype filter. This feature is due to the modulation term, i.e. $e^{j\frac{2\pi}{M}m(k-\frac{D}{2})}$ setting $D = L_f - 1$ in (5.33), that corresponds to the Fourier transform kernel. It is well known that if a discrete input sequence of a Fourier transform is Hermitian symmetric, plus, the first and the center elements are real-valued, then the output sequence of the Fourier transform is entirely real-valued. This property is directly applied for DMT systems. Let us now

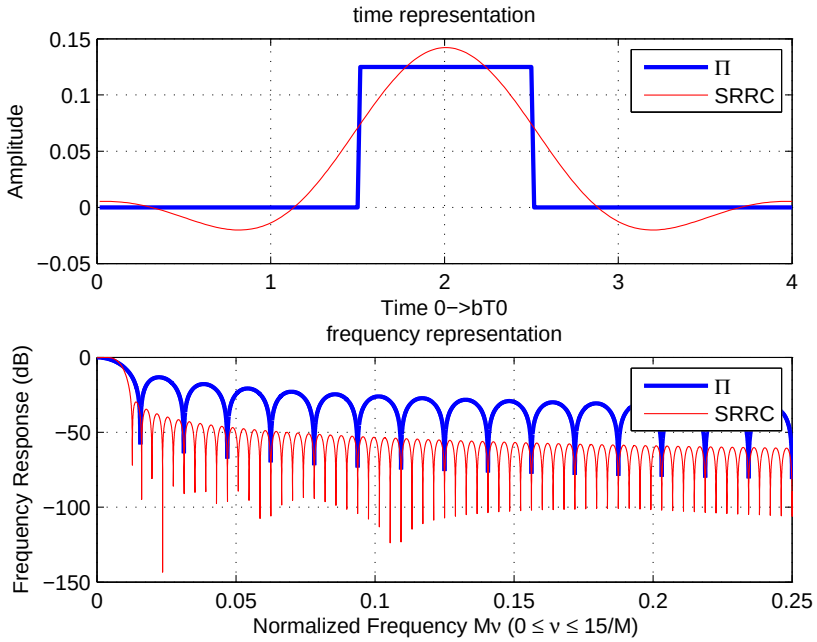

Figure 5.13: Time frequency comparison: The SRRC ($b = 4, r = 0.5$) vs. the rectangular window.

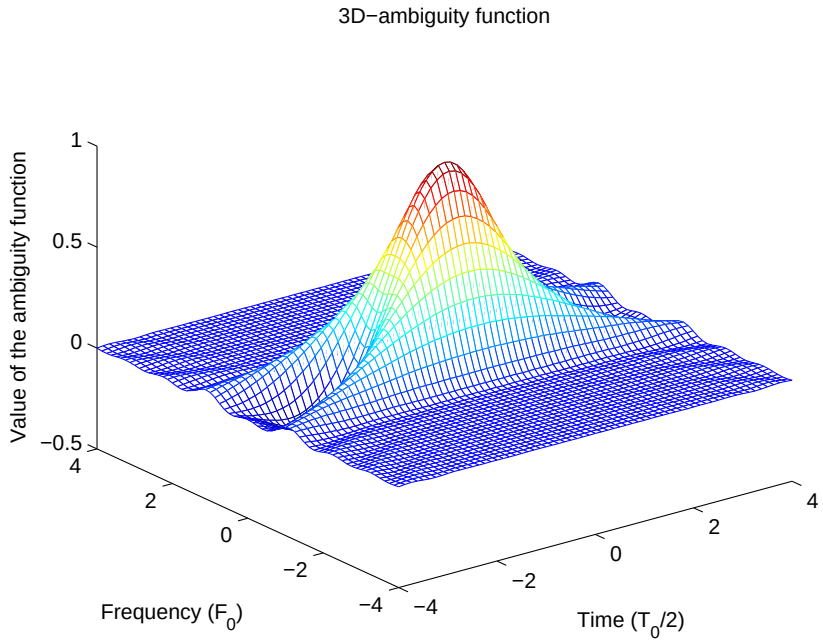

Figure 5.14: Ambiguity function representation for the SRRC filter ($b = 4, r = 0.5$).

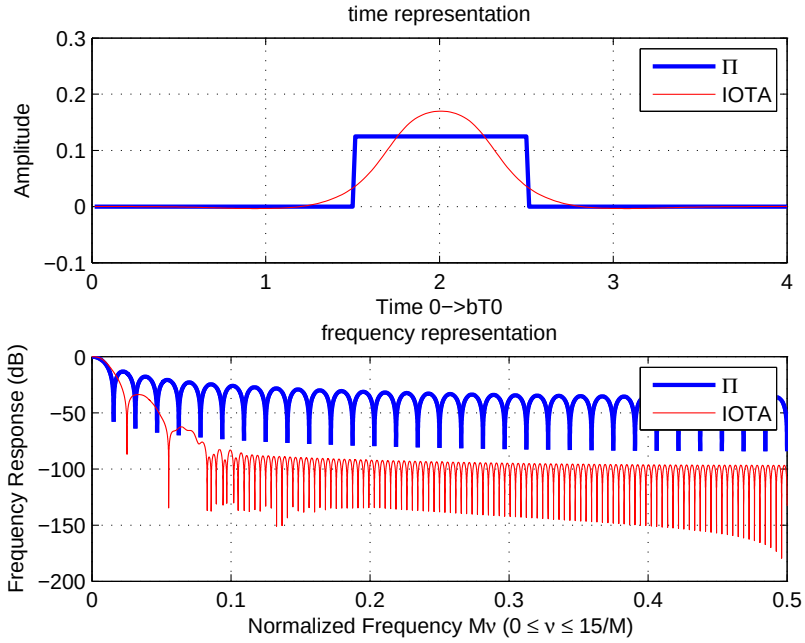

Figure 5.15: Time frequency comparison: The IOTA ($b = 4$) vs. the rectangular window.

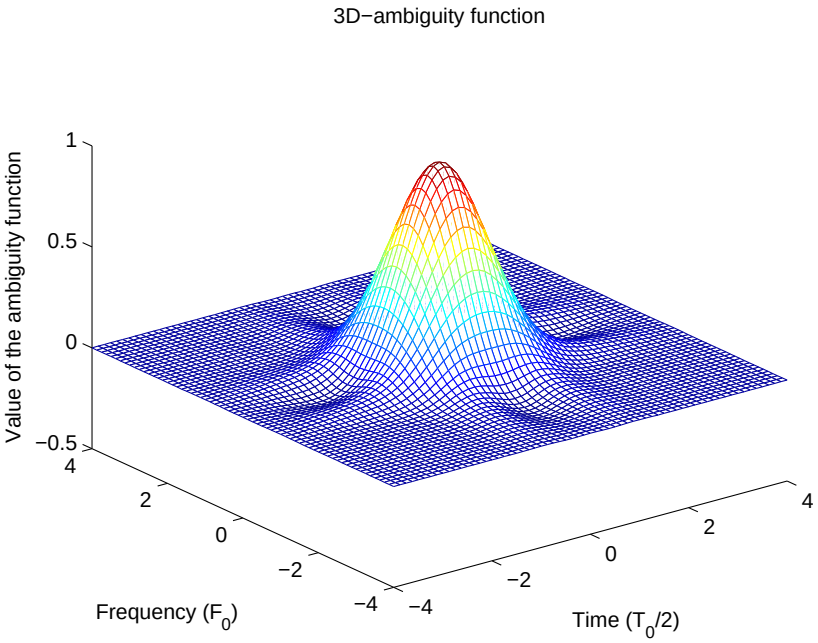

Figure 5.16: Ambiguity function representation for the IOTA filter ($b = 4$).

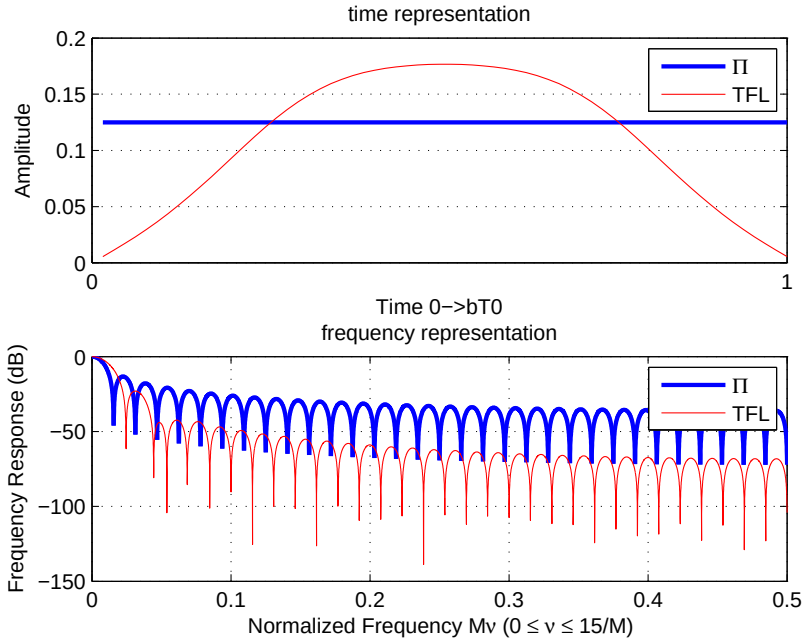

Figure 5.17: Time frequency comparison: The TFL ($b = 1$) vs. the rectangular window.

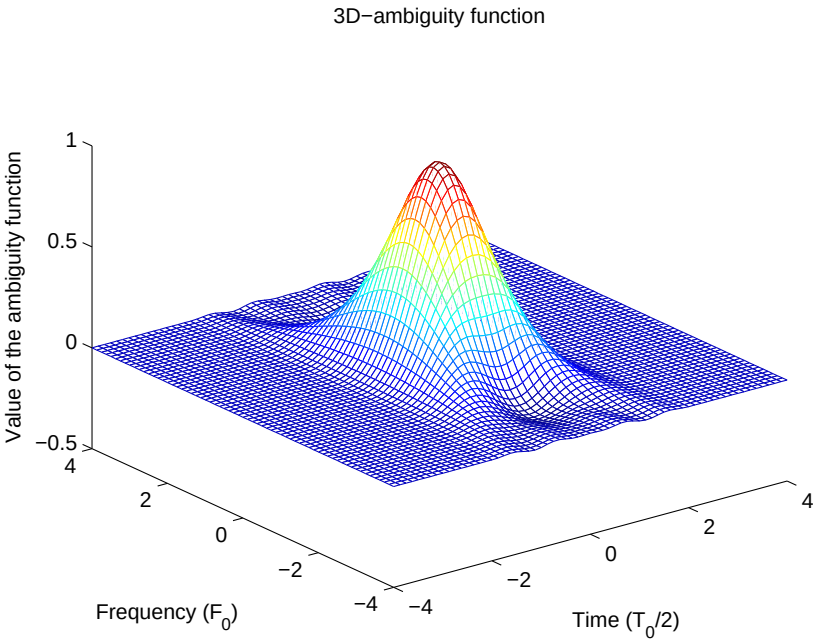

Figure 5.18: Ambiguity function representation for the TFL filter ($b = 1$).

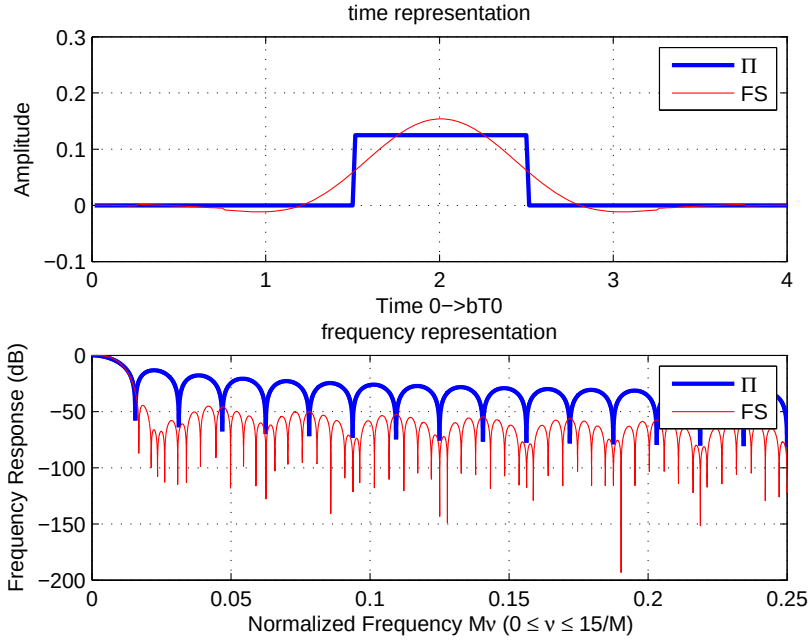

Figure 5.19: Time frequency comparison: The FS ($b = 4, \rho = 1$) vs. the rectangular window.

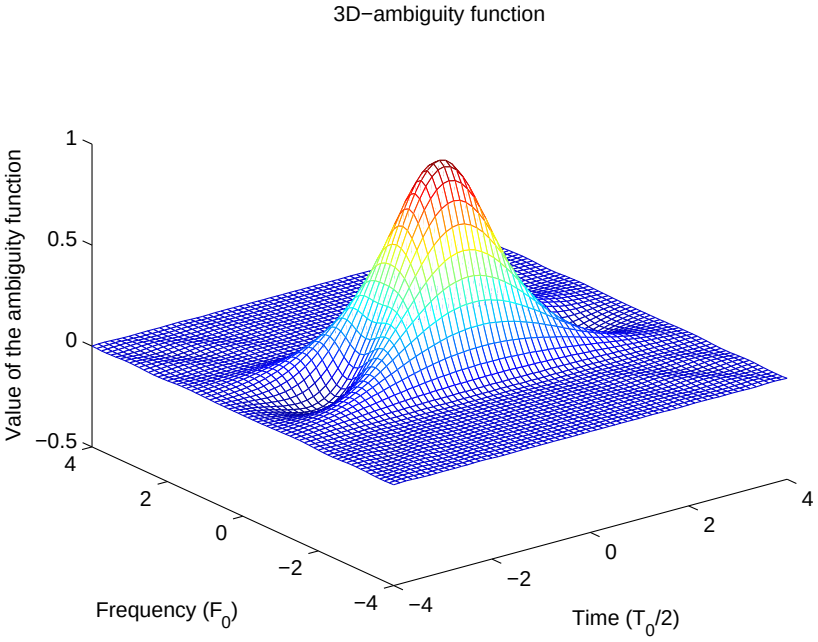

Figure 5.20: Ambiguity function representation for the FS filter ($b = 4, \rho = 1$).

examine, starting from (5.33), how can we adapt it to OFDM/OQAM. We rewrite (5.33) as

$$s[k] = \sum_{n=-\infty}^{\infty} F_{m,n,k} g[k - nN] \tag{5.42}$$

where,

$$F_{m,n,k} = \sum_{m=0}^{N-1} a_{m,n} e^{j\phi_{m,n}} e^{j\frac{\pi}{N}m(k-\frac{D}{2})} + \sum_{m=N}^{M-1} a_{m,n} e^{j\phi_{m,n}} e^{j\frac{\pi}{N}m(k-\frac{D}{2})}. \tag{5.43}$$

$F_{m,n,k}$ can also be rewritten as

$$\begin{aligned} F_{m,n,k} &= \left(a_{0,n} e^{j\phi_{0,n}} + a_{N,n} e^{j\phi_{N,n}} e^{j\pi(k-\frac{D}{2})}\right) \\ &+ \sum_{m=1}^{N-1} \left(a_{m,n} e^{j\phi_{m,n}} e^{j\frac{\pi}{N}m(k-\frac{D}{2})} + a_{M-m,n} e^{j\phi_{M-m,n}} e^{j\frac{\pi}{N}(M-m)(k-\frac{D}{2})}\right). \end{aligned} \tag{5.44}$$

Since the prototype filter $g[k]$ has real-valued coefficients, then, the transmit signal $s[k]$ is real-valued, if

$$a_{0,n} e^{j\phi_{0,n}} + a_{N,n} e^{j\phi_{N,n}} e^{j\pi(k-\frac{D}{2})} \in \mathbb{R}, \tag{5.45}$$

and

$$a_{m,n} e^{j\phi_{m,n}} e^{-j\frac{\pi}{N}m\frac{D}{2}} = \left(a_{M-m,n} e^{j\phi_{M-m,n}} e^{j\frac{\pi}{N}M(k-\frac{D}{2})}\right)^* \tag{5.46}$$

The solution of (5.45), chosen to be independent of k, is

$$a_{0,n} = a_{N,n} = 0. \tag{5.47}$$

Then, substituting (5.34) into condition (5.46) leads to

$$a_{m,n} = a_{M-m,n}(-1)^{D-N-n} e^{-j2\phi_0}. \tag{5.48}$$

Thanks to conditions (8.9, 5.48), (5.42) can be expressed as

$$s[k] = 2\sum_{n\in\mathcal{Z}} g[k - nN] \sum_{m=1}^{N-1} \mathrm{Re}\{a_{m,n} e^{j\phi_{m,n}} e^{j\frac{\pi}{N}m(k-\frac{D}{2})}\}. \tag{5.49}$$

As the prototype filter $g[k]$ is supposed to be real-valued the transmit signal $s[k]$ is purely real. So, (8.9, 5.48) are the conditions for HS-OQAM modulation.

5.5.2 Link with LP-CMFB

Let us now investigate the general TMUX structure of HS-OQAM system, and specify the individual synthesis and analysis filters. Condition (5.48) shows that if we set different values to ϕ_0, the Hermitian condition will be changed as well, then the TMUX structure is also changed. To clarify this point, let us discuss two different cases of $\phi_{m,n}$ used in practice [52], [115]. Note that in the following computation steps, the prototype filter may be of arbitrary length. Remember that, in order to provide causal TMUX structures, this length is expressed at the end as $L_f - 1 = \alpha N - \beta$, with α and β two integers such that $\alpha > 0$ and $0 \leq \beta \leq N - 1$ [115, 113].

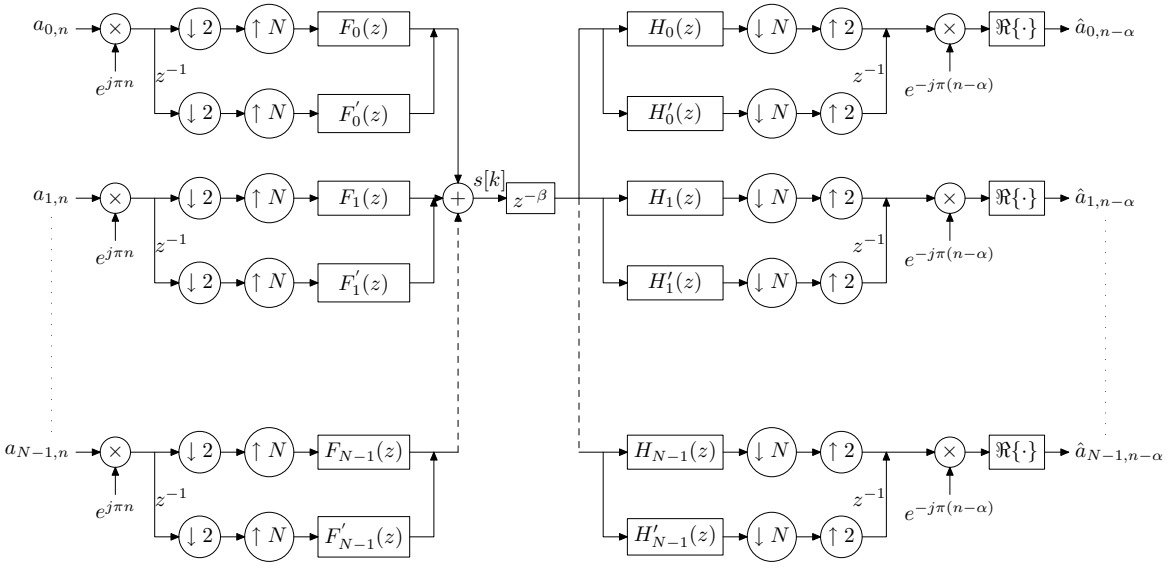

Figure 5.21: Transmultiplexer structure with $\phi_{m,n} = \frac{\pi}{2}(n+m) - \pi mn$.

Case with $\phi_{m,n} = \frac{\pi}{2}(n+m) - \pi mn$ [115]

Then, substituting $\phi_{m,n}$ into (5.49) yields,

$$s[k] = 2\sum_{n=-\infty}^{\infty} p[k-nN] \sum_{m=1}^{N-1} a_{m,n} \underbrace{\cos\left(\frac{\pi}{2}n + \frac{\pi}{N}m(k-nN-\frac{D-N}{2})\right)}_{\gamma_{m,n,k}} \quad (5.50)$$

Obviously $\gamma_{m,n,k}$ depends upon the parity of n, when n is even (say, $n = 2n'$ $n' \in \mathbf{Z}$), it may be expressed as,

$$\gamma_{m,n,k} = (-1)^{\frac{n}{2}} \cos\left(\frac{\pi}{N}m(k-nN-\frac{D-N}{2})\right). \quad (5.51)$$

When n is odd (say, $n = 2n'+1$ $n' \in \mathbf{Z}$), $\gamma_{m,n,k}$ writes as,

$$\gamma_{m,n,k} = (-1)^{\frac{n-1}{2}} \sin\left(\frac{\pi}{N}m(k-nN-\frac{D-N}{2})\right) \quad (5.52)$$

Substituting (5.51, 5.52) into (5.50) yields,

$$\begin{aligned} s[k] &= 2\sum_{m}\sum_{n=-\infty}^{\infty} (-1)^n \left(a_{m,2n} g[k-2nN] \cos\left(\frac{\pi}{N}m(k-2nN-\frac{D-N}{2})\right)\right. \\ &- \left. a_{m,2n+1} g[k-2nN-N] \sin\left(\frac{\pi}{N}m(k-2nN-N-\frac{D-N}{2})\right)\right). \end{aligned} \quad (5.53)$$

Equation (5.53) shows that for each sub-carrier (or tone), the synthesis filter can be further split into two subbranches (i.e., upper and lower branch, respectively). As shown in

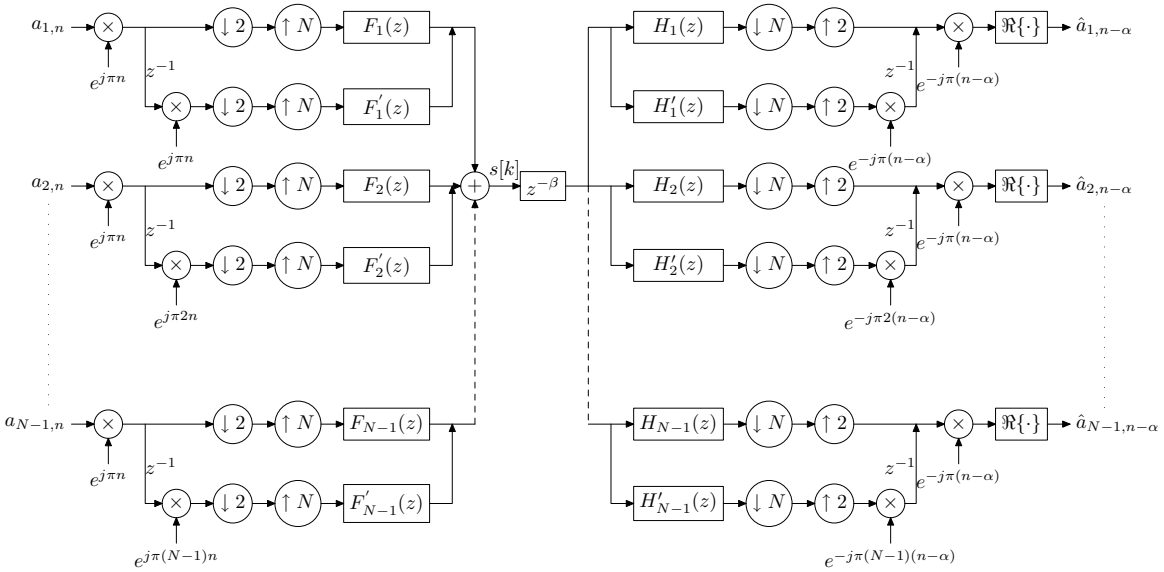

Figure 5.22: Transmultiplexer structure with $\phi_{m,n} = \frac{\pi}{2}(n+m)$.

[51], the relationship between a discrete-time signal $x[k]$ and its decimated version shifted of λ samples, $y[k] = x[kM + \lambda]$, can be expressed in the z domain by

$$z^{-\lambda}Y(z^M) = \frac{1}{M}\sum_{l=0}^{M-1} X(zW_M^l)W_M^{\lambda l}, \tag{5.54}$$

where $W_M = e^{-j\frac{2\pi}{M}}$. Therefore, in the upper branch, the input sequence can be seen as the first polyphase component of the original symbol sequence $a_{m,n}$, i.e., $a_m^{even}(n) = a_m(2n)$. In z domain, it corresponds to $A_m^{even}(z^2) = \frac{1}{2}\sum_{l=0}^{1} A(zW_2^l)$. Similarly for the lower branch, it can be seen as the second polyphase component of the original symbol sequence $a_{m,n}$, $a_m^{odd}(n) = a_m(2n+1)$, leading in z domain to $z^{-1}A_m^{odd}(z^2) = \frac{1}{2}\sum_{l=0}^{1} A(zW_2^l)W_2^l$. That is to say, at each sub-carrier, the data sequence is firstly processed by a decimator with factor of 2, secondly passes through an expander with factor of N, then is filtered by the synthesis filter. At receiver, the analysis filter bank has a similar structure but delays (α and β) are added depending on L_f. Fig. 5.21 depicts the transmultiplexer structure for the case of $\phi_{m,n} = \frac{\pi}{2}(n+m) - \pi mn$.

Case with $\phi_{m,n} = \frac{\pi}{2}(n+m)$ [52]

A similar analysis can be carried out, i.e.,

$$\begin{aligned} s[k] &= 2\sum_m\sum_n (-1)^n \left(a_{m,2n} g[k-2nN] \cos\left(\frac{\pi}{N} m(k-2nN-\frac{D-N}{2})\right)\right. \\ &- \left. a_{m,2n+1} g[k-2nN-N](-1)^{nm} \sin\left(\frac{\pi}{N} m(k-2nN-N-\frac{D-N}{2})\right)\right). \end{aligned}$$

The resulting structure is depicted in Fig. 5.22. Comparing to Fig. 5.21, both cases result in almost the same structure. The only difference comes from the scaled product at the odd subbranch of each m sub-carrier. This product may vary according to the phase component $\phi_{m,n}$.

The synthesis filter of each sub-carrier, with $m = 1...N-1$, can be expressed as

$$f_m[k] = 2g[k]\cos\left(\frac{\pi}{N}m(k-\frac{D-N}{2})\right), \tag{5.55}$$

$$f'_m[k] = -2g[k]\sin\left(\frac{\pi}{N}m(k-\frac{D-N}{2})\right). \tag{5.56}$$

The analysis filters are simply the symmetrical version of the synthesis filters. As in [85, 75], this structure can be also arranged into two blocks, with the upper block being a group of cos filters (5.55) and the lower one being a group of delayed sin filters ((5.56) with delay factor N). Since the condition (8.9) restricts the symbol to null on the first and the middle sub-carrier, the filters for these sub-carriers may be arbitrary.

In addition, the HS-OQAM system has a link with the Discrete Cosine and Sine Transform, more precisely DCT/DST I or II depending on N is even or odd [85, 75]. Furthermore, note also that these filters have a linear-phase property which is different from those of the WOFDM modulator. In [127], the author shows that DCT/DST I and II MFBs also correspond to Wilson based MFBs. Therefore HS-OQAM system may be seen as a dual of Wilson based MFB as well. The practical efficient implementation algorithm will be discoursed in Chap. 8.

5.6 PSD HS-OQAM vs. OFDM/DMT in PLC

In the previous sections, we introduced some well-designed prototype filters. Moreover, we presented a HS-OQAM system that can practically make OFDM/OQAM be applicable in baseband PLC application. In this section, we tend to unveil the first and also a very straightforward interest of using HS-OQAM with well-localized filters in PLC. Recall that the "all-important" requirement of PLC for MCMs is the tone mask fitting. Therefore, DMT modulation requires a windowing process to satisfy this requirement. However, thanks to the flexible and well-designed prototype filters, HS-OQAM system can easily fit into this tone mask. Furthermore, the defined tone mask may be even too loose for HS-OQAM with certain "good" prototype filters. Then what kind of filters are "good" w.r.t. the mask fitting requirement?

Since PLC tone mask is defined in frequency domain, the frequency localization becomes more important to decide whether the modulation can fit into the mask or not. Therefore, the frequency selective feature might be the decisive point to judge the goodness of the filters. In the following, we compare the frequency representation of the different available filters, presented in Sec. 5.4.3, in Fig. 5.23. Although all of the filters have better frequency localization than the rectangular filter, TFL1 filter has the worst frequency selective feature. For IOTA4 filter, the second lobe attenuation may not be the maximum, but the energy is very much concentrated on the shortest "frequency latency". FS4 with $\rho = 1$ has almost the same feature as SRRC4 with $r = 0.5$.

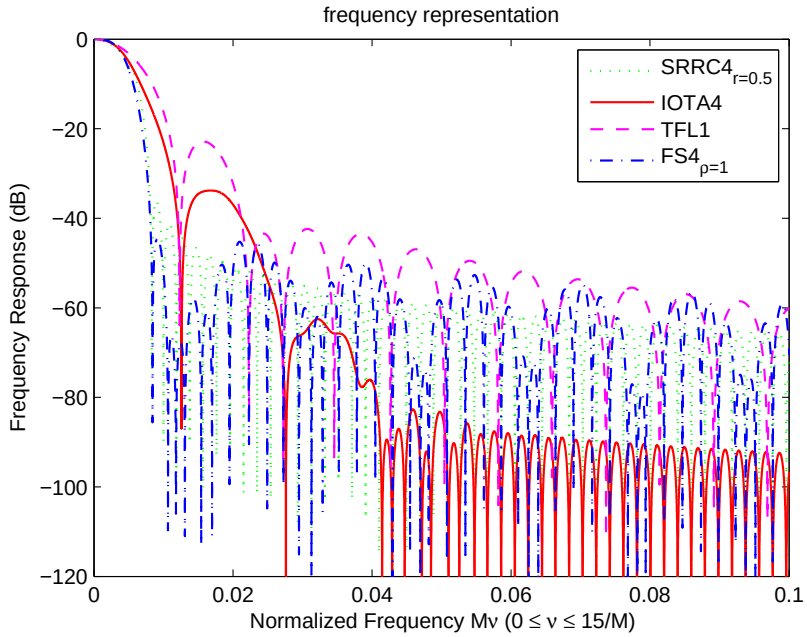

Figure 5.23: Frequency comparison among different filters.

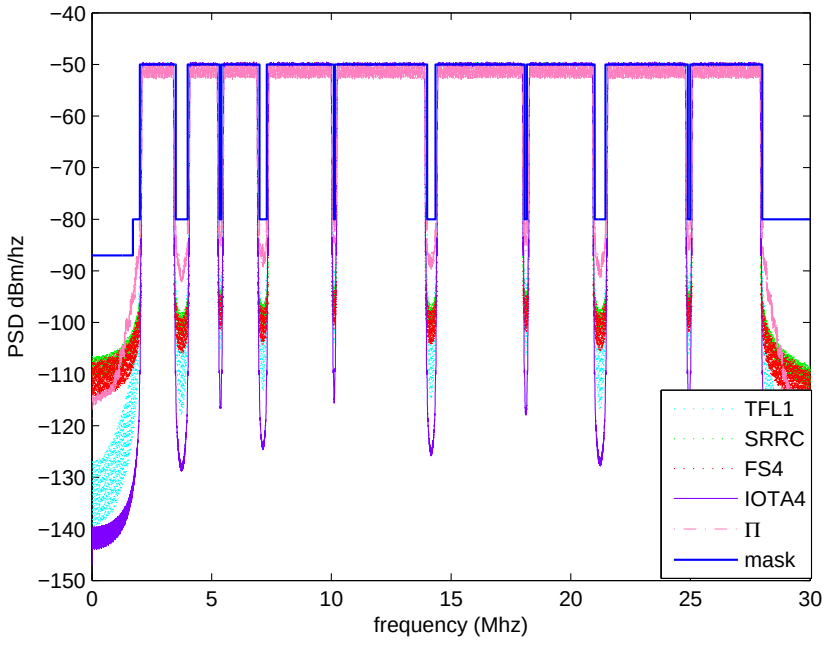

Figure 5.24: Power Spectrum Density comparison.

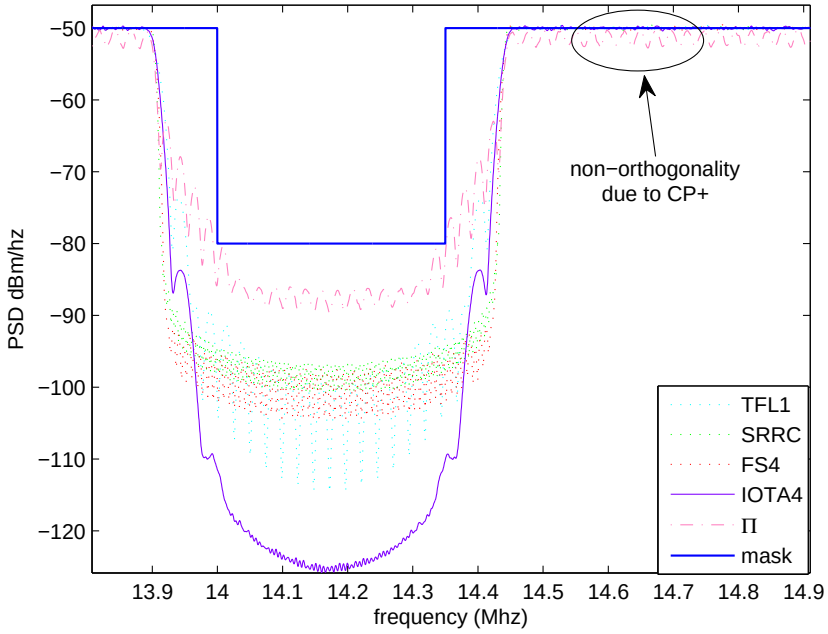

Figure 5.25: Power Spectrum Density comparison.

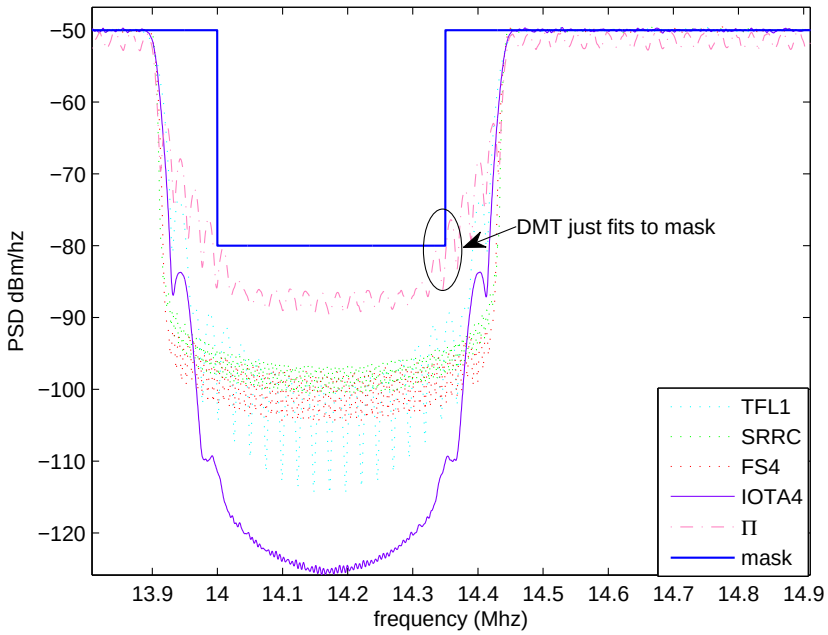

Figure 5.26: Power Spectrum Density comparison.

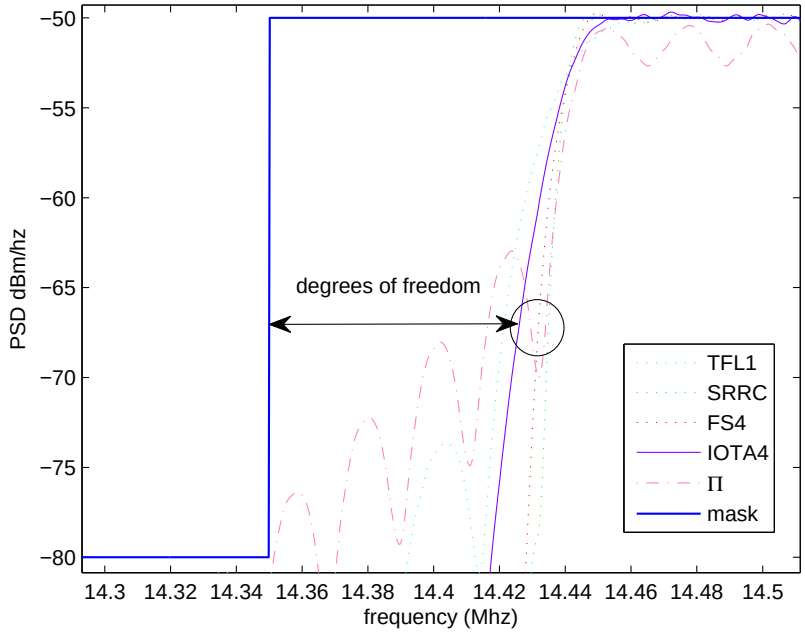

Figure 5.27: Power Spectrum Density comparison.

Let us then take a look at the PSD of HS-OQAM system with above filters depicted in Fig. 5.24, wherein, the legend with the name of Π stands for the windowed DMT modulation and the main parameters are equivalent to those of HPAV, i.e. $M = 3072$, $L_{cp} = 417$, roll-off length for windowed OFDM/DMT is 372, sampling frequency $f_s = 75$ MHz; there are 1155 carriers in the range from 1.8 MHz to 30 MHz. Among these, 917 carriers are used for transmitting the symbols and the others are switched off [5]. Compared with the windowed DMT system, HS-OQAM can easily fit into the tone mask. Moreover, at the place of the center notch zone, IOTA4 filter gives the best shape which can be predicted from Fig. 5.23. Let us further zoom in one notch, see Fig. 5.25, we can first remark that the orthogonality feature of the rectangular filter is broken owing to CP addition which, in the figure, results in the oscillations in the passband regions. Furthermore, due to the bad frequency localization feature, windowed DMT system can just fit into the tone mask (see Fig. 5.26) i.e. it must perfectly obey the defined subcarrier turn on/off rule in HPAV specifications. However, for HS-OQAM modulation, as we can see in Fig. 5.27, it has some degrees of freedom to turn some shielded subcarriers on while still satisfying the mask rule[9]. By this way, the overall throughput compared to DMT is surely increased. Therefore, the first advantage of using HS-OQAM in PLC is that it is robust to narrowband noise, i.e. assuming that HS-OQAM and DMT transmit the same throughput, then, the robustness of HS-OQAM to narrowband noise leads to a higher communication quality of service [117]. Otherwise said, for the same level of narrowband noise suffering, HS-OQAM can transmit data over more subcarriers which results in a higher throughput.

[9]The degree of freedom level depends upon the prototype filter.

5.7 Summary and Conclusion

In this chapter, we discoursed the link from Gabor theory to the practical multi-carrier modulations. Gabor, in his theory, tells us that a Gabor based system cannot form an orthonormal basis, whilst its density is equal to 1, that has good localization in time and frequency. This is further proved by Balian and Low. In practice, the Gabor density 1 corresponds to the critical sampling factor and OFDM/DMT is such a Gabor system with rectangular basis function. Thus, it has orthogonality but not good localization feature. To refine the localization, we need to change the critical sampling system to an over-sampled system which, eventually, leads to a FMT system. A Gabor system that has both critical sampling and orthogonality did not exist in theory until a breakthrough was made while OFDM/OQAM modulation was presented. The staggered process permits to relax the conventional orthogonal condition to real-field. Therefore, more degrees of freedom can be obtained to design a well-localized filter.

In the application of PLC, DMT was proposed as a suitable scheme due to its efficient implementation and simple equalization thanks to CP. However, in order to meet the mask fitting requirement. A windowing process needs to be carried out for DMT. On the other hand, to make OFDM/OQAM be compatible with baseband PLC, meanwhile, keeping the same OFDM/OQAM system structure, the HS constraints were introduced leading to the HS-OQAM system. Compared with DMT, we highlighted the first advantage which is the robustness to the narrowband noise thanks to its well-localized prototype filters. It eventually leads to a throughput increase or performance enhancement. However, as a matter of fact, HS-OQAM, or OFDM/OQAM, cannot always win DMT, i.e. it also has a drawback which is its remaining interference. In the subsequent chapter, this drawback will be analyzed in detail w.r.t. different transmission environments.

Chapter 6

Analysis of OFDM/OQAM Transmission

In the previous chapter, we presented an alternative MCM called OFDM/OQAM modulation, which solves the well-known difficulty, stated by the Balian-Low theorem, in constantly providing 1) good TF localization; 2) full spectral efficiency; 3) orthogonality. Moreover, a straightforward benefit of using HS-OQAM in PLC application was revealed when compared to DMT system. However, at the end of Chap. 5, we mentioned that OFDM/OQAM also has its drawback which is the remaining interference. Furthermore, as we will see in this chapter, the remaining interference level directly links to our prototype filter choice. Actually, the filters are designed with different criteria (cf. Sec. 5.4.3), which should be related to the transmission environment.

For the communications systems including wired and wireless, the transmission channels are usually modelled, without loss of generality, as: either frequency selective or time selective channels or both. The first situation is caused by the fact that the transmitted signal is typically reaching the receiver through multiple propagation paths (reflections from buildings, etc.), each having a different relative delay and amplitude, i.e. the CIR shows a multi-path behavior [125]. The second situation is due to the mobility of transmitter and/or receiver or some other time-varying characteristics of the transmission environment, which introduces a frequency shift on each channel tap and the resulting performance perturbation is usually called Doppler effect [125]. In case of wired communications, such as xDSL or PLC, the transmission channels are supposed to have only frequency selective behavior[1] [97, 87, 11, 56]. But, both time and frequency selective behaviors occur in wireless communications [125]. In the subsequent section, we derive a theoretical model for OFDM/OQAM transmission over time-frequency selective channel. Based on this model, we can analytically draw a link that connects the performance

[1] Although, since recently, some papers talked about the time-varying behavior of power line channels, a fundamental property of the power line channel is that the time varying behavior is actually a periodically time-varying behavior, where the period is typically half the AC mains period (50 or 60 Hz) [26, 35, 120].

resulting from filter choice and channel environment.

6.1 General OFDM/OQAM Transmission Model

6.1.1 Channel Model

Before doing any derivation, we first define our analytical channel model. In Chap. 4, we have already discoursed that in-home PLC channel behaves very much like wireless channel in the sense of multi-path behavior, i.e. FIR channel model can be considered in digital domain. The difference is that in-home PLC is actually a baseband communication such that, Doppler effect is normally neglected. For the moment, let us consider a general environment where both time and frequency selectivity appear as well as Doppler effect, such as mobile communications. In mobile communications, signal is transmitted at a certain carrier frequency, and this frequency might be significantly changing when velocity is introduced at transmitter and/or receiver or in the environment. Consequently, it leads to a frequency mismatch when the receiver shifts the received signal back from carrier frequency to the baseband and this frequency shift caused by velocity is called Doppler shift. We reuse, herein, the baseband equivalent time-varying multi-path channel model proposed in [107, 106], and its continuous-time expression writes:

$$h(t,\tau) = \sum_{i=0}^{P-1} c_i e^{j2\pi f_d^i t} \delta(\tau - \tau_i), \tag{6.1}$$

where P is the number of resolvable path (the first path being the reference path with delay $\tau_0 = 0$) and c_i is the time-varying channel gain to the i-th path which can be expressed as $c_i = \rho_i e^{j\theta_i}$ with ρ_i the attenuation of i-th path and θ_i the phase rotation due to the delay τ_i; f_d^i is the Dopper frequency of the i-th path; $\delta(\cdot)$ is the Dirac delta function.

Assuming that the sampling frequency is f_s, which corresponds to the sampling time interval $T_s = 1/f_s$, then we get the Z-transform version of the discrete-time channel model

$$H(k,z) = \sum_{l=0}^{L_h-1} c_l e^{j2\pi f_d^l k T_s} z^{-l}, \tag{6.2}$$

where we define that

$$c_l = \begin{cases} c_i, & l = \lceil \tau_i f_s \rceil \\ 0, & \text{otherwise} \end{cases} \tag{6.3}$$

with $\lceil a \rceil$ denoting the smallest integer greater or equal to a, and L_h stands for the maximum CIR length (in samples) yielding $L_h = \lceil \tau_{P-1} f_s \rceil$.

6.1.2 Transmission over Time-varying Multi-path Channel

We next look at the OFDM/OQAM transmission model over a time-varying multi-path channel. For the derivation simplicity, we commence with the continuous-time version, recall that the continuous-time OFDM/OQAM modulated signal reads,

$$s(t) = \sum_{m=0}^{M-1} \sum_{n \in \mathbf{Z}} a_{m,n} \underbrace{g(t - n\tau_0) e^{j2\pi m F_0 t} e^{j\phi_{m,n}}}_{g_{m,n}(t)}, \tag{6.4}$$

and let us temporarily forget the background noise effect. Then the baseband received signal yields,

$$\begin{aligned} y(t) &= \sum_{i=0}^{P-1} h(t,\tau_i)s(t-\tau_i) \\ &= \sum_{i=0}^{P-1} c_i e^{j2\pi f_d^i t} \sum_{n\in\mathbf{Z}} \sum_{m=0}^{M-1} a_{m,n} g(t-\tau_i-n\tau_0) e^{j2\pi m F_0(t-\tau_i)} e^{j\phi_{m,n}}. \end{aligned} \tag{6.5}$$

As long as we get the received signal, the demodulation of OFDM/OQAM is processed as follows

$$\begin{aligned} y_{m_0,n_0} &= \int_{-\infty}^{\infty} y(t) g^*_{m_0,n_0}(t)\, dt \\ &= \sum_{n\in\mathbf{Z}} \sum_{m=0}^{M-1} a_{m,n} e^{j\Delta\phi} \sum_{i=0}^{P-1} c_i e^{-j2\pi m F_0 \tau_i} \\ &\times \int_{-\infty}^{\infty} g(t-\tau_i-n\tau_0) g(t-n_0\tau_0) e^{j2\pi((m-m_0)F_0+f_d^i)t}\, dt, \end{aligned} \tag{6.6}$$

where $\Delta\phi = \phi_{m,n} - \phi_{m_0,n_0}$. We can compactly write the demodulated model in an ambiguity function based expression by changing the variables of (6.6) as $t-\tau_i-n\tau_0 = \mu+\frac{\tau'}{2}$ and $t-n_0\tau_0 = \mu-\frac{\tau'}{2}$. After a bunch of calculations, we get

$$\begin{aligned} y_{m_0,n_0} &= \sum_{n\in\mathbf{Z}} \sum_{m=0}^{M-1} a_{m,n} e^{j\Delta\phi} \sum_{i=0}^{P-1} c_i e^{j\pi f_d^i[(n_0+n)\tau_0+\tau_i]} \\ &\times A_g((n_0-n)\tau_0-\tau_i, (m-m_0)F_0+f_d^i) e^{-j\pi(m+m_0)F_0\tau_i}. \end{aligned} \tag{6.7}$$

Here $A_g(\tau,\nu)$ is the ambiguity function of $g(t)$ that we have already mentioned in the preceding chapter and it is defined as:

$$A_g(\tau,\nu) = \int_{-\infty}^{\infty} g(t+\frac{\tau}{2}) g^*(t-\frac{\tau}{2}) e^{j2\pi\nu t}\, dt. \tag{6.8}$$

Next, we can digitize the previous expression to get a discrete-time version and, in order to simplify the expression, we can set $m = m_0 + p$ and $n = n_0 + q$ where p, q are positive or negative integers. The reason of doing this is not only to make the expression compact but also to give a clear view on interference analysis. The arranged discrete-time demodulated model reads

$$\begin{aligned} y_{m_0,n_0} &= \sum_{(p,q)} a_{m_0+p,n_0+q} e^{j\frac{\pi}{2}(p+q+pq)} e^{j\pi p n_0} \sum_{l=0}^{L_h-1} c_l e^{j\pi[(2n_0+q)N+l]f_d^l T_s} \\ &\times A_g[-qN-l, pF_0+f_d^l] e^{-j\frac{\pi(2m_0+p)l}{M}}. \end{aligned} \tag{6.9}$$

We can alternatively separate the previous expression into signal and interference parts,

$$
\begin{aligned}
y_{m_0,n_0} &= \underbrace{\sum_{l=0}^{L_h-1} c_l e^{j\pi[2n_0N+l]f_d^l T_s} A_g[-l, f_d^l] e^{-j\frac{2\pi m_0 l}{M}}}_{\text{distortion}:\ \alpha_{m_0,n_0}} a_{m_0,n_0} \\
&+ \underbrace{\left(\begin{array}{l} \sum_{(p,q)\neq(0,0)} a_{m_0+p,n_0+q} e^{j\frac{\pi}{2}(p+q+pq)} e^{j\pi p n_0} \\ \cdot \sum_{l=0}^{L_h-1} c_l e^{j\pi[(2n_0+q)N+l]f_d^l T_s} A_g[-qN-l, pF_0+f_d^l] e^{-j\frac{\pi(2m_0+p)l}{M}} \end{array} \right)}_{\text{ISI+ICI}:\ J_{m_0,n_0}} \\
&= \alpha_{m_0,n_0} a_{m_0,n_0} + \underbrace{J_{m_0,n_0}|_{(p=0,q\neq 0)}}_{\text{ISI}} + \underbrace{J_{m_0,n_0}|_{(p\neq 0)}}_{\text{ICI}}. \qquad (6.10)
\end{aligned}
$$

So far, we get a quite nice and meaningful expression (6.10), where the first equality clearly shows that the demodulated OFDM/OQAM signal, at the phase-space point (m_0, n_0), is composed of a distorted transmitted symbol a_{m_0,n_0} and of the sum of inter-symbol-interference (ISI) and inter-carrier-interference (ICI). We can also decompose ISI and ICI to separately analyze these two effects as shown in the second equality. The interference

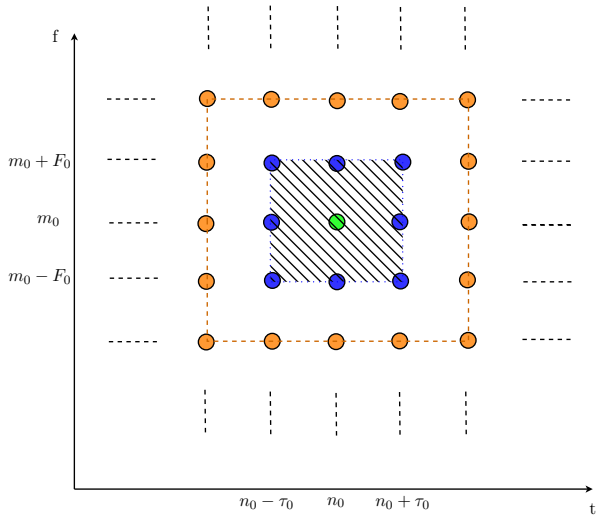

Figure 6.1: Interference analysis in phase-space.

expressions tell us that the interferences are coming from the neighboring symbols which can be better viewed in Fig. 6.1. Furthermore, the integers (p, q) decide the interfere neighboring zone size, i.e. larger $(|p|, |q|)$ denote larger size zone, e.g. from blue zone, $(|p| = |q| = 1)$ to orange zone $(|p| = |q| = 2)$. It is worth noting that if the designed prototype is well-localized in time and frequency, the major interference can be limited into a very small zone (e.g., $|p| = |q| <= 3$ for IOTA4). On the other hand, since the symbols are normally random with zero mean and variance σ_a^2, therefore, the interference

power is equal to its variance and can be calculated as follows

$$\begin{aligned} J_{m_0,n_0} &= \sum_{(p^0,q^0)} a_{m_0+p,n_0+q} e^{j\frac{\pi}{2}(p+q+pq)} e^{j\pi p n_0} \\ &\times \underbrace{\sum_{l=0}^{L_h-1} c_l e^{j\pi[(2n_0+q)N+l]f_d^l T_s} A_g[-qN-l, pF_0+f_d^l] e^{-j\frac{\pi(2m_0+p)l}{M}}}_{H_{m_0,n_0}^{(p,q)}}, \end{aligned} \quad (6.11)$$

where $\sum_{(p^0,q^0)}$ is the compact expression denoting $\sum_{(p,q)\neq(0,0)}$. Then, the interference power writes

$$\begin{aligned} P_{\text{ISI+ICI}}^{\text{demod}}(m_0,n_0) &= \mathrm{E}\left[|J_{m_0,n_0}|^2\right] \\ &= \sum_{(p^0,q^0)} \sum_{(p'^0,q'^0)} \mathrm{E}\left[a_{m_0+p,n_0+q} a_{m_0+p',n_0+q'}\right] \\ &\times e^{j\frac{\pi}{2}(p+q+pq)} e^{j\pi p n_0} e^{-j\frac{\pi}{2}(p'+q'+p'q')} e^{-j\pi p' n_0} H_{m_0,n_0}^{(p,q)} H_{m_0,n_0}^{(p',q')} \\ &= \sigma_a^2 \sum_{(p^0,q^0)} \left|H_{m_0,n_0}^{(p,q)}\right|^2. \end{aligned} \quad (6.12)$$

Note that (6.12) is not the exact interference power at the detector, because we have not taken into account the equalizer and "real-part-taken" operation. (6.12) is just an interference power expression at the output of the demodulator without taking the real-part demodulated symbols. If we now take the real-part of the demodulated symbol without any equalization, the interference after "real-part-taken" operation yields $I_{m_0,n_0} = \mathrm{Re}\{J_{m_0,n_0}\}$. Then its power can be calculated as

$$\begin{aligned} P_{\text{ISI+ICI}}^{\mathrm{Re}\{\text{demod}\}}(m_0,n_0) &= \mathrm{E}\left[|I_{m_0,n_0}|^2\right] \\ &= \sigma_a^2 \sum_{(p^0,q^0)} \left|\mathrm{Re}\left\{e^{j\frac{\pi}{2}(p+q+pq)} H_{m_0,n_0}^{(p,q)}\right\}\right|^2. \end{aligned} \quad (6.13)$$

Thus, the inter-symbol interference and inter-carrier interference power can be respectively written as

$$P_{\text{ISI}}^{\mathrm{Re}\{\text{demod}\}}(m_0,n_0) = \sigma_a^2 \sum_{q\neq 0} \left|\mathrm{Re}\left\{e^{j\frac{\pi}{2}q} H_{m_0,n_0}^{(0,q)}\right\}\right|^2, \quad (6.14)$$

and

$$P_{\text{ICI}}^{\mathrm{Re}\{\text{demod}\}}(m_0,n_0) = \sigma_a^2 \sum_{(p\neq 0, q\in\mathbb{Z})} \left|\mathrm{Re}\left\{e^{j\frac{\pi}{2}(p+q+pq)} H_{m_0,n_0}^{(p,q)}\right\}\right|^2. \quad (6.15)$$

Finally, the Signal-to-Interference Ratio (SIR) at position (m_0,n_0) writes

$$\mathrm{SIR}_{m_0,n_0}^{\mathrm{Re}\{\text{demod}\}} = \frac{|\mathrm{Re}\{\alpha_{m_0,n_0}\}|^2}{P_{\text{ISI+ICI}}^{\mathrm{Re}\{\text{demod}\}}(m_0,n_0)}. \quad (6.16)$$

Straightforwardly, we can also separately express the signal to inter-symbol interference ratio and signal to inter-carrier interference ratio depending upon the objective to analysis.

Up to now, we have derived the demodulated OFDM/OQAM signal model and its interference expressions which permit us to further analytically calculate the interference power (6.13)-(6.15). Here we should highlight the ambiguity function in each interference power expression, because it gives a practical argument for how to compromise TF-localization level in filter design. But, is time-localization more important than frequency-localization or in reverse? To answer that question, one can simply compare the above interference power calculation for different designed prototype filters w.r.t. the given channel environment. Since our assumed channel model is the general time-varying frequency-selective channel model, the derived interference power calculation or SIR calculation can serve for either wired or wireless/mobile communications.

6.2 In-home PLC Transmission: Performance vs. Filters

Let us return back to the PLC case. In [139], Zimmermann *et al.* showed that in-home PLC channel can be modelled as a time-invariant frequency selective channel (cf. Sec. 4.2.1). As there is no significant mobility during transmission, our channel model (6.1) is changed to

$$h(\tau) = \sum_{i=0}^{P-1} c_i \delta(\tau - \tau_i), \tag{6.17}$$

where the conventional Doppler frequency has disappeared. Furthermore, for the PLC channel, the channel gain c_i can be modelled to be real-valued [139, 87]. In this case, the demodulated OFDM/OQAM signal at the phase-space position (m_0, n_0) is re-written as

$$\begin{aligned} y_{m_0,n_0} &= \underbrace{\sum_{l=0}^{L_h-1} c_l A_g[-l,0] e^{-j\frac{2\pi m_0 l}{M}}}_{\text{distortion : } \alpha_{m_0}} a_{m_0,n_0} \\ &+ \underbrace{\sum_{(p,q)\neq(0,0)} a_{m_0+p,n_0+q} e^{j\frac{\pi}{2}(p+q+pq)} e^{j\pi p n_0} \underbrace{\sum_{l=0}^{L_h-1} c_l A_g[-qN-l, pF_0] e^{-j\frac{\pi(2m_0+p)l}{M}}}_{H_{m_0}^{(p,q)}}}_{\text{ISI+ICI : } J_{m_0,n_0}} \\ &= \alpha_{m_0} a_{m_0,n_0} + \underbrace{J_{m_0,n_0}|_{(p=0,q\neq 0)}}_{\text{ISI}} + \underbrace{J_{m_0,n_0}|_{(p\neq 0)}}_{\text{ICI}}, \end{aligned} \tag{6.18}$$

where, we note that since the channel is now time-invariant, then, the distortion weight α_{m_0} and $H_{m_0}^{(p,q)}$ are no longer time dependent which leads to a constant interference power in time, with

$$P_{\text{ISI}}^{\text{Re}\{\text{demod}\}}(m_0) = \sigma_a^2 \sum_{q\neq 0} \left| \text{Re}\left\{ e^{j\frac{\pi}{2}q} H_{m_0}^{(0,q)} \right\} \right|^2, \tag{6.19}$$

and

$$P_{\text{ICI}}^{\text{Re}\{\text{demod}\}}(m_0) = \sigma_a^2 \sum_{(p\neq 0, q\in\mathbb{Z})} \left| \text{Re}\left\{ e^{j\frac{\pi}{2}(p+q+pq)} H_{m_0}^{(p,q)} \right\} \right|^2, \tag{6.20}$$

and a SIR such as

$$\mathrm{SIR}_{m_0}^{\mathrm{Re}\{\mathrm{demod}\}} = \frac{|\mathrm{Re}\{\alpha_{m_0}\}|^2}{P_{\mathrm{ISI+ICI}}^{\mathrm{Re}\{\mathrm{demod}\}}(m_0)}. \tag{6.21}$$

Taking advantage of Eqs. (6.19)-(6.21), we next aim at analyzing the OFDM/OQAM transmission performance w.r.t. the different prototype filters. Some of them were briefly presented in Sec. 5.4.3 and more details will be revealed in this chapter.

6.2.1 Ideal Channel

Before analyzing over the PLC channel, let us first examine the simplest transmission case: ideal channel (i.e. $L_h = 1$ and $c_0 = 1$ in (6.17)). Thus, the distortion weight $\alpha_{m_0}^{\mathrm{ideal}}$ reads

$$\alpha_{m_0}^{\mathrm{ideal}} = A_g[0,0] = 1, \tag{6.22}$$

where the last equality holds only if the prototype filter is normalized which is normally the case in order to unchange the transmission energy. Next, ISI and ICI powers can be calculated as follows

$$P_{\mathrm{ISI}}^{\mathrm{ideal}}(m_0) = \sigma_a^2 \sum_{q\neq 0} \left| \mathrm{Re}\left\{ e^{j\frac{\pi}{2}q} \left(H_{m_0}^{(0,q)} \Big|_{c_0=1}^{L_h=1} \right) \right\} \right|^2, \tag{6.23}$$

and

$$P_{\mathrm{ICI}}^{\mathrm{ideal}}(m_0) = \sigma_a^2 \sum_{(p\neq 0, q\in\mathbb{Z})} \left| \mathrm{Re}\left\{ e^{j\frac{\pi}{2}(p+q+pq)} \left(H_{m_0}^{(p,q)} \Big|_{c_0=1}^{L_h=1} \right) \right\} \right|^2. \tag{6.24}$$

As to the choice of our prototype filter, we always expect to have a good filter with a minimum possible length because of the following reasons. First, a long prototype filter leads to an augmentation of the computational complexity (the complexity issue will be discussed later in this chapter). Second, a long prototype filter results in a long latency for recovering the symbols at the receiver, e.g. if the prototype filter has length $L_f = \gamma N$ with $N = M/2$, the latency leads to a delay $\gamma\tau_0$ to recover the symbols for each subcarrier and the proof is given below

Proof Relation of L_f vs. Latency.

We write the modulated OFDM/OQAM signal as

$$s[k] = \sum_{m=0}^{M-1} \sum_{n=-\infty}^{+\infty} a_{m,n} f_m[k],$$

with $f_m[k] = g[k-nN]e^{j(\frac{2\pi}{M}(k-\frac{D}{2})+\phi_{m,n})}$. Assuming that our prototype filter is real-valued and symmetrical, i.e., $g[k] = g[D-k]$[2], the demodulated signal yields

$$\begin{aligned} y_{m,n} &= \sum_{k=-\infty}^{+\infty} f_m^*[k]s[k] \\ &= \sum_{k=-\infty}^{+\infty} g[k]e^{j\frac{2\pi}{M}(k-\frac{D}{2})} s[D+nN-k]e^{-j(\phi_{m,n}+\pi mn)}. \end{aligned} \tag{6.25}$$

[2]This assumption corresponds to the most frequent case for OFDM/OQAM prototype filters. This symmetry property permits to reduce by a factor of 2 the number of the coefficients to be optimized [130, 37].

Next, following the notation in [115], we can decompose D with two integers γ and β ($\gamma > 0$ and $0 \leq \beta \leq N-1$) by $D = \gamma N - \beta$. Then, in order to get a causal system, (6.25) yields

$$y_{m,n-\gamma} = e^{-j(\phi_{m,(n-\gamma)}+\pi m(n-\gamma))} \sum_{k=-\infty}^{+\infty} h_m[k]s[nN-k-\beta], \tag{6.26}$$

with $h_m[k] = g[k]e^{j\frac{2\pi}{M}(k-\frac{D}{2})}$. The two delay parameters, β and γ, we have introduced have not the same weight, β corresponds to a delay in samples while γ leads to a delay in processing duration (T_0). Therefore, the latency redundant due to the prototype length is $\gamma\tau_0$. For example, we can set $\beta = 1$, then we have $\gamma = \frac{L_f}{N}$.

The third reason, which is not predominant in PLC transmission, of choosing a short filter is that in mobile communications, the Doppler frequency may change significantly in the prototype filter duration which requires the receiver to track every changed Doppler shift for compensation. It surely causes a complexity increase. Let us compare the interference power in the case of an ideal channel using different prototype filters with the same length of M (i.e., $L_f = M$) corresponding to a latency of $\gamma = 2$ and $\beta = 1$. The interference calculation is based on (6.23) and (6.24). Recall that TFL and FS filters are designed in discrete-time domain and are fully orthogonal, i.e., PR prototype filters. At the contrary, SRRC and IOTA are continuous-time infinite duration functions that are no longer orthogonal after truncation and discretization. [3]. The corresponding results are shown in Fig. 6.2, where we can find that for the PR prototype filters, e.g. TFL or FS, even with short filter length, they can still guarantee orthogonality which results in a zero interference power. However, for IOTA or SRRC filters, the short length truncation leads to a significant orthogonality loss. Furthermore, this loss is more serious for the SRRC filter. If we increase the filter length to be $8M$ (corresponding to a latency of $\gamma = 16, \beta = 1$), the orthogonality is improved for IOTA and SRRC filters as shown in Fig. 6.3.

From these figures, we observe that the orthogonality loss for certain filters results in an increase of the interference power which further leads to a reduction of the SIR. This can be checked through performance analysis. Now, we shall take into account the background noise effect by assuming that it follows the Gaussian distribution with zero mean and variance σ_n^2. Therefore, the estimated symbol at (m_0, n_0) after "real-part-taken" operation yields

$$\hat{a}_{m_0,n_0} = \mathrm{Re}\{\alpha_{m_0}^{\mathrm{ideal}}\}a_{m_0,n_0} + I_{m_0,n_0} + \mathrm{Re}\{\eta_{m_0,n_0}\}. \tag{6.27}$$

Noting that η_{m_0,n_0} is the white noise at position (m_0, n_0) with $\mathrm{E}[\mathrm{Re}\{\eta_{m_0,n_0}\}] = 0$ and $\mathrm{Var}[\mathrm{Re}\{\eta_{m_0,n_0}\}] = \sigma_n^2/2$. Then the Signal-to-Interference-Plus-Noise Ratio (SINR) at the subcarrier m_0 after "real-part-taken" operation yields

$$\mathrm{SINR}_{m_0}^{\mathrm{ideal}} = \frac{\left|\mathrm{Re}\{\alpha_{m_0}^{\mathrm{ideal}}\}\right|^2 \sigma_a^2}{P_{\mathrm{ISI+ICI}}^{\mathrm{ideal}}(m_0) + \frac{\sigma_n^2}{2}}. \tag{6.28}$$

As a_{m_0,n_0} can be considered as a PAM modulation, then we can re-construct a complex-valued estimated symbol by doing $\hat{c}_{m_0,n_0} = \hat{a}_{m_0,2n_0} + j\hat{a}_{m_0,2n_0+1}$ (note that the SINR of the

[3] The shorter the truncation length is, the worse the orthogonality loss will be.

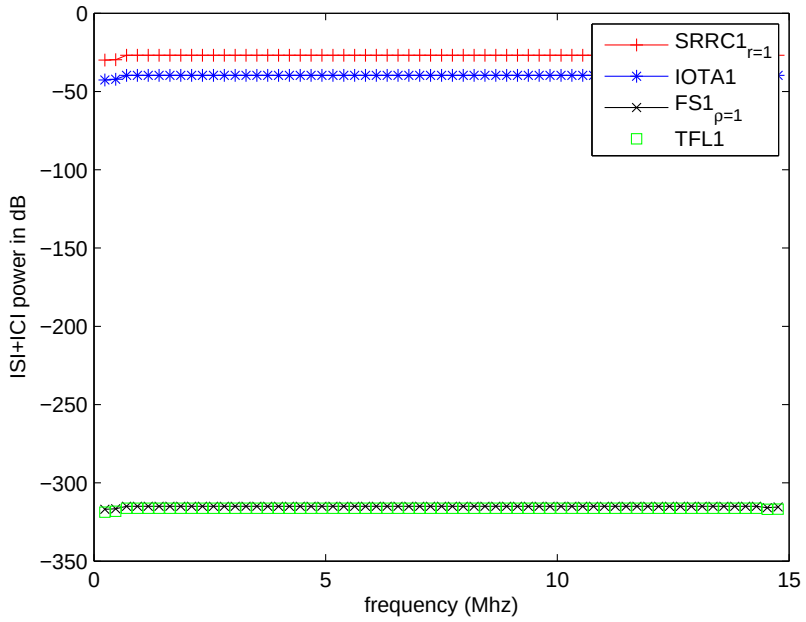

Figure 6.2: Interference Comparison for $M = 128, F_s = 30$ MHz.

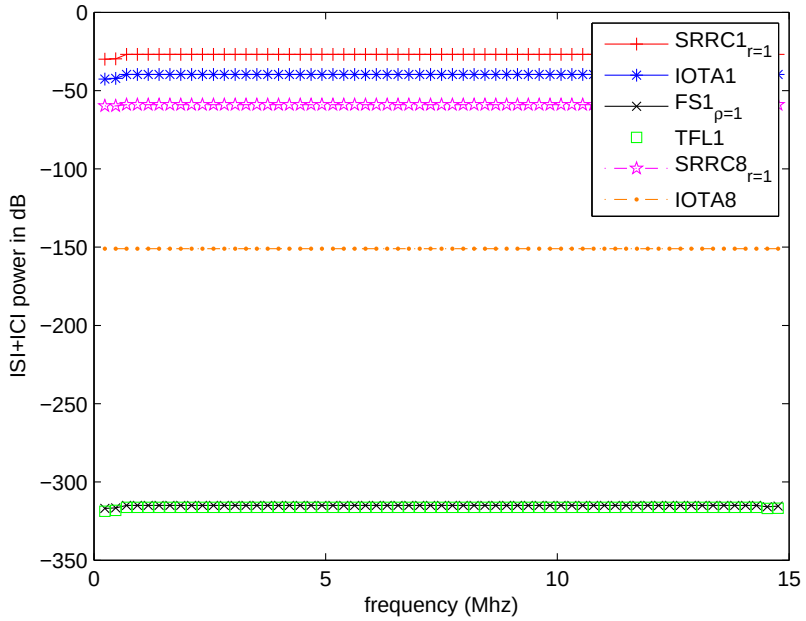

Figure 6.3: Interference Comparison for $M = 128, F_s = 30$ MHz.

combined symbol is still equal to (6.28)). Since the fact that the interference is composed of the sum of random variables, thus the interference can be assumed to have Gaussian distribution. Assuming further the background noise is AWGN, the theoretical Bit Error Rate (BER), P_b^{ideal}, can be calculated using the closed-form expression in below,

$$P_b^{\text{ideal}} = \frac{1}{M} \sum_{m_0=0}^{M-1} P_b^{\text{ideal}}(m_0), \tag{6.29}$$

with,$P_b^{\text{ideal}}(m_0)$, the BER of the m_0-th subcarrier of 2^{2K}-QAM constellations (Gray-coded) yielding [32]

$$\begin{aligned} P_b^{\text{ideal}}(m_0) &\approx \frac{2^K - 1}{2^K \cdot K} \text{erfc}\left(\sqrt{\frac{3}{2} \cdot \frac{\text{SINR}_{m_0}^{\text{ideal}}}{2^{2K} - 1}}\right) \\ &+ \frac{2^K - 2}{2^K \cdot K} \text{erfc}\left(3\sqrt{\frac{3}{2} \cdot \frac{\text{SINR}_{m_0}^{\text{ideal}}}{2^{2K} - 1}}\right). \end{aligned} \tag{6.30}$$

In order to check the correctness of our above derived theoretical expression, we show in Fig. 6.4 the comparison of theoretical BER of TFL1 vs. simulation[4] over an ideal channel with number of carriers $M = 128$ for constellations from QPSK to 64-QAM (The coefficients of TFL1 of this length are given in Appendix 10.2). The result shows that the theory and simulation curves are matched which confirms the correctness of our derived interference power and SINR expression as well as the theoretical BER expression. We then show in Fig. 6.5 the performance loss due to the orthogonality loss of the EGF and SRRC truncation with length $L_f = M$, and this performance loss becomes more obvious in higher order constellation transmissions. When we try to increase the filter length to, for instance, $L_f = 4M$, the performance loss is reduced, which verifies the results of Fig. 6.3. Thus, we can conclude that for the case of transmission over an ideal channel, the proper prototype filter to be chosen is the orthogonal filter (no performance perturbation) with length $L_f = M$ (giving a short latency time)[5]. However, the ideal channel case only exists in theory, the argument of choosing a prototype filter might not be the same in realistic multi-path PLC channel environment.

6.2.2 Frequency Non-Selective Channel

In this part, we assume that our in-home PLC channel has frequency non-selective behavior (i.e. $L_h = 1$ and $|c_0| < 1$ in (6.17)). Actually, this is a very plausible assumption recalling that, in Chap. 4, the analysis of realistic in-home PLC measurements reveals that some channel classes have very short delay spread and appears as non-selective in frequency. Therefore, if the modulated symbol duration is much longer than the channel delay spread, we do have the reason to consider the channel as a frequency non-selective channel.

[4]In this thesis, for the simulation of BER, we transmit $M \times nb$ complex-valued symbols over M carriers ($nb = 20$ in our simulations) and we define it as one realization. The BER is averaged over a total of 1000 such realizations.

[5]In ideal channel case, the minimum prototype length can even be $M/2$.

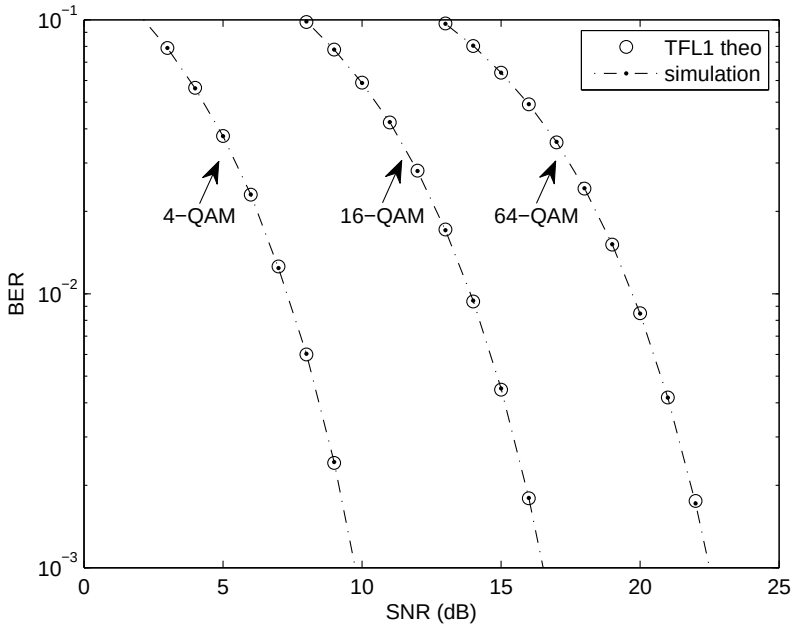

Figure 6.4: Performance comparison: theory vs. simulation, BER over an ideal channel for $M = 128$.

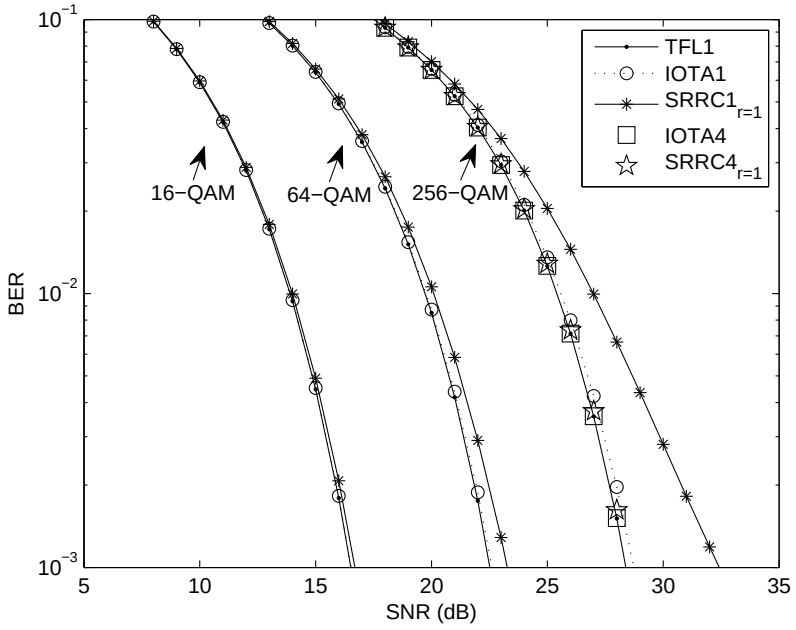

Figure 6.5: Performance loss for IOTA and SRRC filters of length $L_f = M = 128$.

In the frequency non-selective channel case, the distortion weight (denoted $\alpha_{m_0}^{\text{flat}}$), introduced by a flat fading, yields

$$\alpha_{m_0}^{\text{flat}} = c_0 A_g[0,0]. \tag{6.31}$$

Thus, we shall use an equalizer at the output of the demodulator to compensate this distortion. We can assume the equalizer to be a simple one-tap zero-forcing (ZF) equalizer, which eventually leads to the equalized signal after "real-part-taken" operation as

$$\hat{a}_{m_0,n_0} = \text{Re}\left\{\frac{\alpha_{m_0}^{\text{flat}}}{H_{m_0}}\right\} a_{m_0,n_0} + \text{Re}\left\{\frac{J_{m_0,n_0}}{H_{m_0}}\right\} + \text{Re}\left\{\frac{\eta_{m_0,n_0}}{H_{m_0}}\right\}, \tag{6.32}$$

where H_{m_0} is the ZF equalizer coefficient at m_0-th subcarrier and can be calculated in the same way as in the DMT case i.e.,

$$H_{m_0} = \sum_{l=0}^{L_h-1} c_l e^{-j\frac{2\pi m_0 l}{M}} = c_0. \tag{6.33}$$

Then, the interference power yields

$$P_{\text{ISI}}^{\text{flat}}(m_0) = \sigma_a^2 \sum_{q\neq 0} \left| \text{Re}\left\{ \frac{e^{j\frac{\pi}{2}q}\left(H_{m_0}^{(0,q)}\Big|_{|c_0|<1}^{L_h=1}\right)}{c_0} \right\} \right|^2, \tag{6.34}$$

and

$$P_{\text{ICI}}^{\text{flat}}(m_0) = \sigma_a^2 \sum_{(p\neq 0, q\in\mathbb{Z})} \left| \text{Re}\left\{ \frac{e^{j\frac{\pi}{2}(p+q+pq)}\left(H_{m_0}^{(p,q)}\Big|_{|c_0|<1}^{L_h=1}\right)}{c_0} \right\} \right|^2. \tag{6.35}$$

The Signal-to-Interference-Plus-Noise Ratio (SINR) at the subcarrier m_0 after "real-part-taken" operation yields

$$\text{SINR}_{m_0}^{\text{flat}} = \frac{\left|\text{Re}\{\alpha_{m_0}^{\text{flat}}\}\right|^2 \sigma_a^2}{P_{\text{ISI+ICI}}^{\text{flat}}(m_0) + \frac{\sigma_n^2}{2}}. \tag{6.36}$$

Combining by $\hat{c}_{m_0,n_0} = \hat{a}_{m_0,2n_0} + j\hat{a}_{m_0,2n_0+1}$ to get a complex-valued estimated QAM symbol, the theoretical BER can be calculated by

$$P_b^{\text{flat}} = \frac{1}{M}\sum_{m_0=0}^{M-1} P_b^{\text{flat}}(m_0), \tag{6.37}$$

with a subcarrier BER for the 2^{2K}-QAM constellations (Gray-coded), given by,

$$\begin{aligned} P_b^{\text{flat}}(m_0) &\approx \frac{2^K-1}{2^K\cdot K}\text{erfc}\left(\sqrt{\frac{3}{2}\cdot\frac{\text{SINR}_{m_0}^{\text{flat}}}{2^{2K}-1}}\right) \\ &+ \frac{2^K-2}{2^K\cdot K}\text{erfc}\left(3\sqrt{\frac{3}{2}\cdot\frac{\text{SINR}_{m_0}^{\text{flat}}}{2^{2K}-1}}\right). \end{aligned} \tag{6.38}$$

The derivation correctness is verified in Fig. 6.6 over an artificial frequency non-selective channel where we set $c_0 = 0.4$ and further we assume a perfect channel estimation (CE) at the receiver[6]. Note that in Fig. 6.6, the comparison is given by BER versus received SNR ($\mathrm{SNR}_{\mathrm{Rx}}$) and the difference between received SNR and transmitted SNR ($\mathrm{SNR}_{\mathrm{Tx}}$) for PLC transmission is as follows

$$\mathrm{SNR}_{\mathrm{Rx}} = \sum_{l=0}^{L_h-1} |c_l|^2 \cdot \mathrm{SNR}_{\mathrm{Tx}}. \tag{6.39}$$

In this frequency non-selective channel example, we can write $\mathrm{SNR}_{\mathrm{RX}} = |c_0|^2 \cdot \mathrm{SNR}_{\mathrm{TX}}$. The resulting performance comparison w.r.t. the different possible choices of filters is reported in Fig. 6.7. One may wonder why the performance in the frequency non-selective channel case is exactly the same as in the ideal channel case. This is reasonable, since we assume the receiver perfectly knows the channel coefficient and the frequency non-selective channel only creates the distortion. Therefore, by ZF equalizer, this distortion can be compensated resulting in an ideal channel liked transmission. It is worth noting that the performance match between frequency non-selective channel case and ideal channel case holds only when the performance is shown in the BER vs. $\mathrm{SNR}_{\mathrm{Rx}}$. If we plot the performance as BER vs. $\mathrm{SNR}_{\mathrm{Tx}}$, those performance curves over frequency non-selective channel will be decayed by a channel gain in decibels, i.e. $(20 \log_{10} |c_0|)$ dB.

Ultimately, for the frequency non-selective channel case, the previous argument is still valid here, i.e. the proper prototype filter should be orthogonal and as short as possible.

6.2.3 Frequency Selective Channel

Now, let us move to the frequency selective channel. In this case, the distortion weight (denoted $\alpha_{m_0}^{\mathrm{fselect}}$) introduced by the frequency selectivity, yields

$$\alpha_{m_0}^{\mathrm{fselect}} = \sum_{l=0}^{L_h-1} c_l A_g[-l, 0] e^{-j\frac{2\pi m_0 l}{M}}. \tag{6.40}$$

Assume that we still retain the one-tap ZF equalizer with its coefficients being calculated by (6.33). Thus, the interference power at the input of the detector of (m_0)-th subcarrier yields

$$P_{\mathrm{ISI}}^{\mathrm{fselect}}(m_0) = \sigma_a^2 \sum_{q \neq 0} \left| \mathrm{Re}\left\{ \frac{e^{j\frac{\pi}{2}q} H_{m_0}^{(0,q)}}{H_{m_0}} \right\} \right|^2, \tag{6.41}$$

and

$$P_{\mathrm{ICI}}^{\mathrm{fselect}}(m_0) = \sigma_a^2 \sum_{(p \neq 0, q \in \mathbb{Z})} \left| \mathrm{Re}\left\{ \frac{e^{j\frac{\pi}{2}(p+q+pq)} H_{m_0}^{(p,q)}}{H_{m_0}} \right\} \right|^2. \tag{6.42}$$

The Signal-to-Interference-Plus-Noise Ratio (SINR) at the subcarrier m_0 after "real-part-taken" operation yields

$$\mathrm{SINR}_{m_0}^{\mathrm{fselect}} = \frac{\left|\mathrm{Re}\{\alpha_{m_0}^{\mathrm{fselect}}\}\right|^2 \sigma_a^2}{P_{\mathrm{ISI+ICI}}^{\mathrm{fselect}}(m_0) + \frac{\sigma_n^2}{2}}. \tag{6.43}$$

[6]The channel estimation method for OFDM/OQAM system is discussed in Chap. 8.

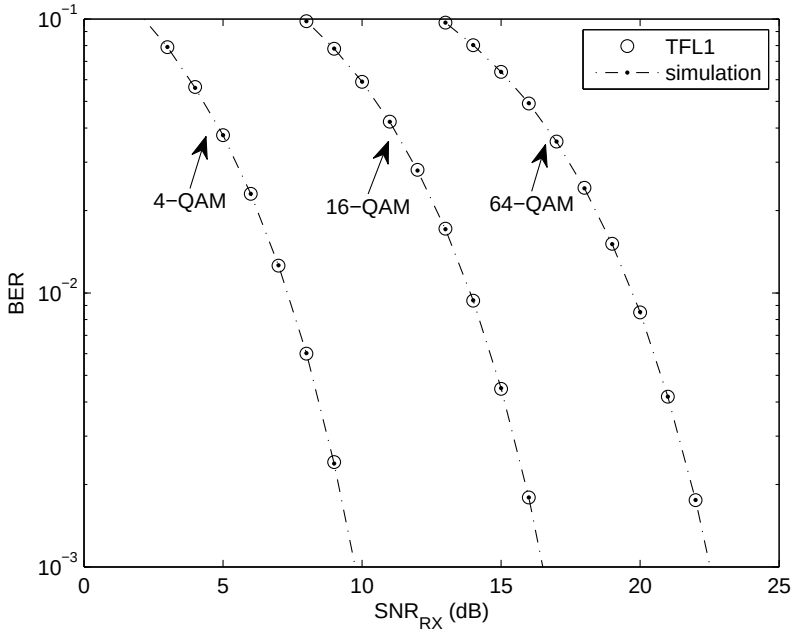

Figure 6.6: Performance comparison: theory vs. simulation over a frequency non-selective channel.

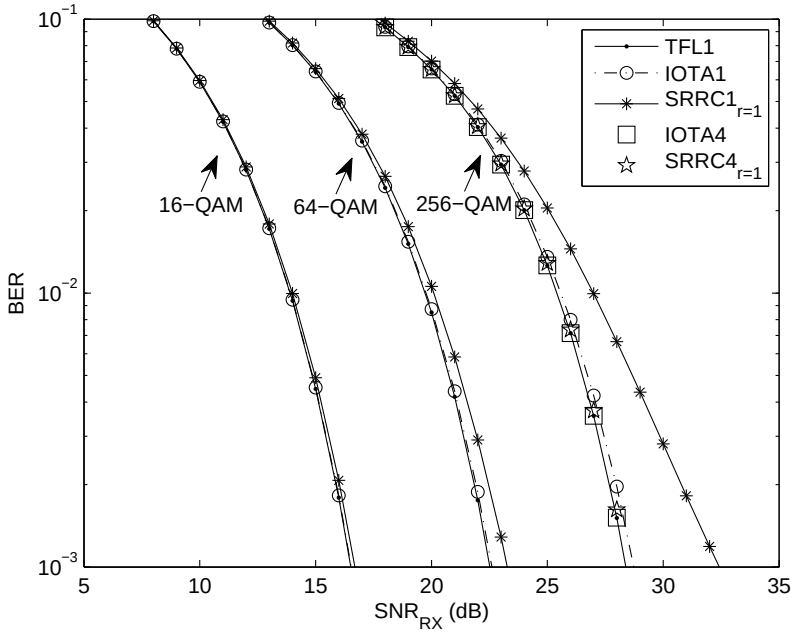

Figure 6.7: Performance loss for IOTA and SRRC filters over a frequency non-selective channel.

Combining by $\hat{c}_{m_0,n_0} = \hat{a}_{m_0,2n_0} + j\hat{a}_{m_0,2n_0+1}$ to get a complex-valued estimated QAM symbol, the theoretical BER can be calculated by

$$P_b^{\text{fselect}} = \frac{1}{M}\sum_{m_0=0}^{M-1} P_b^{\text{fselect}}(m_0), \tag{6.44}$$

with each subcarrier BER for the 2^{2K}-QAM constellations (Gray-coded), i.e.,

$$\begin{aligned} P_b^{\text{fselect}}(m_0) &\approx \frac{2^K-1}{2^K\cdot K}\text{erfc}\left(\sqrt{\frac{3}{2}\cdot\frac{\text{SINR}_{m_0}^{\text{fselect}}}{2^{2K}-1}}\right) \\ &+ \frac{2^K-2}{2^K\cdot K}\text{erfc}\left(3\sqrt{\frac{3}{2}\cdot\frac{\text{SINR}_{m_0}^{\text{fselect}}}{2^{2K}-1}}\right). \end{aligned} \tag{6.45}$$

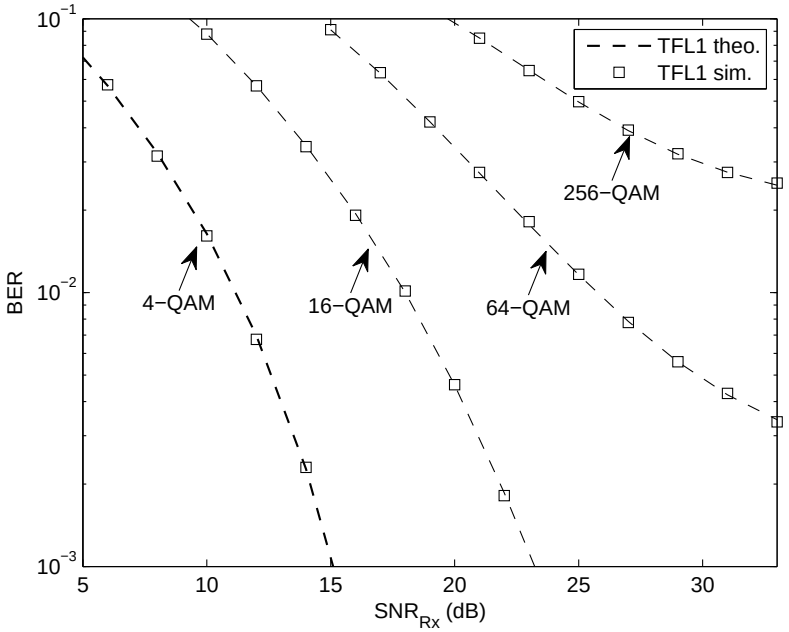

Figure 6.8: Performance comparison: theory vs. simulation over frequency selective channel (Ma's channel [87]).

As usual, in order to check the correctness of the above derivation for frequency selective channel, we compare the theoretical performance with the one by simulations over a theoretical PLC channel that is presented in Ma's paper [87] and this channel is based on the Zimmermann PLC multi-path channel model [139], i.e., amplitude profile (in linear) : $0.2, 0.1, 0.02, 0.01$ and delay profile (μs) : $0, 0.4, 0.6, 0.7$. Other parameters are: sampling frequency $f_s = 10$ MHz; $M = 128$. We plot the performance comparison in Fig. 6.8 for different constellation orders. The results confirm the correctness of our derivations. Furthermore, in the higher order constellation case, a performance floor occurs in

the high SNR region. This verifies what we mentioned at the beginning of this chapter that OFDM/OQAM system has a remaining interference drawback. This drawback may not be remarkable in case of low SNR transmission or small order constellation transmission. Because, comparing with noise power, the interference power becomes negligible. Moreover, revisiting the interference power calculation (6.41) and (6.42), we find that the interference level is linked with the ambiguity function of a chosen prototype filter. If the prototype filter has good TF-localization, the energy of its ambiguity function will be very much concentrated in its phase-space. Thus, less energy spreading over time and/or frequency results in the smaller ISI and/or ICI power. Keeping this argument in mind, we next look at the interference comparison using different prototype filters. This comparison will be only carried out for the channel model provided in [87] setting $M = 128$. So, strictly speaking, we cannot pretend the results will be the same if the channel model and/or the number of carriers changed. Nevertheless, we expect to provide a new and relatively precise insight of some possible trade-off when selecting a prototype filter for OFDM/OQAM.

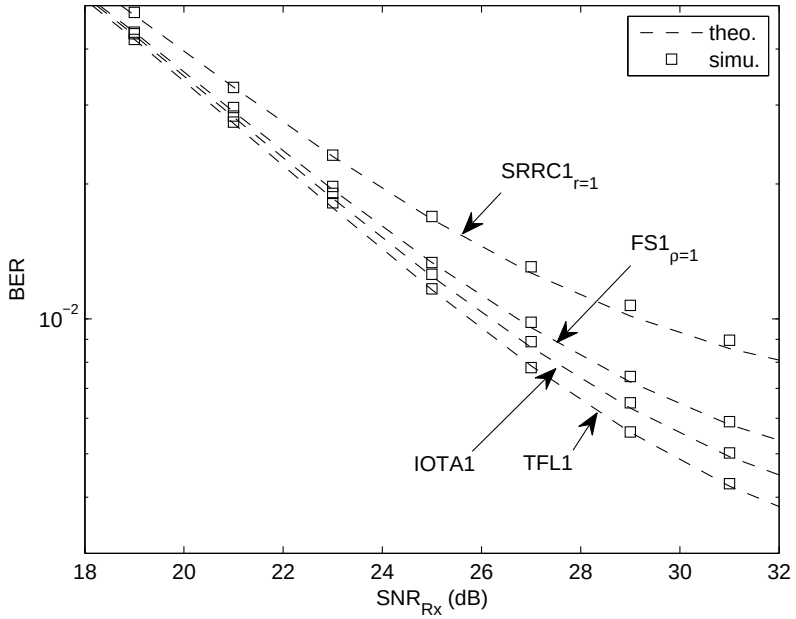

Figure 6.9: 64-QAM performance comparison: filter length $L_f = M = 128$ (Ma's channel [87]).

The first case we intend to show is when the short prototype filters are adopted. We compare four filters: SRRC with roll-off 1, IOTA, FS with roll-off 1 and TFL with the filter length of $L_f = M$ over Ma's PLC channel model for 64-QAM transmission. The performance comparison is reported in Fig. 6.9 and it shows that TFL1 filter has better performance than the other filters, which, naturally, means that TFL1 filter leads to a minimum ISI+ICI interference as shown in Fig. 6.10. Instead, the SRRC filter has a maximum interference power which again illustrates the fact that the short truncation of SRRC cannot provide a good performance. On the other hand, we remark that the

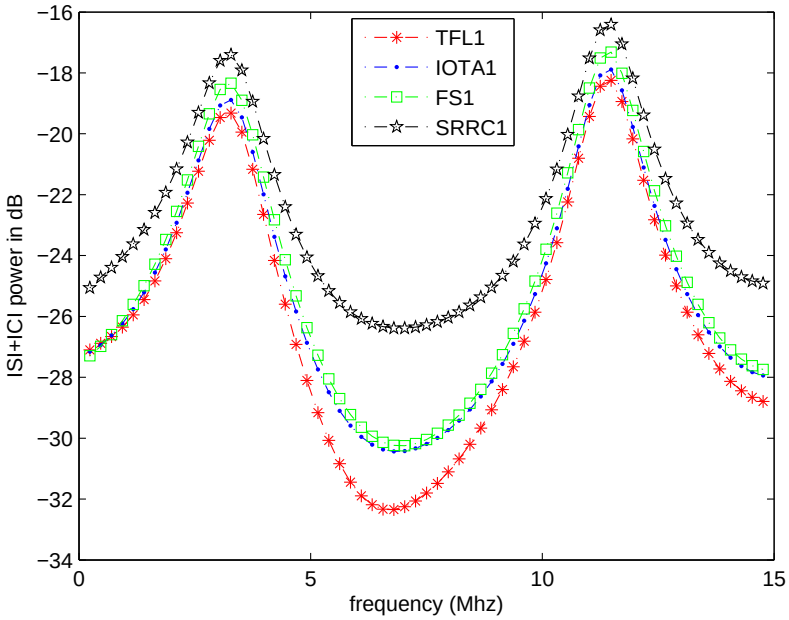

Figure 6.10: Interference comparison (Ma's channel [87]).

interference power of IOTA case is smaller than that of FS case.

Let us further analyze in depth. We have shown that good time localization results in a controlled ISI and good frequency localization leads to ICI immunity. But, which one is the predominant factor in PLC transmission? The answer could be found if we separately analyze these two types of interference power. By using (6.42), the ICI power can be obtained w.r.t. a given prototype filter. For instance, Fig. 6.11 clearly gives the ICI power comparison among different filters, wherein TFL filter gives a minimum ICI power at almost all of the subcarriers and SRRC filter leads to the strongest ICI power. This reveals that TFL has the best frequency localization. We can also double check this fact in Fig. 6.12, where we can see that TFL filter has a relatively smaller stopband energy and SRRC filter has the worse stopband attenuation. Although FS design criterion is targeting to minimizing the "cut-off" band energy (refer to Eq. (5.41)), for such filter design, it usually requires longer filter order (i.e., filter length) to reach a desired performance. The contour versions of energy spreading of ambiguity function for these filters are depicted in Fig. 6.13.

Next, we should check the ISI power using (6.41). The result is given in Fig. 6.14 and shows that there is not much difference among different filters. Thus, it portrays that all the filters have more or less the same level of time localization. This is a logical situation, since short length of a FIR filter always leads to a good time localization even with rectangular filter. However, since TFL is designed to provide the maximum TF-localization, it ultimately leads to the best localization feature in frequency. Moreover, comparing ISI power with ICI power, we find that ICI power is much higher than ISI power. Therefore, we can deduce that, for the transmission over time-invariant frequency selective channel, ICI is a fairly predominant factor to limit the overall performance. Otherwise

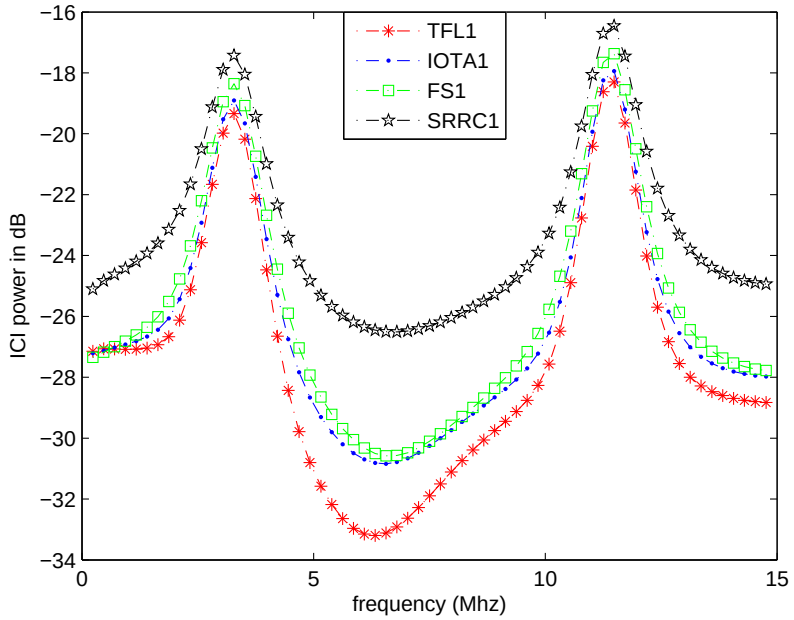

Figure 6.11: Inter-carrier Interference comparison (Ma's channel [87]).

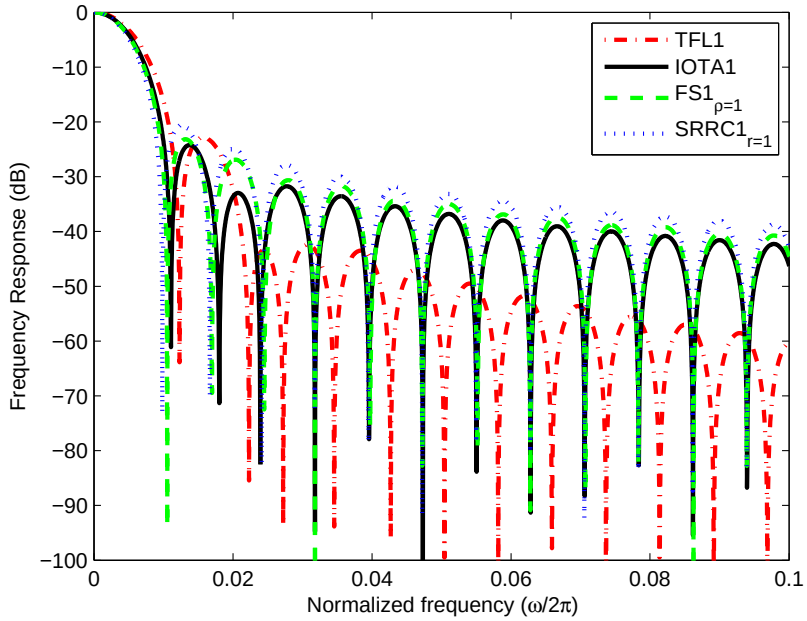

Figure 6.12: Frequency representation comparison for $L_f = M = 128$.

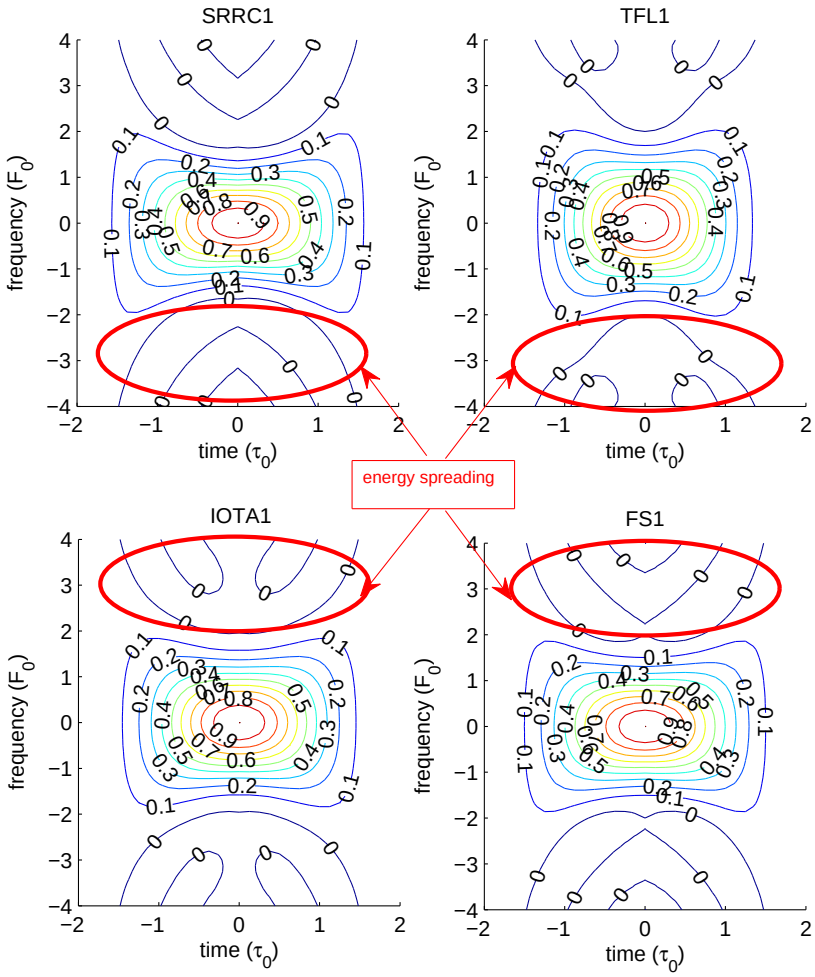

Figure 6.13: Ambiguity function contour representation.

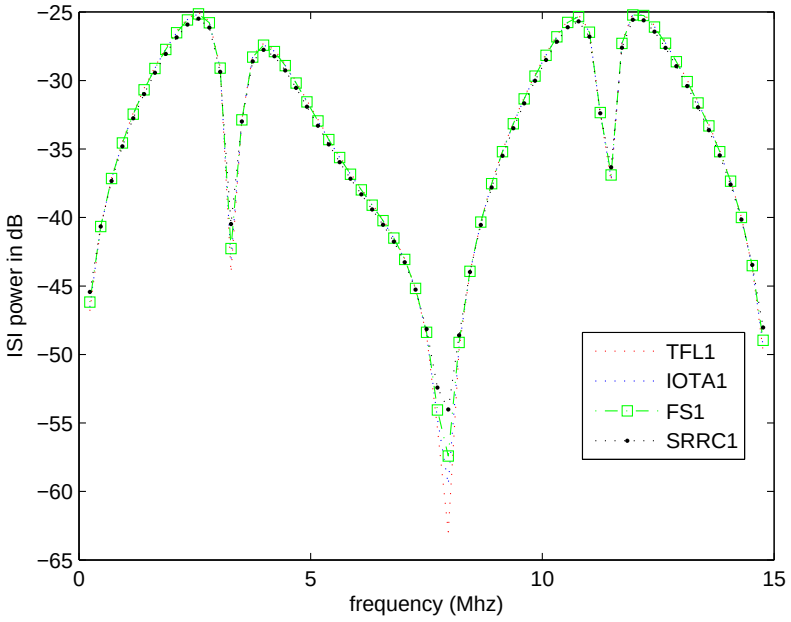

Figure 6.14: Inter-symbol Interference comparison (Ma's channel [87]).

said, when we design a filter for PLC transmission, more attention should be paid on frequency localization.

Nevertheless, a good frequency localization filter design is naturally requiring a filter length augmentation. To verify our inference, we try to increase the filter length up to $L_f = 4M$ such that the frequency localization of FS filter is much refined (see Fig. 6.15) as well as the ones of IOTA and SRRC filters. As expected, a better frequency localization feature leads to a ICI power reduction (see Fig. 6.16). It will normally result in a better performance in terms of BER. In Fig. 6.17, we compare the longer filters with the conventional TFL1 filter and the result shows that all of these longer filters outperform TFL1 filter, which confirms our above inference. Moreover, FS4 and SRRC4 filters have better performance than IOTA4 filter because they have better frequency localization feature. In [133], based on an experimental study, the authors arrive at the same conclusion with the EMFB TMUX.

Based on the above analysis, we remark that for the transmission over frequency selective channel, the orthogonality feature of the prototype filter may not be that much important, since the selectivity will ruin the orthogonality anyway at the receiver. Therefore, it might be judicious to trade the orthogonality with the frequency localization level. Several filter bank design methods have been published that, indeed, propose to relax the perfect orthogonality condition to get a stronger attenuation slope or a reduced out-of-band energy. These approaches lead to the so-called "nearly perfect reconstruction" (NPR) modulated filter banks. Among a large number of design methods, we choose two typical ones to compare with our PR prototype and with the ones obtained by truncation and discretization.

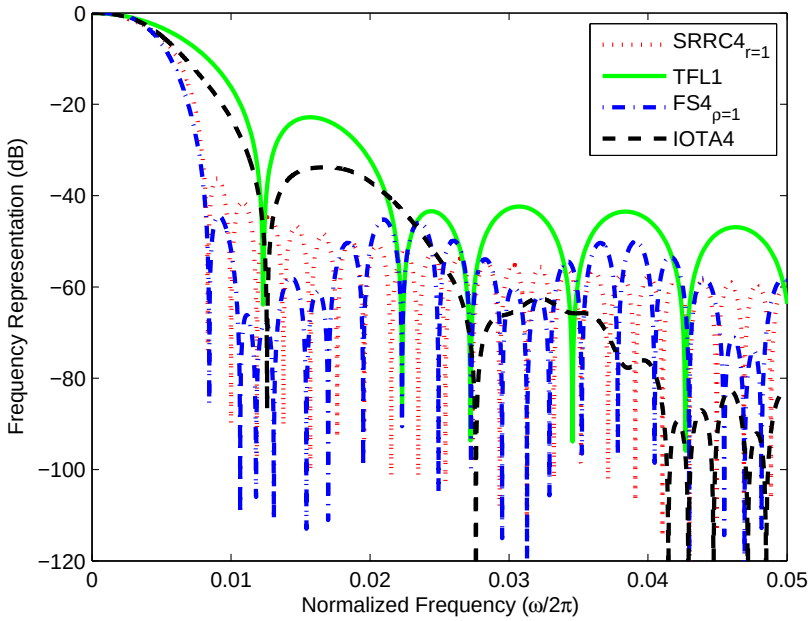

Figure 6.15: Frequency representation comparison for $L_f = 4M$, $M = 128$.

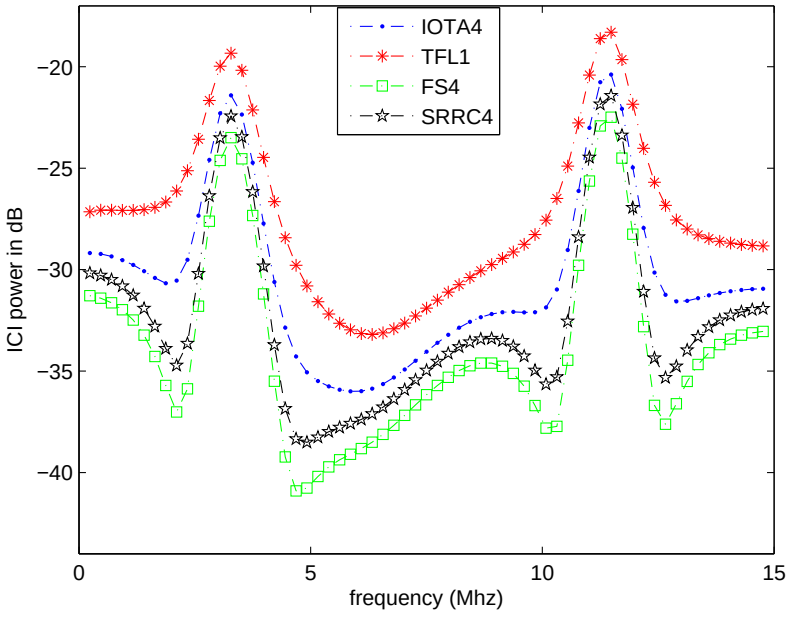

Figure 6.16: Inter-carrier Interference comparison: filter length $L_f = 4M$, $M = 128$ (Ma's channel [87]).

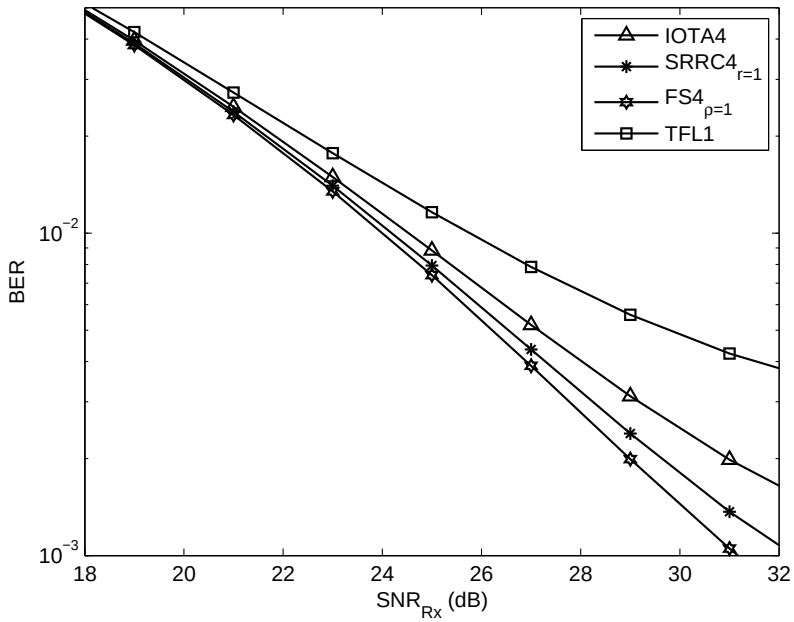

Figure 6.17: 64-QAM performance comparison: filter length $L_f = 4M$, $M = 128$ (Ma's channel [87]).

The first NPR prototype filter is the one designed by Mirabbasi and Martin in [90][7], wherein, the authors proposed a closed-form expression for coefficients generation which is therefore different from the ones using optimization methods [130]. The goal of this method is to generate a filter that has a very fast stopband attenuation decreasing slope which is a termed "fall-off" rate in [90]. The advantages of this method are that: First, it is very simple to obtain the filter coefficients; Second, the obtained filter can have a fast stopband fall-off rate. Furthermore, any fall-off rate can be freely reached by Mirabbasi's method but at a price of filter length augmentation. The disadvantages of this method are: First, a fast fall-off rate requires a high filter order which leads to a complexity increase; Second, the faster fall-off rate does not mean that the filter has surely a small stopband energy (the explication will be discoursed later); Third, the transition band of the designed filter is fixed. The closed-form of Mirabbasi's filter is as follows

$$g[n] = \begin{cases} \frac{1}{bM}\left(k_0 + 2\sum_{l=1}^{b-1} k_l \cos\left(\frac{2\pi l n}{bM}\right)\right), & 0 \le n < L_f \\ 0, & \text{otherwise} \end{cases} \tag{6.46}$$

where $L_f = bM + 1$ with a positive integer b meaning the overlap factor, and k_l $(0 \le l < b)$ are real coefficients (the coefficients are given in [90] for b up to 8).

The second prototype filter design method that we have chosen for our comparison is the one proposed by Rossi *et al.* in [108] where the objective is to minimize the stopband

[7] As pointed out in [12], the prototype designed in [90] is actually the application to the Nyquist filter of the classical frequency sampling FIR design technique. The attention to the relevance of this design technique to cable transmission was raised by Martin [89]

energy and reads

$$\min(\frac{1}{\pi-\omega_s})\int_{\omega_s}^{\pi}|H(e^{j\omega})|^2\,d\omega \tag{6.47}$$

subject to a nearly guaranteed orthogonal condition. Here ω_s is the stopband frequency edge. Same as in FS case, ω_s can be expressed as $\omega_s = \frac{(1+\rho)\pi}{M}$ with a roll-off factor ρ ($0 \leq \rho \leq 1$). The coefficients design is carried out in discrete-time domain using an iterative least square algorithm [108]. The advantages of Rossi's method are: it can generate a filter with a minumum stopband energy and the roll-off factor can be flexibly modified to control the transition band size. The drawbacks of this method are: First, it is computationally more costly than Mirab's method. Second, to get a good stopband performance we need a pretty long filter length.

Note that both of these two NPR filters have a shortcoming in common that is long filter length requirement. So, let us first analyze the filter length effect. In Fig. 6.18, we

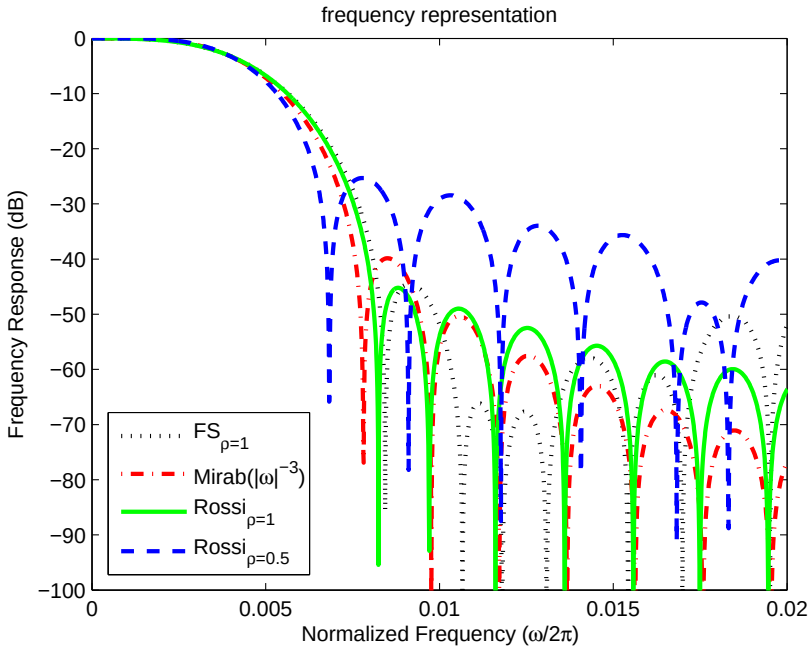

Figure 6.18: Frequency representation comparison for $L_f = 4M$, $M = 128$.

show the frequency representation of the designed filter by Mirab and Rossi's methods, respectively, each with a length of $L_f = 4M$ (corresponding to a fall-off rate approximately $|\omega|^{-3}$ for Mirab filter, cf. [90]) versus FS4 filter. The stopband energy of FS4$_{\rho=1}$, Rossi4$_{\rho=1}$ and Mirab4 filters are given in Tab. 6.1. The comparison clearly shows that Rossi4

Table 6.1: Stopband energy ($L_f = 4M$ with $M = 128$)

	SRRC4$_{r=1}$	FS4$_{\rho=1}$	Rossi4$_{\rho=1}$	Mirab4
stopband energy (J)	0.0224	0.0114	0.0026	0.0036

filter has the minimum stopband energy and SRRC4 has the maximum one. However,

the comparison of Rossi4 vs. Mirab4 also shows that the difference of stopband energy between Rossi4 and Mirab4 is not very significant.

Moreover, if we reduce the roll-off factor of NPR prototype Rossi filter to 0.5, the resulting optimization of the Rossi method does not work properly (i.e., the stopband energy is not being minimized: stopband energy of Rossi4$_{\rho=0.5}$ is 0.2441 (J)), which can be explained according to the nature dependency of filter order $\hat{D}$ on transition band size Δf [130] as

$$\hat{D} = \begin{cases} \frac{-20\log_{10}\sqrt{\delta_1\delta_2}-13}{14.6\Delta f} & \text{(Kaiser's formula)} \\ \frac{2\log_{10}\left(\frac{1}{10\delta_1\delta_2}\right)}{3\Delta f} & \text{(Bellanger's formula),} \end{cases} \tag{6.48}$$

where δ_1 and δ_2 are the peak ripples in passband and stopband, respectively. Therefore, a reduction of transition band in NPR Rossi filter design naturally demands higher filter order, i.e. in order to design a proper Rossi filter with roll-off 0.5, we need to further increase the filter length. Furthermore, we find that the transition band of Mirab filter is approximately equivalent to that of FS filter with roll-off 1. The resulting performances are shown in Fig. 6.19, where we can find that both Mirab and Rossi ($\rho = 1$) prototype filters are outperforming FS1 ($\rho = 1$) prototype filter but they do not address a significant gain, i.e., less than 0.05 dB. Between Mirab and Rossi ($\rho = 1$) prototype filters, Mirab yields a relatively better performance (around 0.03 dB gain). We find, but not shown in this figure, that Rossi ($\rho = 0.5$) prototype filter does not work properly unless we increase the prototype filter length for this roll-off factor case.

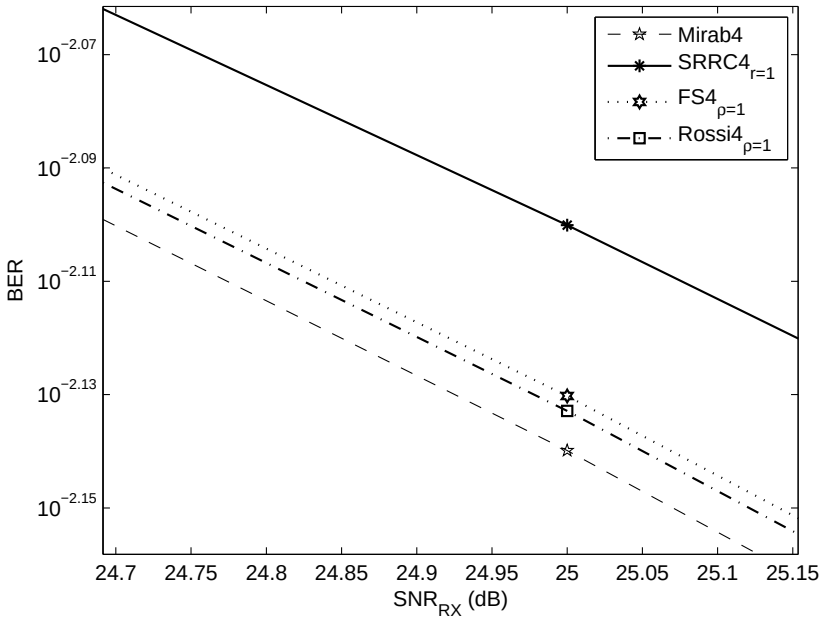

Figure 6.19: 64-QAM performance comparison: filter length $L_f = 4M$ with $M = 128$ (Ma's channel [87]).

To continue verifying the filter length effect, we now increase the filter length to

$L_f = 8M$. Now, we fix the roll-off factor to be 1 for FS, SRRC and Rossi filters. The corresponding frequency representations of above filters are given in Fig. 6.20. Although Mirab filter gives a faster fall-off rate, it might not give the best performance in terms of BER due to its first sidelobe attenuation that is relatively higher than that of Rossi's filter. Since Rossi's method is optimum in the sense of stopband energy minimizing, it should result in a minimum ICI power. The stopband energy values for these filters are given in Tab. 6.2.

Table 6.2: Stopband energy ($L_f = 8M$ with $M = 128$)

	$\text{SRRC8}_{r=1}$	$\text{FS8}_{\rho=1}$	$\text{Rossi8}_{\rho=1}$	Mirab8
stopband energy (J)	0.0051	2.3608e-04	2.8601e-06	2.1452e-05

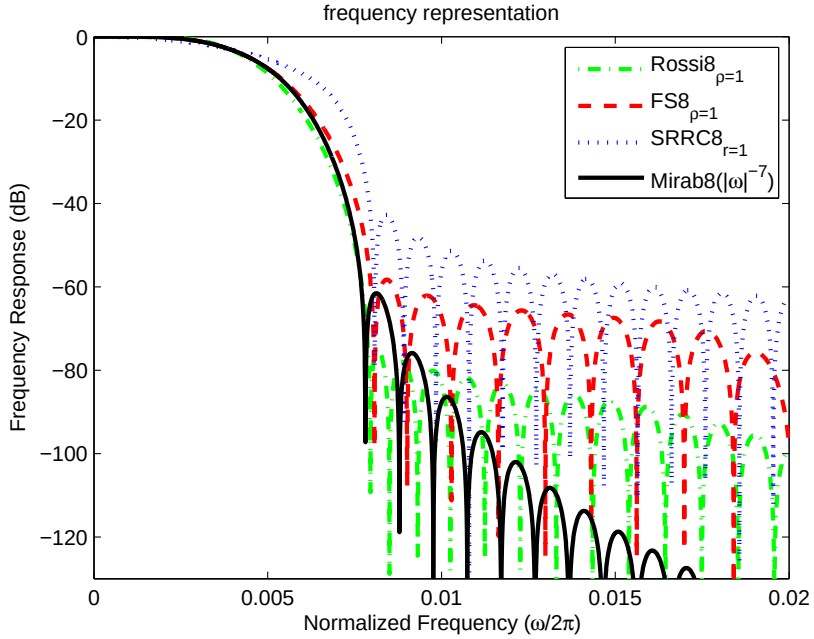

Figure 6.20: Frequency representation comparison for $L_f = 8M$ ($M = 128$).

In Fig. 6.21, we show the performance comparison, the results confirm our argument that Rossi's filter has a better performance than Mirab filter. Thus, stopband energy should be taken more cares than stopband fall-off rate. So far, we have discoursed that a good criterion of designing filter in PLC is to trade between orthogonality and stopband energy. However designing such filter requires a pretty high filter order to get a desired performance. As shown in our examples, Ross's filter begins to outperform the others when the filter length $L_f = 8M$. So, in the next section, we look at the complexity cost.

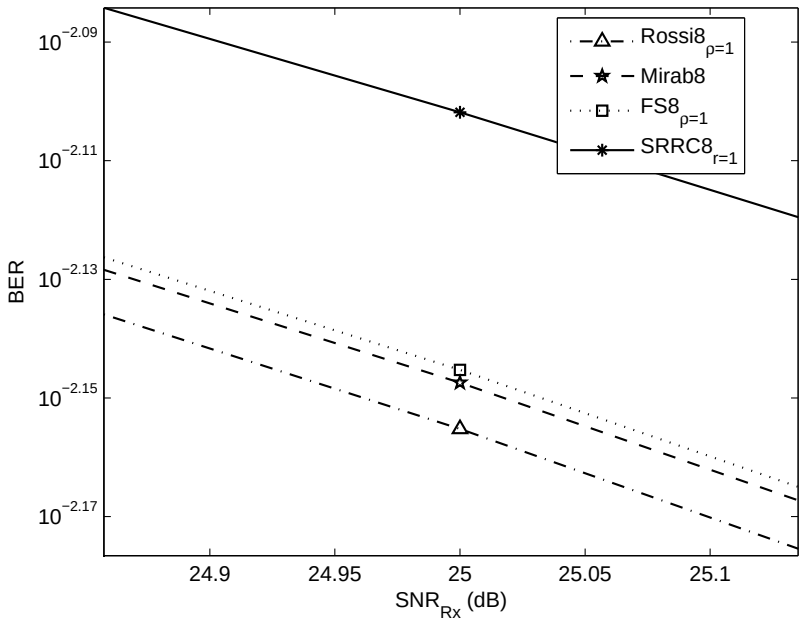

Figure 6.21: 64-QAM performance comparison: filter length $L_f = 8M$ with $M = 128$ (Ma's channel [87]).

6.3 Complexity Issue

Does it mean that if we constantly augment the filter length, we can have a perfect transmission performance? The answer is negative!

This is shown in Fig. 6.22, where we give an illustration with the performance comparison using Rossi prototype filter with different lengths (from $L_f = 4M$ up to $L_f = 10M$). Indeed, we remark that the performance amelioration tends to a saturation when the filter length goes beyond a certain threshold. It means that we have to pay a very high price of complexity and latency delay to get a very limited performance gain. Note that the filter length may not be realistic or practical since we will never use $L_f = 10M$ in applications. We, actually, just intend to give an example saying that always selecting a very long prototype filter, e.g. Rossi10, may be useless.

The latency value has been discussed in Sec. 6.2.1, for the filter with length $L_f = bM$ the latency is equal to $2b\tau_0 = bT_0$ time. As for the complexity, based on polyphase filtering idea [130] and [115], each subcarrier needs to implement a FIR filter with b coefficients which leads to b complex multiplications and $b-1$ complex additions. Note that the polyphase filtering needs to be proceeded twice, one in modulator and the other in demodulator. Thus, the overall complexity due to prototype filtering is $2 \times b \times M$ complex multiplications and $2 \times (b-1) \times M$ complex additions.

Now, a question that we need to ask ourselves is: Is it worth using a long prototype filter rather than a different equalizer? Inspired by this question, we will discuss in the subsequent chapter the alternative equalizers instead of ZF and their performance, complexities.

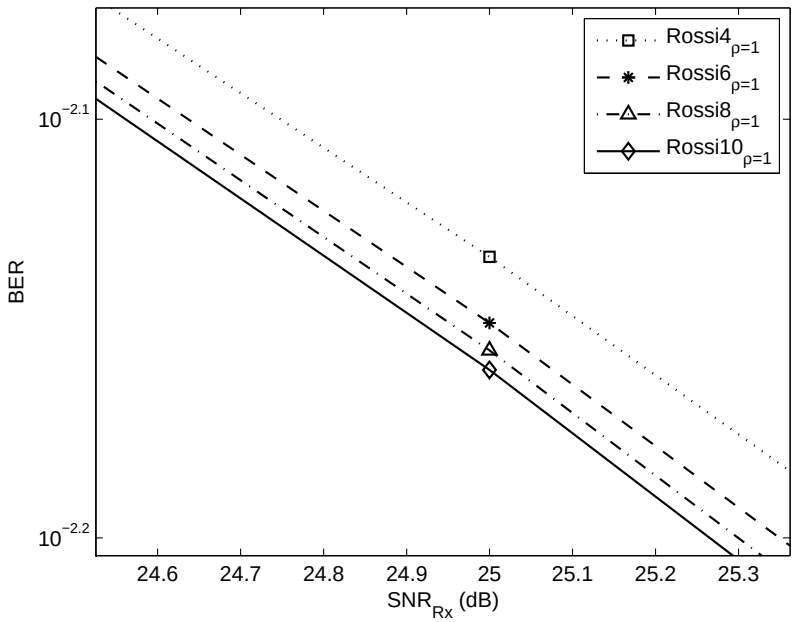

Figure 6.22: 64-QAM performance amelioration w.r.t. L_f for NPR Rossi filter ($\rho = 1$) (Ma's channel [87]).

6.4 Summary and Remarks

In this chapter, we gave the theoretical expressions, including ISI, ICI power calculation and SIR/SINR calculation, for OFDM/OQAM transmission over a general time-varying frequency selective channel model. Then, we focused ourselves in the PLC transmission, where three channel cases were considered, i.e. ideal channel, frequency non-selective channel and frequency selective channel. In the ideal channel or frequency non-selective channel cases, we remark that orthogonal filters should be utilized and truncated filters like IOTA or SRRC lead to a loss in orthogonality which perturbs their transmission performances. Nevertheless, this orthogonality loss can be compensated when we increase the truncation length. However, this way, we introduce a longer latency time at receiver. On the other hand, in the case of frequency selective channels, the ICI effect plays a more important role in transmission. Thus, more efforts would be put to design a filter that provides a good frequency localization level to eliminate the ICI effect. In this case, the NPR filter is preferred since it trades the orthogonality with a very good stopband attenuation. However, designing those filters usually requires pretty long length, which ultimately leads to a long latency time and higher complexity at both transmitter and receiver sides. Then, we further proved that it is unnecessary and useless to always pursue a very long NPR prototype filter, because it results in a very high complexity and long latency but only leads to a limited performance gain. Thus, the trade-off between performance and system complexity/latency should be well compromised for the choice of prototype filter. In the forthcoming chapter, we aim at investigating the different solutions for equalization beyond the simple one-tap ZF.

Chapter 7

OFDM/OQAM Channel Equalization

In the previous chapter, we have provided a theoretical analysis on OFDM/OQAM transmission over LTI frequency selective channel (e.g., PLC channel). The analysis gives us a very important viewpoint, i.e. ICI power in OFDM/OQAM transmission is more significant than ISI power. Furthermore, we showed that the interference power is directly linked with the prototype filter. Therefore, in order to get a satisfactory quality of service, the prototype filter design should be more focused on the filter stopband energy than on a strict orthogonality condition. Two examples of design methods were presented in the preceding chapter and the resulting designed filters of the presented methods gave better performances compared with the conventional PR or the truncated prototype filters. However, since the NPR filters[1] usually require very high filter order, and that way, it ultimately leads to a transceiver with high complexity and long latency. To overcome this drawback, we mentioned an alternative solution to long NPR filters. This solution is to retain a short PR filter (e.g. TFL1) and collaborate with some other equalizers that are normally more complex than a one-tap ZF.

This chapter continues discussing the OFDM/OQAM equalization solution and at the end of the previous chapter, we implicitly left an interesting question: whether shall we use long prototype NPR filter or more complex equalizer in PLC? The answer will be unveiled in this chapter. In the first part of this chapter, we introduce two OFDM/OQAM equalizers other than ZF. The first one is a linear equalizer (LE) called extended ASCET equalizer, which was originally introduced for Exponentially Modulated Filter Banks (EMFB) [69] and in this chapter we intend to adapt it to OFDM/OQAM system. Moreover, the theoretical performance of this LE will also be demonstrated for OFDM/OQAM transmission. The second one is a non-LE called Equalization with Interference Cancellation (EIC) method which is a decision-feedback-like equalizer. Since EIC equalizer is non

[1] In this chapter, when the term "NPR filter" appears, we only mean the prototype filter that is designed in the sense of optimizing the frequency selectivity subject to a nearly orthogonal condition.

linear, the theoretical performance is pretty hard to find. Instead, the efficiency of EIC equalizer will be evaluated by simulations. The second part of this chapter intends to give a comparison between these two transmission solutions (i.e. long NPR filter with one-tap ZF vs. short PR filter with a more complex equalizer), for PLC application, in terms of their performance, system complexity and latency value (here, we chose Rossi4 prototype filter as long NPR filter[2] and TFL1 prototype filter as short PR filter) Ultimately, the comparison results can give us a clear preference for one solution.

7.1 Modified ASCET Equalizer

Per-carrier equalizer for OFDM/OQAM system has already been discussed long time ago by Hirosaki in his papers [65, 66]. However, this method is way of complex and it is not easy to implement [65] due to its re-alignment of QAM in-phase and quadrature components. Later, Qin and Bellanger proposed an adaptive per-carrier equalization using double sampling and critical sampling, respectively [102]. Furthermore, Nedic *et al.*, in [91], also introduced an adaptive per-carrier equalizer for OFDM/OQAM. But its complexity still remains too high. Besides, some references (e.g. [126, 67, 134]) propose a Minimum-Mean-Square FIR per-carrier equalizer for OFDM/OQAM and the high complexity problem still exists due to the inversion of a non-diagonal channel matrix. Differently, in the following part, we consider using a low-complexity point-wise equalizer called Adaptive Sine modulated/Cosine modulated filter bank Equalizer for Transmultiplexer (ASCET).

7.1.1 Equalizer Algorithm

In [69], the authors presented a point-wise subcarrier FIR equalizer, termed ASCET, for EMFB. We intend to adapt it to serve for OFDM/OQAM system. The beauty of the point-wise equalizer is its low-complexity coefficients calculation. However, as we will see in the following, the derivation might be tricky if we do not pay attention to the phase term $\phi_{m,n}$ in Eq. (5.33). Following the notations in [69], the 3-tap ASCET equalizer at frequency index m writes $E_m^{\text{ASCET}}(z) = c_{0m}z + c_{1m} + c_{2m}z^{-1}$, where the equalizer coefficients c_{im} are calculated by evaluating the transfer function, which is set to the target response, at chosen frequency points, wherein half of the chosen frequencies are nothing else than the central carrier frequencies and the rest half can be chosen from the transition band, e.g. the simplest ones could be the middle frequency points between two consecutive subcarrier frequencies. Therefore, the ICI on the chosen frequencies can be perfectly compensated by this method. Knowing the principle, we now try to find the modified coefficients c_{im} for OFDM/OQAM.

In conventional ASCET case, since EMFB is odd-stacked modulation [69], the three chosen frequencies are, as shown in Fig. 7.1, ($\omega = \{0, \frac{\pi}{M}, \frac{2\pi}{M}\}$) for the 0-th subcarrier , and ($\omega = \{\frac{2\pi}{M}, \frac{3\pi}{M}, \frac{4\pi}{M}\}$) for the 1-st subcarrier (note that the middle chosen frequency is the m-th subcarrier frequency), which correspond to the normalized frequencies (down-sampling by $\frac{M}{2}$ at demodulator) ($\omega_{\text{nom}} = \{0, \pi/2, \pi\}$) and ($\omega_{\text{nom}} = \{-\pi, -\pi/2, 0\}$), respectively. Ultimately, thanks to the periodic feature, all of the even subcarriers have the same ω_{nom} values as the 0-th subcarrier and all of the odd subcarriers share the same ω_{nom} values as the

[2]We can also alternatively use Mirab4 filter as they have similar performance.

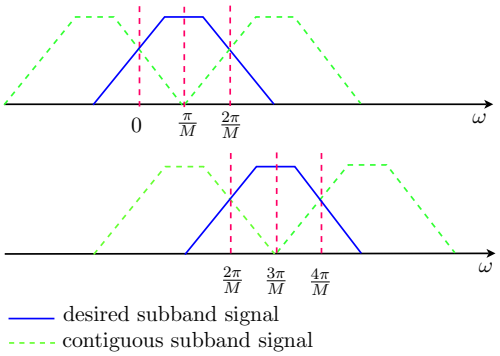

Figure 7.1: Subbands signal for EMFB-TMUX.

1-st subcarrier. Then, we have to line up three equations of $E_m^{\text{ASCET}}(z)$ taking $z = e^{j\omega_{\text{nom}}}$ and set the equations to the target responses. The target responses could be the compensation of the channel distortion at a chosen frequency reading $\eta_{im} = 1/H(e^{(2m+i)\pi/M})$ $(i = 0, 1, 2)$. Then we can get the final coefficients c_{im} for EMFB. The final coefficients expression of EMFB system can be found in [69].

Now switching to OFDM/OQAM modulation, the first modification is that OFDM/OQAM is an even-stacked modulation, i.e. the 0-th subcarrier centers at frequency 0. Therefore, the three frequencies are chosen to be, as shown in Fig. 7.2, $\omega = \{-\frac{\pi}{M}, 0, \frac{\pi}{M}\}$ for the 0-th subcarrier, and $\omega = \{\frac{\pi}{M}, \frac{2\pi}{M}, \frac{3\pi}{M}\}$ for the 1-st subcarrier, which correspond to the normalized frequencies $(\omega_{\text{nom}} = \{-\pi/2, 0, \pi/2\})$ for even subcarrier and $(\omega_{\text{nom}} = \{\pi/2, \pi, 3\pi/2\})$ for odd subcarrier. Straightforwardly, the target responses should also be shifted to be even-stacked as $\eta_{im} = 1/H(e^{(2m+i)\pi/M})$ $(i = -1, 0, 1)$.

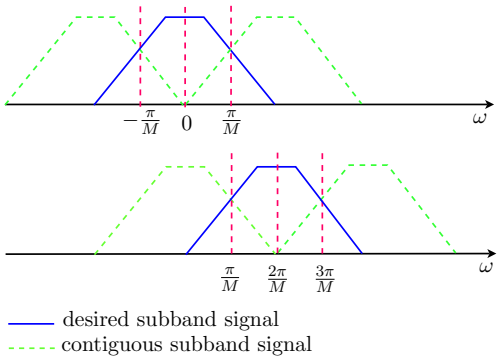

Figure 7.2: Subbands signal for OFDM/OQAM.

Now we should highlight that if we stop at this step and line up the equations to the target responses, the resulting equalizer coefficients cannot provide a desired performance. The trick is caused by the phase term of OFDM/OQAM. Since this phase term is a particular case in OFDM/OQAM, this phase effect is not easy to be viewed for the people who work on other schemes. The conclusion is that if the phase is expressed as $\phi_{m,n} = \frac{\pi}{2}(m + n)$ [52], then the above normalized frequencies should be again shifted by $-\frac{\pi}{2}$ (i.e.,$(\omega_{\text{nom}} = \{-\pi, -\pi/2, 0\})$) for even subcarrier and shifted by $\frac{\pi}{2}$ for odd subcarrier (i.e., $(\omega_{\text{nom}} = \{\pi, 3\pi/2, 2\pi\})$). Or, if $\phi_{m,n} = \frac{\pi}{2}(m+n) - \pi mn$ [115], it leads to a frequency shift

factor by $-\frac{\pi}{2}$ for each subcarrier. The proof is in below,

Proof If $\phi_{m,n} = \frac{\pi}{2}(m+n)$, recalling Eq. (6.26) we have

$$y_{m,n-\gamma} = c_m[n]e^{-j\left(\frac{\pi}{2}(n-\gamma)+\pi m(n-\gamma)\right)} \quad \text{with} \quad c_m[n] = \sum_{k=-\infty}^{+\infty} g[k]e^{j\frac{2\pi}{M}(k-\frac{D+N}{2})}s[nN-k-\beta]. \tag{7.1}$$

This corresponds to a frequency shift in frequency domain as

$$\sum_{n=-\infty}^{+\infty} c_m[n]e^{-j\left(\frac{\pi}{2}(n-\gamma)+\pi m(n-\gamma)\right)}e^{j\omega n} = \sum_{n=-\infty}^{+\infty} c_m[n]e^{j\left(\frac{\pi}{2}+\pi m\right)\gamma}e^{j\left(\omega-\frac{\pi}{2}-\pi m\right)n}.$$

Therefore, the frequency shift factor leads to $-\frac{\pi}{2}$ for the even subcarrier and $\frac{\pi}{2}$ for the odd subcarrier.

However, if $\phi_{m,n} = \frac{\pi}{2}(m+n) - \pi mn$, we have $y_{m,n-\gamma} = c_m[n]e^{-j\frac{\pi}{2}(n-\gamma)}$ which leads to a frequency shift by $-\frac{\pi}{2}$ in the transform domain for each subcarrier such as

$$\sum_{n=-\infty}^{+\infty} c_m[n]e^{-j\frac{\pi}{2}(n-\gamma)}e^{j\omega n} = \sum_{n=-\infty}^{+\infty} c_m[n]e^{j\frac{\pi}{2}\gamma}e^{j(\omega-\frac{\pi}{2})n}. \tag{7.2}$$

Ultimately, we get the modified ASCET equalizer coefficients for OFDM/OQAM as

$$\phi_{m,n} \text{ in [52]} \begin{cases} c_{0m} = -\frac{1}{2}\left(\frac{\eta_{-1m}-\eta_{1m}}{2} - j\left(\eta_{0m} - \frac{\eta_{-1m}+\eta_{1m}}{2}\right)\right) \\ c_{1m} = \frac{\eta_{-1m}+\eta_{1m}}{2} \\ c_{2m} = -\frac{1}{2}\left(\frac{\eta_{-1m}-\eta_{1m}}{2} + j\left(\eta_{0m} - \frac{\eta_{-1m}+\eta_{1m}}{2}\right)\right) \end{cases} \tag{7.3}$$

and

$$\phi_{m,n} \text{ in [115]} \begin{cases} c_{0m} = \mp\frac{1}{2}\left(\frac{\eta_{-1m}-\eta_{1m}}{2} - j\left(\eta_{0m} - \frac{\eta_{-1m}+\eta_{1m}}{2}\right)\right) \\ c_{1m} = \frac{\eta_{-1m}+\eta_{1m}}{2} \\ c_{2m} = \mp\frac{1}{2}\left(\frac{\eta_{-1m}-\eta_{1m}}{2} + j\left(\eta_{0m} - \frac{\eta_{-1m}+\eta_{1m}}{2}\right)\right) \end{cases} \tag{7.4}$$

where, in (7.4), - signs for even subcarrier and + signs for odd subcarrier. In the rest of this thesis, we simply call modified ASCET equalizer as ASCET.

7.1.2 Analytical Performance of OFDM/OQAM using ASCET

In what follows, we aim at finding the theoretical calculation of ISI+ICI for OFDM/OQAM using ASCET equalizer. The equalized symbols after the 3-tap ASCET equalizer read

$$\underbrace{\text{Re}\{\mathbf{e}_{m_0}^T\mathbf{y}_{m_0,n_0}\}}_{\hat{a}'_{m_0,n_0}} = \underbrace{\text{Re}\{\alpha_{m_0}\mathbf{e}_{m_0}^T\mathbf{a}_{m_0,n_0}\}}_{a'_{m_0,n_0}} + \underbrace{\text{Re}\{\mathbf{e}_{m_0}^T\mathbf{J}_{m_0,n_0}\}}_{I_{m_0,n_0}} + \underbrace{\text{Re}\{\mathbf{e}_{m_0}^T\mathbf{b}_{m_0,n_0}\}}_{v_{m_0,n_0}}, \tag{7.5}$$

with

$$\begin{aligned} &\mathbf{e}_{m_0} = [e_{0m_0}, e_{1m_0}, e_{2m_0}]^T, && \mathbf{y}_{m_0,n_0} = [y_{m_0,n_0}, y_{m_0,n_0-1}, y_{m_0,n_0-2}]^T, \\ &\mathbf{a}_{m_0,n_0} = [a_{m_0,n_0}, a_{m_0,n_0-1}, a_{m_0,n_0-2}]^T, && \mathbf{J}_{m_0,n_0} = [J_{m_0,n_0}, J_{m_0,n_0-1}, J_{m_0,n_0-2}]^T, \\ &\mathbf{b}_{m_0,n_0} = [b_{m_0,n_0}, b_{m_0,n_0-1}, b_{m_0,n_0-2}]^T. \end{aligned}$$

After combining $\hat{c}_{m_0,n_0} = \hat{a}'_{m_0,2n_0} + j\hat{a}'_{m_0,2n_0+1}$, we have

$$\hat{c}_{m_0,n_0} = \underbrace{a'_{m_0,2n_0} + ja'_{m_0,2n_0+1}}_{\tilde{a}_{m_0,n_0}} + \underbrace{I_{m_0,2n_0} + jI_{m_0,2n_0+1}}_{\tilde{I}_{m_0,n_0}} + \underbrace{v_{m_0,2n_0} + jv_{m_0,2n_0+1}}_{\tilde{v}_{m_0,n_0}}. \quad (7.6)$$

Since our equalizer is no longer one-tap, then, after equalization, the useful symbol and interferences are mixed up. The exact interferences not only come from $\tilde{I}_{m_0,n_0}$ but also from $\tilde{a}_{m_0,n_0}$. To calculate the interferences power, we first focus on the real part of $\hat{c}_{m_0,n_0}$ (i.e. $\hat{a}'_{m_0,2n_0}$). The same process can be re-applied to the imaginary part later on.

Let us first express $a'_{m_0,2n_0}$ as

$$\begin{aligned} a'_{m_0,2n_0} &= \mathrm{Re}\{\sum_{l=0}^{L_e-1} e_{lm_0}\alpha_{m_0}a_{m_0,2n_0-l}\} \\ &= \sum_{l=0}^{L_e-1} \underbrace{a_{m_0,2n_0-l}}_{a_{0,-l}} \underbrace{\mathrm{Re}\{e_{lm_0}\alpha_{m_0}\}}_{\tilde{e}_{l,m_0}}, \end{aligned} \quad (7.7)$$

where L_e denotes the number of equalizer coefficients (for 3-tap ASCET, $L_e = 3$). So the partial interferences can be separated from $a'_{m_0,2n_0}$ by removing the useful symbol part yielding

$$a'_{m_0,2n_0} - a_{m_0,2n_0-1}\tilde{e}_{1,m_0} = \sum_{\substack{l=0 \\ l\neq 1}}^{L_e-1} a_{0,-l}\tilde{e}_{l,m_0}, \quad (7.8)$$

where $a_{m_0,2n_0-1}$ is now the target symbol due to the delay operation introduced for causality sake (i.e. $z^{-1}E_{\cdot}(z)$).

The $I_{m_0,2n_0}$ term can be expressed as

$$\begin{aligned} I_{m_0,2n_0} &= \mathrm{Re}\{\sum_{l=0}^{L_e-1} e_{lm_0}J_{m_0,2n_0-l}\} \\ &= \mathrm{Re}\left\{\sum_{l=0}^{L_e-1} e_{lm_0} \sum_{p^0,q^0} a_{p,q-l}(-1)^{lp} \underbrace{e^{j\frac{\pi}{2}(p+q+pq)}H_{m_0}^{(p,q)}}_{D_{p,q}}\right\} \\ &= \sum_{l=0}^{L_e-1}\sum_{p^0,q^0} a_{p,q-l}(-1)^{lp} \underbrace{\mathrm{Re}\{e_{lm_0}D_{p,q}\}}_{A_{l,m_0}^{p,q}}, \end{aligned} \quad (7.9)$$

where $\sum_{p^0,q^0}$ means $\sum_{(p,q)\neq(0,0)}$. It is seen that (7.9) includes both the useful symbol and interferences combinations. The resulting interferences can be calculated by abstracting the useful symbol parts as

$$I_{m_0,2n_0} - \sum_{\substack{l=0 \\ l\neq 1}}^{L_e-1} a_{0,-1}A_{l,m_0}^{0,l-1}. \quad (7.10)$$

Thus, the exact overall interferences result in

$$I_{m_0,2n_0}^{\text{exact}} = \underbrace{\sum_{\substack{l=0\\l\neq 1}}^{L_e-1} a_{0,-l}\tilde{e}_{l,m_0}}_{\kappa_1} + \underbrace{I_{m_0,2n_0}}_{\kappa_2} - \underbrace{\sum_{\substack{l'=0\\l'\neq 1}}^{L_e-1} a_{0,-1}A_{l,m_0}^{0,l'-1}}_{\kappa_3}. \tag{7.11}$$

Since $I_{m_0,2n_0}^{\text{exact}}$ is zero mean, the ISI+ICI power after ASCET equalizer yields

$$\begin{aligned}\text{Var}[I_{m_0,2n_0}^{\text{exact}}] &= \text{Var}[\kappa_1] + \text{Var}[\kappa_2] + \text{Var}[\kappa_3] \\ &+ 2\text{Cov}[\kappa_1,\kappa_2] - 2\text{Cov}[\kappa_1,\kappa_3] \\ &- 2\text{Cov}[\kappa_2,\kappa_3],\end{aligned} \tag{7.12}$$

where Cov[·] denotes covariance. After the calculations in Appendix 10.3, the expression of each term on the right side of (7.12) leads respectively to:

The first variance term $\text{Var}[\kappa_1]$ is written as

$$\text{Var}[\kappa_1] = \sigma_a^2 \sum_{\substack{l=0\\l\neq 1}}^{L_e-1} |\tilde{e}_{l,m_0}|^2. \tag{7.13}$$

The second variance term $\text{Var}[\kappa_2]$ is given by

$$\text{Var}[\kappa_2] = \sigma_a^2 \sum_{l=0}^{L_e-1}\sum_{l'=0}^{L_e-1}\sum_{p^0,q^0} (-1)^{(l+l')p} A_{l,m_0}^{p,q} A_{l',m_0}^{p,q-l+l'} \bar{\delta}_{(\{p,0\}\{q,l-l'\})}, \tag{7.14}$$

where $\bar{\delta}_{(\{p,0\}\{q,l-l'\})}$ is the anti-delta function defined as

$$\bar{\delta}_{(\{p,0\}\{q,l-l'\})} = \begin{cases} 0 & \text{if } p=0 \text{ and } l-l'=q \\ 1 & \text{otherwise.}\end{cases}$$

The third variance term $\text{Var}[\kappa_3]$ is given by

$$\text{Var}[\kappa_3] = \sigma_a^2 \sum_{\substack{l=0\\l\neq 1}}^{L_e-1}\sum_{\substack{l'=0\\l'\neq 1}}^{L_e-1} A_{l,m_0}^{0,l-1} A_{l',m_0}^{0,l'-1}. \tag{7.15}$$

The fourth covariance term $\text{Cov}[\kappa_1,\kappa_2]$ is given by

$$\text{Cov}[\kappa_1,\kappa_2] = \sigma_a^2 \sum_{\substack{l=0\\l\neq 1}}^{L_e-1}\sum_{l'=0}^{L_e-1} \tilde{e}_{l,m_0} A_{l',m_0}^{0,l'-l} \tilde{\bar{\delta}}_{\{l',l\}}. \tag{7.16}$$

where $\tilde{\bar{\delta}}_{\{l',l\}}$ is given by

$$\tilde{\bar{\delta}}_{\{l',l\}} = \begin{cases} 0 & \text{if } l'=l \\ 1 & \text{otherwise.}\end{cases}$$

The fifth covariance term $\mathrm{Cov}[\kappa_1, \kappa_3]$ is such as

$$\mathrm{Cov}[\kappa_1, \kappa_3] = 0, \tag{7.17}$$

and the last covariance term $\mathrm{Cov}[\kappa_2, \kappa_3]$ is given by

$$\mathrm{Cov}[\kappa_2, \kappa_3] = \sigma_a^2 \sum_{\substack{l=0 \\ l\neq 1}}^{L_e-1} \sum_{\substack{l'=0 \\ l'\neq 1}}^{L_e-1} A_{l,m_0}^{0,l-1} A_{l',m_0}^{0,l'-1}. \tag{7.18}$$

Substituting (7.13-7.18) into (7.12), we get the interferences power of the exact interferences. Next, we take the same calculation for the imaginary part, i.e. $j\hat{a}'_{m_0,2n_0+1}$. Finally, it leads to the ISI+ICI power

$$P_{\text{ISI+ICI}}^{\text{OQAM-ASCET}}(m_0) = 2\mathrm{Var}[I_{m_0,2n_0}^{\text{exact}}]. \tag{7.19}$$

Next, we calculate the noise power

$$\begin{aligned} v_{m_0,2n_0} &= \mathrm{Re}\{\sum_{l=0}^{L_e-1} e_{lm_0} b_{m_0,2n_0-l}\} \\ &= \sum_{l=0}^{L_e-1} \left(e_{lm_0}^R b_{m_0,2n_0-l}^R + e_{lm_0}^I b_{m_0,2n_0-l}^I\right). \end{aligned}$$

Thus, the noise power can be expressed as

$$\mathrm{Var}[v_{m_0,2n_0}] = \sum_{l=0}^{L_e-1} |e_{lm_0}^R|^2 \mathrm{Var}[b_{m_0,2n_0-l}^R] + |e_{lm_0}^I|^2 \mathrm{Var}[b_{m_0,2n_0-l}^I] = \frac{\sigma_n^2}{2} \sum_{l=0}^{L_e-1} |e_{lm_0}|^2.$$

The same calculation is applied to $\mathrm{Var}[v_{m_0,2n_0+1}]$ and we find $\mathrm{Var}[v_{m_0,2n_0+1}] = \mathrm{Var}[v_{m_0,2n_0}]$. Therefore, the overall noise power yields

$$P_n^{\text{OQAM-ASCET}}(m_0) = \sigma_n^2 \sum_{l=0}^{L_e-1} |e_{lm_0}|^2. \tag{7.20}$$

Finally, the useful signal power is obtained by the summation of all the useful signal parts considering (7.8,7.10) as

$$P_s^{\text{OQAM-ASCET}}(m_0) = \sigma_a^2 \left| \tilde{e}_{1,m_0} + \sum_{\substack{l=0 \\ l\neq 1}}^{L_e-1} A_{l,m_0}^{0,l-1} \right|^2. \tag{7.21}$$

Straightforwardly, we can get the m_0-th subcarrier SINR expression as

$$\mathrm{SINR}_{m_0}^{\text{OQAM-ASCET}} = \frac{P_s^{\text{OQAM-ASCET}}(m_0)}{P_{\text{ISI+ICI}}^{\text{OQAM-ASCET}}(m_0) + P_n^{\text{OQAM-ASCET}}(m_0)}. \tag{7.22}$$

Therefore, we can get the theoretical performance of OFDM/OQAM system using 3-tap ASCET equalizer, i.e.

$$P_b^{\text{OQAM-ASCET}} = \frac{1}{M}\sum_{m_0=0}^{M-1} P_b^{\text{OQAM-ASCET}}(m_0). \tag{7.23}$$

with each subcarrier BER for the 2^{2K}-QAM constellations (Gray-coded), i.e.,

$$\begin{aligned} P_b^{\text{OQAM-ASCET}}(m_0) &\approx \frac{2^K-1}{2^K\cdot K}\text{erfc}\left(\sqrt{\frac{3}{2}\cdot\frac{\text{SINR}_{m_0}^{\text{OQAM-ASCET}}}{2^{2K}-1}}\right) \\ &+ \frac{2^K-2}{2^K\cdot K}\text{erfc}\left(3\sqrt{\frac{3}{2}\cdot\frac{\text{SINR}_{m_0}^{\text{OQAM-ASCET}}}{2^{2K}-1}}\right). \end{aligned} \tag{7.24}$$

To check the correctness of our derivation, we next compare the simulation performance with the theoretical one as shown in Fig. 7.3, where the channel model remains to be Zimmermann's model [87], $M = 128$, with OFDM/OQAM phase term being the case used in [115]. The results confirm our derivation for OFDM/OQAM using ASCET equalizer[3].

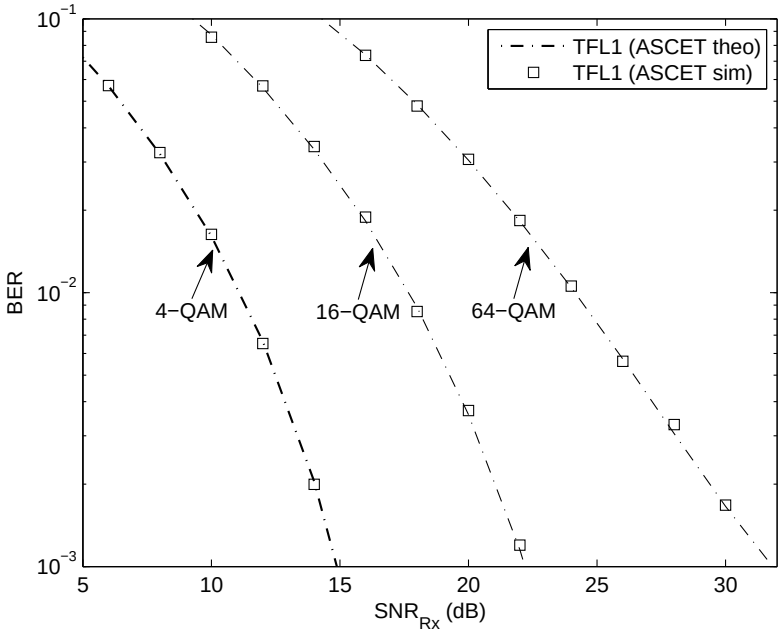

Figure 7.3: ASCET performance comparison: theory vs. simulation (Ma's channel [87]).

7.1.3 Complexity Discussion

Speaking of the complexity issue, the complexity of ASCET equalizer in OFDM/OQAM system is independent of the OFDM/OQAM phase term (i.e. the same for (7.3) and

[3]To prove the generality, we also tested ISI and ICI power over several realistic channels i.e. class 2 to class 9 of [121], and all of the results confirm that ICI power is higher than ISI power.

(7.4)) and it can be separated into periodic and online complexity, the former is due to the filter coefficients calculation and yields, at each subcarrier, 5 CM and 5 CA and 1 diagonal matrix inverse with size λ (DMI_λ). Note that the value of λ depends upon the applications (i.e. bandpass or baseband communications) and this periodic calculation is processed only once when the channel differs (For the transmission over nearly time-invariant channel, this calculation may not be launched very often). The latter complexity comes from the FIR filtering and yields, at each subcarrier, 3 CM and 2 CA. The overall complexity of ASCET equalizer depends upon the applications. For instance, in the case of baseband communications such as ADSL or PLC, the half of the carriers are the symmetrical version of the rest half ones and the first subcarrier is nulled (cf. Sec. 5.5). Therefore, the overall complexity yields: periodic: $5(\frac{M}{2}-1)$ CM and $5(\frac{M}{2}-1)$ CA and 1 DMI_M; online: $3(\frac{M}{2}-1)$ CM and $2(\frac{M}{2}-1)$ CA. On the other hand, for the bandpass communications like IEEE 802.11 or 3G LTE etc., the overall complexity yields: periodic: $5M$ CM and $5M$ CA; online: $3M$ CM and $2M$ CA and 1 DMI_{2M}.

7.2 Two-step EIC Equalizer

The second equalization method that we are about to present for OFDM/OQAM system is the so-called Equalization with Interference Cancellation (EIC). This method is inspired by the fact that since we have found the interference expression, why not approximate this interference and remove it directly.

7.2.1 Theoretical Algorithm

Revisiting Eq. (6.18), we know that the demodulated OFDM/OQAM symbol at the phase-space position (m_0, n_0) is composed of its distorted signal part and interference part. Thus, a well estimated symbol $\hat{a}_{m_0,n_0}$ should be distortion compensated and interference cancelled, i.e.

$$\hat{a}_{m_0,n_0} = \text{Re}\left\{ \frac{y_{m_0,n_0} - \hat{J}_{m_0,n_0}}{\sum_{l=0}^{L_h-1} c_l A_g[-l,0] e^{-j\frac{2\pi m_0 l}{M}}} \right\}. \tag{7.25}$$

The principle of EIC is pretty simple and straightforward. However, to make this idea work we need to approximate the interference term $\hat{J}_{m_0,n_0}$. Expressing interference in below

$$\hat{J}_{m_0,n_0} = \sum_{(p,q)\neq(0,0)} \hat{a}_{m_0+p,n_0+q} e^{j\frac{\pi}{2}(p+q+pq)} e^{j\pi p n_0} \sum_{l=0}^{L_h-1} c_l A_g[-qN-l, pF_0] e^{-j\frac{\pi(2m_0+p)l}{M}}, \tag{7.26}$$

we find that the approximation of interference requests the knowledge of the estimation of transmitted neighboring symbols $\hat{a}_{m_0+p,n_0+q}$. One way of realizing EIC idea is to introduce a two-step process. In the first step, a coarse equalization is carried out to get the estimation of the neighboring symbols $\hat{a}_{m_0+p,n_0+q}$ and this step can use a simple one-tap ZF equalizer. In the second step, a refined equalization is further carried out by applying (7.26,7.25). The general structure of EIC equalizer is given in Fig. 7.4. The

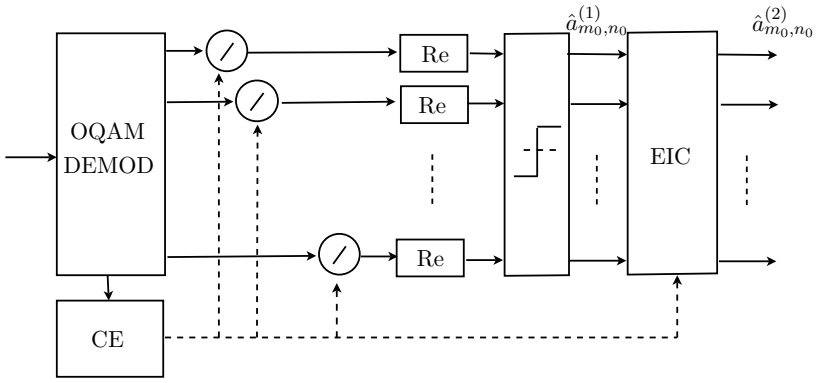

Figure 7.4: Receiver structure with EIC equalizer.

mathematical expressions of EIC equalizer are that in the first step

$$\hat{a}^{(1)}_{m_0,n_0} = \mathrm{HD}\left[\mathrm{Re}\left\{\frac{y_{m_0,n_0}}{H_{m_0}}\right\}\right], \tag{7.27}$$

where HD$[\cdot]$ denotes hard decision and H_{m_0} is the ZF coefficient which is based on the channel estimation[4]. In the second step

$$\hat{a}^{(2)}_{m_0,n_0} = \mathrm{Re}\left\{\frac{y_{m_0,n_0} - \hat{J}_{m_0,n_0}}{\sum_{l=0}^{L_h-1} c_l A_g[-l,0] e^{-j\frac{2\pi m_0 l}{M}}}\right\}. \tag{7.28}$$

However, a direct computation of (7.26) leads to a computational complexity of order M^2 for each time-frequency point (m_0, n_0) with M generally being a fairly large number. In the forthcoming subsection, we discuss the practical implementation of EIC equalizer and its final complexity.

7.2.2 Practical Implementation

In order to make a practical sense for the EIC equalizer, the implementation of EIC must be efficient. In this subsection, we introduce three facts that can significantly reduce the complexity.

- Firstly, with a time-frequency well-localized prototype filter, the summation in (7.26) can be limited to a small size neighborhood around (m_0, n_0).
- Secondly, $\hat{J}_{m_0,n_0}$ can be computed using FFTs and its complexity can be further reduced taking advantage of the symmetry property of the ambiguity function.
- Thirdly, since the channel delay spread is significantly less than T_0 (in discrete time, this means that the channel length, we denote by L_h, is only a fraction of M), then the computation complexity can be reduced with pruned FFT algorithms (cf. [88, 116]).

[4]For the moment, we still assume a perfect channel estimation at the receiver.

Let us illustrate this more in details for the first fact. We denote $\Omega^*_{\Delta m,\Delta n}$ as the target neighborhood zone, with $\Omega^*_{\Delta m,\Delta n} = \Omega_{\Delta m,\Delta n} - (0,0)$ and $\Omega_{\Delta m,\Delta n} = \{(m_0+p, n_0+q), |p| \leq \Delta m, |q| \leq \Delta n\}$. The main interference terms are due to the closest positions, i.e. $|p|$ and $|q|$ less or equal 1 termed as $\Omega^*_{1,1}$.

Next, taking into account the first fact where the interference is assumed to be limited only to $\Omega^*_{1,1}$, we continue discussing the second fact. The interference calculation can be written as

$$\hat{J}_{m_0,n_0} = \sum_{(p,q)\in\Omega^*_{1,1}} \hat{a}_{m_0+p,n_0+q} e^{j\frac{\pi}{2}(p+q+pq+2pn_0)} \underbrace{\sum_{l=0}^{L_h-1} c_l A_g[-qN-l, pF_0] e^{-j\frac{\pi(2m_0+p)l}{M}}}_{B_{m_0}[q,p]},$$

where the term $e^{j\frac{\pi}{2}(p+q+pq+2pn_0)}$ is nothing else than a sign changing operation of either real or imaginary part of $B_{m_0}[q,p]$ and this can be stored "off-line" in a look-up table. For the computation of $B_{m_0}[q,p]$, we note that this calculation can be carried out by FFTs, i.e. for a given m_0, when $p=0$, we have:

$$B_{m_0}[q,p=0] \;=\; \sum_{l=0}^{L_h-1} c_l A_g\left[-q\frac{M}{2}-l, 0\right] e^{-j\frac{2\pi m_0 l}{M}},$$

which can be obtained by a M-point FFT operation of $c_l A_g\left[-q\frac{M}{2}-k, 0\right]$ and for $|p|\neq 0$ we have

$$B_{m_0}[q,p] \;=\; \sum_{l=0}^{L_h-1} c_l A_g\left[-q\frac{M}{2}-l, pF_0\right] e^{-j\frac{2\pi(2m_0+p)l}{2M}},$$

which can be realized by a $2M$-point FFT operation of $c_l A_g\left[-q\frac{M}{2}-l, pF_0\right]$. Moreover, thanks to the symmetry property of the ambiguity function, i.e., $A_g(\tau,\mu) = A_g(\tau,-\mu)$, we find that $B_{m_0}[q,-p]$ is only a frequency shift version of $B_{m_0}[q,p]$. Therefore, as long as we calculated for $B_{m_0}[q,p]$, we can get directly $B_{m_0}[q,-p]$. Furthermore, it is worth mentioning that the calculation of $B_{m_0}[q,p]$ does not depend on time nor on the transmitted symbols, so it can be calculated only at preamble rate, i.e. at a slow rate, triggered by an updated channel estimation.

For the third fact, we assume that normally the channel delay spread length is much shorter than the OFDM/OQAM symbol duration, i.e. $L_h \ll M$ or $c_l = 0$ when $l > L_h - 1$. This actually is a very plausible assumption for PLC applications. Therefore, the above FFT operation can use pruned FFT algorithm which leads to a lower complexity (cf. [88]).

Speaking of the complexity, EIC also has two types of computation. One is the calculations that are triggered only once when the estimated channel coefficients are updated. So we keep the name of periodic complexity for this type of computation. The other one is the calculations that need to be carried out in each τ_0 data symbol period, we denote this one as online complexity. For calculating $\hat{J}_{m_0,n_0}$, part of the calculation is periodic, e.g. $B_{m_0}[q,p]$ and the rest of the calculation is online. In reference to Markel's algorithm [88], a M-point pruned FFT with input sequence of length L ($L < M$) needs $2M\log_2 L - 4L$ real multiplications (RM), and $3M\log_2 L + 2M - 4L$ real additions (RA). Furthermore, the complexity of EIC equalizer directly depends upon the first fact that how large the

neighborhood zone we choose. Let us define an integer κ for a neighborhood zone $\Omega^*_{\kappa,\kappa}$, the larger κ, the higher complexity we will have, but the better performance EIC will result in. In the rest of the thesis, we can shortly write κ-EIC as the EIC equalizer with interference approximation limited to $\Omega^*_{\kappa,\kappa}$.

The arithmetic complexity is summarized in below, with (1CM=4RM+2RA).

bandpass communications		
1st step	online	periodic
RM	$4M$	0
RA	$2M$	0
DMI(λ)	0	$1(M)$
2nd step	online	periodic
RM	$(16\kappa^2+16\kappa+4)M$	$(8\kappa^2+8\kappa+4)M\log_2 L_h - 4L_h$
RA	$(16\kappa^2+16\kappa+2)M$	$(4\kappa^2+4\kappa+2)(3M\log_2 L_h+2M)$ $-(2\kappa^2+3\kappa+3)2L_h$
DMI(λ)	0	$1(M)$

baseband communications		
1st step	online	periodic
RM	$2M-4$	0
RA	$M-2$	0
DMI(λ)	0	$1(M/2-1)$
2nd step	online	periodic
RM	$(4\kappa^2+4\kappa+1)(2M-4)$	$(8\kappa^2+8\kappa+4)M\log_2 L_h - 4L_h$
RA	$(8\kappa^2+8\kappa+1)(M-2)$	$(4\kappa^2+4\kappa+2)(3M\log_2 L_h+2M)$ $-(2\kappa^2+3\kappa+3)2L_h$
DMI(λ)	0	$1(M/2-1)$

7.3 Long NPR filter or Complex Equalizer in PLC?

So far, we have discoursed two OFDM/OQAM transmission solutions for PLC. The first one is to use a well designed NPR long prototype filter that has minimum stopband energy then apply a one-tap ZF equalizer at the receiver; the second one is to keep using a short PR prototype filter incorporating a more complex equalizer at the receiver (e.g., modified ASCET or κ-EIC). In this section, we intend to make a comparison between these two solutions. In our comparison, the phase $\phi_{m,n}$ of OFDM/OQAM system is fixed as in [115]. For the first solution, we choose Rossi filter of length $4M$ and roll-off factor $\rho = 1$ (Rossi4$_{\rho=1}$) as the NPR prototype filter. For the second solution, we choose TFL1 filter as the prototype filter and apply the modified 3-tap ASCET or 1-EIC equalizer at the receiver. The PLC channel model in our comparison remains the Ma's channel model [87] where the channel coefficients are that amplitude profile (in linear) : $0.2, 0.1, 0.02, 0.01$ and delay profile (μs) : $0, 0.4, 0.6, 0.7$. Other parameters in our simulation are: $M = 128$; sampling frequency 10 MHz; constellation: 64-QAM; the perfect channel estimation and synchronization are supposed at the receiver. For the other NPR filters discussed in Chap. 6, i.e. Mirab filter, since it has only tiny different performance from that of Rossi filter, in this section we only use Rossi filter in our comparisons.

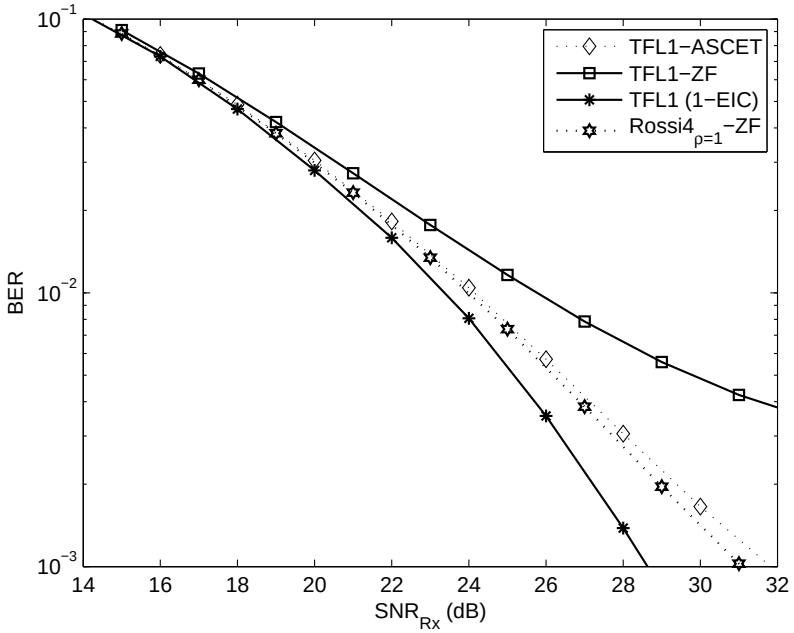

Figure 7.5: 64-QAM performance comparison (Ma's channel [87] and $M = 128$).

The results are depicted in Fig. 7.5, where we can clearly see that TFL1 prototype filter cannot provide a good performance using ZF equalizer especially compared with Rossi4$_{\rho=1}$ filter. Indeed, the smaller stopband energy of Rossi filter leads to a smaller interference. However, when we utilize ASCET equalizer instead of ZF for TFL1 filter, it ultimately results in the almost same performance as OFDM/OQAM system using Rossi4$_{\rho=1}$ filter with ZF equalizer at BER of 10^{-2}. Likewise, if we apply κ-EIC equalizer with $\kappa = 1$, we can finally get the best performance compared with the above two cases. Furthermore, as shown in Fig. 6.22, the performance gain of using longer Rossi filter than Rossi4 filter is fairly trivial. That means, it might not be worth considering always the long NPR filter as the proper solution. The complexity and latency comparison among Rossi4 filter with ZF equalizer, TFL1 filter with ASCET equalizer and TFL1 filter with κ-EIC is reported in Tab. 7.1, noting that, for Rossi4 filter, b stands for Rossi filter with length $L_f = bM$. The complexity is compared only in real operations i.e. RM and RA and it is shown in both expressions and numeric forms where we assume that 1CM=4RM+2RA and 1CA=2RA.

In the case of PLC, we care more about the complexity of the sum of polyphase complexity and online equalizer complexity. Therefore, TFL1-ASCET has the minimum complexity (even taking into account the periodic complexity) and shortest latency. Rossi4-ZF yields the maximum complexity and longest latency. Although, TFL1-EIC ($\kappa = 1$) is placed in between for online complexity, its periodic complexity is relatively the highest, thus, if the channel is varying, this periodic complexity might become important. It is worth mentioning that in our simulation we take the PLC scenario as an example which is a typical application of baseband communications. As we discussed in the former section, for baseband communications, per-carrier equalizer only concerns the half of the total carriers. So, in this case, using short prototype filter with ASCET or EIC equalizer might be

Table 7.1: Complexity and latency comparisons (for $M = 128$).

	TFL1-ASCET			Rossi4-ZF			TFL1-EIC ($\kappa = 1$)		
	Polyphase	Equalizer		Polyphase	Equalizer		Polyphase	Equalizer	
		online	periodic		online	periodic		online	periodic
RM	$8M$	$6M-6$	$10M-20$	$8bM$	$2M-4$	0	$8M$	$36(\frac{M}{2}-1)$ $+2M-4$	$20M\log_2 L_h$ $-4L_h$
RA	$4M$	$5M-7$	$10M-20$	$4M(2b-1)$	$M-2$	0	$4M$	$34(\frac{M}{2}-1)$ $+M-2$	$30M\log_2 L_h$ $+20M-16L_h$
DMI(λ)	0	0	$1(M)$	0	0	$1(\frac{M}{2}-1)$	0	0	$2(\frac{M}{2}-1)$
RM	1024	762	1260	4096	252	0	1024	2520	7648
RA	512	633	1260	3584	126	0	512	2268	13952
Latency	$2\tau_0$			$8\tau_0$			$(2+\kappa)\tau_0 = 3\tau_0$		

more interesting than using long prototype NPR filter with ZF equalizer. Furthermore, for PLC, most of the time the proposed channel models are static. Thus, the periodic complexity becomes less important. However, for bandpass communications, if the channel is not time-invariant, then the complexity comparison should take into account both online and periodic calculations. As to the latency, if the application requires high demand in latency such as voice service, the system should avoid using long prototype filters in order to make the latency as small as possible.

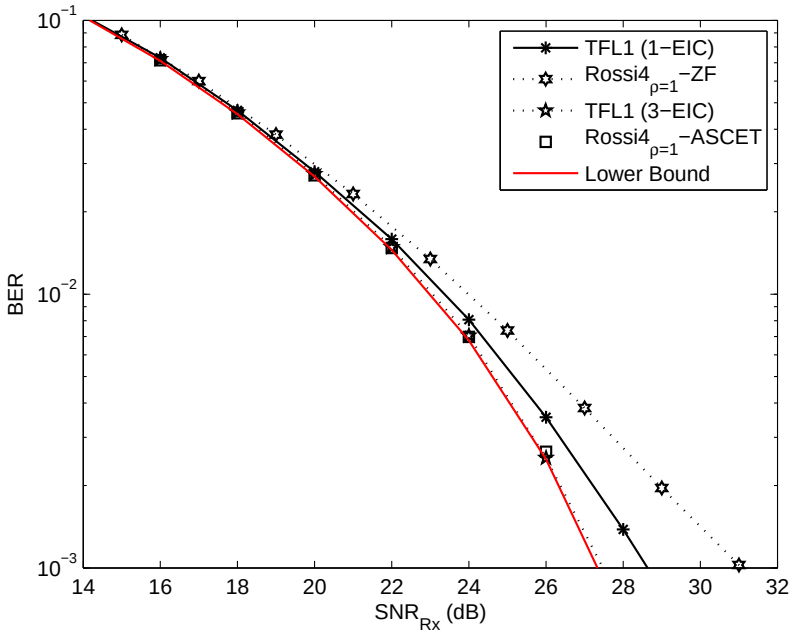

Figure 7.6: 64-QAM performance comparison (Ma's channel [87] and $M = 128$).

In the case that the receiver only cares about the performance, we can either increase the κ value of EIC equalizer for getting a better performance or to combine long NPR prototype filter with ASCET equalizer, for instance, in Fig. 7.6, we give an example of OFDM/OQAM using TFL1 with 3-EIC and Rossi4-ASCET. Moreover, we also give a performance lower bound which is calculated by Eqs. (7.23,7.24) replacing SINR by SNR,

i.e. assuming interference-free transmission. The result shows that either TFL1 with 4-EIC or Rossi4-ASCET can almost attain the lower bound. That means both way can totally remove the interference but, normally, at a price of an augmentation of complexity and latency.

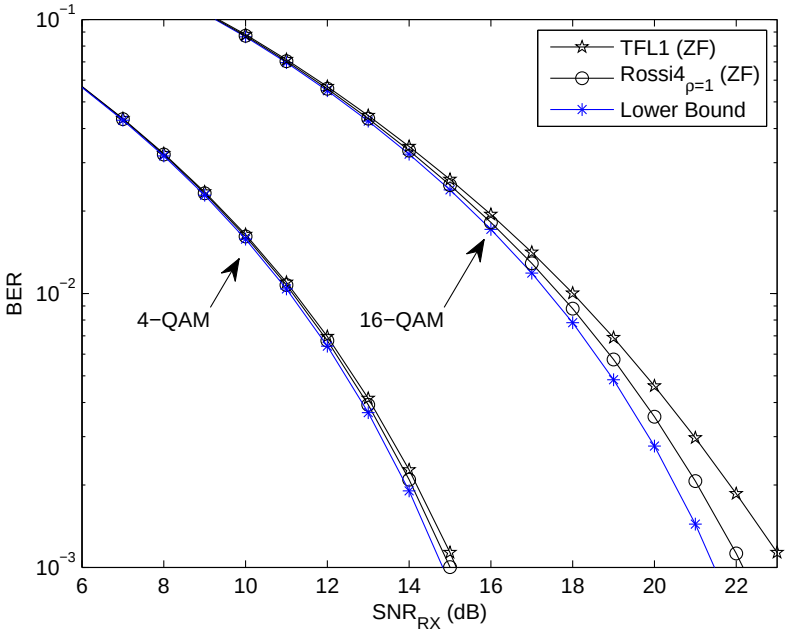

Figure 7.7: 4 and 16-QAM performance comparison (Ma's channel [87] and $M = 128$).

Last, we see the performances for lower constellations (e.g. 4-QAM and 16-QAM) in order to show whether we should consider using long NPR prototype filter or complex equalizer. As shown in Fig. 7.7, for small constellation such as 4-QAM, the use of TFL1-ZF does not make much difference between Rossi4-ZF and its performance is very close to the lower bound. So for the case of small constellation order transmission, we shall always use short PR filter (e.g. TFL1) and one-tap ZF is enough for the receiver. When the constellation is increased till 16-QAM, Rossi4-ZF has already outperformed TFL1-ZF, but the gain is not significant. Therefore, we can expect a quasi-similar performance between Rossi4-ZF and TFL1-ZF when channel coding is utilized. However, when the constellation order increases to 64-QAM or above, complex equalizers or longer NPR filters should be considered.

In the CP-OFDM transmission case, if the CP length is always longer than the CIR length, then the ISI and ICI can be perfectly avoided. Thus, the BER curve of CP-OFDM system attains the lower bound. However, in our simulations, the figures plot the results of BER versus SNR which do not take into account the spectral efficiency loss in CP-OFDM case. A fair comparison between CP-OFDM and OFDM/OQAM should consider this spectral loss, e.g. BER versus E_b/N_0 (the energy per useful bit to noise power spectral

density ratio) should be plotted using the following equation without channel coding, i.e.,

$$E_b/N_0 = 10\log_{10}\left(\frac{M+L_{\text{cp}}}{M}\frac{1}{2K}\right) + \text{SNR}, \tag{7.29}$$

where we assume the constellation with order 2^{2K}-QAM. It is worth mentioning that if the OFDM/OQAM BER curve attains the lower bound, for instance in Fig. 7.7 for 4-QAM case, then it can surely have a better performance than the CP-OFDM in the BER versus E_b/N_0 plot.

7.4 Conclusion and Remarks

In this chapter, we introduced two OFDM/OQAM equalization methods, i.e. modified ASCET and κ-EIC. Furthermore, we gave a theoretical performance analysis on OFDM/OQAM transmission using modified ASCET equalizer. This equalizer is pointwise based, therefore, it yields very low complexity for calculating the equalizer coefficients and can be practically implemented. On the other hand, κ-EIC idea is inspired by the derivation of interference calculation and it ultimately can be realized by a two-step equalizer. Its first step is a traditional one-tap ZF and its second step is an interference approximating-cancelling process. Comparing the performance of TFL1-ASCET with Rossi4-ZF, they have almost the same performance over Ma's PLC channel, but the former solution yields a lower complexity and shorter latency than the latter one. Comparing the performance of TFL1-EIC ($\kappa = 1$) with Rossi4-ZF or TFL1-ASCET, κ-EIC method has the best performance but its complexity is also the highest.

Chapter 8

Transmission Capacity and Flexibility in PLC

The flexibility is of great importance in modern communications. Multi-Carrier modulation is a very good example for one purpose of bit-loading, where the transmitted bit numbers of each useful carrier are flexible w.r.t. the transmission environment. Thus, eventually, it leads to a performance gain compared with non-bit-loading case and this gain is, actually, due to the flexibility. In this chapter, we show two types of flexibility gains that we could exploit in PLC. The first one is the flexibility of modulations. As the name indicates, this expected gain comes from combining the variant modulation schemes of PLC. Actually, every modulation scheme, no matter what DMT or HS-OQAM etc., has its own pros and cons. There does not exist a scheme that can win the others all the time. Therefore, if we can find a modulator that can possess all the advantages of the available schemes and meanwhile can get rid of all their shortcomings, then this modulator can finally be the best of the best. This chapter effectively addresses a unified MCM modulator and its implementation algorithm. Since this modulator can generate HS-OQAM, DMT and also WOFDM. Therefore, by a proper selection of the modulation scheme, the flexibility gain can be obtained. The second flexibility that we will talk about is the one over prototype filters for OFDM/OQAM system. This flexibility feature can very much serve for the channel estimation. We show that there exists a decisive factor for channel estimation in OFDM/OQAM system. Furthermore, this factor is very much dependent on the prototype filter. Therefore, a good channel estimation performance is related to finding a proper prototype filter that is designed subjected to this decisive factor.

8.1 Capacity Analysis From Theory to Practice

In this section, let us first discuss about the flexibility over modulation for PLC. The investigation of this aspect is inspired from the capacity analysis. Therefore, before directly going into the flexibility topic, we should show the capacity analysis for two individual

MCM in PLC (i.e., HS-OQAM and DMT). This analysis will help us to better understand this flexibility meaning.

8.1.1 Capacity Calculation for HS-OQAM and DMT

Let us start with OFDM/OQAM system (or HS-OQAM in PLC). The transmission capacity can be formulated as follows

$$R = F_0 \sum_{m=0}^{M_u-1} \log_2 \left(1 + \frac{\text{SINR}_m}{\Gamma}\right), \tag{8.1}$$

where SINR_m is the signal to interference plus noise ratio at m-th subcarrier; F_0 is the subcarrier spacing; Γ is the SNR gap that is used to measure how far a system is operating from the Shannon capacity and, in the case of no channel coding as well as ignoring other unpredictable channel impairments, it only depends on the target symbol error rate (SER), i.e., $\Gamma = \frac{1}{3}\left[\mathbf{Q}^{-1}(\frac{\text{SER}}{4})\right]^2$ [33, 59] for the no-coded case. M_u stands for the number of useful carriers.

From Eq. (8.1), we observe that the capacity is decided directly by the subcarrier SINR which is impacted by the equalization method. In order to find an analytical expression of capacity, we assume to use linear equalizers, i.e. ZF or ASCET. Recall in Chap. 6 and 7, the subcarrier SINR after ZF and ASCET equalizations can be expressed by Eqs. (6.43) and (7.22), respectively. Then, we can rewrite Eq. (8.1), w.r.t. different equalizers, as

$$R_{\text{OQAM-ZF}} = F_0 \sum_{m=0}^{M_u-1} \log_2 \left(1 + \frac{\text{SINR}_m^{\text{OQAM-ZF}}}{\Gamma}\right), \tag{8.2}$$

and

$$R_{\text{OQAM-ASCET}} = F_0 \sum_{m=0}^{M_u-1} \log_2 \left(1 + \frac{\text{SINR}_m^{\text{OQAM-ASCET}}}{\Gamma}\right), \tag{8.3}$$

where the SINR expressions can be found in Eqs. (6.43) and (7.22) and we highlight that these capacity expressions are independent of the OFDM/OQAM phase term.

For DMT system, we have discoursed, in Chap. 5, that for the transmission over time-invariant and frequency selective channels, if the CP length is longer than the maximum channel impulse response (CIR) length, then we can expect an interference-free transmission (i.e., ISI+ICI-free). In this case, the subcarrier SINR is equal to SNR. However, when the CP length is not sufficiently long enough, then the resulting interference (ISI+ICI) power can be expressed as [64]

$$N_{\text{ISI+ICI}}(m) = 2\sigma_c^2 \sum_{l=L_{\text{cp}}+1}^{L_h-1} \left| \sum_{i=l}^{L_h-1} c_i e^{-j\frac{2\pi}{M} im} \right|^2, \tag{8.4}$$

where σ_c^2 stands for the variance of complex-valued DMT entry symbols $c_{m,n}$; c is the CIR with length L_h; L_{cp} is the CP length; m is the subcarrier index ($m = 0, \cdots, M_u - 1$). Note that, this calculation is located at the output of the DMT demodulator. If we assume that

a one-tap ZF equalizer is utilized for DMT, then the power of ISI+ICI at the output of the equalizer yields

$$P_{\text{ISI+ICI}}(m) = \frac{N_{\text{ISI+ICI}}(m)}{|H_m|^2}, \tag{8.5}$$

where H_m is the channel coefficient at the m-th subcarrier. Based on Henkel's work [64], Golubović et al. showed that, for DMT, the maximum throughput happens when the CP length is smaller than the maximum CIR length [60]. This was restated later on in [124] and [92] independently. In other words, for a fixed throughput transmission, the DMT system with an optimally-length chosen CP offers the best performance in terms of the Bit Error Rate (BER). Finally, we can formulate the capacity expression for DMT system as

$$R_{\text{DMT}} = \frac{M}{M + L_{\text{cp}}} F_0 \sum_{m=0}^{M_u - 1} \log_2 \left(1 + \frac{\text{SINR}_m^{\text{DMT}}}{\Gamma}\right),$$

where the sub-carrier SINR expression can be approximated as [112, 92]

$$\text{SINR}_m^{\text{DMT}} \approx \frac{|H_m|^2 \sigma_c^2}{\sigma_n^2 + N_{\text{ISI+ICI}}(m)}.$$

8.1.2 Capacity Comparison HS-OQAM vs. DMT

Now, we aim to show the transmission capacity comparison between DMT and HS-OQAM versus the CP length, wherein, the prototype filter for HS-OQAM is Rossi4$_{\rho=1}$. Since HS-OQAM does not have CP, its capacity is plotted as a flat line. For the channel models, we chose the channel class 2,4,6,8 [121] in our comparisons. The number of carriers is 512. The target SER is fixed to 10^{-4} for this comparison. The sampling frequency is 30 MHz and we fix, for the moment, the received SNR (SNR_{Rx}) to 15 dB and the averaged capacity is obtained over 100 realizations.

Let us first compare DMT with HS-OQAM using one-tap ZF equalizer (HS-OQAM-ZF). The comparison result is depicted in Fig. 8.1, where the CIR length for the class 2,4,6,8 are (in samples) 54,40,26,7, respectively. The DMT capacity tendency versus CP length is consistent with the analysis in [60, 124, 92], i.e. the optimal capacity happens when the CP is smaller than the maximum CIR length. Moreover, the transmission over the larger PLC class number channel has a higher capacity. On the other hand, in the case of HS-OQAM-ZF vs. DMT, we find that the capacity of HS-OQAM-ZF is higher than the optimal DMT capacity for each class.

To find the explanation, let us take look at two cases, e.g. class 2 and 6, and check their $P_{\text{ISI+ICI}}$. The $P_{\text{ISI+ICI}}$, in channel class 2 case, is depicted in Fig. 8.2. We observe that the ISI+ICI power of DMT without CP (DMT-WO-CP in blue) is much higher than that of HS-OQAM-ZF (in red). We next see the case of HS-OQAM-ZF vs. DMT with optimal CP (DMT-OCP). Since the CP length is not sufficiently long for DMT to cancel all the ISI+ICI, therefore there still remains some interferences. Comparing to HS-OQAM-ZF, the $P_{\text{ISI+ICI}}$ for DMT-OCP is generally lower, but, the overall capacity for DMT-OCP is smaller than that of HS-OQAM-ZF. This is due to the spectral efficiency loss. Thus, we can reasonably deduce that if the $P_{\text{ISI+ICI}}$ of DMT-OCP is close to that of HS-OQAM-ZF, then HS-OQAM-ZF will further win DMT-OCP in terms of the throughput. In other

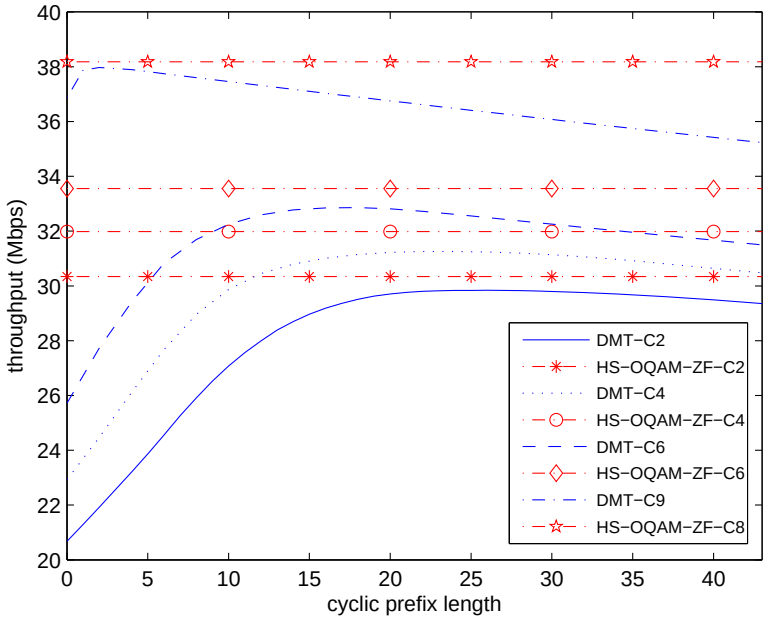

Figure 8.1: Capacity comparison with $M = 512$, $\mathrm{SNR}_{\mathrm{Rx}}$=15 dB.

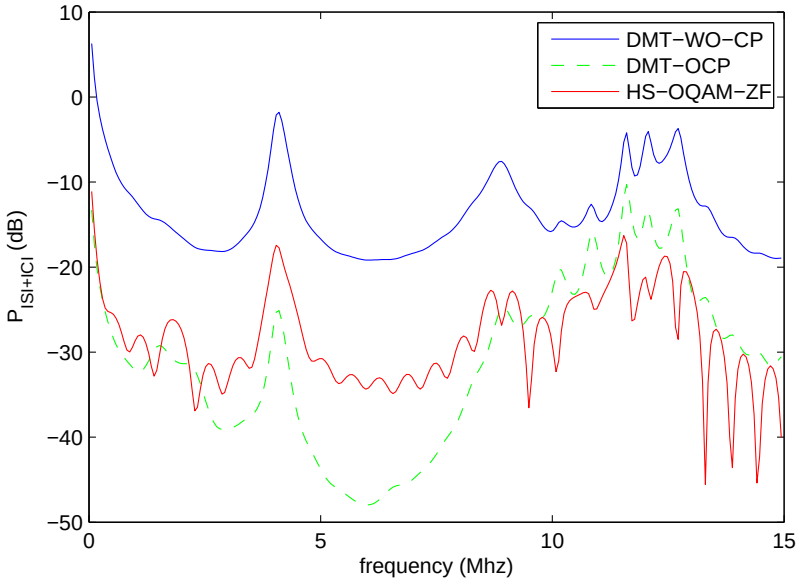

Figure 8.2: ISI+ICI power comparison for class 2 channel for $\mathrm{SNR}_{\mathrm{Rx}}$=15 dB.

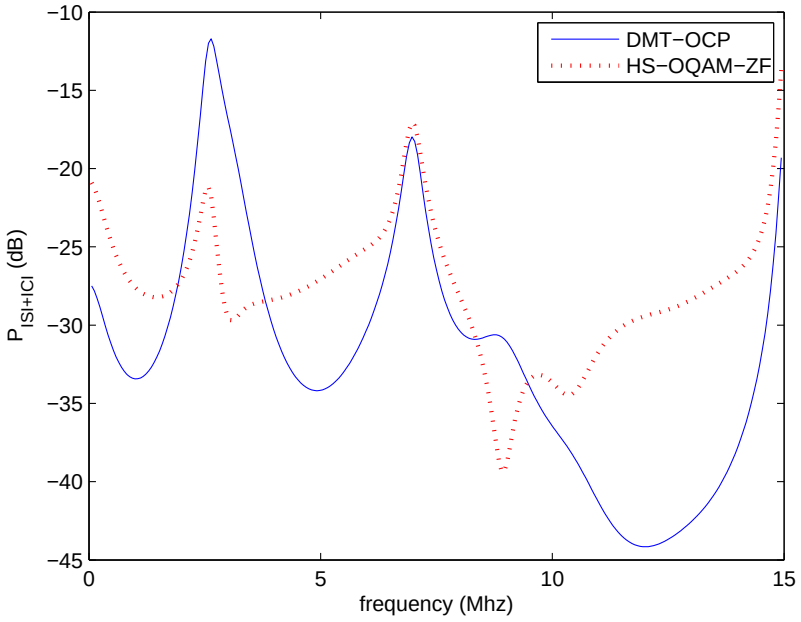

Figure 8.3: ISI+ICI power comparison for class 6 channel for SNR_{Rx}=15 dB.

words, for a fixed throughput transmission, HS-OQAM-ZF outperforms DMT-OCP in terms of the BER.

This inference can be verified by checking the capacity comparison of class 6 case in Fig. 8.1. We see that the capacity of HS-OQAM-ZF is higher than that of DMT-OCP, then it can be expected that the $P_{\text{ISI+ICI}}$ of HS-OQAM-ZF will be close to the one of DMT-OCP. The $P_{\text{ISI+ICI}}$ plot confirms our words (see, Fig. 8.3). Thus, it seems that the judgement on which one is better, between DMT and HS-OQAM for PLC, depends upon the $P_{\text{ISI+ICI}}$ competition. Furthermore, if we change the HS-OQAM system to use a 3-tap ASCET equalizer (HS-OQAM-ASCET), its $P_{\text{ISI+ICI}}$ is smaller than that of HS-OQAM-ZF and gets close to that of DMT-OCP as shown in Figs. 8.4 and 8.5. Naturally, this results in a capacity gain compared to DMT and HS-OQAM-ZF. Fig. 8.6. gives the capacity comparison among HS-OQAM-ZF, HS-OQAM-ASCET and DMT in the channel class 2 and 6 cases.

Next, we further investigate the SNR influence on the battle of DMT vs. HS-OQAM. Constellation order and SNR are closely connected. Indeed, increasing the constellation size requires increasing the SNR. Then, the overall capacity is surely augmented, but at the same time, the ISI+ICI becomes a more predominant term to limit the throughput comparing to the noise effect. Hence, for a given SER, the optimal CP length for DMT tends to the maximum channel delay spread in order to reduce the ISI+ICI. This argument can be proved by checking the capacity comparison in Fig. 8.7, where we changed the SNR_{Rx} from 15 dB to 25 dB, and kept the rest of the parameters unchanged. We observe that the overall capacities of both systems are increased. Furthermore, for DMT, the optimal CP length is moving towards the maximum channel length direction for each class case. Differently to the low SNR_{Rx} case, the capacity comparison shows that DMT-OCP

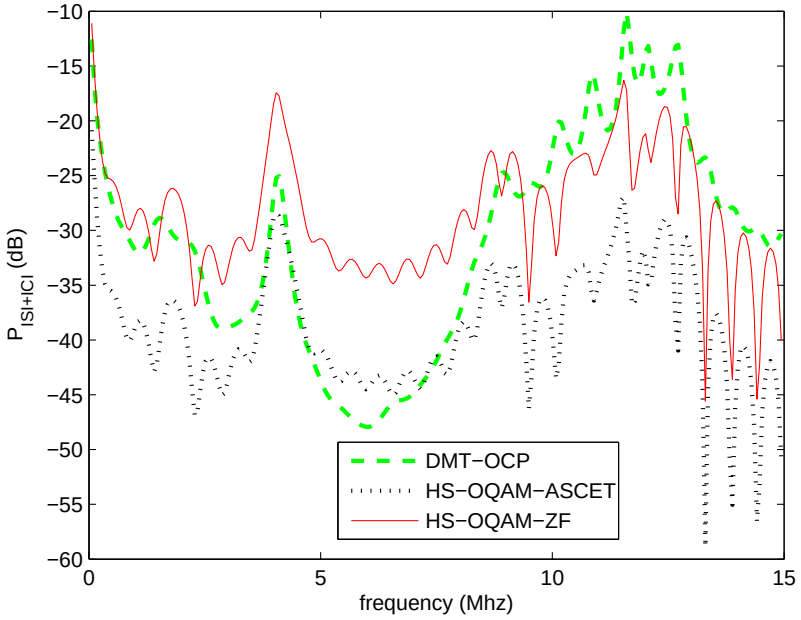

Figure 8.4: ISI+ICI power comparison for class 2 channel for SNR_{Rx}=15 dB.

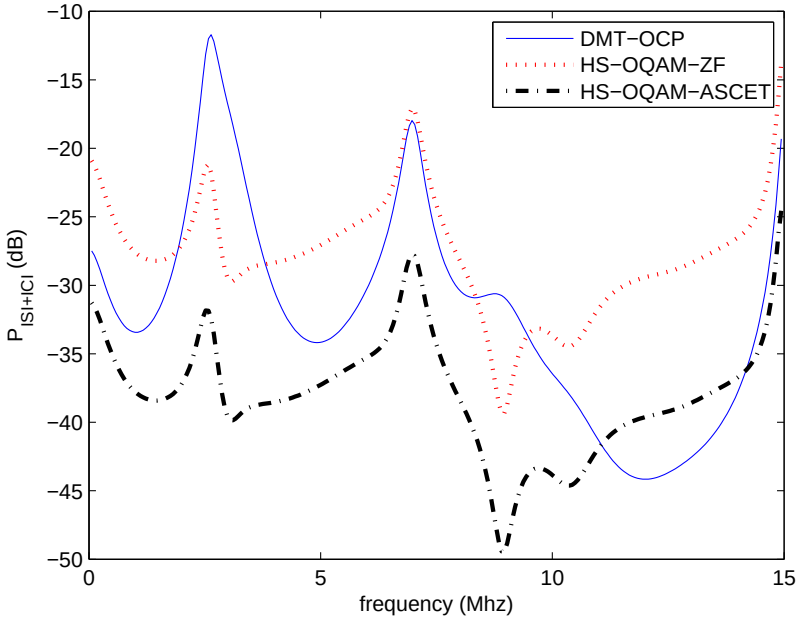

Figure 8.5: ISI+ICI power comparison for class 6 channel for SNR_{Rx}=15 dB.

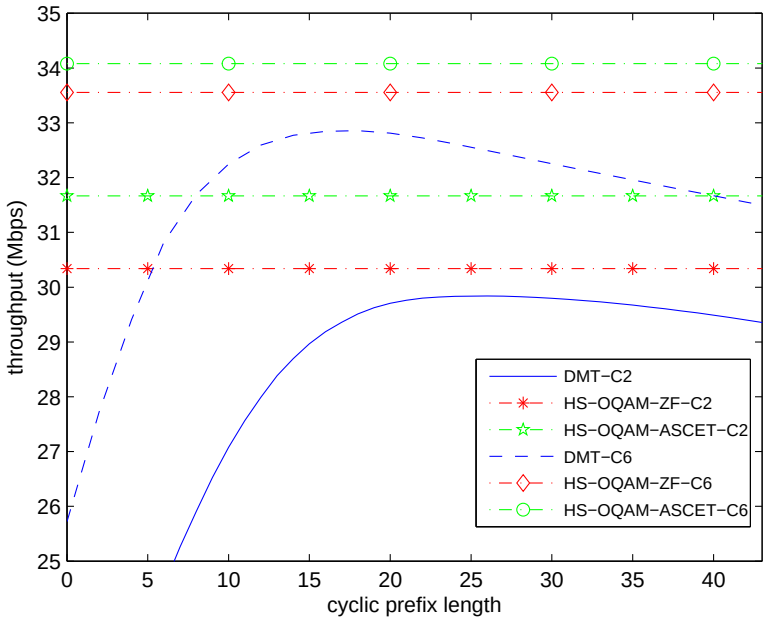

Figure 8.6: Capacity comparison with $M = 512$, $\mathrm{SNR}_{\mathrm{Rx}}$=15 dB.

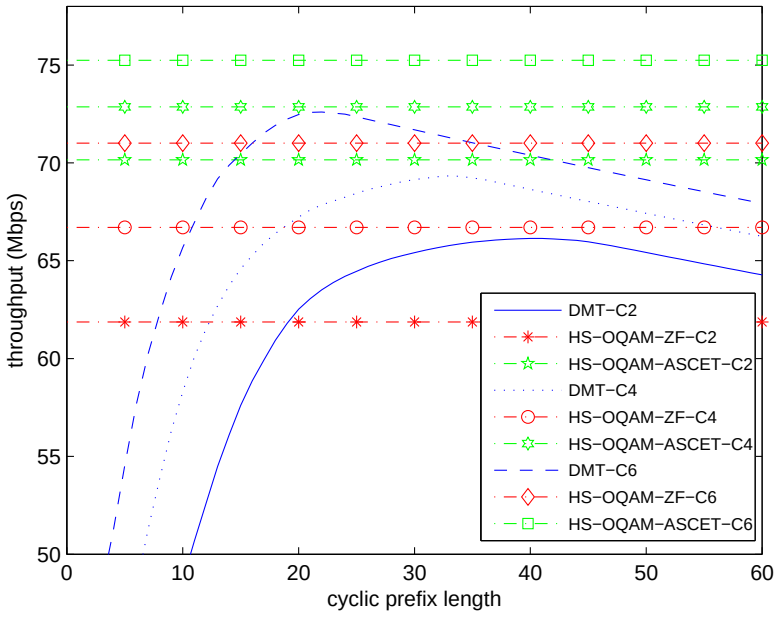

Figure 8.7: Capacity comparison with $M = 512$, $\mathrm{SNR}_{\mathrm{Rx}}$=25 dB.

wins against HS-OQAM-ZF. The explanation is as follows: Since the noise power becomes less important compared with interference power in high $\mathrm{SNR}_{\mathrm{Rx}}$ case, ISI+ICI becomes the main weakness to limit the capacity. Fortunately, as the optimal CP length for DMT increases for optimally controlling the ISI+ICI power, it results in an augmentation in throughput. However, HS-OQAM-ZF does not have CP and a one-tap ZF equalizer cannot efficiently control the ISI+ICI power anymore, which limits the capacity augmentation. Fig. 8.8 gives the evidence for our explanation, the $P_{\mathrm{ISI+ICI}}$ of DMT-OCP at 25 dB $\mathrm{SNR}_{\mathrm{Rx}}$ becomes much less than the one of HS-OQAM-ZF. That also means that if we want HS-OQAM to be the winner again, the $P_{\mathrm{ISI+ICI}}$ of HS-OQAM needs to be close to that of DMT-OCP in Fig. 8.8. Consequently, one-tap ZF equalizer cannot be qualified. For the solution, we expect to use a more powerful equalizer for HS-OQAM instead of one-tap ZF (e.g. 3-tap ASCET). The capacity comparison, in Fig. 8.7, shows that, for some channel classes, HS-OQAM-ASCET has a similar capacity as DMT-OCP for 25 dB $\mathrm{SNR}_{\mathrm{Rx}}$ case. However, it turns out that if we continue increasing $\mathrm{SNR}_{\mathrm{Rx}}$, the transmission capacity of DMT-OCP will exceed that of HS-OQAM-ASCET. Consequently, we shall use some more powerful equalizers.

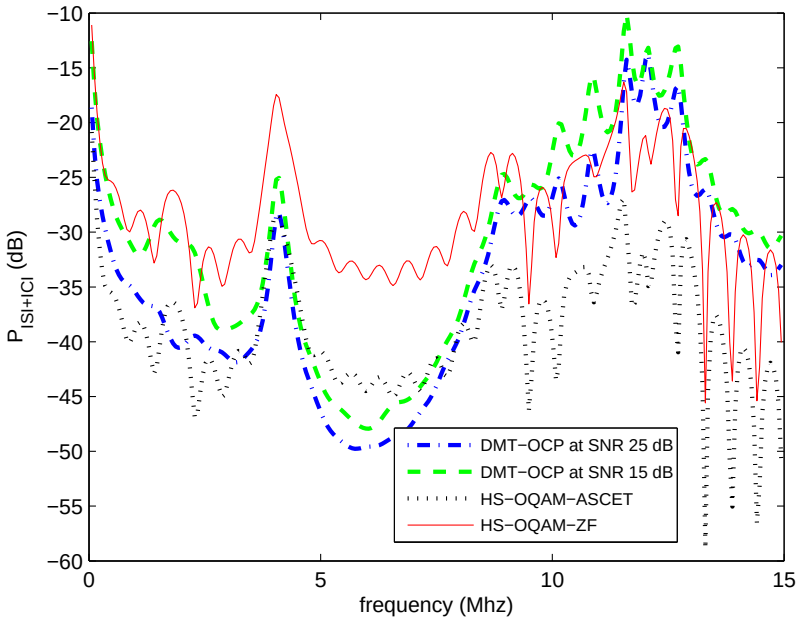

Figure 8.8: ISI+ICI power comparison for class 2 channel.

Previously, we said that the competition between HS-OQAM vs. DMT depends on their $P_{\mathrm{ISI+ICI}}$ competition. Now we further find that this competition is very much related to the given $\mathrm{SNR}_{\mathrm{Rx}}$. Thus, we can conclude that there exists a $\mathrm{SNR}_{\mathrm{Rx}}$ threshold for DMT-OCP vs. HS-OQAM using different equalizers. Below this $\mathrm{SNR}_{\mathrm{Rx}}$ threshold, HS-OQAM will win against DMT in terms of the capacity and beyond this threshold, DMT-OCP will be the winner. Fig. 8.9 clearly evaluates this $\mathrm{SNR}_{\mathrm{Rx}}$ threshold for each channel class case. For example, when the PLC channel behaves like class 2, HS-OQAM using ZF can better perform than DMT-OCP until $\mathrm{SNR}_{\mathrm{Rx}}$ getting 20 dB. But, if we use 3-tap ASCET

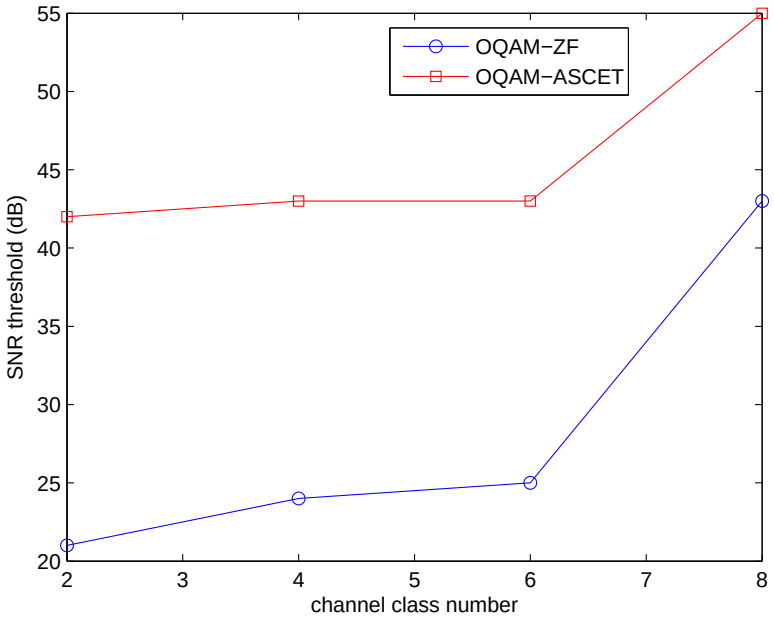

Figure 8.9: HS-OQAM $\mathrm{SNR}_{\mathrm{Rx}}$ threshold for $M = 512$.

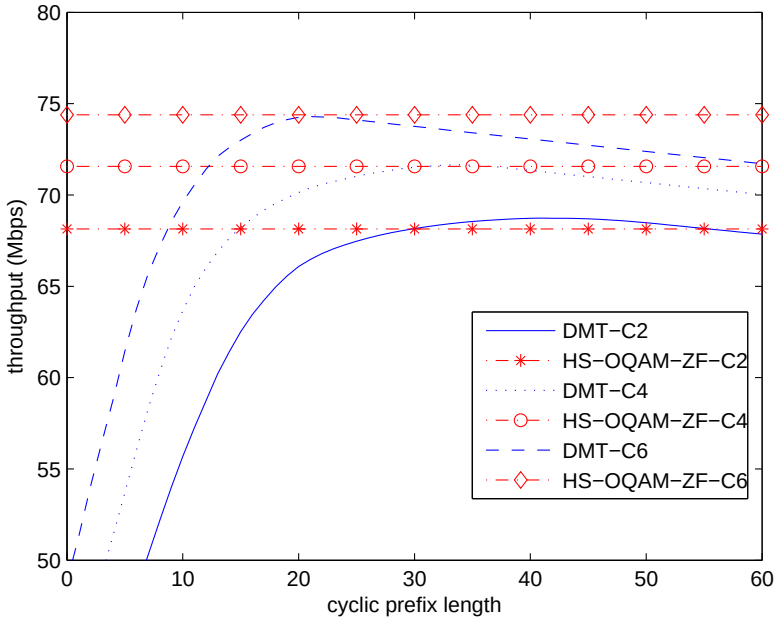

Figure 8.10: Capacity comparison with $M = 1024$, $\mathrm{SNR}_{\mathrm{Rx}}$=25 dB.

Table 8.1: SNR_{Tx} threshold table for HomePlug AV specification.

SNR_{Tx} seuil (dB)	classe 2	classe 3	classe 4	classe 5	classe 6	classe 7	classe 8	classe 9
HS-OQAM-ZF	79	73.5	72	67	65	63	60.2	60
HS-OQAM-ASCET	83	78	75.6	71	69	66	63.5	63

Table 8.2: Throughput threshold table for HomePlug AV specification.

Throughput threshold (Mbits/s)	class 2	class 3	class 4	class 5	class 6	class 7	class 8	class 9
HS-OQAM-ZF	170	200	245	286	340	440	462	540
HS-OQAM-ASCET	220	250	290	328	380	478	500	578

equalizer for HS-OQAM system, then this SNR_{Rx} threshold is increased to around 42 dB. On the other hand, it is worth noting that, in practice, the CP length of DMT might not be optimally chosen. So when the CP length is chosen to be equal to CIR length, then the SNR_{Rx} threshold will be further increased.

The other solution, besides changing equalizer for HS-OQAM, is to increase the number of carriers. The reason is: When we increase the number of carriers, the CIR length becomes shorter referencing to the symbol duration T_0. Then the system suffers less from interference effects. The capacity comparison using 1024 number of carriers is plotted in Fig. 8.10. It is easy to see that the capacities of HS-OQAM-ZF get close to those of DMT-OCP for each channel class case compared to Fig. 8.7. Thus, for larger number of carrier case (e.g. $M = 1024$), we can also find a corresponding SNR_{Rx} threshold for HS-OQAM vs. DMT over each channel class case. Then, by referencing to these SNR_{Rx} thresholds, we are able to decide which modulation should be chosen for PLC. Note that, the reported SNR_{Rx} thresholds in this part are available for HS-OQAM for a given prototype filter. Note that different prototype filters lead to different SNR threshold values.

In the following, we evaluate the SNR_{Tx} (Transmitted SNR, refer to Eq. 6.39) threshold for HS-OQAM vs. DMT in the HomePlug AV specification context [5] wherein, FFT size is 3072; Sampling frequency 75 MHz; CP length for DMT is 417 samples, and we always target an SER at 10^{-4}. The prototype filter used is TFL1 for HS-OQAM system because its short length permits to save simulation time. For this simple comparison, we do not introduce notches at particular frequencies [5] and the background noise remains to be additive white gaussian noise. The SNR_{Tx} thresholds are shown in Table 8.1, where the frequency transfer function of the realistic channel model of each class is given in Appendix 10.1. Then we can decide whether shall we choose DMT or HS-OQAM by referencing this look-up table. Alternatively, we can also make our decisions depending on the throughput look-up table as shown in Table 8.2 which tells us the throughput threshold for whether HS-OQAM, using ZF or ASCET, outperforms DMT.

It is worth mentioning that here we assume a perfect channel estimation, i.e. the receiver knows the exact CIR coefficients. In practice, for PLC, the preamble-based channel estimation using a simple least-square (LS) method in frequency domain is applied for DMT [5]. Compared with DMT, HS-OQAM can benefit of the remaining interferences to virtually boost the received preamble power at the receiver using a same LS method. Consequently, the resulting comparison can lead to a 2$\sim$3 dB gain in favor of HS-OQAM compared to DMT. The details will be discussed later in this chapter.

8.1.3 Practical Scenario

Previously, we have discoursed that there exists a SNR threshold in PLC for judging whether OFDM/DMT is better than HS-OQAM or in reverse. However, in the practical scenario, there are some constraints on the data transmission, such as, the transmit signal power is usually limited to a certain value as well as the maximum transmit bit number per sub-carrier. Therefore, in this part, we aim at evaluating the transmission capacity comparison between OFDM/DMT and HS-OQAM in a more practical/realistic scenario. The parameters are derived from the HPAV specifications [5], i.e.,

- prototype filter for HS-OQAM: TFL1 and Rossi4 with roll-off factor 1;
- FFT size: 3072; sampling frequency: 75 MHz;
- CP length of OFDM/DMT is chosen to use the minimum length 417 samples; sampling frequency: 75 MHz;
- notches: 1155 carriers are employed in the range from 1.8 MHz to 30 MHz. Of these, 917 carriers are used for transmitting the symbols and the other ones are switched off;
- possible constellations: BPSK, 4-QAM, 8-QAM, 16-QAM, 64-QAM, 256-QAM and 1024-QAM;
- noise: the background noise is assumed to be additive white Gaussian noise[1] and no impulsive noise is included;
- target SER: 10^{-3} (we take this value from [61]);
- channel coding: no channel coding is applied, i.e., $\Gamma = \frac{1}{3}\left[\mathbf{Q}^{-1}(\frac{\mathrm{SER}}{4})\right]^2$;
- channel estimation and synchronization: perfect;
- equalization: one-tap ZF.

The comparison results are reported in Figs. 8.11-8.14, wherein only one mean channel realization per class was used for this more lengthly set of simulations. To have a clear idea of the practical SNR operation region, we plot the throughput versus transmitted SNR ($\mathrm{SNR}_{\mathrm{Tx}}$, cf. Eq. (6.39)). Note that, as reported in [121], the maximum $\mathrm{SNR}_{\mathrm{Tx}}$ in PLC is around 90 dB.

In the case of channel class 2 and 4, we observe that there still exists a remarkable capacity intersection between HS-OQAM and OFDM/DMT and this intersection happens at higher $\mathrm{SNR}_{\mathrm{Tx}}$ threshold when we use Rossi4 prototype filter instead of using TFL1[2]. Therefore, in the practical PLC operation region, we can still define a $\mathrm{SNR}_{\mathrm{Tx}}$ threshold to optimally adjust the proper MCM scheme. However, in the case of channel class beyond

[1] New models of realistic coloured background noise are being elaborated in Orange Labs in Lannion, in future work the comparison will be carried out with these models.

[2] Note that, if we change the ZF equalizer to the ASCET for TFL1, then, it leads to a similar capacity as the one provided when using Rossi4 with ZF, because TFL1-ASCET and Rossi4-ZF have a similar subcarrier SINR (refer to Chap. 7).

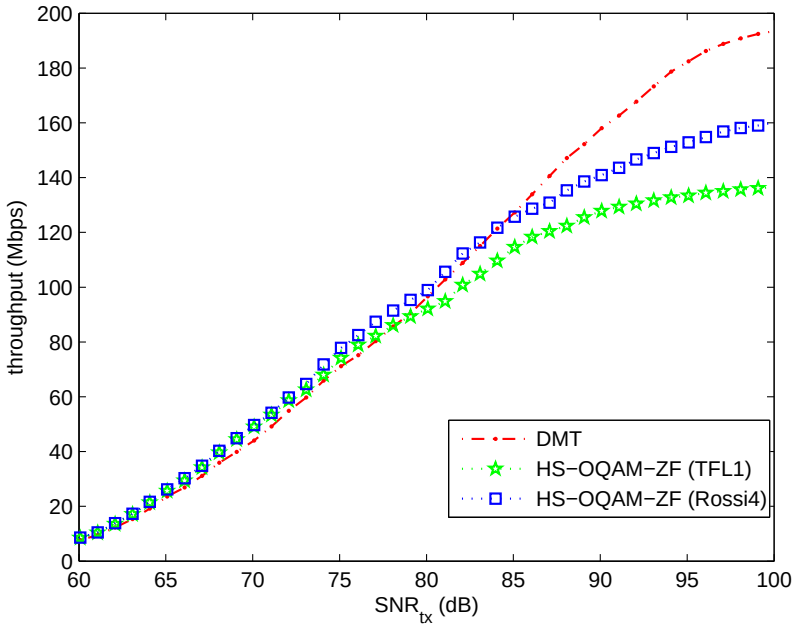

Figure 8.11: Throughput comparison: DMT vs. HS-OQAM over class 2 channel.

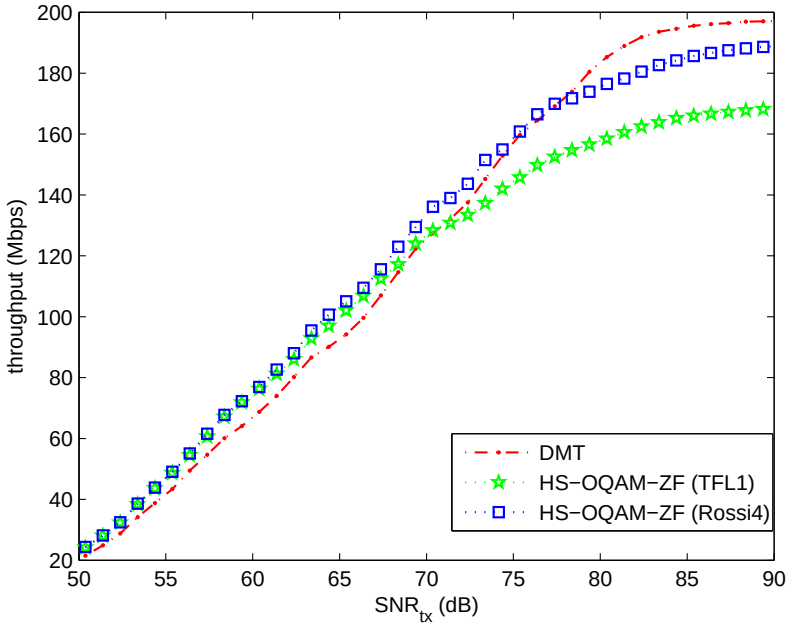

Figure 8.12: Throughput comparison: DMT vs. HS-OQAM over class 4 channel.

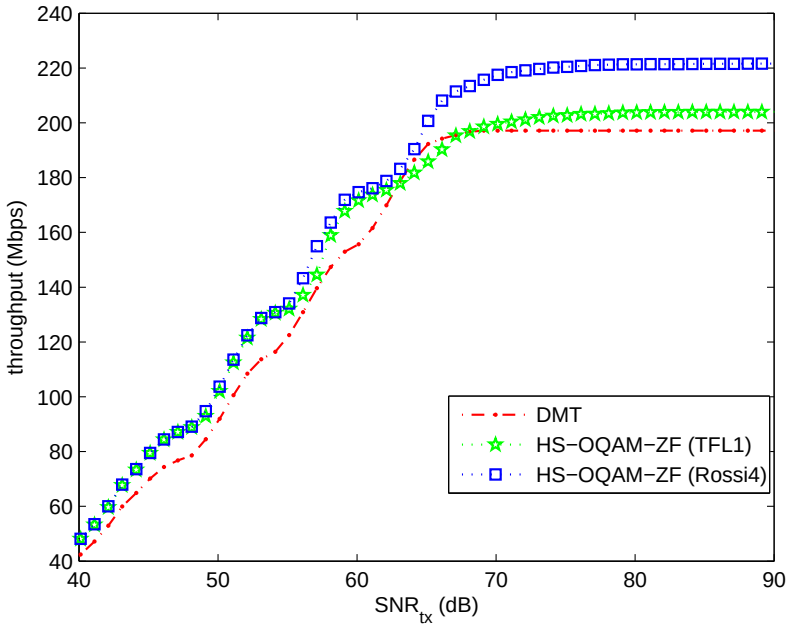

Figure 8.13: Throughput comparison: DMT vs. HS-OQAM over class 6 channel.

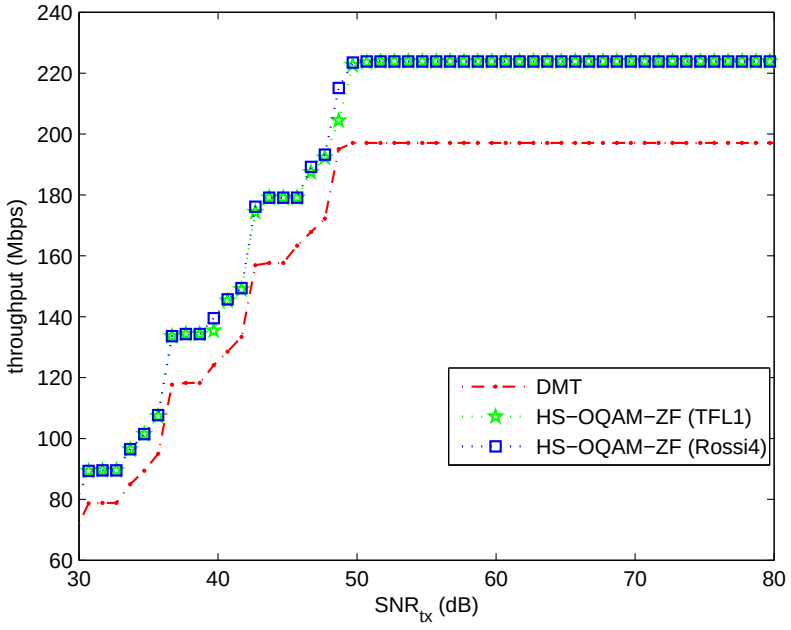

Figure 8.14: Throughput comparison: DMT vs. HS-OQAM over class 8 channel.

4 (i.e., class 6 and class 8), HS-OQAM system using Rossi4 prototype filter always wins against OFDM/DMT system. Further, in the case of channel class 8, HS-OQAM system using TFL1 prototype filter has almost the same capacity as the one of using Rossi4 prototype filter. In this case, TFL1 prototype filter is preferred because its short filter length can lead to a low system complexity and short latency.

8.2 A Unified MCM transceiver

In the preceding section, we have evaluated the capacity comparison between HS-OQAM and DMT schemes both in theory and practical scenario. In the theory case, we observe that a SNR threshold (either Tx or Rx) can be derived in each PLC channel class case to judge whether HS-OQAM performs better than DMT or in reverse. However, this sort of SNR threshold, in some channel cases (e.g., channel class beyond 4), seems to be unpractical when we evaluate the capacity w.r.t. the HPAV specifications, meaning that, subject to the most recent PLC specifications, HS-OQAM can provide a higher capacity than OFDM/DMT in most of the PLC channel cases. Nevertheless, when the maximum constellation order is increased in the future specifications, a practical SNR threshold might still exist. Thus, we can naturally exploit a gain if we are able to flexibly switch these two schemes from one to the other subject to the transmission environments and this gain can be termed as *modulation flexibility gain*. In this section, we introduce a unified MCM transceiver which addresses this flexibility issue.

The investigation of the unified MCM transceiver is not only motivated by the PLC capacity issue, it can also serve, for instance, the future ITU G.hn standard, which is a unified existing-wire home networking standard (i.e., phone wires, coaxial cables and power lines) [53], wherein, we will face many more variant channel conditions and the flexibility of the unified MCM transceiver is meant to be of interest. Furthermore, in the recent PLC draft standard (IEEE P1901) [1], a controversy happens due to the dual-PHY MCM schemes. Thus, the unified MCM transceiver can effectively solve this problem.

The contributions that our unified MCM transceiver can provide are: 1) it gives a way for obtaining the above-mentioned modulation flexibility gain; 2) it can overcome the controversy that is currently met due to the dual PHY layer proposal of IEEE P1901, i.e. the problem of sharing the medium resource with the user-devices equipped with two different systems (OFDM and WOFDM)[3]. With a unified MCM transceiver the transmitters can feel free to use either OFDM or WOFDM systems and the receivers are, as well, able to detect whatever systems by only an informational signal. Furthermore, the unified MCM transceiver should also include the advantages, namely, the following: 1) efficient implementation feasibility; 2) good regularity for implementation facilitation; 3) good flexibility (fit for the power of 2 length); 4) a low computational complexity.

The principle of our unified MCM transceiver can be concluded to a transform kernel sharing idea. A main difference among OFDM/DMT, HS-OQAM and WOFDM is that they do not have a similar transform kernel. Thus, if we can design a system that can generate all of these systems with an identical kernel, then a unified MCM transceiver turns out to be feasible. In the following, we first show the implementation of HS-OQAM

[3]The most recent solution for this controversy is to use an Inter-PHY Protocol (IPP), which is actually similar to the principle of TDMA, to separately serve two systems by time slots, cf. [58].

and WOFDM with a Fourier transform kernel, since Fourier transform kernel is used by both HS-OQAM and DMT, thus we first consider using this one. Then, inspired by Chan *et al.* [27] and Lee [80], we will change the transform kernel to a Fast Cosine/Sine-like transform (FCT/FST) kernel due to the consideration of aforementioned factors.

Let us define four types of fast cosine-like transform kernel matrices for the forthcoming use, for $k, n = 0, ..., N-1$,

$$\begin{aligned}
[\mathrm{FCT_I}]_{k,n} &= C_{2N}^{kn} = \cos\left(kn\frac{2\pi}{2N}\right), \\
[\mathrm{FCT_{II}}]_{k,n} &= C_{2N}^{k(n+\frac{1}{2})} = \cos\left(k(n+\frac{1}{2})\frac{2\pi}{2N}\right), \\
[\mathrm{FCT_{III}}]_{k,n} &= C_{2N}^{(k+\frac{1}{2})n} = \cos\left((k+\frac{1}{2})n\frac{2\pi}{2N}\right), \\
[\mathrm{FCT_{IV}}]_{k,n} &= C_{2N}^{(k+\frac{1}{2})(n+\frac{1}{2})} = \cos\left((k+\frac{1}{2})(n+\frac{1}{2})\frac{2\pi}{2N}\right),
\end{aligned} \tag{8.6}$$

where k stands for the entry index and n denotes the output index. If we replace the cosine operation with sine, it results in a set of sine-like transform kernel matrices, i.e.

$$\begin{aligned}
[\mathrm{FST_I}]_{k,n} &= S_{2N}^{kn} = \sin\left(kn\frac{2\pi}{2N}\right), \\
[\mathrm{FST_{II}}]_{k,n} &= S_{2N}^{k(n+\frac{1}{2})} = \sin\left(k(n+\frac{1}{2})\frac{2\pi}{2N}\right), \\
[\mathrm{FST_{III}}]_{k,n} &= S_{2N}^{(k+\frac{1}{2})n} = \sin\left((k+\frac{1}{2})n\frac{2\pi}{2N}\right), \\
[\mathrm{FST_{IV}}]_{k,n} &= S_{2N}^{(k+\frac{1}{2})(n+\frac{1}{2})} = \sin\left((k+\frac{1}{2})(n+\frac{1}{2})\frac{2\pi}{2N}\right).
\end{aligned} \tag{8.7}$$

8.2.1 Unified MCM Modulator using FFT Kernel

HS-OQAM Modulator

We first introduce the implementation of HS-OQAM modulator using FFTs. The HS-OQAM modulator structure is depicted in Fig. 8.15. Recall in Chap. 5, the discrete-time modulated HS-OQAM signal can be written as

$$u[k] = \sum_{m=0}^{M-1} \sum_{n\in\mathbf{Z}} a_{m,n} g[k-nN] e^{j(\frac{2\pi}{M}m(k-\frac{D}{2})+\phi_{m,n})}, \tag{8.8}$$

with $M = 2N$ and HS constraints given, for $m = 1, \cdots, N-1$, by

$$\begin{aligned}
a_{0,n} = a_{N,n} &= 0; \\
a_{m,n} &= a_{M-m,n}(-1)^{D-N-n} e^{-j2\phi_0},
\end{aligned} \tag{8.9}$$

where we set $D = L_f - 1$; $u[k]$ stands for the modulated symbols[4]. Let us assume that $\phi_0 = -\pi mn$ [115], after a simple mathematical combination, (8.8) can be alternatively

[4]Note that we now use $u[k]$ to represent the modulated symbols instead of the conventional $s[k]$ in the previous chapters. This is because that we will define s as an acronym for sin operation in the following sections and in order to avoid confusion we temporarily change the notation $s[k]$ to $u[k]$ in this chapter.

expressed as

$$u[k] = \sum_{m=0}^{M-1} \sum_{n \in \mathbf{Z}} x_m^0[n] f_m[k - nN], \tag{8.10}$$

where $x_m^0[n] = a_{m,n} j^n$ and a phase rotation term, j^n, permits to have the staggered offset QAM structure [115]; The synthesis filters form as $f_m[k] = g[k] e^{j\frac{2\pi}{M} m(k - \frac{D-N}{2})}$.

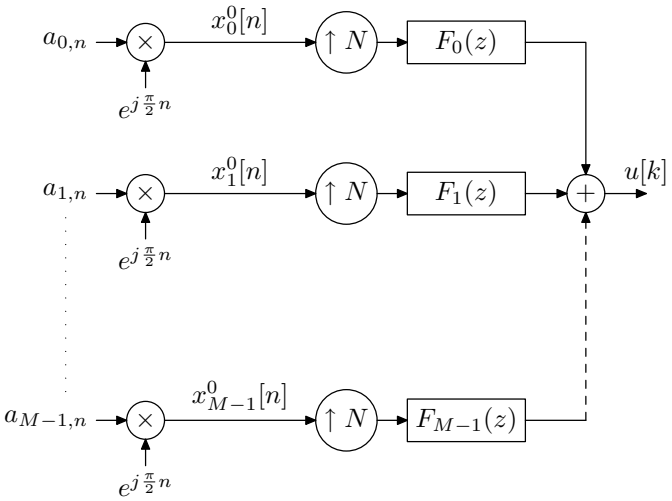

Figure 8.15: HS-OQAM modulator.

Taking the Z-transform of $u[k]$ yields

$$U(z) = \sum_{m=0}^{M-1} X_m^0(z^N) F_m(z), \tag{8.11}$$

where $X_m^0(z)$ is the Z-transform of $x_m^0(n)$ leading to $X_m^0(z) = Z\{a_{m,n} j^n\} = A_m(-jz)$; $F_m(z)$ is the Z-transform of $f_m[k]$ forming as

$$F_m(z) \;=\; \sum_k f_m[k] z^{-k} = W^{m\frac{D-N}{2}} P(zW^m), \tag{8.12}$$

where $W = e^{-j\frac{2\pi}{M}}$. Then, (8.12) can be equivalently written as (polyphase type 1) [130]

$$F_m(z) \;=\; \sum_{l=0}^{M-1} z^{-l} W^{m\frac{D-N}{2}} W^{-ml} G_l(z^M), \tag{8.13}$$

where $G_l(z) = \sum_{n \in \mathbf{Z}} g[2nN + l] z^{-n}$. Substituting (8.13) into (8.11) results in

$$U(z) \;=\; \sum_{l=0}^{M-1} z^{-(M-1-l)} \left[G_{l'}(z^2) \sum_{m=0}^{M-1} X_m^0(z) W^{m\frac{D-N}{2}} W^{-ml'} \right]_{\uparrow_N} \tag{8.14}$$

where $l' = M - 1 - l$; $[\cdot]_{\uparrow_N}$ denotes expander operation with factor N. The expression, (8.14), gives us a FFT-based efficient implementation solution. We can alternatively write

the overall modulation process in matrix form, by defining $\mathbf{a}_{M\times Q}$ as a entrance symbol matrix with size $M \times Q$ and $\mathbf{u}_{1\times(Q+b-1)M}$ as a row vector of size $1 \times (Q + b - 1)M$ with b the overlapping factor of the prototype filter ($L_f = bM$), as

$$\mathbf{u}_{1\times(Q+b-1)M} = \underbrace{[\mathbf{PS}]\mathbf{G}_{\text{diag}}}_{\text{POP}}(\sqrt{M}\mathbf{F}_M^H)\underbrace{\mathbf{W}_{\text{diag}}^{\dagger}}_{\text{PRP}}\mathbf{a}_{M\times Q}, \tag{8.15}$$

where $\mathbf{W}_{\text{diag}}^{\dagger}$ is a diagonal matrix with size $M \times M$, i.e.

$$\mathbf{W}_{\text{diag}}^{\dagger} = \text{diag}\left[j^n, \cdots, (j)^n W^{m\frac{D-N}{2}}, \cdots, (j)^n W^{(M-1)\frac{D-N}{2}}\right], \tag{8.16}$$

with n standing for the time index, which has a range in $[0, Q-1]$ and it varies depending upon the input matrix column index; $\mathbf{F}_M^H$ is the inverse FFT transform matrix with size $M \times M$; $\mathbf{G}_{\text{diag}}$ is the polyphase filtering matrix with size $M \times M$ expressed as

$$\mathbf{G}_{\text{diag}} = \text{diag}[G_0(z^2), \cdots, G_{M-1}(z^2)].$$

Note that, if the prototype filter has the length equal to symbol duration M, then for each carrier, the polyphase filter has only one coefficient. The [**PS**] matrix performs a parallel to serial operation as shown in Fig. 8.16.

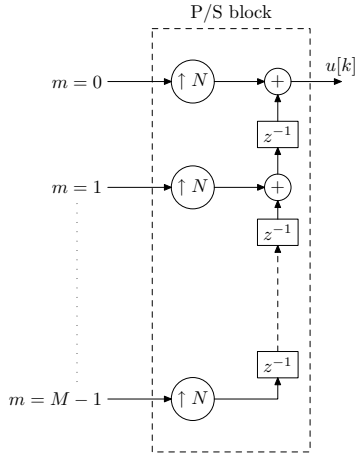

Figure 8.16: HS-OQAM P/S block.

The HS-OQAM modulator implementation structure using a FFT kernel is reported in Fig. 8.17, where the PRP and POP blocks denote pre-processing and post-processing, respectively and the processes inside them can be referred to (8.15).

Note that, there are a large number of algorithms for implementing FFTs. Among them, the split-radix algorithm proposed by Duhamel and Hollmann in 1984 [48] has been proved to have a low computational complexity. Its basic principle is to use a mixed radix factorization, radix-2 and -4, to reduce the number of non-trivial multiplications. Furthermore, the entrance symbol conditions (8.9) lead the input sequences of the IFFT to have a symmetry property. Thus, we can further use the real-split-radix (RSR) algorithm [47], whereby, the reported complexity yields only half of the one of the complex-split-radix

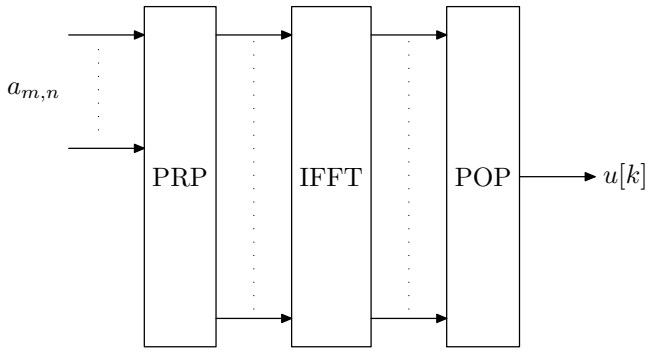

Figure 8.17: Efficient FFT-based implementation of HS-OQAM modulator.

(CSR) in [48]. However, the drawback of the RSR algorithm as well as CSR algorithm, compared with the Cooley-Tukey radix-2 (CTR2) algorithm [34], is that it has worse regularity than CTR2, therefore it is more complicated to be programmed and implemented.

The efficient implementation of DMT modulator implementation using FFTs has been discoursed in Sec. 5.2.3 and depicted in Fig. 5.4. Its entrance symbols must satisfy symmetry conditions, i.e. w.r.t. Fig. 5.4 that $c_{0,n} = c_{N,n} = 0$ and $c_{m,n} = c^*_{M-m,n}$ for $m = 1, \cdots, N-1$. Thus, the RSR algorithm can be directly applied to DMT modulator.

WOFDM Modulator

The WOFDM modulation was firstly introduced in PLC application by Koga *et al.* [77]. The general modulator structure is depicted in Fig. 8.18. We find that the number of sub-carriers of WOFDM is half of the DMT and HS-OQAM ones. Furthermore the entry symbols of WOFDM are multi-level PAM, plus the synthesis filters of WOFDM are cosine modulated kernel, therefore, WOFDM can directly generate a real-valued baseband modulated signal without any symmetry constraints.

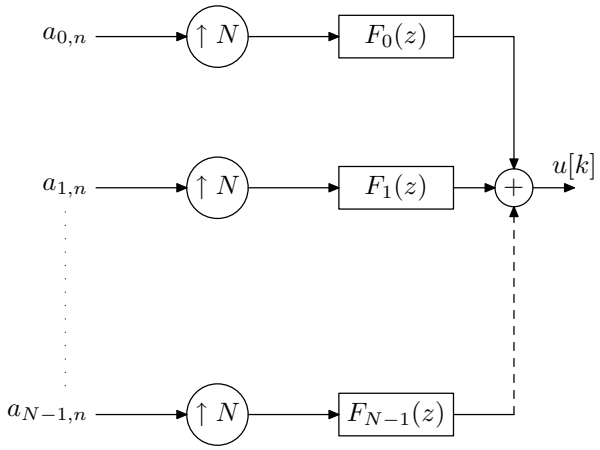

Figure 8.18: WOFDM modulator.

The discrete-time modulated WOFDM signal yields [71]

$$u[k] = \sum_{m=0}^{N-1} \sum_{n \in \mathbf{Z}} a_{m,n} f_m[k - nN], \tag{8.17}$$

with the synthesis filters

$$f_m[k] = 2p_0[k] \cos\left(\frac{\pi}{N}(m+0.5)\left(k - \frac{L_f - 1}{2}\right) - \theta_m\right),$$

where $a_{m,n}$ are multi-level PAM symbols; $\theta_m = (-1)^m \frac{\pi}{4}$; $p_0(k)$ is the prototype filter and L_f is the length of $p_0(k)$, we can also simply set $D = L_f - 1$. Note that WOFDM can use the same prototype filter as in HS-OQAM system[5], since they have the same perfect reconstruction conditions (cf. Chap. 5).

In order to implement WOFDM with FFT kernel, a modification of its mathematical expression, as given in (8.17), is needed to make the discrete Fourier transform appear setting

$$u[k] = 2\mathrm{Re}\left\{\sum_{m=0}^{N-1} \sum_{n \in \mathbf{Z}} a_{m,n} f'_m[k - nN]\right\}, \tag{8.18}$$

where $f'_m(k) = e^{j\left(\frac{\pi}{N}(m+0.5)\left(k - \frac{D}{2}\right) - \theta_m\right)}$. One may note at this point a similarity with the Exponential Modulated Filter Banks [132]. Then, taking the Z-transform of (8.18) leads to

$$U(z) = 2\mathrm{Re}\left\{\sum_{m=0}^{N-1} A_m(z^N) F'_m(z)\right\}, \tag{8.19}$$

with

$$F'_m(z) = W^{(m+0.5)\frac{D}{2}} e^{-j\theta_m} P_0\left(zW^{m+\frac{1}{2}}\right), \tag{8.20}$$

which can be compactly written as (polyphase type 2) [130]

$$F'_m(z) = \sum_{l=0}^{M-1} z^{-(M-1-l)} R_{l,m}(-z^M), \tag{8.21}$$

with

$$R_{l,m}(-z^M) = W^{(m+0.5)(\frac{D}{2} - l')} e^{-j\theta_m} G_{l'}(-z^M),$$

where $l' = M - 1 - l$. Substituting (8.21) into (8.19) results in

$$U(z) \;=\; 2\mathrm{Re}\left\{\sum_{l=0}^{M-1} z^{-(M-1-l)} \left[G_{l'}(-z^2) \sum_{m=0}^{N-1} X_m(z) W^{-(m+\frac{1}{2})l'}\right]_{\uparrow N}\right\}, \tag{8.22}$$

where $X_m(z) = W^{(m+0.5)\frac{D}{2}} e^{-j\theta_m} A_m(z)$. Then, the feasibility of FFT based implementation is confirmed. However, the Fourier transform shown in (8.22) is not an equal-input-output transform, i.e. the length of the input sequence is only the half of the output one

[5] This is to say that the same prototype filter with length L_f can be used in HS-OQAM system with M carriers and also in WOFDM system with N carriers ($M = 2N$).

which forces us to append zeros for completing the process. The matrix expression of WOFDM implementation is shown in below, assuming the prototype filter length being $L_f = bM$, i.e.,

$$\mathbf{u}_{1\times(Q+b-1)M} = \underbrace{2[\mathbf{PS}]\mathbf{Re}_{M\times M}\tilde{\mathbf{G}}_{\text{diag}}\tilde{\mathbf{W}}_{\text{diag}}}_{\text{POP}}(\sqrt{M}\mathbf{F}_M^H)\underbrace{\begin{bmatrix}\mathbf{W}_{\text{diag}}^{\ddagger}\\ \mathbf{0}_{N\times N}\end{bmatrix}}_{\text{PRP}}\mathbf{a}_{N\times Q}, \tag{8.23}$$

where $\mathbf{Re}_{M\times M}$ is a $M\times M$ matrix that has the function of real-part-taken, i.e.,

$$\mathbf{Re}_{M\times M} = \text{diag}[\text{Re}\{\cdot\},\cdots,\text{Re}\{\cdot\}]; \tag{8.24}$$

$\tilde{\mathbf{G}}_{\text{diag}}$, with size $M\times M$, can be expressed as

$$\tilde{\mathbf{G}}_{\text{diag}} = \text{diag}[G_0(-z^2),\cdots,G_{M-1}(-z^2)]; \tag{8.25}$$

$\tilde{\mathbf{W}}_{\text{diag}}$ is a $M\times M$ matrix as

$$\tilde{\mathbf{W}}_{\text{diag}} = \text{diag}\left[1,\cdots,W^{-\frac{1}{2}(M-1)}\right]; \tag{8.26}$$

$\mathbf{F}^H$ is the same as in HS-OQAM case denoting IFFT transform matrix with size $M\times M$; $\mathbf{W}_{\text{diag}}^{\ddagger}$ diagonal matrix, size $N\times N$, is expressed as

$$\mathbf{W}_{\text{diag}}^{\ddagger} = \text{diag}\left[W^{\frac{D}{4}}e^{-j\theta_0},\cdots,W^{(N+0.5)\frac{D}{2}}e^{-j\theta_{N-1}}\right]; \tag{8.27}$$

$\mathbf{0}_{N\times N}$ is a $N\times N$ zero matrix. Like HS-OQAM, WOFDM implementation can be similarly carried out as shown in Fig. 8.19. However, each of the block processing of PRP and POP is different from that of the HS-OQAM case and is expressed in (8.23).

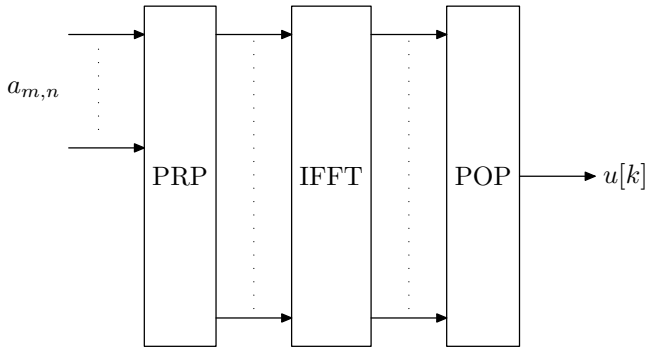

Figure 8.19: Efficient FFT-based implementation of WOFDM modulator.

Now, let us take a look at the IFFT algorithm for WOFDM implementation. Differently from HS-OQAM and DMT cases, the input sequences of IFFT transform in Fig. 8.19 are complex-valued without symmetry property. Thus, the RSR algorithm cannot be applied (cf. (8.23)). Instead, since half of the input sequence are zeros, the proper algorithm can be considered to use the pruned FFT algorithm as proposed by Markel [88]

and Skinner [116]. However, this pruned idea cannot be directly used for DMT and HS-OQAM FFT kernel implementations. Thus, a possible solution could be considered is to program different algorithms, or to implement different hardware, for HS-OQMA/DMT or WOFDM separately, whereas, this way breaks the principle of our unified idea. Therefore, in order to create a unified MCM modulator, in which, each different modulation scheme can share a common transform kernel (i.e., FFT kernel), the feasible solutions are either to use the CSR algorithm or to use the CTR2 algorithm. However, the drawback of doing this is apparent, i.e. neither CTR2 nor CSR can take advantage of the symmetry property of HS-OQAM or the pruned-input property of WOFDM to further reduce the arithmetic complexity. Nevertheless, CSR algorithm does have less complexity than CTR2 but at a price of regularity reduction.

8.2.2 Unified MCM Modulator using FCT/FST Kernel

HS-OQAM Modulator

A low-complexity implementation requires the unified MCM modulator to take advantage of the symmetry property of HS-OQAM, DMT systems and the pruned-input property of WOFDM system. Therefore, in what follows, we consider switching our kernel to FCT/FST based transform. The FCT/FST transform kernels can be efficiently implemented by a radix-2 based *divide and conquer* algorithm which has a perfect regularity (i.e., easily programmed) and flexibility (i.e., fits for base-2 input sequence length) and it also has a very low complexity.

Recalling the symmetry condition (8.9), we can get that, with $\phi_0 = -\pi mn$ and for $m = 1, \cdots, N-1$,

$$X^0_{M-m}(z) \;=\; Z\{x^0_{M-m}[n]\} = (-1)^{N-D} A_m(jz). \tag{8.28}$$

Revisiting Eq. (8.14), i.e.,

$$U(z) \;=\; \sum_{l=0}^{M-1} z^{-(M-1-l)} \left[G_{l'}(z^2) \underbrace{\sum_{m=0}^{M-1} X^0_m(z) W^{m\frac{D-N}{2}} W^{-ml'}}_{T_{l'}(z)} \right]_{\uparrow N} \tag{8.29}$$

and considering the above symmetry property, we can decompose $T_{l'}(z)$ of (8.14) into

$$\begin{aligned} T_{l'}(z) &= \sum_{m=0}^{N-1} \left[X^0_m(z) W^{m\frac{D-N}{2}} W^{-ml'} + X^0_{M-m}(z) W^{(M-m)\frac{D-N}{2}} W^{-(M-m)l'} \right] \\ &= 2 \sum_{m=0}^{N-1} \mathrm{Re}\{A_m(-jz) W^{m\frac{D-N}{2}} W^{-ml'}\}. \end{aligned} \tag{8.30}$$

Defining that $X_m(z) = A_m(-jz) W^{m\frac{D-N}{2}} = X^r_m(z) + jX^i_m(z)$, where X^r_m and X^i_m are the real and imaginary part of $X_m(z)$, respectively, then, we find a FCT/FST type I

(FCT/FST-I) based expression, for $l' = 0, \cdots, M-1$, as

$$\begin{aligned} T_{l'}(z) &= 2\sum_{m=0}^{N-1}\left[X_m^r(z)C_{2N}^{ml'} - X_m^i(z)S_{2N}^{ml'}\right] \\ &= 2[\mathrm{FCT_I}(l') - \mathrm{FST_I}(l')]. \end{aligned} \tag{8.31}$$

Substituting (8.31) into (8.29) leads to

$$U(z) = 2\sum_{l=0}^{M-1} z^{-(M-1-l)}\left[G_{l'}(z^2)[\mathrm{FCT_I}(l') - \mathrm{FST_I}(l')]\right]_{\uparrow_N}. \tag{8.32}$$

Note that the FCT/FST-I transforms have some symmetry properties that we could take advantage of to calculate only a N-point transform instead of a M-point, i.e., for $l = 0, \cdots, N-1$,

$$\mathrm{FCT_I}(l) = \mathrm{FCT_I}(M-l), \tag{8.33}$$

$$\mathrm{FST_I}(l) = -\mathrm{FST_I}(M-l), \tag{8.34}$$

$$\mathrm{FCT_I}(N) = \sum_{m=0}^{N-1} x_{m,n}^r(-1)^m, \tag{8.35}$$

$$\mathrm{FST_I}(N) = 0. \tag{8.36}$$

The matrix form of HS-OQAM implementation using FCT/FST-I can be written as

$$\mathbf{u}_{1\times(Q+b-1)M} = \underbrace{2[\mathbf{PS}]\mathbf{G}_{\mathrm{diag}}\bar{\mathbf{P}}_{M\times(M+1)}}_{\mathrm{POP}} \begin{bmatrix} \mathbf{C}_N^{\mathrm{I}} & \mathbf{0}_{N\times N} \\ \boldsymbol{\phi}_{1\times N} & \mathbf{0}_{1\times N} \\ \mathbf{0}_{N\times N} & \mathbf{S}_N^{\mathrm{I}} \end{bmatrix} \underbrace{\begin{bmatrix} \mathbf{Re}_{N\times N}\mathbf{I}_N \\ \mathbf{Im}_{N\times N}\mathbf{I}_N \end{bmatrix} \mathbf{W}_{\mathrm{diag}}^{\dagger}}_{\mathrm{PRP}} \mathbf{a}_{M\times Q}, \tag{8.37}$$

where the matrices $[\mathbf{PS}]$, $\mathbf{G}_{\mathrm{diag}}$ and $\mathbf{W}_{\mathrm{diag}}^{\dagger}$ are the same as in (8.15); the function of matrix $\bar{\mathbf{P}}_{M\times(M+1)}$ is in charge of realizing the sum of the FCT/FST transform pair w.r.t. (8.32) and (8.33)-(8.36), i.e. assume that we have a matrix composed with two matrices $\mathbf{A}_{(N+1)\times Q}$ and $\mathbf{B}_{N\times Q}$, then we have

$$\bar{\mathbf{P}}_{M\times(M+1)} \begin{bmatrix} \mathbf{A}_{(N+1)\times Q} \\ \mathbf{B}_{N\times Q} \end{bmatrix} = \begin{bmatrix} \mathbf{A}_{0,(0:Q-1)} \\ \mathbf{A}_{(1:N-1),(0:Q-1)} - \mathbf{B}_{(1:N-1),(0:Q-1)} \\ \mathbf{A}_{N,(0:Q-1)} \\ \mathbf{A}_{(1:N-1),(0:Q-1)} + \mathbf{B}_{(1:N-1),(0:Q-1)} \end{bmatrix}, \tag{8.38}$$

where the notation $\mathbf{A}_{a,(b:c)}$ stands for a row vector at a-th row and column indices from b to c; Likewise, $\mathbf{A}_{(a:b),c}$ stands for a column vector at c-th column and row indices from a to b; The matrices $\mathbf{C}_N^{\mathrm{I}}$ and $\mathbf{S}_N^{\mathrm{I}}$ are the $N \times N$ FCT-I and FST-I transform matrices, respectively; $\boldsymbol{\phi}_{1\times N}$ is a $1 \times N$ row vector with the expression as

$$\boldsymbol{\phi}_{1\times N} = [1, -1, 1, -1, \cdots, 1]. \tag{8.39}$$

It is worth reminding that $\boldsymbol{\phi}_{1\times N}$ is, actually, corresponding to the process for calculating the N-th point FCT, i.e. (8.35), and therefore it should be classified into a POP process.

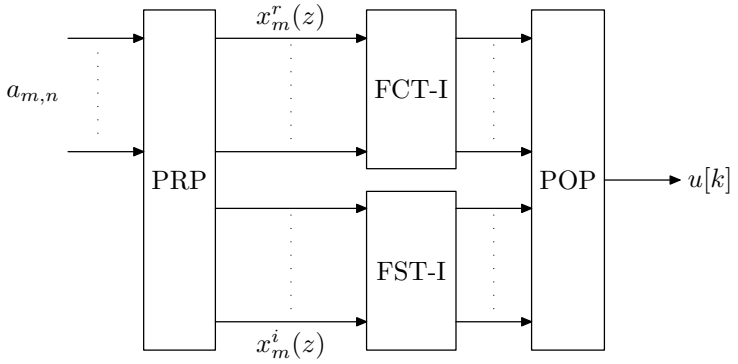

Figure 8.20: Efficient FCT/FST-I based blocks for HS-OQAM modulation.

The efficient structure for implementing HS-OQAM modulator using FCT/FST-I can be viewed in Fig. 8.20, where the FCT/FST-I implementation algorithm uses a radix-2 idea [80] and it is presented in Appendix 10.4. The complexity of this transform kernel will be discussed later in this chapter. The feasibility of implementing FCT/FST-I for DMT modulator has been proved in Chan's paper [27]. The overall block structure is similar to the one reported in Fig. 8.20. The only difference comes from the processing elements contained in the PRP and POP blocks. Hence, here we will not repeat the implementation derivation for DMT modulator. The readers who are interested in DMT implementations can refer to [27].

WOFDM Modulator

Entering into WOFDM modulation case, let us revisit the WOFDM modulated signal derivation using FFT kernel, i.e.,

$$U(z) = 2\mathrm{Re}\left\{\sum_{l=0}^{M-1} z^{-(M-1-l)}\left[G_{l'}(-z^2)\sum_{m=0}^{N-1} X_m(z)\underbrace{W^{-(m+\frac{1}{2})l'}}_{\text{kernel}}\right]_{\uparrow_N}\right\}, \quad (8.40)$$

where we remind that $l' = M-1-l$. Next, we can write the Fourier kernel by a sum of cosine-sine pair as

$$W^{-(m+\frac{1}{2})l'} = C_{2N}^{(m+\frac{1}{2})l'} + jS_{2N}^{(m+\frac{1}{2})l'}. \quad (8.41)$$

Substituting (8.41) into (8.40) we have

$$\begin{aligned} U(z) &= 2\sum_{l=0}^{M-1} z^{-(M-1-l)}\left[G_{l'}(-z^2)\right. \\ &\times \left.\left(\sum_{m=0}^{N-1} X_m^r(z)C_{2N}^{(m+\frac{1}{2})l'} - \sum_{m=0}^{N-1} X_m^i(z)S_{2N}^{(m+\frac{1}{2})l'}\right)\right]_{\uparrow_N} \\ &= \sum_{l=0}^{M-1} z^{-l'}\left[G_{l'}(-z^2)\left[2\left(\mathrm{FCT}_{\mathrm{III}}(l') - \mathrm{FST}_{\mathrm{III}}(l')\right)\right]\right]_{\uparrow_N}, \end{aligned} \quad (8.42)$$

with $l' = 0, \cdots, M-1$. So far, we have found a pair of FCT/FST type III (FCT/FST-III) based implementation. Furthermore, only half of the outputs are needed regarding the following symmetry properties of FCT/FST-III, i.e., for $l = 1, \cdots, N-1$,

$$\mathrm{FCT}_{\mathrm{III}}(l) = -\mathrm{FCT}_{\mathrm{III}}(M-l) \tag{8.43}$$

$$\mathrm{FST}_{\mathrm{III}}(l) = \mathrm{FST}_{\mathrm{I}}(M-l) \tag{8.44}$$

$$\mathrm{FCT}_{\mathrm{III}}(N) = 0 \tag{8.45}$$

$$\mathrm{FST}_{\mathrm{III}}(N) = \sum_{m=0}^{N-1} X_m^i(z)(-1)^m \tag{8.46}$$

$$\mathrm{FCT}_{\mathrm{III}}(0) = \sum_{m=0}^{N-1} X_m^r(z) \tag{8.47}$$

$$\mathrm{FST}_{\mathrm{III}}(0) = 0 \tag{8.48}$$

The overall implementation of WOFDM using FCT/FST-III can be re-written in a matrix form as

$$\mathbf{u}_{1\times(Q+b-1)M} = \underbrace{[\mathbf{PS}]\mathbf{G}_{\mathrm{diag}}\tilde{\mathbf{P}}_{M\times(M+1)}}_{\mathrm{POP}} \begin{bmatrix} \mathbf{C}_{N\times N}^{\mathrm{III}} & \mathbf{0}_N \\ \mathbf{0}_{N\times N} & \mathbf{S}_N^{\mathrm{III}} \\ \mathbf{0}_{1\times N} & \boldsymbol{\phi}_{1\times N} \end{bmatrix} \underbrace{\begin{bmatrix} \mathbf{Re}_{N\times N}\mathbf{I}_N \\ \mathbf{Im}_{N\times N}\mathbf{I}_N \end{bmatrix} \mathbf{W}_{\mathrm{diag}}^{\ddagger}}_{\mathrm{PRP}} \mathbf{a}_{N\times Q}, \tag{8.49}$$

where the matrices $[\mathbf{PS}]$, $\mathbf{G}_{\mathrm{diag}}$ and $\mathbf{W}_{\mathrm{diag}}^{\ddagger}$ are the same as in (8.23); the function of $\tilde{\mathbf{P}}_{M\times(M+1)}$ is in charge of realizing the sum of the FCT/FST transform pair w.r.t. (8.42) and (8.43)-(8.48), i.e.,

$$\tilde{\mathbf{P}}_{M\times(M+1)} \begin{bmatrix} \mathbf{A}_{N\times Q} \\ \mathbf{B}_{N+1\times Q} \end{bmatrix} = \begin{bmatrix} \mathbf{A}_{0,(0:Q-1)} \\ \mathbf{A}_{(1:N-1),(0:Q-1)} - \mathbf{B}_{(1:N-1),(0:Q-1)} \\ -\mathbf{B}_{N,(0:Q-1)} \\ -\mathbf{A}_{(1:N-1),(0:Q-1)} - \mathbf{B}_{(1:N-1),(0:Q-1)} \end{bmatrix}, \tag{8.50}$$

The implementation block structure is shown in Fig. 8.21. The efficient implementation of FCT/FST-III is presented in Appendix 10.6.

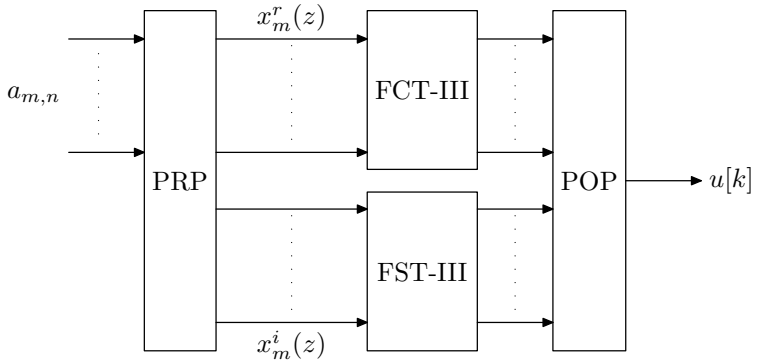

Figure 8.21: Efficient FCT/FST-III based blocks for WOFDM modulation.

Recall that a desired unified MCM modulator should have a common kernel for each modulation scheme. With this requirement in mind, we next show a FCT/FST-III kernel implementation using FCT/FST-I transforms.

Expressing the FCT-III transform as

$$y(l) = \sum_{m=0}^{N-1} x[m] C_{2N}^{(m+0.5)l} = \sum_{m=0}^{N-1} x[m] \tilde{C}_{2N}^{(2m+1)l}, \tag{8.51}$$

where we define $\tilde{C}_{2N}^{ml} \triangleq \cos\left(\frac{\pi}{2N} ml\right)$ and the following equality can be proved by the trigonometric identity, i.e.

$$2\tilde{C}_{2N}^{l} \tilde{C}_{2N}^{(2m+1)l} = \tilde{C}_{2N}^{(2m)l} + \tilde{C}_{2N}^{2(m+1)l}, \tag{8.52}$$

Using the above trigonometric identity into (8.51), we have

$$\begin{aligned} y(l) &= \frac{1}{2\tilde{C}_{2N}^{l}} \left(\sum_{m=0}^{N-1} x[m] \tilde{C}_{2N}^{(2m)l} + \sum_{m=0}^{N-1} x[m] \tilde{C}_{2N}^{2(m+1)l} \right) \\ &= \frac{1}{2\tilde{C}_{2N}^{l}} \left(x[N-1](-1)^l + \sum_{m=0}^{N-1} (x[m] + x[m-1]) \tilde{C}_{2N}^{(2m)l} \right), \end{aligned} \tag{8.53}$$

since $\tilde{C}_{2N}^{(2m)l} = C_{2N}^{ml}$, is actually the transform kernel of a N-point FCT-I. Thereby, N-point FCT-III can be realized based on FCT-I (see, Fig. 8.22). A similar process can be applied to FST-III, i.e.

$$y(l) = \sum_{m=0}^{N-1} x[m] S_{2N}^{(m+0.5)l} = \sum_{m=0}^{N-1} x[m] \tilde{S}_{2N}^{(2m+1)l}. \tag{8.54}$$

Recalling the trigonometric identity, i.e.

$$2\tilde{C}_{2N}^{l} \tilde{S}_{2N}^{(2m+1)l} = \tilde{S}_{2N}^{(2m)l} + \tilde{S}_{2N}^{2(m+1)l}, \tag{8.55}$$

and applying this identity to (8.54) yields

$$\begin{aligned} y(l) &= \frac{1}{2\tilde{C}_{2N}^{l}} \left(\sum_{m=0}^{N-1} x[m] \tilde{S}_{2N}^{(2m)l} + \sum_{m=0}^{N-1} x[m] \tilde{S}_{2N}^{2(m+1)l} \right) \\ &= \frac{1}{2\tilde{C}_{2N}^{l}} \sum_{m=0}^{N-1} (x[m] + x[m-1]) \tilde{S}_{2N}^{(2m)l}. \end{aligned} \tag{8.56}$$

Again, since $\tilde{S}_{2N}^{(2m)l} = S_{2N}^{ml}$, which is the transform kernel of a N-point FST-I, the FST-III can be implemented by FST-I as shown in Fig. 8.23.

Thus, in the block structure of Fig. 8.21, we can replace the kernel by a FCT/FST-I and put the process before and after the FCT/FST-I kernels, w.r.t. Figs. 8.22 and 8.23, into the PRP and POP blocks.

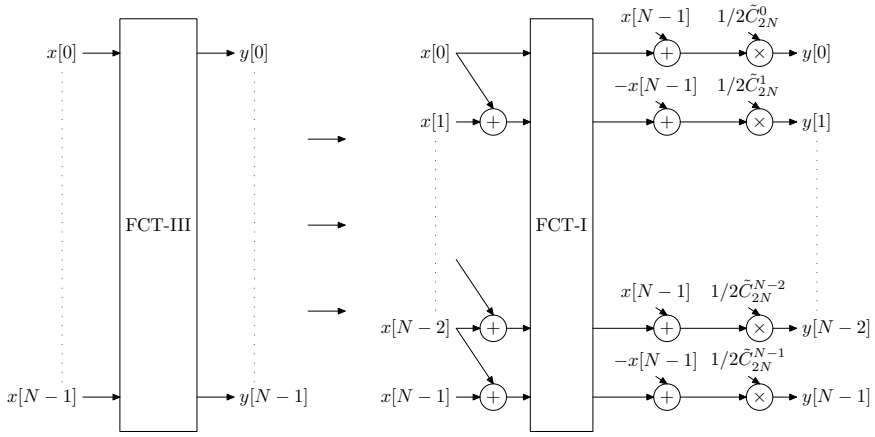

Figure 8.22: Implementation of FCT-III by FCT-I.

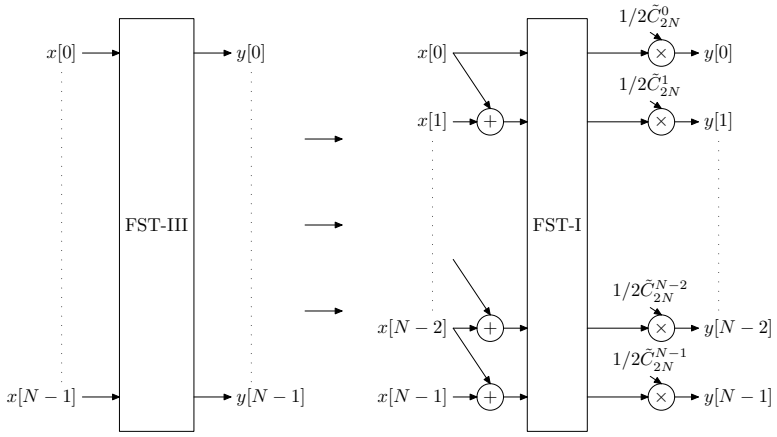

Figure 8.23: Implementation of FST-III by FST-I

8.2.3 Complexity Comparison Between Different Kernel Cases

So far, we have discoursed that a unified MCM modulator can be expected to exploit the modulation adaptation gain, i.e. a flexibility of arbitrarily switching the modulation schemes. Moreover, we have demonstrated that the efficient implementation of this unified MCM modulator can either use FFT kernel or FCT/FST-I kernel.

Fig. 8.24 gives the unified MCM modulator structure with FFT kernel, where each PRP and POP block of HS-OQAM and WOFDM modulator has been demonstrated in the preceding pages. Furthermore, a parameter, named Modulation Selection (ModSel), is introduced in this unified MCM modulator for the operator to decide which system is desired at the moment. Furthermore, we have also proved the feasibility of generating a unified MCM modulator with FCT/FST-I kernel as shown in Fig. 8.25. The difference between FFT kernel and FCT/FST-I kernel is only in the complexity issue. As to the performance, they do not have any difference at all. Thus, in this part, we need to discuss the complexity issue and make a comparison between these two kernel cases.

In the case of a unified MCM modulator using FFT kernel, we have discussed that

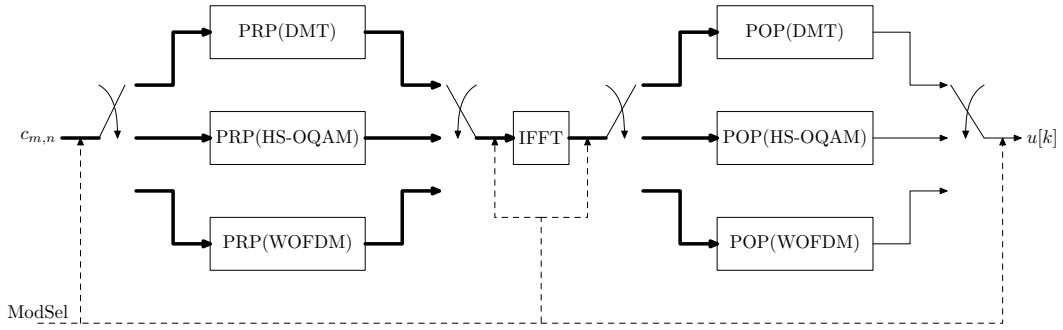

Figure 8.24: Unified MCM modulator with FFT kernel.

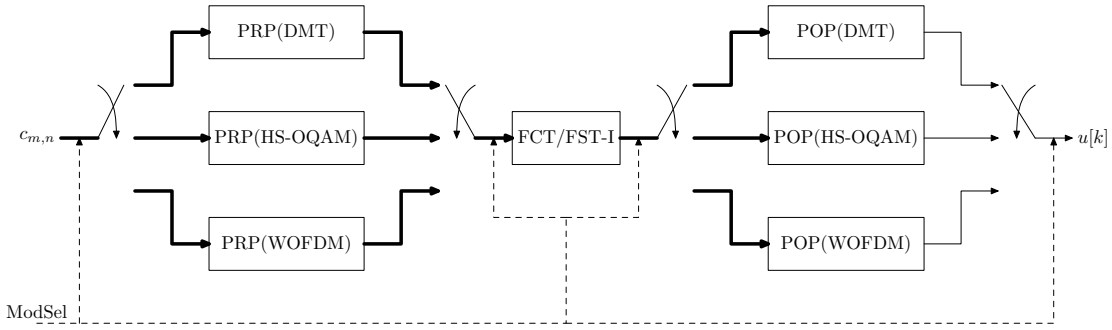

Figure 8.25: Unified MCM modulator with FCT/FST-I kernel.

the feasible IFFT algorithms are either the CSR or the CTR2[6]. The former solution has low complexity but high irregularity. The latter solution has high regularity but high complexity. The arithmetic complexity of these two solutions are layout in Tab. 8.3, where two cases are considered, i.e., 1CM=4RM+2RA (4/2) and 1CM=3RM+3RA (3/3)

On the other hand, in the case of a unified MCM modulator using FCT/FST-I kernel, the arithmetic complexity of implementing FCT-I plus FST-I is given in Appendix 10.5, i.e.

RM	$N\log_2 N - 2N + 2$
RA	$(9/2)N\log_2 N - 7N + 5$

However, in order to make our comparison fair enough for these two kernel solutions, we need to take into account the additional calculations for FCT/FST-I for performing an equivalent IFFT transform, i.e., in HS-OQAM case, taking into account (8.35) for the N-th point and the FCT/FST pair summation process $\bar{\mathbf{P}}_{M\times(M+1)}$ in (8.49) for one processing time slot (i.e. τ_0 for HS-OQAM and WOFDM and T_0 for DMT). Thus, these operations require in total $3N-2$ RA leading the final FCT/FST-I complexity to the one reported in Tab. 8.4. In Tabs. 8.5 and 8.6, we layout the arithmetic complexity comparison between FFT kernel and FCT/FST-I kernel.

Note that the aforementioned complexity expressions are valid only for the kernel implementation which is not the complexity of the overall modulator system, because we

[6]The higher radix-bases, e.g. -4 or -8, lose the flexibility and therefore we do not recommend.

Table 8.3: Arithmetic complexity of M-point FFT kernel.

	CTR2 [34]		CSR [118]	
	(3/3)	(4/2)	(3/3)	(4/2)
RM	$(3/2)M\log_2 M$	$2M\log_2 M$	$M\log_2 M - 3M + 4$	$(4/3)M\log_2 M - (38/9)M + 6 + (2/9)(-1)^{\log_2 M}$
RA	$(7/2)M\log_2 M$	$3M\log_2 M$	$3M\log_2 M - 3M + 4$	$(8/3)M\log_2 M - (16/9)M + 2 + (2/9)(-1)^{\log_2 M}$

Table 8.4: Arithmetic complexity of equivalent M-point ($M = 2N$) FFT kernel using FCT/FST-I.

RM	$N\log_2 N - 2N + 2$
RA	$(9/2)N\log_2 N - 4N + 3$

did not take into account the polyphase filtering and pre-processing calculation. However, since those calculations are the same for both kernel cases, so the main complexity difference appears in the kernel implementation. It is of interest to indicate that the processing rate of the DMT system (T_0) is 2 times lower than that of the HS-OQAM and WOFDM systems (τ_0). Furthermore, we need to remind that, in the case of WOFDM using FCT/FST kernel, the kernel complexity should also include the additional calculations coming from the operation of adapting FCT/FST type III to I (see. Figs. 8.22 and 8.23), which yields $2N - 2$ additional RM and $3N - 2$ additional RA. Likewise, for FFT-based WOFDM case, the additional complexity comes from the weighting process, $\tilde{\mathbf{W}}^{\dagger}_{\text{diag}}$, which leads to $M-1$ CM. However, since a real-part-taken operation is carried out right after this weighting process (that means we only need the real part of the results), thus, it eventually results in $2(M-1)$ additional RM and $M-1$ additional RA.

Thus, it is now obvious that for the unified MCM modulator, the preferred kernel must be FCT/FST-I, due to the facts that it has the lowest arithmetic complexity; its flexibility is good; its regularity is perfect (radix-2 based); it can be easily programmed.

8.2.4 Unified MCM Demodulator using FFT Kernel

For completing the transceiver structure, we next show the demodulator implementation of our unified system. Similarly, the demodulator kernel can be chosen between FFT or FCT/FST-I. However, as we will see later, the FCT/FST-I kernel is not necessarily preferred in demodulator process. However, this kernel is still highly recommended in this thesis due to its programming convenience.

HS-OQAM Demodulator

The HS-OQAM demodulator structure is plotted in Fig. 8.26 where the delay factors α and β are depending upon the prototype filter length (cf. Chap. 7).

Referencing to Fig. 8.26, the signal at the output of the decimation of the m-th subcarrier can be expressed in Z-transform, denoting $Y_m(z)$, as

$$Y_m(z) = \Big[H_m(z)z^{-\beta}U(z)\Big]_{\downarrow_N}, \tag{8.57}$$

Table 8.5: Real multiplications comparison: M-point FFT vs. FCT/FST-I kernel.

M	FCT/FST-I	CTR2(3/3)	CTR2(4/2)	CSR(3/3)	CSR(4/2)
8	2	36	48	4	4
16	10	96	128	20	24
32	34	240	320	68	84
64	98	576	768	196	248
128	258	1344	1792	516	660
256	642	3072	4096	1284	1656
512	1538	6912	9216	3076	3988
1024	3586	15360	20480	7172	9336

Table 8.6: Real additions comparison: M-point FFT vs. FCT/FST-I kernel.

M	FCT/FST-I	CTR2(3/3)	CTR2(4/2)	CSR(3/3)	CSR(4/2)
8	23	84	72	52	52
16	79	224	192	148	144
32	227	560	480	388	372
64	595	1344	1152	964	912
128	1475	3136	8688	2308	2164
256	3523	7168	6144	5380	5008
512	8195	16128	13824	12292	11380
1024	18691	35840	30720	27652	25488

where $H_m(z)$ is the m-th analysis filter, which can be expressed in the following way

$$\begin{aligned} H_m(z) &= \sum_k h_m(k) z^{-k} \\ &= \sum_{l=0}^{M-1} z^{-l} W^{-ml} W^{m\frac{D+N}{2}} G_l(z^M) \\ &= \sum_{l=0}^{M-1} z^{-l} E_{m,l}(z^M). \end{aligned} \tag{8.58}$$

Substituting (8.58) into (8.57) leads to

$$\begin{aligned} Y_m(z) &= \left[\sum_{l=0}^{M-1} z^{-l} E_{m,l}(z^M) z^{-\beta} U(z) \right]_{\downarrow N} \\ &= \left[\sum_{l=0}^{M-1} z^{-l} z^{-\beta} U(z) \right]_{\downarrow N} E_{m,l}(z^2) \\ &= \sum_{l=0}^{M-1} \underbrace{\left[z^{-l} z^{-\beta} U(z) \right]_{\downarrow N} G_l(z^2)}_{\tilde{U}_l(z)} W^{-ml} W^{m\frac{D+N}{2}}, \end{aligned} \tag{8.59}$$

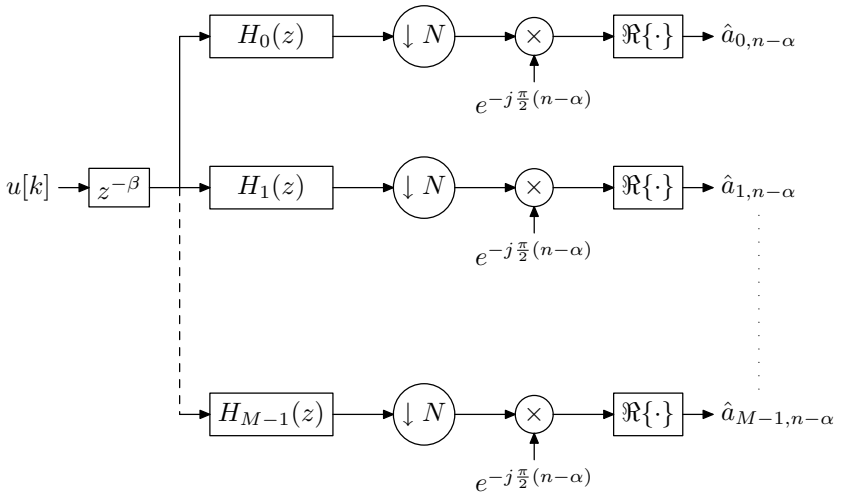

Figure 8.26: HS-OQAM receiver.

where $[\cdot]_{\downarrow_N}$ stands for the decimation operation with a factor of N. Thus, following the process of Fig. 8.26, we have the estimated symbol, $\hat{a}_{m,n}$,

$$\hat{a}_{m,n} = \mathrm{Re}\{e^{-j\frac{\pi}{2}(n-\alpha)} y_{m,n}\}. \tag{8.60}$$

We can write the matrix form for the HS-OQAM demodulator using FFT kernel, i.e.,

$$\hat{\mathbf{a}}_{N\times Q} = \underbrace{\mathbf{D}^{\alpha\tau_0}_{N\times N}\mathbf{Re}_{N\times N}\left[\begin{array}{cc}\mathbf{I}_N & \mathbf{0}_{N\times N}\end{array}\right]\hat{\mathbf{W}}^{\dagger}_{\mathrm{diag}}}_{\mathrm{POP}}\left(\sqrt{M}\mathbf{F}^{H}_{M}\right)\underbrace{\mathbf{G}_{\mathrm{diag}}[\mathbf{SP}]\mathbf{D}^{\beta}_{1\times 1}}_{\mathrm{PRP}}\mathbf{u}_{1\times(Q+b-1)M}, \tag{8.61}$$

where $\hat{\mathbf{a}}_{N\times Q}$ is the demodulated symbol matrix with size $N \times Q$, here we write N instead of M is because we only care about the half of the total carriers due to the symmetry conditions (8.9); $\mathbf{D}^{\alpha\tau_0}_{N\times N}$ is defined as a $N \times N$ delay operation matrix with a delay in sampling interval (in T_s), i.e.

$$\mathbf{D}^{\alpha\tau_0}_{N\times N} = \mathrm{diag}[z^{-\alpha\tau_0}, \cdots, z^{-\alpha\tau_0}]; \tag{8.62}$$

$\hat{\mathbf{W}}^{\dagger}_{\mathrm{diag}}$ is a weighting matrix and it has the following link with $\mathbf{W}^{\dagger}_{\mathrm{diag}}$ in (8.49)

$$\hat{\mathbf{W}}^{\dagger}_{\mathrm{diag}} = (-1)^{n+1} j^{\alpha} \mathbf{W}^{\dagger}_{\mathrm{diag}}; \tag{8.63}$$

$\mathbf{G}_{\mathrm{diag}}$, the polyphase filtering matrix, is equivalent to that of in (8.49); [**SP**] stands for the serial to parallel process as shown in Fig. 8.27. The efficient implementation block is reported in Fig. 8.28.

For the IFFT implementation, we can use the RSR [47], due to the fact that the received signal $u[k]$ is real-valued and the PRP process does not change the nature of the signal, i.e. still remains to be real-valued, see (8.61). Thus, the input sequences of the IFFT transform are real-valued. The same case happens in the DMT demodulator, i.e., the input sequence of the IFFT transform is purely real-valued.

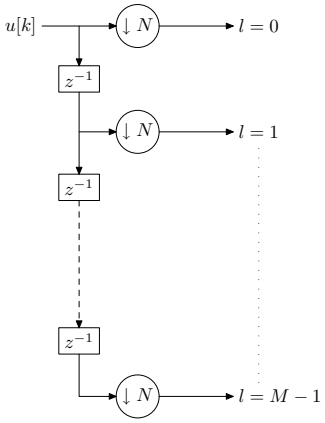

Figure 8.27: HS-OQAM S/P block.

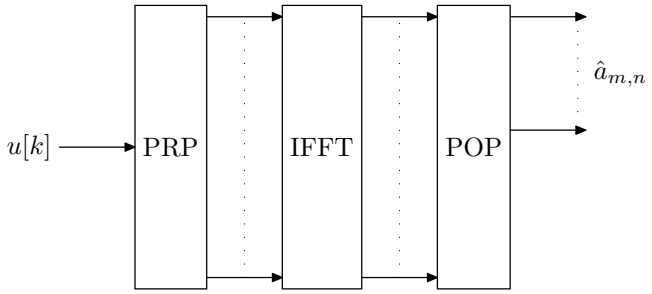

Figure 8.28: Efficient FFT-based implementation of HS-OQAM demodulator.

WOFDM Demodulator

The baseband WOFDM demodulator structure is depicted in Fig. 8.29. The analysis filters, referencing to (8.2.1), can be written as $h_m(k) = 2\mathrm{Re}\{h'_m(k)\}$, with $h'_m(k) = e^{j\left(\frac{\pi}{N}(m+0.5)\left(k-\frac{D}{2}\right)+\theta_m\right)}$. From Fig. 8.29, we see that the demodulated symbol (in Z-transform) has the form as

$$\hat{A}_m(z) = \left[z^{-\beta}U(z)H_m(z)\right]_{\downarrow N} = 2\mathrm{Re}\left\{\left[z^{-\beta}U(z)H'_m(z)\right]_{\downarrow N}\right\}, \tag{8.64}$$

where

$$\begin{aligned} H'_m(z) &= \sum_k p_0(k)W^{(m+0.5)\frac{D}{2}}W^{-(m+0.5)k}e^{j\theta_m}z^{-k} \\ &= W^{(m+0.5)\frac{D}{2}}e^{j\theta_m}P_0\left(zW^{m+\frac{1}{2}}\right). \end{aligned} \tag{8.65}$$

Expressing $P_0(z)$ with its polyphase version yields

$$\begin{aligned} H'_m(z) &= W^{(m+0.5)\frac{D}{2}}e^{j\theta_m}\sum_{l=0}^{M-1} z^{-l}W^{-(m+0.5)l}G_l(-z^M) \\ &= \sum_{l=0}^{M-1} z^{-l}E_{m,l}(-z^M). \end{aligned} \tag{8.66}$$

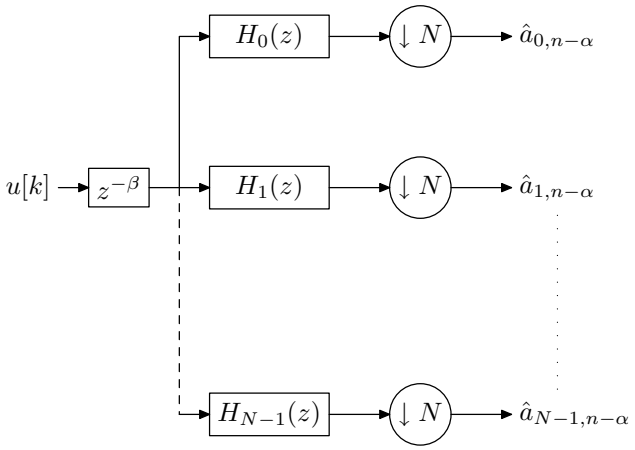

Figure 8.29: WOFDM demodulator.

Therefore, $\hat{A}_m(z)$ can be re-written as

$$\begin{aligned}\hat{A}_m(z) &= 2\mathrm{Re}\left\{\left[z^{-\beta}U(z)\sum_{l=0}^{M-1}z^{-l}E_{m,l}(-z^M)\right]_{\downarrow N}\right\}\\ &= 2\mathrm{Re}\left\{\sum_{l=0}^{M-1}\left[U(z)z^{-(l+\beta)}\right]_{\downarrow N}E_{m,l}(-z^2)\right\}\\ &= 2\mathrm{Re}\left\{\sum_{l=0}^{M-1}\left[U(z)z^{-(l+\beta)}\right]_{\downarrow N}G_l(-z^2)W^{-(m+0.5)l}W^{(m+0.5)\frac{D}{2}}e^{j\theta_m}\right\}.\end{aligned} \tag{8.67}$$

It is equivalent to the following matrix expression

$$\hat{\mathbf{a}}_{N\times Q} = \underbrace{2\mathbf{D}_{N\times N}^{\alpha\tau_0}\mathbf{Re}_{N\times N}\left[\begin{array}{cc}\hat{\mathbf{W}}_{\mathrm{diag}}^{\ddagger}\mathbf{I}_N & \mathbf{0}_{N\times N}\end{array}\right]\tilde{\mathbf{W}}_{\mathrm{diag}}}_{\mathrm{POP}}\left(\sqrt{M}\mathbf{F}_M^H\right)\underbrace{\tilde{\mathbf{G}}_{\mathrm{diag}}[\mathbf{SP}]\mathbf{D}_{1\times 1}^{\beta}}_{\mathrm{PRP}}\mathbf{u}_{1\times(Q+b-1)M}, \tag{8.68}$$

where $\mathbf{D}_{N\times N}^{\alpha\tau_0}$ and $\mathbf{D}_{1\times 1}^{\beta}$ have the same functions as in HS-OQAM demodulator case; $\hat{\mathbf{W}}_{\mathrm{diag}}^{\ddagger}$ has the form related to $\mathbf{W}_{\mathrm{diag}}^{\ddagger}$ in (8.23), i.e.

$$\hat{\mathbf{W}}_{\mathrm{diag}}^{\ddagger} = \mathrm{diag}[e^{j2\theta_0},\cdots,e^{j2\theta_{N-1}}]\cdot\mathbf{W}_{\mathrm{diag}}^{\ddagger}; \tag{8.69}$$

$\mathbf{W}_{\mathrm{diag}}$, $\tilde{\mathbf{G}}_{\mathrm{diag}}$ and $[\mathbf{SP}]$ remain the same as in (8.23). Therefore, the overall block structure of WOFDM demodulator can be seen as in Fig. 8.30.

Differently to the modulator implementation, for WOFDM demodulator implementation, we can finally use the RSR algorithm due the fact that the received signal is real-valued and this nature will not be changed during the PRP process.

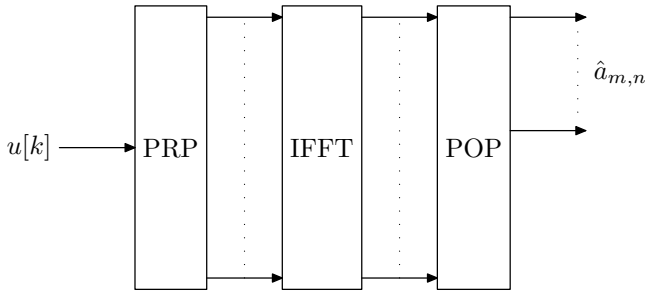

Figure 8.30: Efficient FFT-based implementation of WOFDM demodulator.

8.2.5 Unified MCM Demodulator using FCT/FST Kernel

HS-OQAM Demodulator

Revisiting Eq. (8.59) as

$$Y_m(z) = \sum_{l=0}^{M-1} \underbrace{\left[z^{-l}z^{-\beta}U(z)\right]_{\downarrow N} G_l(z^2)}_{\tilde{U}_l(z)} W^{-ml}W^{m\frac{D+N}{2}}, \tag{8.70}$$

the modulated HS-OQAM signal $u[k]$ is real-valued as well as the prototype filter, so that $\tilde{U}_l(z)$ is real-valued. Then, we can have the following equation

$$\sum_{l=0}^{M-1} \tilde{U}_l(z)W^{-ml} = \sum_{l=0}^{M-1} \tilde{U}_l(z)C_{2N}^{ml} + j\sum_{l=0}^{M-1} \tilde{U}_l(z)S_{2N}^{ml}. \tag{8.71}$$

For simplifying the notation, we observe that z and l are two orthogonal dimensions, therefore, when we focus on the process in l dimension we can temporarily neglect the notation of z, i.e., in what follows, we note $\tilde{U}(l)$ instead of $\tilde{U}_l(z)$ for the Fourier calculation at each τ_0.

We can then make $\tilde{U}(l)$ as a combination of symmetric and anti-symmetric sequences $\tilde{U}_s(l)$ and $\tilde{U}_{as}(l)$, respectively as, for $l = 1, ..., N-1$,

$$\begin{aligned} \tilde{U}_s(l) &= \tfrac{1}{2}\left[\tilde{U}(l) + \tilde{U}(M-l)\right] \\ \tilde{U}_{as}(l) &= \tfrac{1}{2}\left[\tilde{U}(l) - \tilde{U}(M-l)\right]. \end{aligned} \tag{8.72}$$

The relations among $\tilde{U}(l)$, $\tilde{U}_s(l)$ and $\tilde{U}_{as}(l)$ as, for $l = 1, ..., N-1$,

$$\begin{aligned} \tilde{U}(l) &= \tilde{U}_s(l) + \tilde{U}_{as}(l) \\ \tilde{U}(M-l) &= \tilde{U}_s(l) - \tilde{U}_{as}(l). \end{aligned} \tag{8.73}$$

Substituting (8.77) into (8.71), we can reduce the M-point transform to the N-point

transform, such as, for $m = 0, ..., N-1$,

$$\begin{aligned}\sum_{l=0}^{M-1} \tilde{U}(l) W^{-ml} &= \tilde{U}(0) + \tilde{U}(N)(-1)^m \\ &+ 2\left[\sum_{l=0}^{N-1} \tilde{U}_s(l) C_{2N}^{ml} + j \sum_{l=0}^{N-1} \tilde{U}_{as}(l) S_{2N}^{ml}\right] \\ &= \tilde{U}(0) + \tilde{U}(N)(-1)^m + 2\left[\mathrm{IFCT_I}(m) + j\mathrm{IFST_I}(m)\right], \end{aligned} \quad (8.74)$$

where we set $\tilde{U}_s(0) = 0$ and $\tilde{U}_{as}(0) = 0$. Note that, compared with FCT/FST-I, the inverse FCT/FST-I (IFCT/IFST-I) has only a difference in switching the input-output indices of m and l. Therefore, IFCT/IFST-I can be practically replaced by FCT/FST-I transform. Then, the matrix expression yields

$$\begin{aligned}\hat{\mathbf{a}}_{N\times Q} &= \underbrace{\mathbf{D}_{N\times N}^{\alpha\tau_0}\mathbf{Re}_{N\times N}\left(\begin{bmatrix}\mathbf{I}_N & \mathbf{0}_{N\times N}\end{bmatrix}\hat{\mathbf{W}}_{\mathrm{diag}}^{\dagger}\right)\left(\hat{\mathbf{U}}_{N\times Q} + 2\begin{bmatrix}\mathbf{I}_N & j\mathbf{I}_N\end{bmatrix}\right.}_{\mathrm{POP}} \\ &\times \left.\begin{bmatrix}\mathbf{C}_N^{\mathrm{I}} & \mathbf{0}_{N\times N} \\ \mathbf{0}_{N\times N} & \mathbf{S}_N^{\mathrm{I}}\end{bmatrix}\underbrace{\begin{bmatrix}\mathbf{P}_{N\times N}^{s} \\ \mathbf{P}_{N\times N}^{as}\end{bmatrix}\mathbf{G}_{\mathrm{diag}}[\mathbf{SP}][\mathbf{D}^{\beta T_s}]}_{\mathrm{PRP}}\mathbf{u}_{1\times(Q+b-1)M}\right), \end{aligned} \quad (8.75)$$

where $\mathbf{P}_{N\times N}^{s}$ and $\mathbf{P}_{N\times N}^{as}$ matrices are in charge of processing (8.72); $\hat{\mathbf{U}}_{N\times Q}$ is a $N\times Q$ matrix with the each column being $[\tilde{U}(0)+\tilde{U}(N), \tilde{U}(0)-\tilde{U}(N), \cdots, \tilde{U}(0)+\tilde{U}(N)(-1)^{N-1}]^T$.

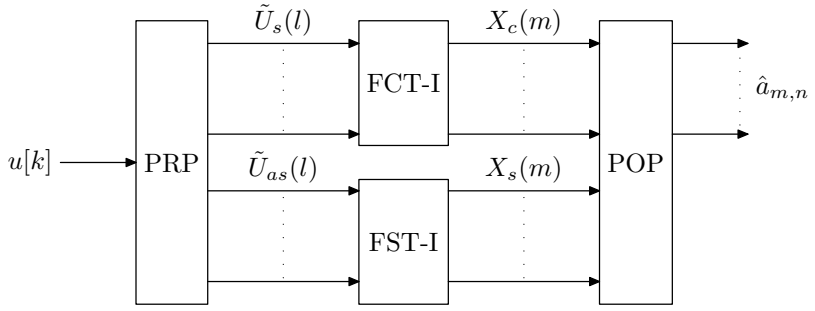

Figure 8.31: Efficient FCT/FST-I based blocks for HS-OQAM demodulation.

WOFDM Demodulator

Recall the WOFDM demodulated signal expression, i.e.

$$\hat{A}_m(z) = 2\mathrm{Re}\left\{\sum_{l=0}^{M-1}\underbrace{\left[U(z)z^{-(l+\beta)}\right]_{\downarrow N}}_{\tilde{U}(l)} G_l(-z^2)\, W^{-(m+0.5)l} W^{(m+0.5)\frac{D}{2}} e^{j\theta_m}\right\} \quad (8.76)$$

Same as for the HS-OQAM demodulator case, we again set, for $l = 1, ..., N-1$,

$$\begin{aligned} \tilde{U}_s(l) &= \frac{1}{2}\left[\tilde{U}(l) + \tilde{U}(M-l)\right] \\ \tilde{U}_{as}(l) &= \frac{1}{2}\left[\tilde{U}(l) - \tilde{U}(M-l)\right]. \end{aligned} \tag{8.77}$$

Substituting (8.72) into (8.76) and, after computation, we have for $m = 0, ..., N-1$,

$$\begin{aligned} \hat{A}_m(z) &= 2\mathrm{Re}\left\{\left[\tilde{U}(0) + j\tilde{U}(N)(-1)^m \right.\right. \\ &+ \left.\left. 2\left(\sum_{l=0}^{N-1}\tilde{U}_{as}(l)C_{2N}^{(m+\frac{1}{2})l} + j\sum_{l=0}^{N-1}\tilde{U}_s(l)S_{2N}^{(m+\frac{1}{2})l}\right)\right] W^{(m+0.5)\frac{D}{2}}e^{j\theta_m}\right\} \\ &= 2\mathrm{Re}\left\{\left(\tilde{U}(0) + j\tilde{U}(N)(-1)^m \right.\right. \\ &+ \left.\left. 2\left[\mathrm{IFCT}_{\mathrm{III}}(m) + j\mathrm{IFST}_{\mathrm{III}}(m)\right]\right) W^{(m+0.5)\frac{D}{2}}e^{j\theta_m}\right\}, \end{aligned} \tag{8.78}$$

where $\tilde{U}_s(0) = \tilde{U}_{as}(0) = 0$. The matrix form can be expressed as

$$\begin{aligned} \hat{\mathbf{a}}_{N\times Q} &= \underbrace{2\mathbf{D}_{N\times N}^{\alpha\tau_0}\mathbf{Re}_{N\times N}\left[\begin{array}{cc}\hat{\mathbf{W}}_{\mathrm{diag}}^{\ddagger}\mathbf{I}_N & \mathbf{0}_{N\times N}\end{array}\right]\left(\check{\mathbf{U}}_{N\times Q} + 2\left[\begin{array}{cc}\mathbf{I}_N & j\mathbf{I}_N\end{array}\right]\right.}_{\mathrm{POP}} \\ &\times \left.\left[\begin{array}{cc}[\mathbf{C}_N^{\mathrm{III}}]^T & \mathbf{0}_{N\times N} \\ \mathbf{0}_{N\times N} & [\mathbf{S}_N^{\mathrm{III}}]^T\end{array}\right]\underbrace{\left[\begin{array}{c}\mathbf{P}_{N\times N}^{s} \\ \mathbf{P}_{N\times N}^{as}\end{array}\right]\tilde{\mathbf{G}}_{\mathrm{diag}}[\mathbf{SP}]\mathbf{D}_{1\times 1}^{\beta}}_{\mathrm{PRP}}\mathbf{u}_{1\times(Q+b-1)M}\right), \end{aligned} \tag{8.79}$$

where $[\mathbf{C}_N^{\mathrm{III}}]^T$ and $[\mathbf{C}_N^{\mathrm{III}}]^T$ stand for IFCT-III and IFST-III transform matrices, respectively; $\check{\mathbf{U}}_{N\times Q}$ is a matrix with size $N \times Q$ and each column vector being $[\tilde{U}(0) + j\tilde{U}(N), \tilde{U}(0) - j\tilde{U}(N), \cdots, \tilde{U}(0) + j\tilde{U}(N)(-1)^{N-1}]^T$; $\hat{\mathbf{W}}_{\mathrm{diag}}^{\ddagger}$ and $\tilde{\mathbf{G}}_{\mathrm{diag}}$ are the same as in (8.68).

The direct implementation of IFCT/IFST-III is reported in Appendix 10.6. Alternatively, we can also implement IFCT/IFST-III using FCT/FST-I using the "transposed" version of FCT/FST-III blocks, i.e. reversing the input-output of Figs. 8.22 and 8.23.

Complexity of the unified MCM demodulator

The unified MCM demodulator can be presented in either Fig. 8.32 for FFT kernel or Fig. 8.33 for using FCT/FST-I kernel. In Fig. 8.32, although the implementation of DMT demodulator using IFFT transform is different from the conventional FFT transform. However, taking the conjugate operation for the output of the IFFT transform leads to an equivalent demodulator as in Fig. 5.4. In Fig. 8.33, the realization of DMT demodulator with FCT/FST-I kernel can be found in [27].

As discoursed in the preceding pages, for the unified MCM demodulator using FFT kernel, we can choose RSR algorithm for implementing the IFFT transform. Thus, the complexity can be significantly reduced (the reported arithmetic complexities of M-point RSR are listed in Tab. 8.7).

Table 8.7: Arithmetic complexity of RSR-FFT kernel [47].

RM	$(M/2)\log_2 M - (3/2)M + 2$
RA	$(3/2)M\log_2 M - (5/2)M + 4$

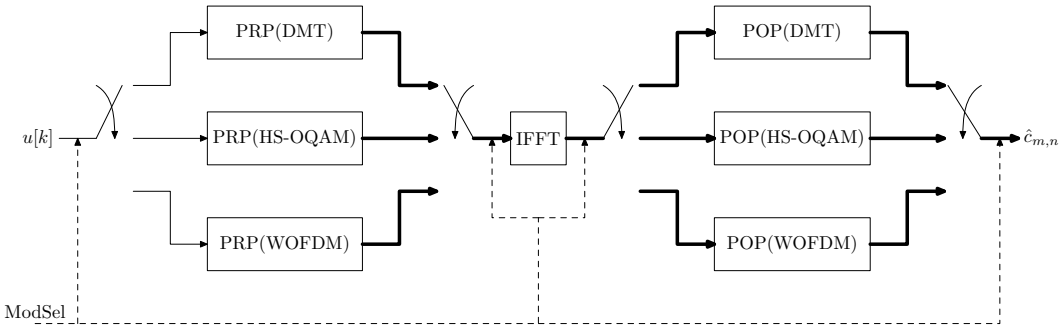

Figure 8.32: Unified MCM demodulator with FFT kernel.

On the other hand, our unified MCM demodulator can be realized by FCT/FST-I kernel. The complexity of this kernel is somewhat reduced compared with the modulator side due to the fact that we only need to compute the half of the carriers. In Tab. 8.8, we show the FCT/FST-I kernel complexity for the unified MCM demodulator.

Table 8.8: Arithmetic complexity of FCT/FST-I kernel.

RM	$N\log_2 N - 2N + 2$
RA	$(9/2)N\log_2 N - 5N + 4$

In Tab. 8.9, we give a comparison between these two kernels in terms of their arithmetic complexities.

The result reveals that RSR and FCT/FST-I kernels have the same complexity in real multiplications number and RSR has less real additions number than FCT/FST-I kernel, however, the difference is not huge. Therefore, if the unified MCM demodulator developers care much more about the complexity issue, FFT kernel with RSR algorithm should be chosen. Nevertheless, the irregularity of RSR algorithm makes the programming procedure more complicated. On the other hand, if the developers are willing to sacrifice a bit complexity to get an implementation algorithm with high regularity, FCT/FST-I kernel must be a good choice.

8.2.6 Unified MCM Transceiver Performance

In the following part, we report the performance gain when we use the unified MCM transceiver compared with the conventional non-flexible transceivers. We simulate the example when the comparison is based on an unified MCM transceiver vs. a pure HS-OQAM vs. a pure DMT. The unified MCM transceiver in our simulation is implemented using FCT/FST-I kernel.

If the transmission channel is not ideal, the receiver needs to use equalizer to com-

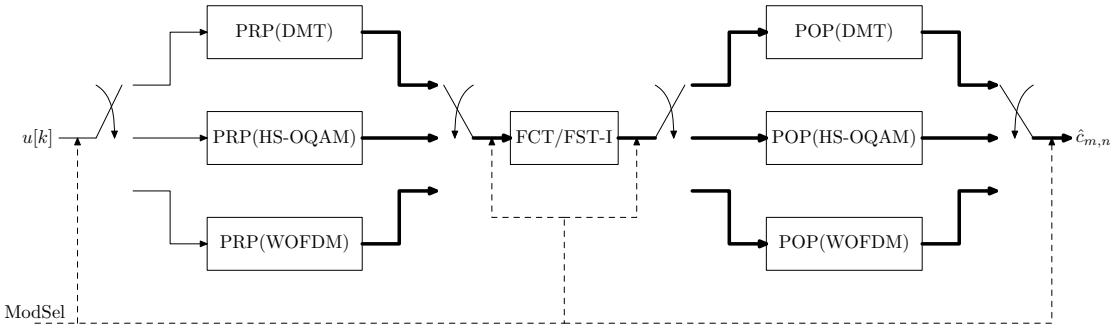

Figure 8.33: Unified MCM demodulator with FCT/FST-I kernel.

Table 8.9: Arithmetic complexity comparison for M carriers.

	real multiplications		real additions	
M	FCT/FST-I	RSR	FCT/FST-I	RSR
8	2	2	20	20
16	10	10	72	60
32	34	34	212	164
64	98	98	564	420
128	258	258	1412	1024
256	642	642	3396	2436
512	1538	1538	7940	5636
1024	3586	3586	18180	12804

pensate the channel distortion and to cancel the interference. Therefore, the equalizer can be implemented in the POP block of Fig. 8.33. In the following, we show the flexibility/adaptation gain that the unified MCM transceiver can provide. We compare the transmission throughput of HS-OQAM vs. DMT vs. unified MCM transceiver, the equalizer for DMT is ZF and for HS-OQAM is either ZF or ASCET. The channel models are realistic PLC models (class 3, 5 and 9). Channel estimation and synchronization are still assumed to be perfect. The prototype filter for HS-OQAM chain is Rossi4$_{\rho=1}$. Transmission parameters are related to HPAV specifications, i.e. FFT size: 3072[7]; CP for DMT: 417; Sampling frequency: 75 MHz. For unified MCM transceiver, the selection rule between DMT and HS-OQAM scheme is decided by Tab. 8.1. The results are reported in Figs. 8.34-8.36. We observe that with the unified MCM transceiver we always stay at the peak capacity situation. This gain comes from the "modulation flexibility gain" we introduced.

8.3 Flexibility over Prototype Filter

8.3.1 OFDM/OQAM Channel Estimation

For the topic of receiver processing, to perform a coherent detection, it is necessary to know the channel information. This can be done with the aid of the channel estimation (CE)

[7]This FFT size can be implemented using the prime factorized algorithm, i.e., $3072 = 2^{10} \times 3$.

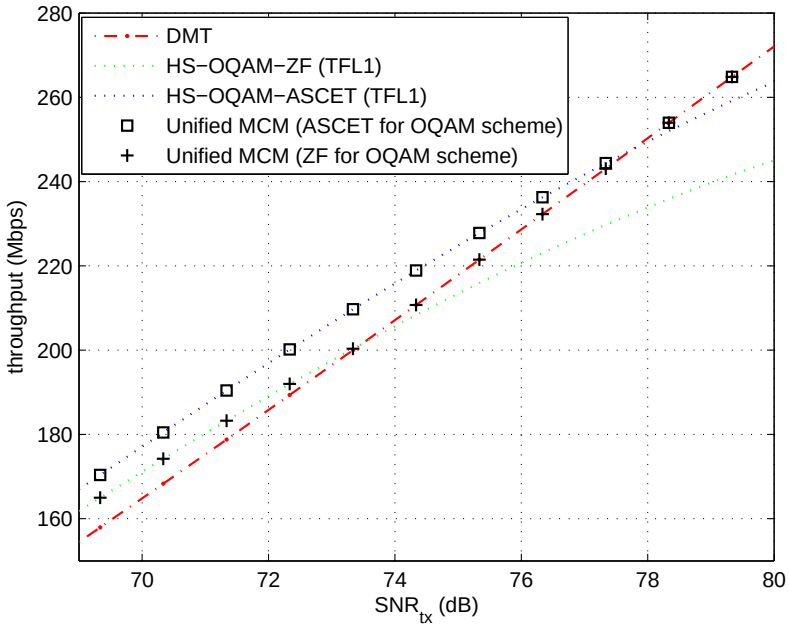

Figure 8.34: Throughput comparison: DMT vs. HS-OQAM vs. Unified MCM transceiver over Class 3.

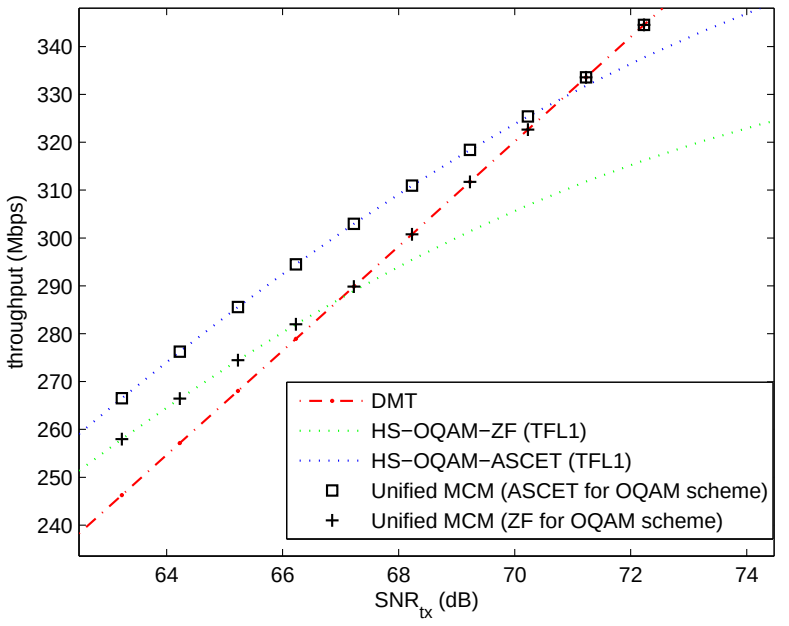

Figure 8.35: Throughput comparison: DMT vs. HS-OQAM vs. Unified MCM transceiver over Class 5.

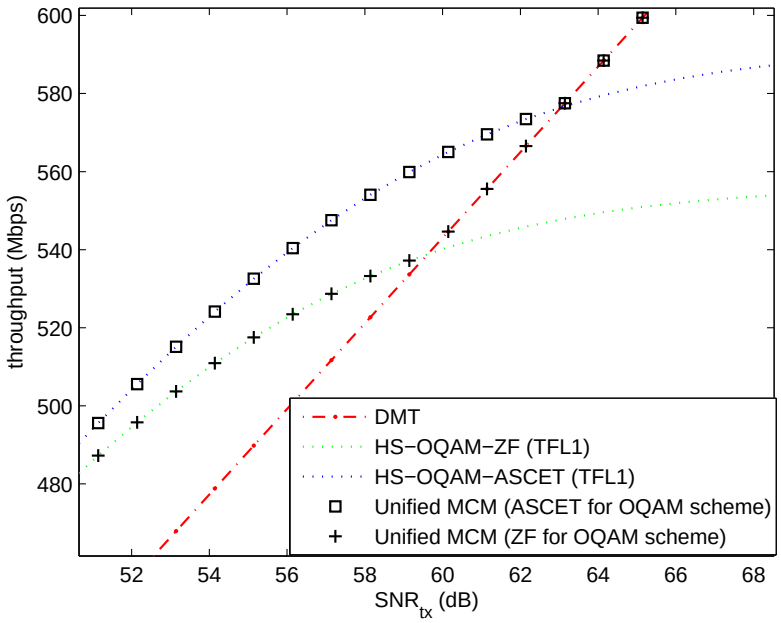

Figure 8.36: Throughput comparison: DMT vs. HS-OQAM vs. Unified MCM transceiver over Class 9.

process. In HPAV specification, a preamble sequence is inserted in the head of each frame for the purpose of synchronization and CE. At the receiver, for the OFDM system, due to the orthogonality feature at each subcarrier, the channel coefficients can be obtained by a simple Least-Square (LS) approach. Unfortunately, for the OFDM/OQAM system, the CE technique has just been touched recently [79, 72], where the authors presented a CE method using auxiliary pilots to cancel the so-called "intrinsic" interference. Inspired by these pioneer publications, the preamble-based CE methods were firstly presented in [83] for PLC and in [82] for wireless, therein the authors re-used the same channel model that was discussed in [79], and proposed two CE methods. The first proposed method was called Pair of Pilots (POP) and the second one was named Interference Approximation Method (IAM). It turns out that the POP method can provide a good performance when the noise is feeble or even absent. Furthermore, this method leads to a complexity augmentation compared to the LS approach. The IAM method, on the other hand, is proved to provide a very satisfying performance. Contrary to the "intrinsic-interference-cancellation" idea [79], IAM method not only keeps the intrinsic interference, but also takes advantage of the interference to further outperform OFDM for its noise immunity. Moreover, this method has the same computational complexity as the OFDM-CE. It was shown in [83] that the IAM method is prototype filter dependent, i.e., the different prototype filters give different performances. In this subsection, we focus on the IAM method and give a brief introduction of the CE model for the OFDM/OQAM system.

Channel Estimation Model

The feasibility of the CE for the OFDM/OQAM transmission is based on an approximation of the CE model. Let us analyze this model in details, recall that the OFDM/OQAM demodulator signal expression at the TF position (m_0, n_0) as (refer to Eq. (6.18)):

$$\begin{aligned} y_{m_0,n_0} &= \underbrace{\sum_{l=0}^{L_h-1} c_l A_g[-l,0] e^{-j\frac{2\pi m_0 l}{M}}}_{\alpha_{m_0}} a_{m_0,n_0} \\ &+ \sum_{(p,q)\neq(0,0)} a_{m_0+p,n_0+q} e^{j\frac{\pi}{2}(p+q+pq)} e^{j\pi p n_0} \underbrace{\sum_{l=0}^{L_h-1} c_l A_g[-qN-l, pF_0] e^{-j\frac{\pi(2m_0+p)l}{M}}}_{H_{m_0}^{(p,q)}}. \end{aligned}$$

The first approximation is based on the assumption that the ambiguity function does not vary too much for $l = 0, \cdots, L_h - 1$, i.e., $A_g[-l, 0] \simeq A_g[0, 0] = 1$ and $A_g[-qN - l, pF_0] \simeq A_g[-qN, pF_0]$. Thus, we have

$$\alpha_{m_0} \simeq \sum_{l=0}^{L_h-1} c_l e^{-j\frac{2\pi m_0 l}{M}} = H_{m_0}^c, \tag{8.80}$$

where we denote $H_{m_0}^c$ as the channel coefficient at the m_0-th carrier.

The second approximation is based on the second assumption that the immediate neighboring carriers w.r.t. (m_0, n_0) position experience the same channel characteristics and let us denote this immediate neighborhood zone as $\Omega_{1,1}^*$, i.e., for the time-invariant channel,

$$H_{m_0}^c \simeq \sum_{l=0}^{L_h-1} c_l e^{-j\frac{\pi(2m_0+p)l}{2M}} \Bigg| \, p \in \Omega_{1,1}^*. \tag{8.81}$$

The third approximation is that when the prototype is designed to have a good localization feature in time-frequency domain, the energy is assumed to be very much concentrated inside the zone of $\Omega_{1,1}^*$, i.e. the interference outside of $\Omega_{1,1}^*$ (denoted by $\bar{\Omega}_{1,1}^*$) is negligible comparing to the interference inside of $\Omega_{1,1}^*$.

Thus, the above demodulation model can be approximated as

$$y_{m_0,n_0} \simeq H_{m_0}^c (a_{m_0,n_0} + j a_{m_0,n_0}^{(i)}), \tag{8.82}$$

where $j a_{m_0,n_0}^{(i)}$ is the so-called "intrinsic" interference [79] having the form as

$$j a_{m_0,n_0}^{(i)} = j \sum_{(p,q)\in\Omega_{1,1}^*} a_{m_0+p,n_0+q} \underbrace{e^{j\frac{\pi}{2}(p+q+pq)} e^{j\pi p n_0} A_g[-qN, pF_0]}_{\langle g \rangle_{m_0+p,n_0+q}^{m_0,n_0}}. \tag{8.83}$$

Here, we retain the notation of $\langle g \rangle_{m_0+p,n_0+q}^{m_0,n_0}$ given in [83] meaning the scalar product of two base functions $g_{m_0,n_0}[k]$ and $g_{m_0+p,n_0+q}[k]$. As stated in Chap. 5 as well as in [83], the orthogonal condition restricts the term $\langle g \rangle_{m_0+p,n_0+q}^{m_0,n_0}$ for $(p, q) \neq (0, 0)$ to be a pure real-valued. It is easy to verify that the intrinsic interference is, then, a pure imaginary-valued

term. Thus, as long as we get the information of a_{m_0,n_0} and intrinsic interference $a^{(i)}_{m_0,n_0}$, the channel coefficient at the m_0-th carrier straightforwardly yields

$$H^c_{m_0} = \frac{y_{m_0,n_0}}{a_{m_0,n_0} + ja^{(i)}_{m_0,n_0}}. \tag{8.84}$$

Assume that we know the denominator part of (8.84) by using preamble sequence, say $p_{m_0,n_0} + jp^{(i)}_{m_0,n_0}$ (here p stands for preamble or pilot), given a name as "pseudo-pilot" in [83] and in the following we denote it as $\tilde{p}_{m_0,n_0}$. In the presence of a noise term b_{m_0,n_0}, the stronger the pseudo-pilot is, the better the CE performs, i.e.,

$$\hat{H}^c_{m_0} = H^c_{m_0} + \frac{b_{m_0,n_0}}{\underbrace{p_{m_0,n_0} + jp^{(i)}_{m_0,n_0}}_{\tilde{p}_{m_0,n_0}}}. \tag{8.85}$$

IAM Method

By using a preamble sequence, p_{m_0,n_0} is known by the receiver, but the knowledge of $p^{(i)}_{m_0,n_0}$ is not straightforward. Recently, Lélé *et al.* proposed an IAM method [83] that approximates this intrinsic interference with an intentionally generated preamble structure, such that the CE process (8.84) can be carried out. The basic IAM preamble structure is as follows. We insert a preamble sequence with a duration of $3\tau_0$, e.g., $p_{m,0}, p_{m,1}, p_{m,2}$, as shown in Fig. 8.37. Each pilot $p_{m,n}$ for $m \in [0, 2M-1]$ and $n \in [0, 2]$ can be randomly

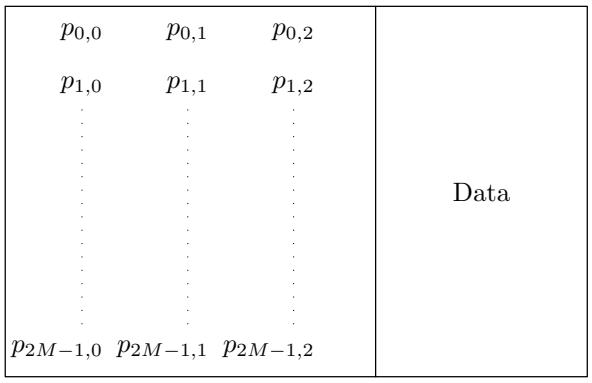

Figure 8.37: IAM preamble structure.

generated by taking either the real or imaginary part of a QPSK symbol, i.e., $p_{m,n} = \pm\sigma_a^2$. This leads to the proposed preamble structure called IAM2 in [83]. Then, on the receiver side, the CE is performed on the middle preamble column only, i.e.,

$$\hat{H}^c_{m_0} = H^c_{m_0} + \frac{b_{m_0,1}}{\tilde{p}_{m_0,1}}. \tag{8.86}$$

Thus, as proved in [81], the pseudo-pilot power of this preamble structure is not strong, i.e.

$$\mathrm{E}[|\tilde{p}_{m,1}|^2] < 2\sigma_a^2 = \sigma_c^2, \tag{8.87}$$

where σ_c^2 is the pilot power of the OFDM system. That means the CE performance using this IAM preamble structure is worse than that of OFDM system (see the simulation results in [83]).

To augment the pseudo-pilot power, in [83], the authors proposed a particular preamble structure called IAM1. The IAM1 structure can be presented as $p_{m,0} = p_{m,2} = 0$ and $p_{4k,1} = p_{4k+1,1} = 1$; $p_{4k+2,1} = p_{4k+3,1} = -1$ with $k = 0, \cdots, \frac{M}{4} - 1$ (see Fig. 8.38). This

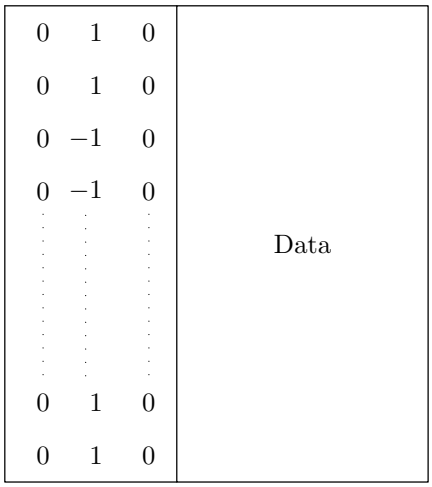

Figure 8.38: IAM1 preamble structure.

way, we can concentrate the preamble power on the middle column. Further, using IAM1 preamble structure, the pseudo-pilot power can be increased up to [81]

$$\mathrm{E}[|\tilde{p}_{m,1}|^2] = 2\sigma_a^2(1 + 4|\langle g\rangle_{m+1,1}^{m,1}|^2) > 2\sigma_a^2, \tag{8.88}$$

which results in a performance gain comparing with OFDM system. On the other hand, as the pseudo-pilot power is directly related to the prototype filter, for instance in [83] the authors showed that TFL1 filter performs better than IOTA4 filter. Therefore, this link should be analyzed in depth in order to find a proper criterion for filter design. In the forthcoming subsection, we analyze a decisive factor for OFDM/OQAM channel estimation and then present a good prototype filter that can better serve for the channel estimation.

8.3.2 Prototype Filter Flexibility for Channel Estimation

In this subsection, we study the decisive factor that directly judges the channel estimation performance. Moreover, we remark that, for the preamble-based CE with IAM1 preamble structure, since the receiver knows the pseudo-pilot value, besides, the interference from every even-tap neighborhood (in frequency domain) symbols are automatically destructed [81], the conventionally supposed orthogonality constraint of the prototype filter design for preamble transmission may not be necessary. Thus, relaxing the orthogonality constraint can provide greater degree of freedom to ameliorate this decisive factor.

Decisive Factor

The IAM1 preamble structure was originally proposed in [83] where 3 column preambles are introduced denoting $p_{m,0}, p_{m,1}, p_{m,2}$, respectively, with $p_{m,0} = p_{m,2} = 0$ and $p_{4k,1} = p_{4k+1,1} = 1$; $p_{4k+2,1} = p_{4k+3,1} = -1$ with $k = 0, \cdots, \frac{M}{4} - 1$. In this way, the pseudo-pilot at the m-th frequency index and the middle column yields [83]

$$\tilde{p}_{m,1} \approx p_{m,1} + j(2p_{m+1,1} \langle g \rangle_{m+1,1}^{m,1}). \tag{8.89}$$

Let us denote $| \langle g \rangle_{m+1,1}^{m,1} | = \beta_0$, thus, the pseudo-pilot power results in

$$\mathrm{E}[|b_{m,1}|^2] = 2\sigma_a^2(1 + 4\beta_0^2), \tag{8.90}$$

and the resulting CE noise power yields $\frac{\sigma_n^2}{2\sigma_a^2(1+4\beta_0^2)}$ where σ_n^2 is the noise variance. Then, it is obvious that the noise power depends upon the value of β_0. We can expect that the larger β_0 value is, the better CE will be. For example, in [83], two different prototype filters are compared, i.e., TFL1 and IOTA4. The results showed that TFL1 outperforms IOTA4 and the values of β_0 for these two filters are 0.538 for TFL1 and 0.441 for IOTA4, which confirms our argument. Therefore, it seems that β_0 is the decisive factor to affect the efficiency of OFDM/OQAM CE. Next, we write

$$\langle g \rangle_{m+1,1}^{m,1} = \sum_{k \in \mathbf{Z}} g_{m,1}[k] g_{m+1,1}^*[k] = jA_g[0,1]. \tag{8.91}$$

Hence, $A_g[0,1]$ can be re-written as

$$A_g[0,1] = \sum_{k \in \mathbf{Z}} g^2[k] e^{j2\pi \frac{k}{M}} = \sum_{k \in \mathbf{Z}} g^2[k] \cos\left(2\pi \frac{k}{M}\right), \tag{8.92}$$

where the last equation is because we assume that the filter $g[k]$ is a real and even function and, for the economical purpose as well as to avoid interfering with the payload, the designed filter has a length of M (e.g., $L_f = M$). Then β_0 can be expressed as

$$\beta_0 = |jA_g[0,1]| = \left| \sum_{k=-\frac{M}{2}}^{\frac{M}{2}-1} g^2[k] \cos(2\pi \frac{k}{M}) \right|. \tag{8.93}$$

Maximizing β_0 is equivalent to maximizing the term of $|\sum_k g^2[k] \cos(2\pi \frac{k}{M})|$. Moreover, since we fix the prototype filter length to M, the term $\cos(2\pi \frac{k}{M})$ gives one period of cosine mask, as shown in Fig. 8.39 where β_0 links to the sum of the products of $g^2[k]$ and $\cos(2\pi \frac{k}{M})$. Then naturally, we expect that the energy of $g^2[k]$ concentrates on the peak of the cosine mask. For example, for the three forms of functions $f_1[k], f_2[k]$ and $f_3[k]$ in Fig. 8.39, defining $\beta_0(g^2[k] = f_i[k]) := \beta_0(f_i)$, we have

$$\beta_0(f_1) > \beta_0(f_2) > \beta_0(f_3). \tag{8.94}$$

Consequently, the energy concentration can be viewed as a measure of time localization (TL) of the prototype filter $g[k]$.

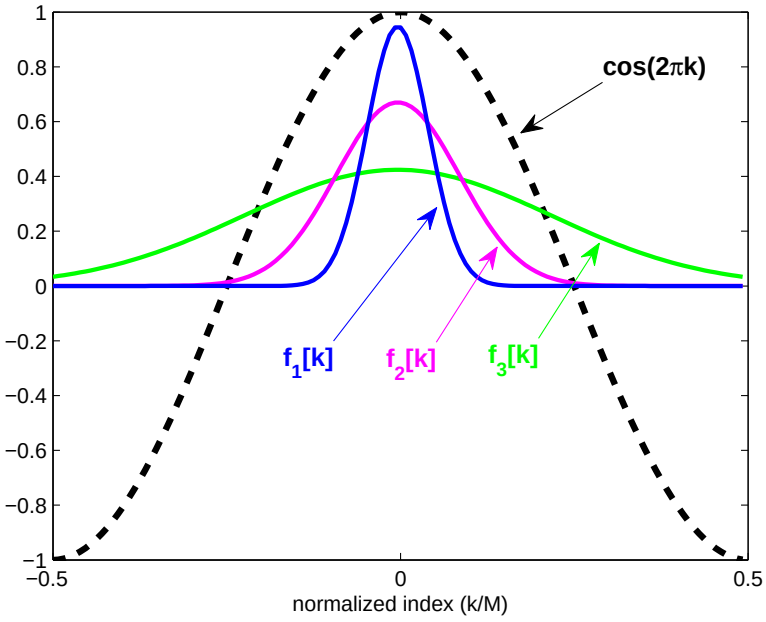

Figure 8.39: β_0 analysis.

Localization Compromise

So, does this mean that by simply maximizing this TL measure of $g[k]$, we will get the best filter for CE? The answer is negative, due to the neglected interference in (8.82). This interference is related to the scalar product $\langle g \rangle_{m+p,1}^{m,1}$ with $|p| > 1$ leading to $\langle g \rangle_{m+p,1}^{m,1} = j^p A_g[0,p]$. We then introduce another parameter, say β_I, that directly impacts the total interference power, and is given by $\beta_I = |\sum_p \langle g \rangle_{m+p,1}^{m,1}|$ for $p = \pm 2, \pm 3 \cdots$. Thanks to the particular preamble structure of IAM1 and the symmetry property of $A_g[0,p]$, the interferences only come from the even index of p and can be formulated, for $p = 2, 4, \cdots$, as

$$\beta_I = \left| 2 \sum_p \sum_k g^2[k] \cos(2\pi \frac{pk}{M}) \right|. \tag{8.95}$$

From (8.95), we find that if we maximize/minimize β_0 by refining/relaxing the TL of $g[k]$, the interference impact β_I will be increased/decreased simultaneously. Since β_I eventually verifies the validation of the approximation model (8.82), the compromise of both β_0 and β_I needs to be treated. Furthermore, the interference impact β_I can be essentially understood as a measure of the frequency localization (FL) of $g[k]$.

So far, we discoursed that we need to consider both TL and FL measures (β_0 and β_I), for a desired filter in order to get a good CE for the OFDM/OQAM system. As a matter of fact, the time-frequency (TF) localization degree of a discrete filter can be checked by a factor ξ, deduced from Doroslovački [44], related to the product of second order moments in time and frequency yielding

$$\xi = \frac{1}{4\pi\sqrt{m_2 M_2}} \leq 1, \tag{8.96}$$

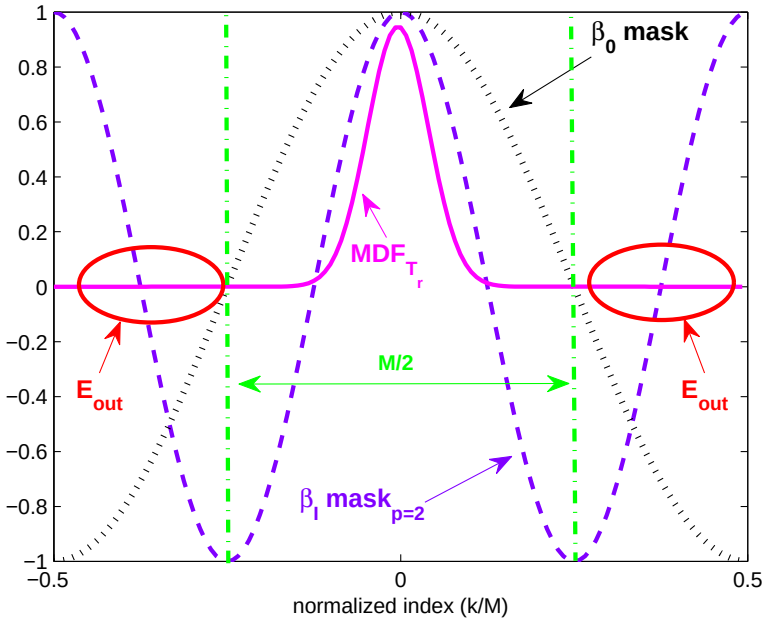

Figure 8.40: MOE criterion description.

where m_2 and M_2 are the second moment in time and frequency, respectively. Their expressions can be found in Sec. 5.1.5. The meaning of m_2 can be understood as the proportion of TL measure (i.e. $\beta_0 \propto \frac{1}{\sqrt{m_2}}$) and M_2 can be seen as the proportion of FL measure (i.e. $\beta_I \propto \sqrt{M_2}$). The ξ has an upper bound equal to 1. Moreover, Doroslovački also gave, in [44], a non-orthogonal and optimally-localized discrete filter, shortly named Doro filter, which attains the ξ upper bound and yields

$$g[k] = \frac{F(0)}{2^K} \frac{\Gamma(K+1)}{\Gamma(K/2+1-k)\Gamma(K/2+1+k)}, \tag{8.97}$$

for any given $K > \frac{1}{2}$, where $\Gamma(\cdot)$ is the Gamma function, and $F(0)$ can be simply set to 1. The Doro filter meets our requirement since it is non-orthogonal and attains the ξ bound. In what follows, we aim at designing a Modified Doro Filter (MDF) for our particular use of CE.

Proposed MDF Design Algorithms

Based on the Doro filter, we further introduce a time resolution parameter T_r to get a new MDF expressed as

$$g[k] = \frac{1}{2^K} \frac{\Gamma(K+1)}{\Gamma(K/2+1-kT_r)\Gamma(K/2+1+kT_r)}, \tag{8.98}$$

where K is fixed to $L_f - 1$ with $L_f = M$ being the filter length. By modifying T_r parameter, we can then arbitrarily play around with the compromise of TL and FL to satisfy our CE requirement, whilst still retaining the product of TF localization being maximum (i.e.

$\xi = 1$). The interest of using MDF is that since MDF has $\xi = 1$, so, compared with other possible non-orthogonal filters of length $L_f = M$, it leads to the minimum β_I for a same level of the β_0 and vice versa. Therefore, the goal now is to find an appropriate T_r by which the corresponding MDF can best serve the CE. In the following, we propose two criteria to design our MDF. The first one is called Maximum Outside Energy (MOE) criterion and the other is named Maximum Weighted Combining $\beta_{\{0,I\}}$ (MWCβ) criterion.

MOE Criterion

This criterion is inspired by the remark that, for β_I, the interference mask is now $\cos(\frac{2\pi pk}{M})$, i.e., with increasing p, the corresponding cosine mask becomes much denser than the mask of β_0, e.g., p periods during filter length ($L_f = M$) and since, $g^2[k]$ is always positive-valued spreading the energy of $g^2[k]$ (by means of relaxing the TL of $g[k]$) into the negative area of the interference mask, the β_I can be automatically reduced. Meanwhile, in order to keep β_0 to be a predominant value, we need to concentrate most of the energy of $g^2[k]$ in the positive area of β_0 mask.

The MOE criterion description is depicted in Fig. 8.40, where we start by a MDF with $T_r = 1$, then we shrink the T_r by a step δ until the outside energy E_{out} of the MDF goes beyond a defined threshold ϵ. This operation is equivalent to relaxing the TL of MDF. Note that during this operation we need to constantly monitor the ξ value of every updated MDF in order to keep $\xi \simeq 1$ (e.g. $1 - \xi < \xi_T = 10^{-3}$). The MDF design based on MOE criterion can be implemented as below, where we set $\delta = \frac{1}{M}$, $\epsilon = 10^{-3}$.

Algorithm 1 MOE Criterion

initial $T_r = 1$, $\delta = \frac{1}{M}$, $\epsilon = 10^{-3}$, $\xi_T = 10^{-3}$
generate MDF with $T_r := \text{MDF}_{T_r}$
while $E_{\text{out}}(\text{MDF}_{T_r}) < \epsilon$ **do**
  $T_r = T_r - \delta$
  if $1 - \xi(\text{MDF}_{T_r}) > \xi_T$ **then**
    $T_r = T_r + \delta$; break
  end if
end while

MWCβ Criterion

The MWCβ criterion is quite straightforward, which aims to solve

$$\max_{T_r}\{w\beta_0 - (1-w)\beta_I\} \quad \text{subject to} \quad \xi(T_r) \in [1-\xi_T, 1]$$

where w is the weighting factor with $0 \leq w \leq 1$ indicating the importance between β_0 and β_I. The optimal value of w can be determined by the simulations targeting the best performance. The algorithm is detailed in **Algorithm 2** table, where the initial maximum value $\Delta_{\max}$ should be set as small as possible to launch the algorithm.

Algorithm 2 MWCβ Criterion

initial $T_r = 1$, $\delta = \frac{1}{M}$, w, $\Delta_{\max} = -10^3$, $\xi_T = 10^{-3}$
generate MD_{T_r}
while $w\beta_0(\mathrm{MD}_{T_r}) - (1-w)\beta_I(\mathrm{MD}_{T_r}) > \Delta_{\max}$ **do**
  $\Delta_{\max} = w\beta_0(\mathrm{MD}_{T_r}) - (1-w)\beta_I(\mathrm{MD}_{T_r})$
  $T_r = T_r - \delta$
  if $1 - \xi(\mathrm{MD}_{T_r}) > \xi_T$ **then**
    $T_r = T_r + \delta$; break
  end if
end while

Prototype Filter Flexibility

The flexibility of the prototype filter in OFDM/OQAM system has been noticed in this thesis. However, this property has not been well addressed yet in literature. In this section, we introduce a prototype filter flexibility gain for CE process. To exploit this gain, we intend to separately choose variant prototype filters for preamble and payload transmissions, respectively, i.e., we select the MDF to be the prototype filter for preamble modulation and demodulation. Meanwhile, we select the PR or NPR filters for payload transmission. This way, we are able to play around with the time-frequency localization compromise of the prototype filter to serve for different purposes, e.g., CE or payload transmission.

In the following, we present our simulation results. In our simulations, we evaluate the channel estimation efficiency in terms of BER versus E_b/N_0 plotting. The simulated systems are CP-OFDM, conventional OFDM/OQAM system using a constant prototype filter (TFL1 or Rossi4$_{\rho=1}$) and proposed OFDM/OQAM system using a flexible prototype filters, i.e. MDF for preamble transmission and TFL1/Rossi4$_{\rho=1}$ for payload transmission. We keep the same simulation environment as [83], i.e., the channel model is Ma's channel [87] (normalized); the number of carriers is $M = 128$ and the CP length for CP-OFDM is fixed to be $M/8$; the sampling frequency is 10 MHz.

Let us first see the QPSK case, i.e., payload symbols are obtained from QPSK constellations. The reason of checking this case is that the interference effect for OFDM/OQAM system is not significant in QPSK transmission. Thus, we can focus on the CE efficiency. The result is reported in Fig. 8.41, where the simulated cases are CP-OFDM (denoted CP-OFDM in the figure), conventional OFDM/OQAM using TFL1 prototype filter for both preamble and payload transmission (denoted OQAM-TFL1), conventional OFDM/OQAM using Rossi4$_{\rho=1}$ for both preamble and payload transmission (denoted OQAM-Rossi4) and the proposed OFDM/OQAM system separately using MDF and TFL1 prototype filters for preamble and payload transmissions with aforementioned two algorithms (denoted MOE-TFL1 and MWCβ-TFL1, respectively). Furthermore, in the figure, we also show two lower bounds (LBs) for CP-OFDM and OFDM/OQAM. These bounds are obtained by assuming the receiver perfectly knows the channel coefficients. The channel equalization in this simulation is ZF for all the curves.

From the figure, we observe that the OQAM-TFL1 and OQAM-Rossi4 systems outperform CP-OFDM. This is due to the noise robustness of OFDM/OQAM with IAM

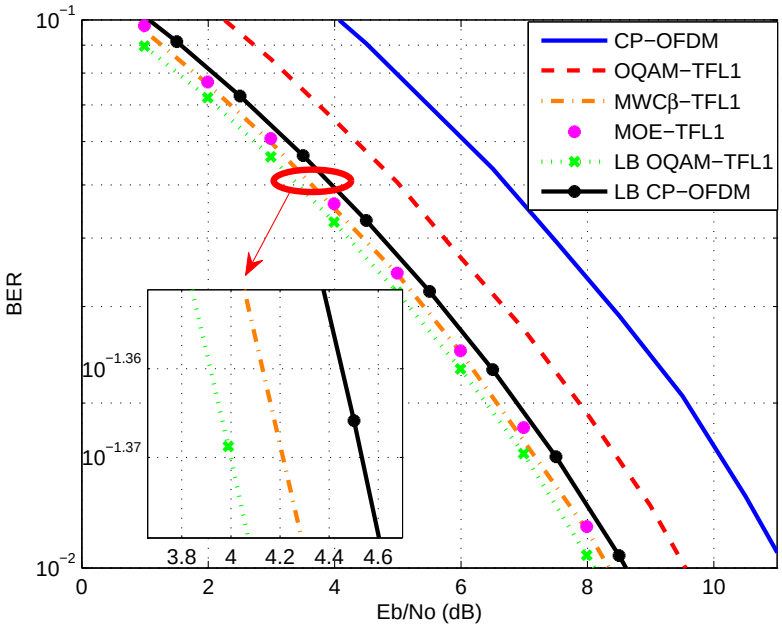

Figure 8.41: BER vs. E_b/N_0 results for QPSK transmission.

(refer to Sec. 8.3.1). Moreover, OQAM-TFL1 further outperforms OQAM-Rossi4. This is because TFL1 filter has a higher value for the decisive factor β_0 (β_0(TFL1)=0.538, β_0(Rossi4)=0.261). Compared to CP-OFDM, OQAM-TFL1 has a gain of 1.5 dB. Next, we take a look at the result for our proposed OFDM/OQAM system using flexible MDF and TFL1 filters. The MOE-TFL1 and MWCβ-TFL1 curves have very close performance (MWCβ-TFL1 is somewhat better) and the resulting T_r for these two algorithms are T_r(MOE)=0.4062 and T_r(MWCβ)=0.46094 corresponding to the decisive factor values as $\beta_0(\text{MDF}_{\text{MOE}}) = 0.8901$ and $\beta_0(\text{MDF}_{\text{MWC}\beta}) = 0.9136$. Compared to CP-OFDM, MWCβ-TFL1 has a 3 dB gain at the coding cut-off (CCO) range (i.e. around BER 5×10^{-2} for Turbo or LDPC) and it even outperforms the CP-OFDM LB case. Compared to OQAM-TFL LB, MWCβ-TFL1 can almost attain this bound with only 0.2 dB distance.

Next, we see the case when the payload constellation is increased to be 64-QAM as shown in Fig. 8.42. Since in high constellation transmission case, the remaining interference problem becomes more obvious for OFDM/OQAM system, we can clearly see a performance floor for OQAM-TFL and OQAM-Rossi4. However, at the CCO range, they can still outperform CP-OFDM, but this time the performance gain is reduced (e.g. around 1 dB better than CP-OFDM for OQAM-TFL). Move to the proposed OFDM/OQAM using flexible prototype filter case[8], MWCβ-TFL1 outperforms CP-OFDM 2.5 dB gain at CCO range. We can further replace TFL1 by Rossi4 filter (denoted MWCβ-Rossi4) since Rossi4 filter is more suitable for payload transmission (refer to Chap. 6). Thus, MWCβ-Rossi4 can provide 2.7 dB gain compared to CP-OFDM. Furthermore, we can use a more powerful equalizer (say, ASCET) for OFDM/OQAM system to reduce the interference effect. Thus,

[8]We focus on the MWCβ algorithm case since it gives a better performance.

the curve, MWCβ-Rossi4-ASCET, gives the best performance and it can almost retain 3 dB gain comparing to CP-OFDM. Compared to CP-OFDM LB, MWCβ-Rossi4-ASCET can attain this bound and has 0.2 dB distance from the MWCβ-Rossi4-ZF LB.

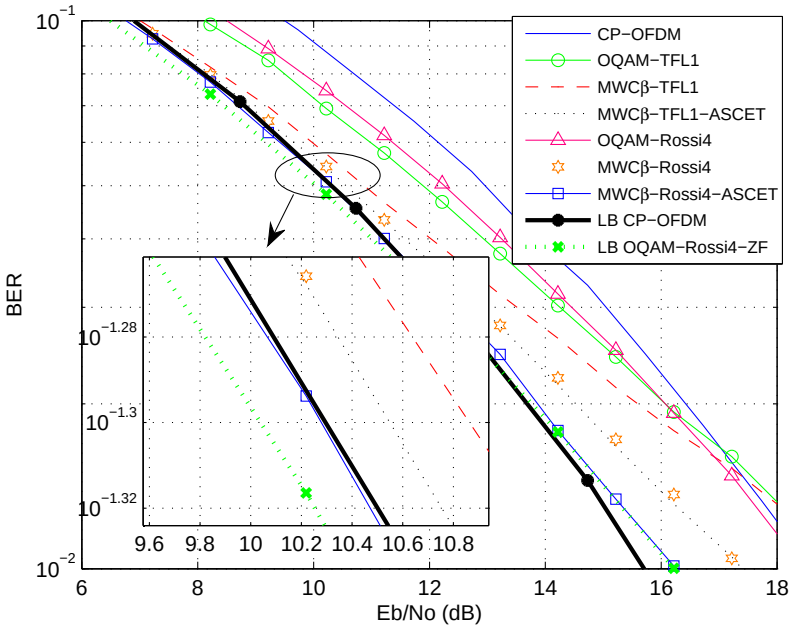

Figure 8.42: BER vs. E_b/N_0 results for 64-QAM transmission.

Finally, let us see the case of 256-QAM transmission (see Fig. 8.43). For this constellation case, the interference effect in OFDM/OQAM becomes extremely serious. In result, the conventional OQAM-TFL1 and OQAM-Rossi4 systems cannot work property, i.e. they do not have performance gain compared to CP-OFDM at the CCO range (OQAM-TFL1 performance even worse than CP-OFDM). However, thanks to our proposed scheme, MWCβ-Rossi4, the enlarged gain can be retained at the CCO range (0.7 dB compared to CP-OFDM). Furthermore, MWCβ-Rossi4 curve can still have more than 2 dB gain compared to CP-OFDM at the CCO range. Compared to the LB cases, MWCβ-Rossi4, this time, attains the MWCβ-Rossi4-ZF LB and has 0.5 dB distance from the CP-OFDM LB.

As to the complexity issue, our proposed OFDM/OQAM with flexible prototype filters has exactly the same complexity as in the conventional OFDM/OQAM case.

8.4 Conclusion

This chapter addresses the flexibility issue in PLC. We first analyzed the transmission capacity over PLC channels for HS-OQAM and OFDM/DMT systems. The theoretical analysis shows that in each PLC channel class case, there exists a SNR threshold, beyond which, OFDM/DMT can provide higher capacity than HS-OQAM scheme. Therefore, the flexibility comes from the MCM scheme adjustability w.r.t. the channel conditions. Al-

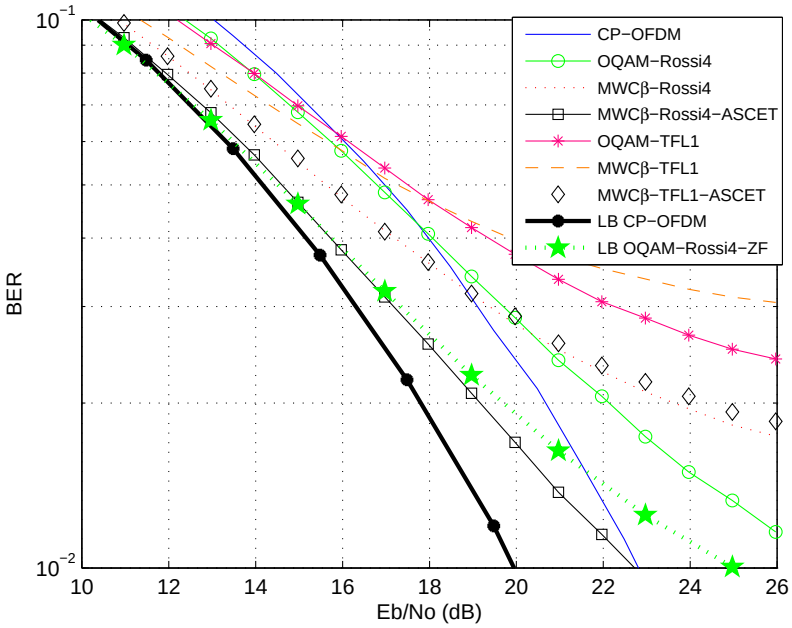

Figure 8.43: BER vs. E_b/N_0 results for 256-QAM transmission.

though, we pointed out that, subject to the recent HPAV specifications, this SNR threshold in some channel classes is not practical (i.e., HS-OQAM always has higher capacity than OFDM/DMT in the operation region), this flexibility issue still has its interest in the future standard. Next, we proposed a unified MCM transceiver, by which, this modulation flexibility can be realized. Furthermore, this unified MCM transceiver can be efficiently implemented using FCT/FST-I which has been proved to have less complexity than FFTs.

The second flexibility property is called prototype filter flexibility. This feature only exists for prototype filter shaped multi-carrier modulations, i.e., OFDM does not belong to this category. The flexibility of using different prototype filter gives the freedom to design the prototype for some particular uses, e.g. payload transmission or preamble for channel estimation. In this chapter, we studied the preamble-based channel estimation method, IAM, for the OFDM/OQAM system. We observed that for the channel estimation using the IAM1 preamble structure, the preamble part does not need to be filtered by an orthogonal prototype filter. Otherwise said, more degrees of freedom could be created, when reducing the orthogonality condition, and be given to prototype filter design w.r.t. the decisive factor. The modified Doro filter is that one. It is a non-orthogonal filter; it attains the maximum localization bound and it also maximizes the decisive factor. Therefore, when separately assigning the prototype filter to preamble filtering and payload filtering, we can have a gain due to the prototype filter flexibility.

Chapter 9

Conclusion

The main focus of this dissertation is the study of new communication technologies in PLC context. This is a really timing topic, because PLC has not yet had an official standard and the issue of the advanced communication technologies have rarely been addressed in literature. Actually, many problems, such as how to properly choose a modulation technique and the corresponding receiver methods, still remain to be solved. P1901 working group is entering the phase for preparing a draft PLC standard, wherein, multi-carrier idea has eventually been selected to be the modulation technique in the future final standard.

Thus, OFDM was straightforwardly proposed, with HPAV, to be a suitable candidate, owing to the fact that it has been widely used in many multi-carrier-based applications (e.g., WiFi, LTE etc.). Panasonic, as a strong competitor, suggests a wavelet OFDM (WOFDM) modulation scheme. These two schemes have been both selected in the current draft standard and a new PHY layer called dual-PHY layer has been resulted. France Telecom, on the other hand, comes up with an OFDM/OQAM proposal (first proposal was in ISPLC'07 conference). This OQAM idea was invented in 1966, but has been highlighted since 1995. Since then, many publications have appeared on this topic and a recent European PHY layer research project, PHYDYAS, particularly focuses on the scheme in the radio context [3]. Thus, OFDM/OQAM can be reasonably regarded as the future alternative to OFDM. Based on the above history, this dissertation talks about several aspects: in-home PLC channel analysis, OFDM/OQAM-based transmission design, theoretical analysis on OFDM/OQAM-based transmission, OFDM/OQAM channel equalization, OFDM/OQAM channel estimation and flexibility discussion in the PLC context.

The main results reported in this thesis are listed in the following:

- PLC channel analysis using Maximum Entropy Method (MEM) and Degree of Freedom (DoF) analyses.
- Theoretical OFDM/OQAM transmission model derivation over frequency selective channel.
- Prototype filter design criterion analysis.

- OFDM/OQAM transmission capacity analysis.
- OFDM/OQAM equalization techniques.
- A unified MCM transceiver proposal.
- Preamble-based OFDM/OQAM channel estimation using flexible prototype filters.

In the second chapter, we gave a brief overview of power line communications including the potential interests, the remaining challenges, the general network structure, the technologies lacking situation, and an introduction to IEEE P1901 working group. This chapter aims to stimulate the motivation of this thesis and gives the explanation why this thesis topic is timing and important for contributing in the PLC context.

In the third chapter, we introduced a new channel characteristic analyzing idea based on information theoretical tools and some channel modelling methods were presented in this chapter. The first tool was maximum entropy method (MEM), which can provide some information about the relationship between bandwidth and modelling entropy. We remarked that, for in-home PLC channels, the samples from the narrowband region can give us more information than those from high frequency region, i.e. wider-band might not be as helpful as expected for the channel modelling. Moreover, this situation appears more obviously in the case when the channel has higher capacity (larger class number channel). Furthermore, the power delay spectrum analysis told us that the small class number channels have longer delay spread, weaker channel gain than the large class number channels. The second introduced method was degree of freedom (DoF) method which is based on the subspace analysis theory. Combining the analyzed results of MEM and DoF, we pointed out that large number PLC channel case is more suitable for multiband systems.

The topic of multi-carrier system was commenced in the fourth chapter, wherein, general system structures of OFDM/DMT, WOFDM and OFDM/OQAM were presented. But, the main objective of this chapter was the study of OFDM and OFDM/OQAM. The PLC oriented multi-carrier versions, i.e. Windowed OFDM and HS-OQAM, were detailed in this chapter. Furthermore, we showed that a direct/straightforward advantage of using OFDM/OQAM, compared with OFDM, was the spectrum shape. This advantage can already provide more transmission data rate.

In the fifth chapter, we gave a deep insight into the OFDM/OQAM transmission. A general analytical OFDM/OQAM transmission model was derived therein, and this model could be utilized either in the radio or in the PLC context. Furthermore, based on this model, we, theoretically, proved and checked by simulations the fact that inter-carrier interference plays a more important role than inter-symbol interference in the OFDM/OQAM transmission over the PLC channel. This is contrary to the fact that for OFDM without CP, the inter-symbol interference and inter-carrier interference have the same importance [64]. Thus, we pointed out that more cares of inter-carrier interference should be taken for prototype filter design. However, a potential problem behind was the transceiver complexity and latency issue.

Inspired by this thought, in the sixth chapter, we discussed a very interesting question: “whether shall we use a long NPR prototype filter with a simple one-tap equalizer at the receiver or a short PR prototype filter with a more complex equalizer at receiver

when the channel has frequency selective behavior?". Two equalization methods were introduced in this chapter, i.e. modified ASCET and EIC. The former one is an extension of the existing point-wise equalizer, which has low complexity in the filter coefficients calculation. The latter one is a decision-feedback-like equalizer which takes advantage of the OFDM/OQAM transmission model to approximate the interference term and then to cancel it. At the end of this chapter, we concluded that a long NPR prototype filter can lead to an overall transmission with a better performance than when using a short PR filter, both using a simple one-tap equalizer, but at the price of high system complexity and latency. In the case of using a more complex equalizer, such as the modified ASCET, the receiver has, of course, a higher computational complexity for equalization than using a simple one-tap equalizer. However, the short PR filter leads to a small complexity in polyphase filtering process and small system latency, the overall system complexity of this case remains to be less than the one obtained for a long NPR prototype filter with simple one-tap equalizer. Furthermore, the performances of these two cases are close. In the case of the EIC equalizer, on the other hand, it results in the best performance but it leads also to the highest complexity. Therefore, the optimum choice among prototype filter, one-tap equalizer, ASCET or EIC should depend on the service requirements. In addition, the combination conception in the possible cases, e.g. long NPR with ASCET or EIC without high constraints on complexity or latency can further improve the system performance.

In the seventh chapter, we unveiled two novel flexibility gains, i.e. modulation flexibility and prototype filter flexibility gain. They can help us to exploit some additional gains in the PLC context. The inspiration of looking for the modulation flexibility came from the capacity analysis on the OFDM and OFDM/OQAM transmissions. We found that each scheme had its own pros and cons, i.e., OFDM does not have interference due to the CP appending, but also because of this CP, it has spectrum efficiency loss. OFDM/OQAM has full spectrum efficiency but it remains interference. Thus, there is no way we can announce a winner without taking into account transmission environments. So, in the sixth chapter, we pointed out, for each different in-home PLC channel situation, a SNR threshold, by which we can effectively judge whether OFDM is better than OFDM/OQAM or in reverse. Following this track, we next proposed a unified transceiver idea, which can be seen as a universal modulator-demodulator that can perform OFDM, OFDM/OQAM and WOFDM transmissions. Therefore, by referencing to the SNR threshold, we can arbitrarily switch the modulation scheme from one to the other for exploiting the modulation flexibility gain. Moreover, the proposed unified transceiver can be implemented using either FFT kernel or FCT/FST kernel. But FCT/FST kernel-based implementation was highly recommended in this chapter due to the fact that it has low complexity, high regularity and high flexibility. The second presented gain was the prototype filter flexibility gain. Since the OFDM/OQAM can flexibly choose its prototype filter, it actually leads to a sort of degree of freedom. Thereby, we can design different prototype filters for meeting different needs, i.e., variant criteria for payload transmission and preamble-based channel estimation. In this chapter, we also presented a modified Doro filter, based on the original paper of Doroslovački [44], that is proved to be optimum for the preamble-based OFDM/OQAM channel estimation with IAM1 preamble structure [83].

Due to the time limit, we cannot complete all the PHY technologies during this thesis. For instance, the synchronization techniques for OFDM/OQAM, coding topics, impulsive noise treatment, etc. Therefore, this thesis is not the end of the PLC research. It

actually opened a right door to the future research direction. Furthermore, some other topics have been studied during this Ph.D. program relating with multi-carrier systems, such as OFDM/OQAM system with CP option as well as MIMO space-time coding for OFDM/OQAM and vector-based OFDM. But they were not included in this thesis context because of either lacking of close relations with PLC or lacking of completeness of the work.

Chapter 10

Appendices

10.1 Examples of realistic PLC channel models

Here, we plot representive examples of the realistic channel models obtained by the PLC channel generator with sampling frequency $F_s = 75$ MHz. [121].

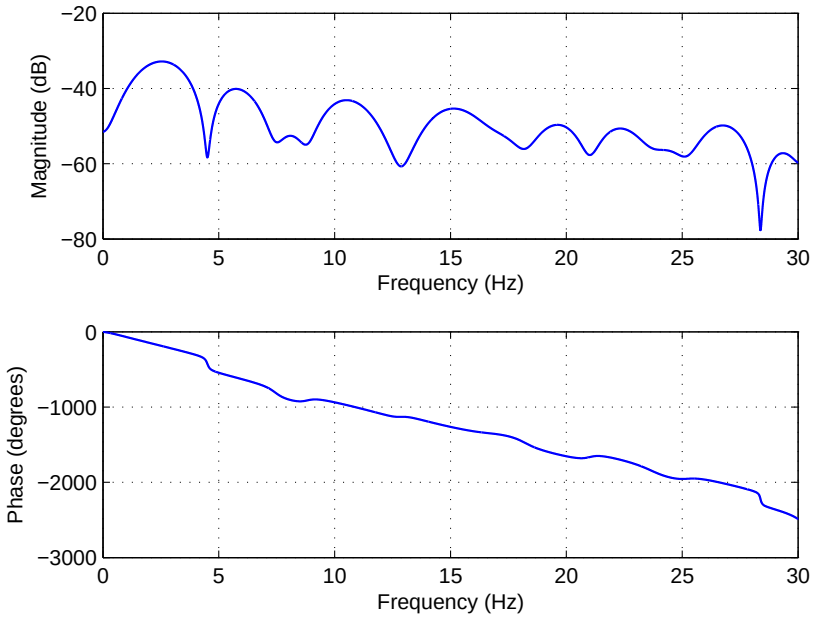

Figure 10.1: Example of channel class 2.

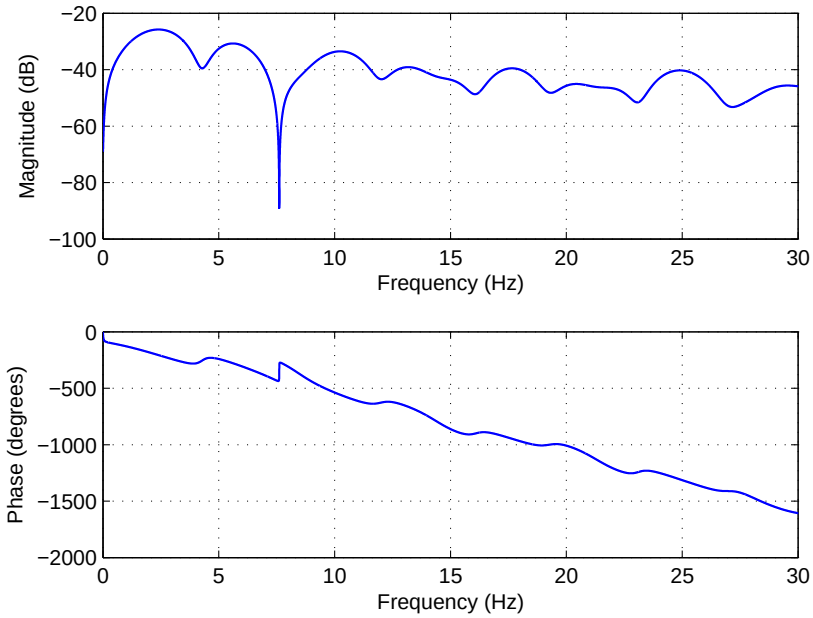

Figure 10.2: Example of channel class 3.

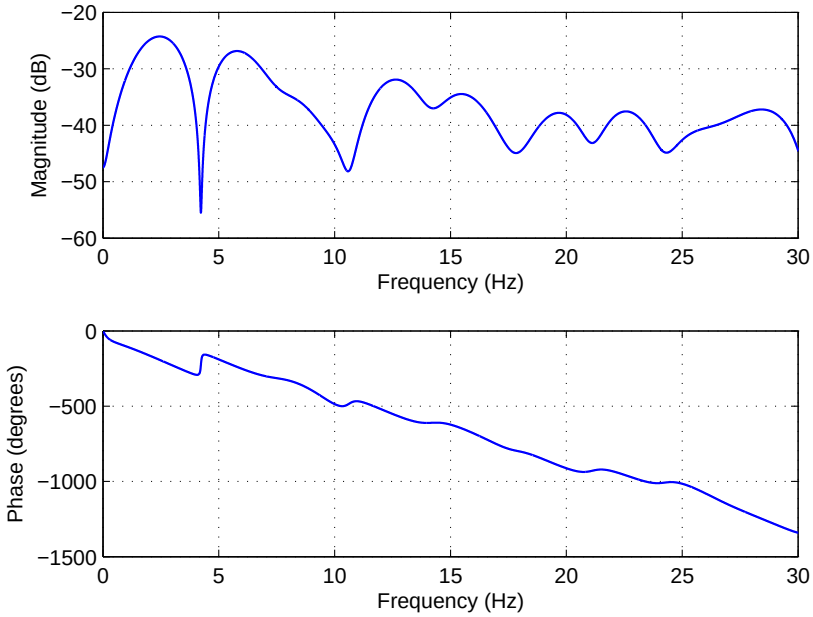

Figure 10.3: Example of channel class 4.

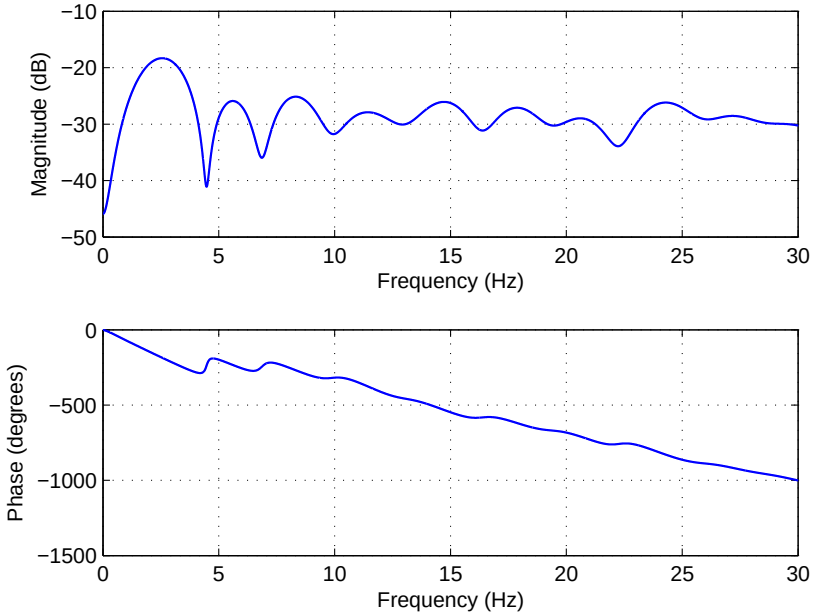

Figure 10.4: Example of channel class 5.

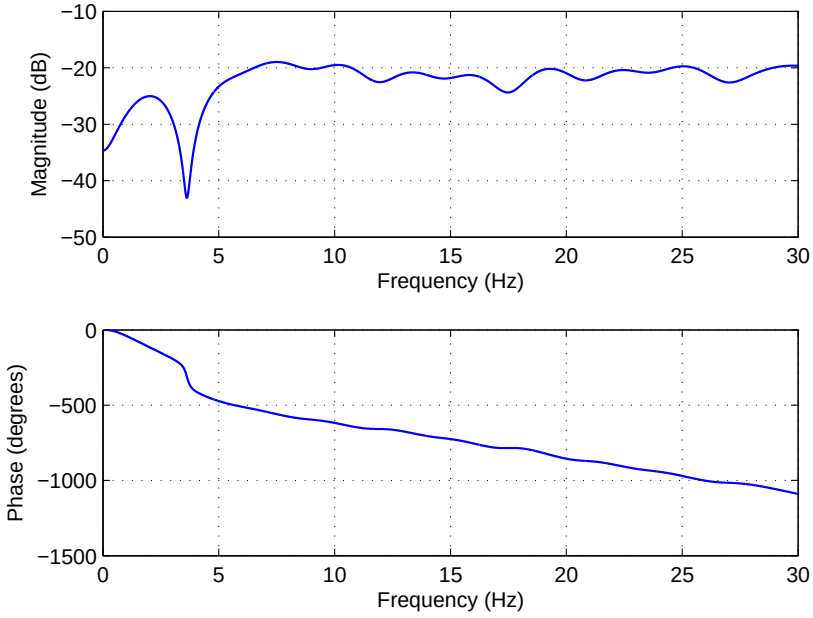

Figure 10.5: Example of channel class 6.

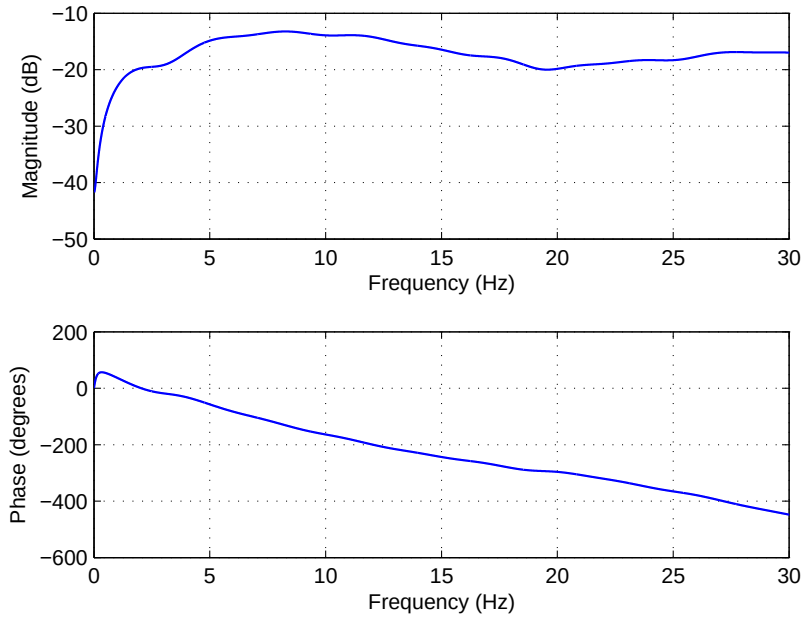

Figure 10.6: Example of channel class 7.

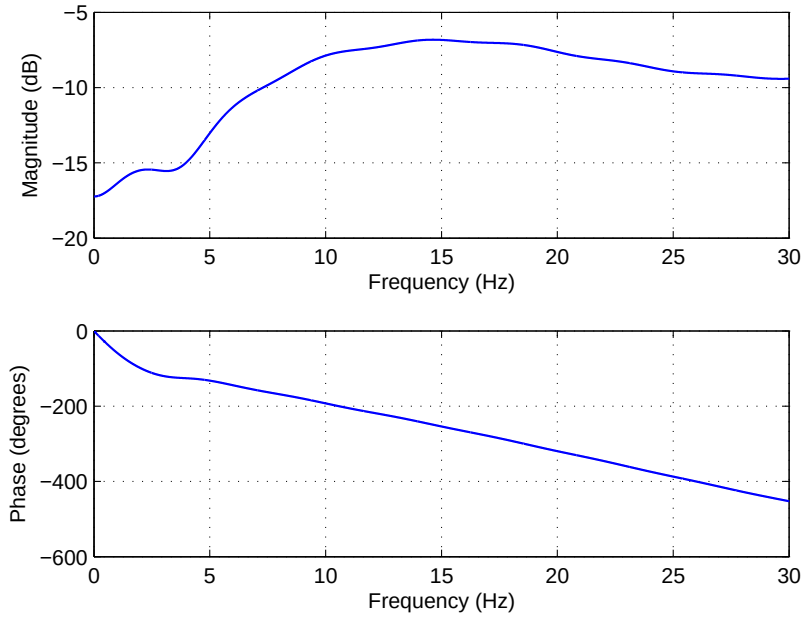

Figure 10.7: Example of channel class 8.

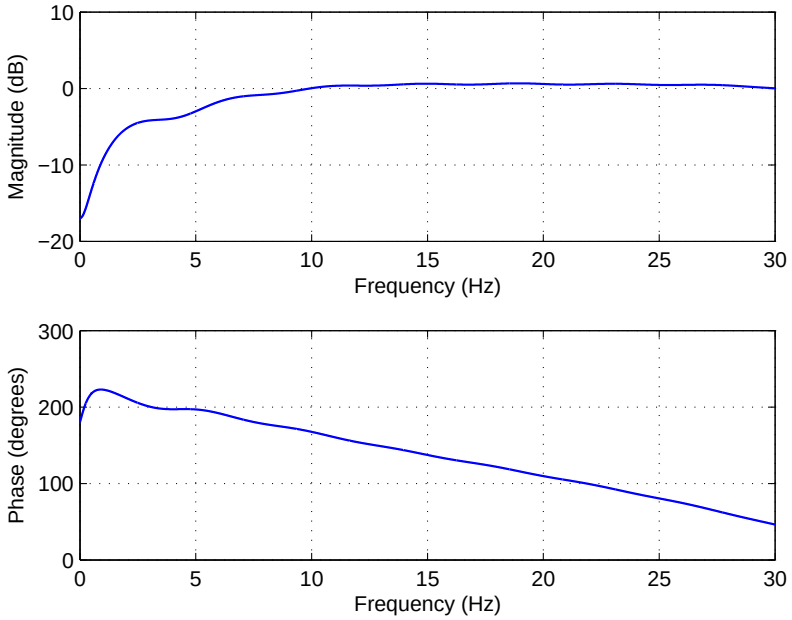

Figure 10.8: Example of channel class 9.

10.2 TFL prototype filter coefficients

In Tab. 10.1, we give the coefficients of the TFL prototype filter with length of $L_f = M = 128$.

10.3 Derivations of Eq. (7.12)

In what follows, we need to individually calculate each term in (7.12). Referencing to (7.11), the variance term of $\mathrm{Var}[\kappa_1]$ yields

$$\begin{aligned} \mathrm{Var}\left[\kappa_1\right] &= \sum_{\substack{l=0 \\ l\neq 1}}^{L_e-1} \sum_{\substack{l'=0 \\ l'\neq 1}}^{L_e-1} \tilde{e}_{l,m_0} \tilde{e}_{l',m_0} \mathrm{E}\left[a_{0,-l} a_{0,-l'}\right] \\ &= \sigma_a^2 \sum_{\substack{l=0 \\ l\neq 1}}^{L_e-1} |\tilde{e}_{l,m_0}|^2. \end{aligned} \tag{10.1}$$

Furthermore, since the variables in term κ_1 and κ_3 are totally independent, we have

$$\mathrm{Cov}\left[\kappa_1, \kappa_3\right] = 0. \tag{10.2}$$

Table 10.1: First half of the coefficients of the symmetric TFL prototype filter with length $L_f = M = 128$.

n	$g[n]$	n	$g[n]$	n	$g[n]$	n	$g[n]$
0	0.002000	16	0.040060	32	0.089813	48	0.119344
1	0.004010	17	0.043011	33	0.092588	49	0.120183
2	0.006040	18	0.046026	34	0.095255	50	0.120932
3	0.008097	19	0.049099	35	0.097806	51	0.121597
4	0.010190	20	0.052222	36	0.100235	52	0.122185
5	0.012326	21	0.055388	37	0.102537	53	0.122700
6	0.014513	22	0.058587	38	0.104708	54	0.123150
7	0.016755	23	0.061808	39	0.106746	55	0.123538
8	0.019059	24	0.065041	40	0.108650	56	0.123872
9	0.021429	25	0.068273	41	0.110420	57	0.124155
10	0.023868	26	0.071492	42	0.112059	58	0.124391
11	0.026380	27	0.074685	43	0.113569	59	0.124584
12	0.028967	28	0.077839	44	0.114953	60	0.124738
13	0.031628	29	0.080942	45	0.116218	61	0.124854
14	0.034366	30	0.083979	46	0.117367	62	0.124936
15	0.037177	31	0.086940	47	0.118407	63	0.124984

The calculation of $\mathrm{Var}[\kappa_2]$ is as follows

$$\begin{aligned}
\mathrm{Var}\left[\kappa_2\right] &= \mathrm{E}\left[\sum_{l=0}^{L_e-1}\sum_{l'=0}^{L_e-1}\sum_{p^0,q^0}\sum_{p'^0,q'^0}(-1)^{lp+l'p'}a_{p,q-l}a_{p',q'-l'}A_{l,m_0}^{p,q}A_{l',m_0}^{p',q'}\right] \\
&= \sum_{l=0}^{L_e-1}\sum_{l'=0}^{L_e-1}\sum_{p^0,q^0}\sum_{p'^0,q'^0}(-1)^{lp+l'p'}\mathrm{E}\left[a_{p,q-l}a_{p',q'-l'}\right]A_{l,m_0}^{p,q}A_{l',m_0}^{p',q'} \\
&= \sigma_a^2\sum_{l=0}^{L_e-1}\sum_{l'=0}^{L_e-1}\sum_{p^0,q^0}(-1)^{(l+l')p}A_{l,m_0}^{p,q}A_{l',m_0}^{p,q-l+l'}\bar{\delta}_{(\{p,0\}\{q,l-l'\})},
\end{aligned} \tag{10.3}$$

with

$$\bar{\delta}_{(\{p,0\}\{q,l-l'\})} = \begin{cases} 0 & \text{if } p=0 \text{ and } l-l'=q \\ 1 & \text{otherwise.} \end{cases}$$

The calculation of $\mathrm{Var}[\kappa_3]$ yields

$$\begin{aligned}
\mathrm{Var}\left[\kappa_3\right] &= \sum_{\substack{l=0\\l\neq 1}}^{L_e-1}\sum_{\substack{l'=0\\l'\neq 1}}^{L_e-1}A_{l,m_0}^{0,l-1}A_{l',m_0}^{0,l'-1}\mathrm{E}\left[a_{0,-1}a_{0,-1}\right] \\
&= \sigma_a^2\sum_{\substack{l=0\\l\neq 1}}^{L_e-1}\sum_{\substack{l'=0\\l'\neq 1}}^{L_e-1}A_{l,m_0}^{0,l-1}A_{l',m_0}^{0,l'-1}.
\end{aligned} \tag{10.4}$$

The covariance between κ_1 and κ_2 results in

$$\begin{aligned}\mathrm{Cov}\left[\kappa_1,\kappa_2\right] &= \sum_{\substack{l=0\\l\neq 1}}^{L_e-1}\sum_{l'=0}^{L_e-1}\sum_{p^0,q^0}\tilde{e}_{l,m_0}(-1)^{l'p}A^{p,q}_{l',m_0}\mathrm{E}\left[a_{0,-l}a_{p,q-l'}\right]\\ &= \sigma_a^2\sum_{\substack{l=0\\l\neq 1}}^{L_e-1}\sum_{l'=0}^{L_e-1}\tilde{e}_{l,m_0}A^{0,l'-l}_{l',m_0}\tilde{\tilde{\delta}}_{\{l',l\}}.\end{aligned} \tag{10.5}$$

with

$$\tilde{\tilde{\delta}}_{\{l',l\}} = \begin{cases} 0 & \text{if } l'=l\\ 1 & \text{otherwise.}\end{cases}$$

The last covariance between κ_2 and κ_3 yields

$$\begin{aligned}\mathrm{Cov}\left[\kappa_2,\kappa_3\right] &= \sum_{l=0}^{L_e-1}\sum_{\substack{l'=0\\l'\neq 1}}^{L_e-1}\sum_{p^0,q^0}(-1)^{lp}A^{p,q}_{l,m_0}A^{0,l'-1}_{l',m_0}\mathrm{E}\left[a_{0,-1}a_{p,q-l}\right]\\ &= \sigma_a^2\sum_{\substack{l=0\\l\neq 1}}^{L_e-1}\sum_{\substack{l'=0\\l'\neq 1}}^{L_e-1}A^{0,l-1}_{l,m_0}A^{0,l'-1}_{l',m_0}.\end{aligned} \tag{10.6}$$

10.4 Efficient Implementation of FCT/FST-I Transform

In this part, we briefly demonstrate the efficient implementation of FCT/FST-I given in [27]. For the N-point FCT-I, with $N=2^k$ and k a positive integer, we have

$$\mathrm{FCT_I}(l) = \sum_{m=0}^{N-1} x[m]C^{ml}_{2N}, \quad \text{for} \quad l=0,...,N-1. \tag{10.7}$$

Then, we decompose m of (10.7) into even and odd indices, for $l=0,...,\frac{N}{2}-1$, as

$$\mathrm{FCT_I}(l) = \sum_{m=0}^{N/2-1} x[2m]C^{ml}_{N} + \sum_{m=0}^{N/2-1} x[2m+1]C^{(2m+1)l}_{2N}. \tag{10.8}$$

Next, based on Lee's algorithm [80], (10.8) can be expressed, for $l=0,...,\frac{N}{2}-1$, as

$$\begin{aligned}\mathrm{FCT_I}(l) &= \underbrace{\sum_{m=0}^{N/2-1} x[2m]C^{ml}_{N}}_{g[l]}\\ &+ \frac{1}{2C^l_{2N}}\left[\underbrace{\sum_{m=0}^{N/2-1}\left(x[2m+1]+x[2m-1]\right)C^{ml}_{N}}_{h[l]} + \underbrace{x[N-1](-1)^l}_{q[l]}\right],\end{aligned} \tag{10.9}$$

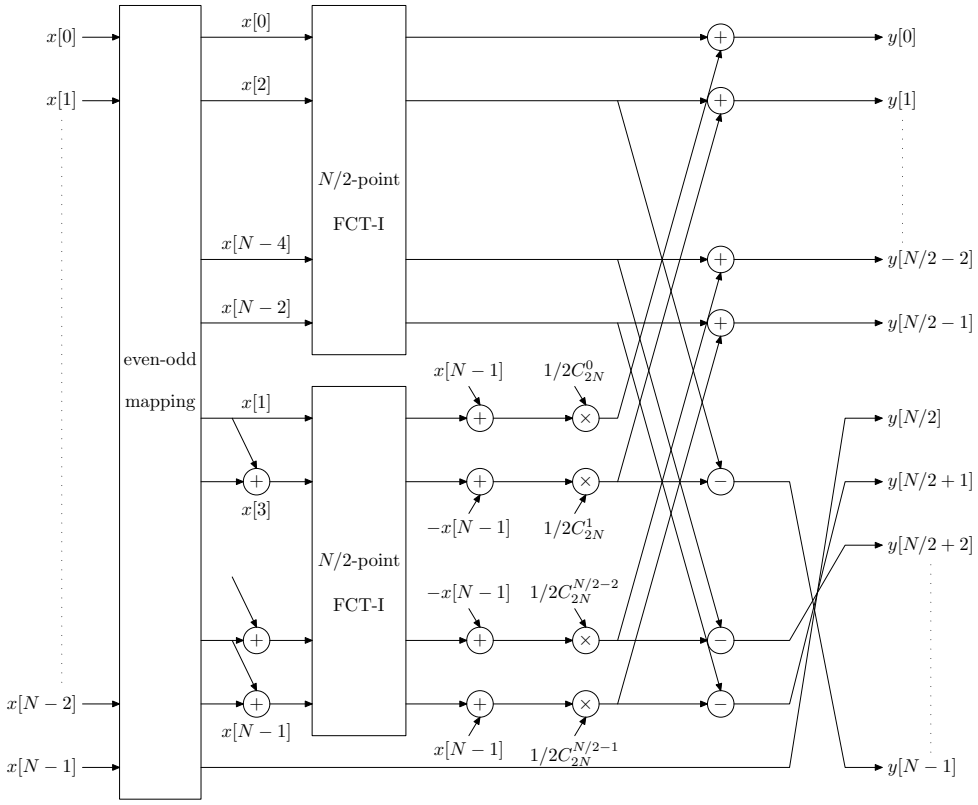

Figure 10.9: Efficient implementation of FCT-I.

where we assume $x[-1] = 0$. For the rest half $\mathrm{FCT_I}$ outputs we have

$$\mathrm{FCT_I}(N-l) = g[l] - \frac{1}{2C_{2N}^{l}}(h[l] + q[l]). \tag{10.10}$$

The special case $\mathrm{FCT_I}(N/2)$ yields

$$\mathrm{FCT_I}\left(\frac{N}{2}\right) = \sum_{m=0}^{N-1} x[m] \cos\frac{m\pi}{2}. \tag{10.11}$$

As shown in (10.9), the N-point FCT-I can be decomposed into two $N/2$-point FCT-Is. Then we can apply the technique of *divide-and-conquer* to recursively expand the N-point FCT-I until 1-point FCT-I. Note that the output of the 1-point FCT-I is equivalent to its input, i.e.

$$\mathrm{FCT_I}(0) = \sum_{m=0}^{0} x[m] C_{2N}^{0} = x[0]. \tag{10.12}$$

The implementation structure of FCT-I is depicted in Fig. 10.9.

A similar algorithm is found for FST-I transform implementation, i.e., for $l = 0, \cdots, N/2-1$, in which we have

$$\mathrm{FST_I}(l) = \sum_{m=0}^{N/2-1} x[2m] S_N^{ml} + \frac{1}{2C_{2N}^{l}} \sum_{m=0}^{N/2-1} \left(x[2m+1] + x[2m-1]\right) S_N^{ml}, \tag{10.13}$$

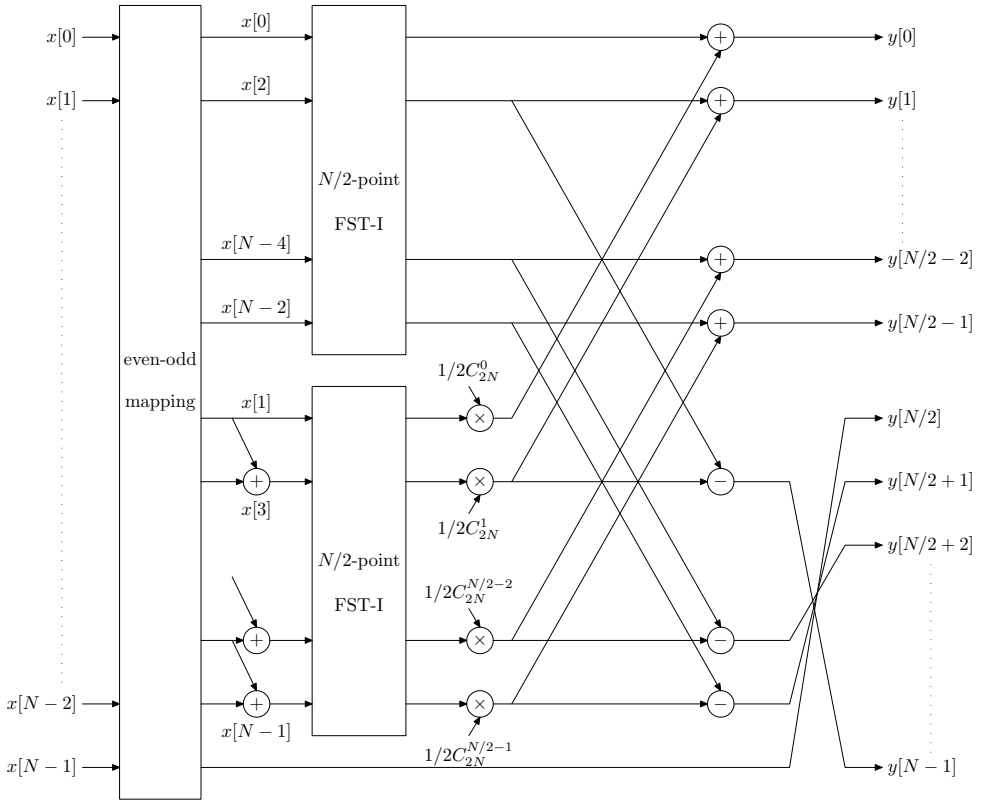

Figure 10.10: Efficient implementation of FST-I.

and

$$\mathrm{FST_I}(N-l) = -\sum_{m=0}^{N/2-1} x[2m] S_N^{ml} + \frac{1}{2C_{2N}^{l}} \sum_{m=0}^{N/2-1} \left(x[2m+1] + x[2m-1]\right) S_N^{ml}. \quad (10.14)$$

A special case results in

$$\mathrm{FST_I}(N/2) = \sum_{m=0}^{N-1} x[m] \sin\frac{k\pi}{2}. \quad (10.15)$$

Thus, same as in FCT-I case, we can decompose the N-point FST-I into 2 $N/2$-point FST-Is and forward until getting 1-point FST-I. The output of the 1-point FST-I is always zero. The implementation structure of FST-I is depicted in Fig. 10.10.

10.5 Complexity Analysis of FCT/FST-I

In this section, we discuss the complexity issue of FCT/FST-I transform comparing with FFTs. Although, in Chan's paper [27, 80], the complexity has already been given, however, the authors did not explain how to get these numbers. During the calculation by ourselves, we remarked that the complexity figures we found were not exactly the same as the ones given in [27], for the number of additions. Therefore, in the following subsection, we develop in detail our own computation.

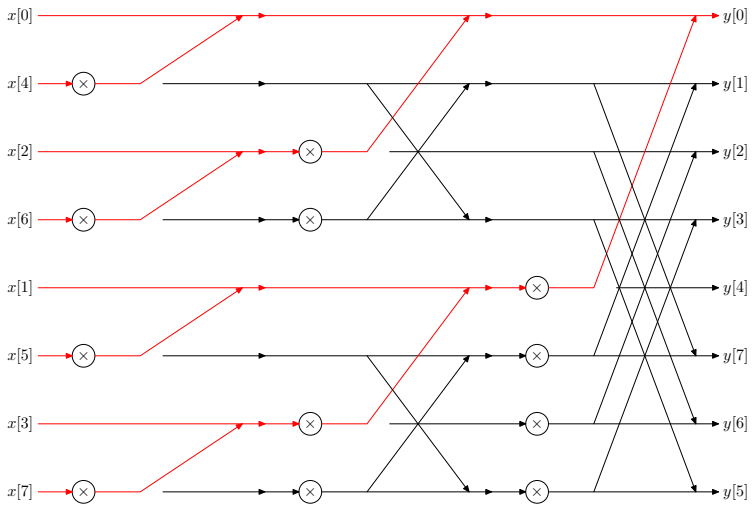

Figure 10.11: Example of partial 8-point FST-I.

10.5.1 Number of Multiplications

Let us first count the number of real multiplications. For FCT-I transform, in reference to (10.9) as well as Fig. 10.9, the multiply operation happens at each lower FCT-I outputs for each pair of decomposition and only in the recursion process. In addition, none of the weight factors, i.e. $1/2C_{2N}^{l}$, will be multiplied by a constant zero input. Therefore, for each recursion stage, the number of multiplications, for N-point FCT-I, yields $N/2$ and we have in total $\log_2 N$ stages which leads the total number of multiplications, due to the weight factors, to $\frac{N}{2}\log_2 N$. However, for the case of $l = 0$, it leads to $1/2C_{2N}^{0} = 0.5$, which is a trivial multiplication (i.e. bit shift operation). So we should not account this special case. Finally, the multiplication numbers are: $\frac{N}{2}\log_2 N - N + 1$. The other possible case for using multiplications is the special case of FCT-I, cf. Eq. (10.11), at each stage. However, we observe, due to the fact that the indices of m in Eq. (10.11) are always integers, that the multiplicands $\cos\frac{m\pi}{2}$ are either positive/negative ones or zeros, periodically. Thus, we do not need multiplications anymore, the whole calculation of this special case can be realized only with additions (note that, here we simple count a substraction as an addition). Since in the FCT-I transform all operations are in real field, so this complexity denotes real multiplications (RM). Next, we look at FST-I case, the principle of FST-I implementation is equivalent to that of FCT-I, however, FST-I outputs a zero at 1-point transform case. That means, some of the multipliers do not need to be calculated because their inputs are zeros. Given that, to calculate the overall multiplications number for FST-I, we can first count all the existing multipliers as in FCT-I case and they are $\frac{N}{2}\log_2 N$ units for the N-point transform. Then we shall remove the useless multipliers due to the zero inputs. In Fig. 10.11, we give an example of partial 8-point FST-I, where we only show the multipliers and on the recursion side of FST-I algorithm. The red arrows indicate the zeros paths and the black arrows are non-zero paths. The broken-connected arrows stand for the special case paths. Therefore, each multiplier that is passed by a red arrow should be removed. Then, it is obvious that the number of multipliers that should be removed, for a N-point transform, is $N - 1$. So the overall complexity for N-point FST-I results in

$\frac{N}{2}\log_2 N - N + 1$ RM. To sum up, the overall number of multiplications for FCT/FST-I is

$$\text{(RM)} \quad \text{FCT/FST-I}: \quad N\log_2 N - 2N + 2, \tag{10.16}$$

which is equivalent to the number of RM reported in [27].

10.5.2 Number of Additions

Next, we calculate how many additions do N-point FCT/FST-I need. In FCT-I case, the first addition process takes place in the *divide* stage which corresponds to the summation in the parentheses of $h[l]$ term in (10.9) and we can call this process as odd sum process. The complexity of this process leads, cf. [80], to $\frac{N}{2}\log_2 N - N + 1$ real additions (RA). The second addition process occurs in the recursion stage, i.e. the injected term $q[l]$ in (10.9) and we term it as injection process. For each recursion stage we need $N/2$ RA, which results the ultimate number of additions in $\frac{N}{2}\log_2 N$ for this addition process. The third addition process is due to the butterfly operations, as shown in Fig. 10.9, called butterfly process. By carefully looking at this butterfly shape, we can remark that this is not an ordinary butterfly shape, i.e. it misses the first butterfly wing which is replaced by a special case calculation, see Eq. (10.11). The butterfly operations require $N\log_2 N - N + 1$ RA. For the special case calculation, as we discussed above, the periodic property of cosine function decides half of the coefficients in Eq. (10.11) are nulled which means we only need to do the additions for the rest half of the coefficients. Thereby, the number of RA is $(N/2) \times \log_2 N$. However, by this way, we over-counted the number of RA. Because when the N-point FCT-I is divided/decomposed until 1-point, no special case calculations are needed. Furthermore, for the 2-point FCT-I, since

$$\text{FCT}_\text{I}\left(\frac{N=2}{2}\right) = \sum_{m=0}^{1} x[m]\cos\frac{m\pi}{2} = x[0], \tag{10.17}$$

we do not need additions neither. Thereby, the number of stages that we really need is $\log_2 N - 2$, which results the final RM number for special case in $\frac{N}{2}\log_2 N - N$. To conclude, we get the list of the RA for N-point FCT-I as

Table 10.2: RA numbers in FCT-I.

odd-sum	$(N/2)\log_2 N - N + 1$
injection	$(N/2)\log_2 N$
butterfly	$N\log_2 N - N + 1$
special-case	$(N/2)\log_2 N - N$

Then, we move to N-point FST-I case. In the odd sum process, it has the same complexity as in FCT-I, i.e. $(N/2)\log_2 N - N + 1$. Differently from FCT-I, FST-I does not have injection process. For the butterfly process, besides the fact of one wing is missing as in the case of FCT-I, further wings do not need to be computed due to the zero path of FST-I, i.e. in Fig. 10.11) the butterfly wings with red color do not need to be computed. Therefore, this process needs $N\log_2 N - 2N + 2$ RA. For the special case process, FST-I needs also $(N/2)\log_2 N - N$ RA. Thus, the list of RA is the one reported in Tab. 10.3 for N-point FST-I, The total RA number for FCT/FST-I yields

Table 10.3: RA numbers in FST-I.

odd-sum	$(N/2)\log_2 N - N + 1$
injection	0
butterfly	$N\log_2 N - 2N + 2$
special-case	$(N/2)\log_2 N - N$

$$\text{(RA)} \quad \text{FCT/FST-I}: \quad \frac{9}{2}N\log_2 N - 7N + 5, \tag{10.18}$$

which is different with the number of RA in [27]. Actually, our RA number is lower than that of [27].

10.6 Efficient Implementation of IFCT/IFST-III and FCT/FST-III Transforms

In this section, we derive the fast algorithm for IFCT/IFST-III. Actually, there are two ways of implementation. One is direct implementation and the other one is based on FCT/FST-I. Let us first see the case of direct implementation. For N-point IFCT-III we decompose to $N/2$-point IFCT-III

$$\begin{aligned} y[m] &= \sum_{l=0}^{N-1} x[l]C_{2N}^{(m+0.5)l} = \sum_{l=0}^{N-1} x[l]\tilde{C}_{2N}^{(2m+1)l} \\ &= \sum_{l=0}^{\frac{N}{2}-1} x[2l]\tilde{C}_{2N}^{(2m+1)2l} + \sum_{l=0}^{\frac{N}{2}-1} x[2l+1]\tilde{C}_{2N}^{(2m+1)(2l+1)} \\ &= \sum_{l=0}^{\frac{N}{2}-1} x[2l]\tilde{C}_{2N}^{(2m+1)2l} \\ &+ \frac{1}{2\tilde{C}_{2N}^{(2m+1)}}\left(\sum_{l=0}^{\frac{N}{2}-1}(x[2l+1]+x[2l-1])\tilde{C}_{2N}^{(2m+1)2l}\right), \end{aligned} \tag{10.19}$$

with $m = 0, ..., N/2-1$, and by checking the symmetry property, we have

$$\begin{aligned} y[N-1-m] &= \sum_{l=0}^{\frac{N}{2}-1} x[2l]\tilde{C}_{2N}^{(2m+1)2l} \\ &- \frac{1}{2\tilde{C}_{2N}^{(2m+1)}}\left(\sum_{l=0}^{\frac{N}{2}-1}(x[2l+1]+x[2l-1])\tilde{C}_{2N}^{(2m+1)2l}\right), \end{aligned} \tag{10.20}$$

with $m = 0, ..., N/2-1$. Then we can further decompose until 1-point IFCT-III. Note also that the output of the 1-point IFCT-III is equivalent to its input, i.e. $y[0] = \sum_{m=0}^{0} x[l]C_{2N}^{0} = x[0]$. Note that, the direct implementation of FCT-III can be obtained by "transposing" the IFCT-III, i.e., reversing the direction of the arrows in Fig. 10.12.

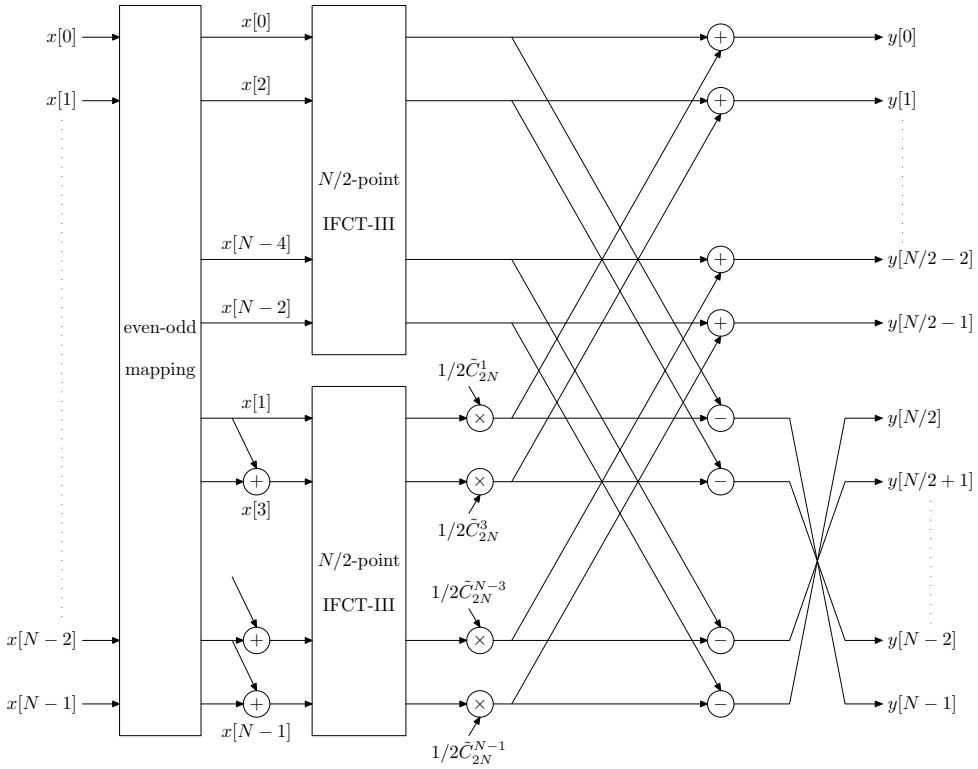

Figure 10.12: IFCT-III direct implementaion.

In the case of IFST-III, we decompose N-point IFST-III as

$$\begin{aligned} y[m] &= \sum_{l=0}^{N-1} x[l] S_{2N}^{(m+0.5)l} = \sum_{l=0}^{N-1} x[l] \tilde{S}_{2N}^{(2m+1)l} \\ &= \sum_{l=0}^{\frac{N}{2}-1} x[2l] \tilde{S}_{2N}^{(2m+1)2l} + \sum_{l=0}^{\frac{N}{2}-1} x[2l+1] \tilde{S}_{2N}^{(2m+1)(2l+1)} \\ &= \sum_{l=0}^{\frac{N}{2}-1} x[2l] \tilde{S}_{2N}^{(2m+1)2l} + \frac{1}{2\tilde{C}_{2N}^{(2m+1)}} \\ &\times \left(\sum_{l=0}^{\frac{N}{2}-1} (x[2l+1] + x[2l-1]) \tilde{S}_{2N}^{(2m+1)2l} + x(N-1)(-1)^m \right), \end{aligned} \tag{10.21}$$

with $m = 0, ..., N/2 - 1$, and by symmetry property we have

$$\begin{aligned} y[N-1-m] &= -\sum_{l=0}^{\frac{N}{2}-1} x[2l] \tilde{S}_{2N}^{(2m+1)2l} + \frac{1}{2\tilde{C}_{2N}^{(2m+1)}} \\ &\times \left(\sum_{l=0}^{\frac{N}{2}-1} (x[2l+1] + x[2l-1]) \tilde{S}_{2N}^{(2m+1)2l} + x(N-1)(-1)^m \right), \end{aligned} \tag{10.22}$$

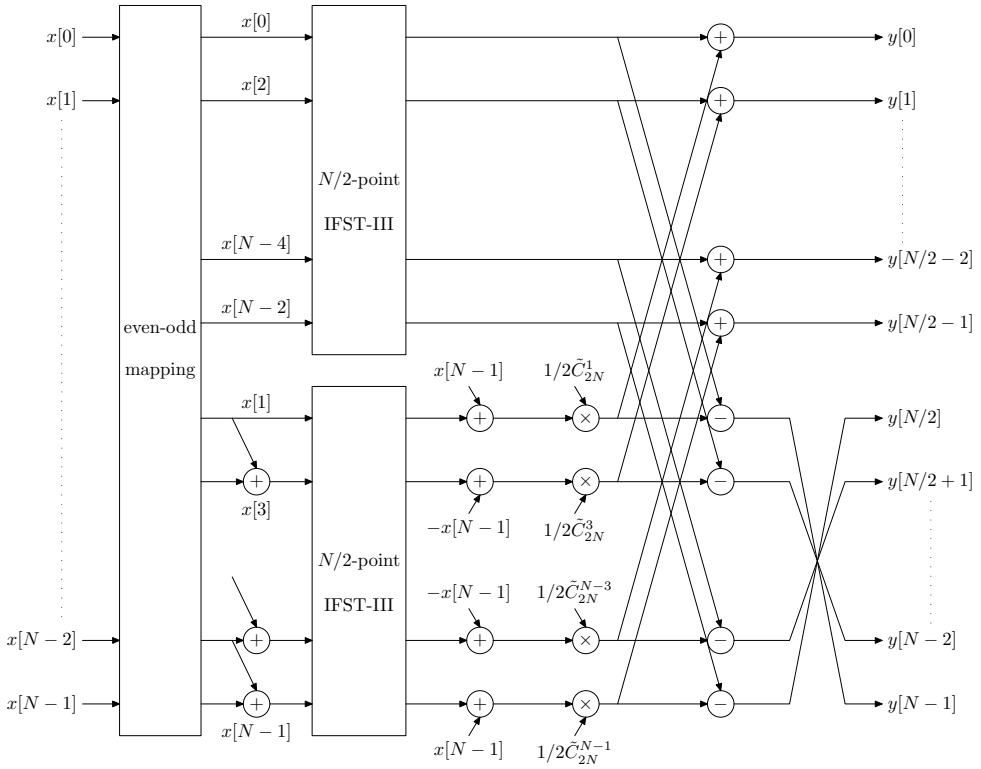

Figure 10.13: IFST-III direct implementation.

with $m = 0, ..., N/2 - 1$. Then we can further decompose until to get 2-point IFST-III, then we have

$$y[0] = x[0] \sin \frac{\pi}{4}, \quad y[1] = x[1] \sin \frac{3\pi}{4}. \tag{10.23}$$

Likewise, the implementation of FST-III can be obtained by reversing the direction of the arrows in Fig. 10.13.

10.7 Complexity Analysis on IFCT/IFST-III

The complexity analysis on IFCT/IFST-III is similar to FCT/FST-I case. Let us first see IFCT-III transform.

10.7.1 Number of Multiplications

In reference to Fig. 10.12, the multiplication operations only occur at the lower branches of the decomposed pair transform which is the same as in FCT-I transform. Thereby, the total number of RM yields $(N/2) \log_2 N$. For IFST-III transform, since we decompose N-point input to finally 2-point, therefore, IFST-III has one stage less than IFCT-III. However, as shown in (10.23), the outputs of 2-point IFST-III need to be obtained by 2 multiplications, which does not exist in IFCT-III case. So we have to compensate these

numbers of RM with a value of N. Thus, the total RM for N-point IFCT/IFST-III is

$$(\text{RM}): \quad (N/2)\log_2 N + (N/2)(\log_2 N - 1) + N = N\log_2 N + N/2. \tag{10.24}$$

10.7.2 Number of Additions

For IFCT-III transform (see Fig. 10.12), the odd sum process needs $(N/2)\log_2 N - N + 1$ RA. The butterfly process needs $N\log_2 N$ RA. For IFST-III transform (see Fig. 10.13), the odd sum process leads to $(N/2)\log_2 N - N + 1$ RA. The butterfly process needs $N(\log_2 N - 1)$ RA. The injection process leads to $(N/2)(\log_2 N - 1)$. Thus, the overall RA for N-point IFCT/IFST-III is

$$(\text{RA}): \quad \frac{7}{2}N\log_2 N - \frac{7}{2}N + 2. \tag{10.25}$$

Since the FCT/FST-III direct implementation is nothing else than the transposed version of IFCT/IFST-III, it leads to the same complexity in terms of RM and RA.

Contributions

Conference papers

- H. Lin and P. Siohan, "OFDM/OQAM with hermitian symmetry: Design and performance for baseband communications," *ICC '08*, Beijing, China, May 2008.

- H. Lin, C. Lélé and P. Siohan, "Equalization with Interference Cancellation for Hermitian Symmetric OFDM/OQAM systems," *ISPLC '08*, Jeju Island, South Korea, Apr. 2008.

- H. Lin and P. Siohan, "A new transceiver design for OFDM/OQAM modulation with cyclic prefix," *PIMRC '08*, Cannes, France, Sept. 2008.

- H. Lin, A. Hayar and P. Siohan, "An information theoretical analysis on indoor PLC channel characterizations," *ISPLC '09*, Dresden, Germany, Mar. 2009.

- H. Lin and P. Siohan, "Transmission Capacity for Indoor PLC: A comparison between DMT and HS-OQAM," *ISPLC '09*, Dresden, Germany, Mar. 2009.

- H. Lin, C. Lélé and P. Siohan, "A pseudo Alamouti transceiver design for OFDM/OQAM modulation with cyclic prefix," *SPAWC '09*, Perugia, Italy, Jun. 2009.

- H. Lin and P. Siohan, "A Unified Structure for Multi-Carrier Modulations in Power-Line Communications," *Globecom '09*, Hawaii, USA, Nov. 2009.

- H. Lin and P. Siohan, "HS-OQAM PLC: Long Prototype Filter or Equalizer?," *WSPLC '09*, Udine, Italy, Oct. 2009.

- H. Lin and P. Siohan, "Modulation Diversity in Wideband In-Home PLC," *WSPLC '09*, Udine, Italy, Oct. 2009.

Journal papers

- H. Lin, P. Siohan, P. Tanguy and J-P. Javaudin "An analysis of EIC for OFDM/OQAM systems," *Journal of Communications (JCM)*, vol. 4, no. 1, pp. 52-60, Feb. 2008.

- H. Lin and P. Siohan, "Capacity analysis for PLC with different multi-carrier modulations," *IEEE Trans. on Power Delivery*, Vol. 25, no. 1, pp. 113-124, Jan. 2010.

- H. Lin and P. Siohan, "Robust channel estimation for OFDM/OQAM," *IEEE Communications Letters*, Vol. 13, no. 10, pp. 724-726, Oct. 2009.

- H. Lin and P. Siohan, "Modulation Flexibility in PLC: A Unified MCM Transceiver Design and Implementation" *revised in* 2009.

- H. Lin and P. Siohan, "Long Prototype Filter or Complex Equalizer? When OFDM/OQAM Meets Frequency Selective Fading," *submitted*, 2009.

Patents

- H. Lin, C. Lélé and P. Siohan, "Procédé de transmission et de réception d'un signal multiporteuse comprenant un intervalle de garde, produits programme d'ordinateur, et dispositifs d'émission et de réception correspondants," 2008.

- H. Lin and P. Siohan, "Dispositif et procédé de modulation pour la mise en oeuvre d'au moins deux techniques de modulation distinctes, dispositif et procédé de démodulation et programmes d'ordinateur correspondants," 2009.

- H. Lin and P. Siohan, " Procédé d'émission et de réception d'un signal multiporteuse mettant en oeuvre des filtres prototypes, dispositifs d'émission et de réception, signal et programme d'ordinateur correspondants," 2009.

Awards

- Best paper award of *ISPLC '09*, Dresden, Germany, Mar. 2009.

Bibliography

[1] IEEE P1901 working group official website. http://grouper.ieee.org/groups/1901/.

[2] Intuilink connectivity software. http://www.home.agilent.com/agilent/product.jspx?nid=-536902427.536882050.00&cc=CA&lc=fre.

[3] Phydyas project website. http://www.ict-phydyas.org/index.php/camax/page/view?id=21.

[4] *Wideband Air Interface Isotropic Orthogonal Transform Algorithm-Public Safety Wideband Data Standards Project CDigital Radio Technical Standards*. 2003.

[5] *HomePlug AV Specification*. Version 1.0.05, Oct. 2005.

[6] K.H. Afkhamie, S. Katar, L. Yonge, and R. Newman. An overview of the upcoming HomePlug AV standard. In *Proc. IEEE International Symposium on Power Line Communications and its Applications*, Vancouver, Canada, Apr. 2005.

[7] M. Alard. Construction of a multicarrier signal. Patent WO/35278, 1998.

[8] M. Alard, C. Roche, and P. Siohan. A new family of functions with a nearly optimal localization property. Technical report, Modyr Project, 1999.

[9] T.W. Anderson. *An Introduction to Multivariate Statistical Analysis*. Wiley, 1984.

[10] R. Balian. Un principe d'incertitude fort en théorie du signal ou en mécanique quantique. *C. R. Acad. Sci*, 292:1357–1362, 1981.

[11] T. Banwell and S. Galli. A novel approach to the modeling of the indoor power line channel Part I: Circuit analysis and companion model. *IEEE Trans. on Power Delivery*, 20(2):655–663, Jul. 2005.

[12] M.G. Bellanger. Specification and design of a prototype filter for filter bank based multicarrier transmission. In *ICASSP*, Salt Lake City, UT, USA, May 2001.

[13] M.G. Bellanger and J.L. Daguet. TDM-FDM Transmultiplexer: Digital Polyphase and FFT. *IEEE Trans. on communications*, COM-22(9):1199–1205, Sept. 1974.

[14] M. Bellec and P. Pirat. OQAM performances and complexity. In *IEEE P802.22 Wireless Regional Area Network*, Jan. 2006.

[15] N. Benvenuto, G. Cherubini, and L. Tomba. Achievable bit rates of DMT and FMT systems in the presence of phase noise and multipath. In *VTC2000-Spring*, Tokyo, Japan, May 2000.

[16] H. Bölcskei. *Oversampled filter banks and predictive subband coders.* PhD thesis, Vienna Univ. Technol., 1997.

[17] H. Bölcskei. *Advances in Gabor Analysis*, chapter Orthogonal frequency division multiplexing based on offset QAM, pages 321–352. 2003.

[18] H. Bölcskei, P. Duhamel, and R. Hleiss. Design of pulse shaping OFDM-OQAM systems for high data-rate transmission over wireless channels. In *ICC*, Vancouver B.C., Canada, Jun. 1999.

[19] H. Bölcskei, P. Duhamel, and R. Hleiss. Orthogonalization of OFDM-OQAM pulse shaping filters using the discrete Zak transform. *EURASIP*, 83(7), Jul. 2003.

[20] H. Bölcskei, F. Hlawatsch, and H.G. Feichtinger. Frame-Theoretic Analysis of Oversampled Filter Banks. *IEEE trans. on signal processing*, 46(12):3256–3268, Dec. 1998.

[21] G. Bonnerot, M. Coudreuse, and M.G. Bellanger. Digital Processing Techniques in the 60 Channel Transmultiplexer. *IEEE Trans. on communications*, COM-26(5):698–706, May. 1978.

[22] M. Le Bot. Galacsy specification : HPAV PLC chain v4. Technical Report Release 2.0, France Telecom, Orange Labs, Mar. 2009.

[23] R. Bultitude, R. Hahn, and R. Davies. Propagation considerations for the design of indoor broadband communications system at EHF. *IEEE Trans. on Veh. Tech.*, 47(1):23–30, Feb. 1998.

[24] J.P. Burg. *Maximum Entropy Spectral Analysis.* PhD thesis, Stanford University, 1975.

[25] L.C. Calvez and P. Vilbé. On the uncertainty principle in discrete-signals. *IEEE Trans. Circuits Systems II*, 39(6):394–395, Jun. 1992.

[26] I. Hakki Cavdar. Performance Analysis of FSK Power Line Communications Systems Over the Time-Varying Channels: Measurements and Modeling. *IEEE Trans. on Power Delivery*, 19(1):111–117, Jan. 2004.

[27] T.S. Chan, J.C. Kuo, and A.Y. Wu. A reduced-complexity fast algorithm for software implementation of the IFFT/FFT in DMT systems. *EURASIP Journal on Advances in Signal Processing*, 9:961–974, 2002.

[28] R. W. Chang. Synthesis of band-limited orthogonal signals for multi-channel data transmission. *Bell. Syst. Tech. Journal*, 45:1775–1796, dec. 1966.

[29] G. Cherubini, E. Eleftheriou, and S. Olçer. Filtered Multitone Modulation for VDSL. In *GLOBCOM*, Rio de Janeiro, Brazil, Dec. 1999.

[30] G. Cherubini, E. Eleftheriou, and S. Olçer. Filtered Multitone Modulation for Very High-Speed Digital Subscriber Lines. *IEEE J. Select. Areas Commun.*, 20:1016–1028, Jun. 2002.

[31] G. Cherubini, E. Eleftheriou, and S. Olcer. A discrete multitone transreceiver system for HDSL applications. *IEEE J. Select. Areas Commun.*, 9:895–908, Aug. 1991.

[32] K. Cho and D. Yoon. On the general ber expression of one- and two-dimensional amplitude modulations. *IEEE Trans. on communications*, 50(7):1074 – 1080, July 2002.

[33] J.M. Cioffi. A Multicarrier Primer. http://www.stanford.edu/group/cioffi/, Sep. 2006.

[34] J.W. Cooley and J. W. Tukey. An algorithm for machine computation of complex Fourier series. *Math Comput.*, 19(90):297–301, 1965.

[35] F.J.C. Corripio, J.C. Arrabal, L.D. del Río, and J.T.E. Munoz. Analysis of the cyclic short-term variation of indoor power line channels. *IEEE J. Select. Areas Commun.*, 24(7):1327–1338, Jul. 2006.

[36] T.M. Cover and J.A. Thomas. *Elements of Information Theory*. Wiley, second edition, 2006.

[37] R.E. Crochiere and L.R. Rabiner. *Multirate Digital Signal Processing*. Prentice-Hall signal processing series, 1983.

[38] Z. Cvetković and M. Vetterli. Oversampled filter banks. *IEEE trans. on signal processing*, 46(5):1245–1255, May 1998.

[39] Omega Deliverable D2.1. State of the art, application scenario and specific requirements for PLC. http://www.ict-omega.eu/fileadmin/documents/deliverables/Omega_D3.1.pdf, Mar. 2008.

[40] I. Daubechies. The Wavelet Transform, Time-Frequency Localization and Signal Analysis. *IEEE Trans. on Information Theory*, 36(5):961–1005, Sept. 1990.

[41] R.L. de Lacerda, A. Menouni, M. Debbah, and B.H. Fleury. A Maximum Entropy Approach To UWB channel modelling. In *ICASSP*, Philadelphia, PA, USA, Mar. 2005.

[42] V. Degardin, M. Lienard, A. Zeddam, F. Gauthier, and P. Degauque. Classification and characterization of impulsive noise on indoor power lines used for data communications. *IEEE Trans. Consum. Electron.*, 48(4):913–918, Nov. 2002.

[43] M.L. Doelz, E.T. Heald, and D.L. Martin. Binary Data Transmission Techniques for Linear Systems. In *Proc. I.R.E.*, May 1957.

[44] M.I. Doroslovački. Product of second moments in time and frequency for discrete-time signals and the uncertainty limit. *Signal Processing*, 67(1), May 1998.

[45] K. Dostert. *Powerline Communications*. Prentice Hall, 2001.

[46] R.J. Duffin and A.C. Schaeffer. A class of nonharmonic Fourier series. *Trans. Am. Math. Soc.*, 72:341–366, 1952.

[47] P. Duhamel. Implementation of "Split-Radix" FFT Algorithms for Complex, Real, and Real-Symmetric Data. *IEEE Trans. on Acoust., Speech, and Signal Processing*, ASSP-34(2):285–295, Apr. 1986.

[48] P. Duhamel and H. Hollmann. Split-radix FFT transform. *Electron. Lett.*, 20:14–16, Jan. 1984.

[49] T. Esmailian, F.R. Kschischang, and P. Glenn Gulak. In-building power lines as high-speed communication channels: channel characterization and a test channel ensemble. *Int. J. Comm. Sys.*, (16), May 2003.

[50] H.G. Feichtinger and T. Strohmer. *Gabor Analysis and Algorithm - Theory and Applications*. Birkhäuser, Boston-Basel-Berlin, 1998.

[51] N.J. Fliege. *Multirate digital signal processing*. John Wiley & Sons, Chichester, 1994.

[52] B. Le Floch, M. Alard, and C. Berrou. Coded Orthogonal Frequency Division Multiplex. *Proceedings of the IEEE*, 83:982–996, jun. 1995.

[53] HomeGrid Forum. http://homegridforum.typepad.com/homegrid_forum/.

[54] D. Gabor. Theory of communications. *J. Inst. Elect. Eng.*, 93(III):429–457, 1946.

[55] S. Galli. Power Line Communications: Applications, Trends and IEEE Standardization Efforts. In *Workshop on Network Design and Protocol Engineering for Powerline Communications*, Dresden, Germany, Sept. 2007.

[56] S. Galli and T. Banwell. A novel approach to the modeling of the indoor power line channelPart II: Transfer function and its properties. *IEEE Trans. on Power Delivery*, 20(3):1869–1878, Jul. 2005.

[57] S. Galli, H. Koga, and N. Kodama. Advanced signal processing for PLCs: Wavelet-OFDM. In *Proc. IEEE International Symposium on Power Line Communications and its Applications*, Jeju, Korea, Apr. 2008.

[58] S. Galli, A. Kurobe, and M. Ohura. The inter-PHY protocol (IPP): A simple coexistence protocol for shared media. In *Proc. IEEE International Symposium on Power Line Communications and its Applications*, Dresden, Germany, Mar. 2009.

[59] A. Garcia-Armada. SNR Gap Approximation for M-PSK-Based Bit Loading. *IEEE Trans. on Wireless Comm.*, 5(1):57–60, Jan. 2006.

[60] V. M. Golubović and Z. R. Petrović. The Impact of Cyclic Prefix Length in DMT on the PLC System Design. In *TELSIKS*, Serbia, Sept. 2007.

[61] E. Guerrini, G. DellAmico, P. Bisaglia, and L. Guerrieri. Bit-loading algorithms and SNR estimate for HomePlug AV. In *Proc. IEEE International Symposium on Power Line Communications and its Applications*, Pisa, Italy, Mar. 2007.

[62] R. Haas. *Applications of multicarrier modulation in mobile radio communications*. PhD thesis, Ecole Nationale Supérieure des Télécommunications, Paris, France, 1996.

[63] R. Haas and J.-C. Belfiore. A Time-Frequency Well-localized Pulse for Multiple Carrier Transmission. *Wireless Personal Communications*, 18(1):1–18, Jul. 1997.

[64] W. Henkel, G. Taubock, P. Odling, P. O. Borjesson, and N. Petersson. The Cyclic Prefix of OFDM/DMT - An Analysis. In *Internatinal Zurich Seminar on Broadband Communications Access-Transmission-Networking*, Zurich, Switzerland, Feb. 2002.

[65] B. Hirosaki. An analysis of automatic equalizers for orthogonally multiplexed QAM systems. *IEEE trans. on Comm.*, COM-28(1):73–83, Jan. 1980.

[66] B. Hirosaki. An orthogonally multiplexed QAM system using the discrete Fourier transform. *IEEE Trans. on Communications*, 29(7):982–989, jul. 1981.

[67] R. Hleiss. *Conception et égalisation de nouvelles structures de modulations multi-porteuses*. PhD thesis, Ecole Nationale Supérieure des Télécommunications, Paris, France, Jan. 2000.

[68] H. Hrasnica, A. Haidine, and R. Lehnert. *Broadband Powerline Communications: Network Design*. WILEY, 2002.

[69] T. Ihalainen, T. H. Stitz, , M. Rinne, and M. Renfors. Channel Equalization in Filter Bank Based Multicarrier Modulation for Wireless Communications. *EURASIP Journal on Advances in Signal Processing*, 2007(ID 49389), Aug. 2007.

[70] R. Ishii and K. Furukawa. The uncertainty principle in discrete signals. *IEEE Trans. Circuits Systems II*, 33(10):1032–1034, Oct. 1986.

[71] K. Izumi, D. Umehara, and S. Denno. Performance evaluation of Wavelet OFDM using ASCET. In *Proc. ISPLC*, Pisa, Italy, 2007.

[72] J.P. Javaudin, D. Lacroix, and A. Rouxel. Pilot-aided channel estimation for OFDM/OQAM. In *Proc. IEEE Vehicular Technology Conf.*, volume 3, Jeju Island, Korea, Apr. 2003.

[73] I. Kalet. The multitone channel. *IEEE Trans. on communications*, 37:119–124, Feb. 1989.

[74] T. Karp and N.J. Fliege. MDFT filter banks with perfect reconstruction. In *Proc. IEEE Int. Symp. Circuits and Systems*, pages 744–747, Seattle, WA, May 2003.

[75] T. Karp, P.N. Heller, and T.Q. Nguyen. A general formulation of modulated filter banks. *IEEE Trans. on Signal Processing*, 47(4):986–1002, Apr. 1999.

[76] E. Kobayashi. Keynote IEEE ISPLC: Part 2. http://www.isplc2008.org/Keynote.asp, Apr. 2008.

[77] H. Koga, N. Kodama, and T. Konishi. High-speed power line communication system based on wavelet OFDM. In *Proc. ISPLC*, Kyoto, Japan, Mar. 2003.

[78] W. Kozek and A.F. Molisch. Nonorthogonal Pulseshapes for Multicarrier Communications in Doubly Dispersive Channels. *IEEE J. Select. Areas Commun.*, 16(8):1579–1589, 1998.

[79] D. Lacroix and J.P. Javaudin. A new channel estimation method for OFDM/OQAM. In *Proc. of* 7^th *International OFDM Workshop*, Sept. 2002.

[80] B.H. Lee. A new algorithm to compute the discrete cosine transform. *IEEE Trans. Acoustics, Speech, Signal Processing*, ASSP-32(6):1243–1245, Dec. 1984.

[81] C. Lélé. *OFDM/OQAM modulation: Channel estimation methods, and applications to multicarrier CDMA and multi-antenna transmission.* PhD thesis, Conservatoire National des Arts et Métiers, Paris, France, Nov. 2008.

[82] C. Lélé, R. Legouable, J.-P. Javaudin, A.Skrzypczak, and P. Siohan. Channel estimation methods for preamble-based OFDM/OQAM modulations. In *European wireless*, Paris, France, Apr. 2007.

[83] C. Lélé, P. Siohan, R. Legouable, and J.-P. Javaudin. Preamble-based channel estimation techniques for OFDM/OQAM over the powerline. In *Proc. IEEE International Symposium on Power Line Communications and its Applications*, pages 59–64, Pisa, Italy, Mar. 2007.

[84] H. Lin and P. Siohan. OFDM/OQAM with hermitian symmetry: Design and performance for baseband communication. In *International Conference on Communications*, Beijing, China, May 2008.

[85] Y.P. Lin and P.P. Vaidyanathan. Linear Phase Cosine Modulated Maximally Decimated Filter Banks with Perfect Reconstruction. *IEEE Trans. on Signal Processing*, 42(11):2525–2539, Nov. 1995.

[86] F. Low. Complete sets of wave packets. *A Passion for Physics - Essay in Honor of Geoffrey Chew (C. DeTar et al., eds.)*, pages 17–22, 1985.

[87] Y.H. Ma, P.L. So, and E. Gunawan. Performance analysis of OFDM systems for broadband power line communications under impulsive noise and multipath effects. *IEEE Trans. on Power Delivery*, 20(2):674–682, Apr. 2005.

[88] J. D. Markel. FFT Pruning. *IEEE Trans. Audio Electroacoust*, AU-19:305–311, Dec. 1971.

[89] K.W. Martin. Small Side-Lobe Filter Design for Multitone Data-Communication Applications. *IEEE Trans. on Circuits and Systems II: Analog and Digital Signal Processing*, 45(8):1155–1161, Aug. 1998.

[90] S. Mirabbasi and K. Martin. Overlapped Complex-Modulated Transmultiplexer Filters With Simplified Design and Superior Stopbands. *IEEE Trans. on circuits and systems II: analog and digital signal processing*, 50(8):456–469, Aug. 2003.

[91] S. Nedič and N. Popovic. Per-bin DFE for Advanced OQAM-based Multicarrier Wireless Data Transmission Systems. In *International Zurich Seminar on Broadband Communications Access-Transmission-Networking*, number 38, pages 1–6, Zurich, Switzerland, Feb. 2002.

[92] M. Ouzzif and J. Le Masson. Statistical analysis of the cyclic prefix impact on indoor PLC capacity. In *Proc. IEEE International Symposium on Power Line Communications and its Applications*, Dresden, Germany, Mar. 2009.

[93] P. Pagani, M. Tlich, A. Zeddam, A. Tonello, F. Pecile, S. D'Alessandro, G. Mijic, and K. Kriznar. PLC Channel Transfer Function Models for the OMEGA ICT project. In *ICT-MobileSummit 2009 Conference Proceedings*, Santander, Spain, Jun. 2009.

[94] A. Peled and A. Ruiz. Frequency domain data transmission using reduced computational complexity algorithms. In *ICASSP*, Denver, Colorado, USA, Apr. 1980.

[95] S. Pfletschinger and J. Speidel. Optimized impluses for multicarrier offset-QAM. In *Globecom*, San Antonio, Texas, USA, Nov. 2001.

[96] H. Philipps. Modelling of powerline communication channels. In *Proc. IEEE International Symposium on Power Line Communications and its Applications*, Lancaster, UK, Mar. 1999.

[97] H. Philipps. Development of a Statistical Model for Power Line Communications Channels. In *Proc. IEEE International Symposium on Power Line Communications and its Applications*, Limerick, Ireland, Apr. 2000.

[98] D. Pinchon, P. Siohan, and C. Siclet. A fast design method for orthogonal modulated filter banks. In *ICASSP'02*, Orlando, USA, May 2002.

[99] D. Pinchon, P. Siohan, and C. Siclet. Design techniques for orthogonal modulated filterbanks based on a compact representation. *IEEE Trans. on signal processing*, 52(6):1682 – 1692, June 2004.

[100] T. V. Prasad, S. Srikanth, C. N. Krishnan, and P. V. Ramakrishna. Wideband Characterization of Low Voltage outdoor Powerline Communication Channels in India. In *Proc. IEEE International Symposium on Power Line Communications and its Applications*, Malmö, Sweden, Apr. 2001.

[101] J.G. Proakis and D.G. Manolakis. *Digital Signal Processing: Principle, Algorithms, and Applications*. Prentice-Hall, 1996.

[102] L. Qin and M. Bellanger. Adaptive Sub-Channel Equalization in Multicarrier Transmission. In *ICASSP*, Munich, Germany, Apr. 1997.

[103] J. Ramanathan and T. Steger. Incompleteness of sparse coherent states. *Appl. Comp. Harm. Anal.*, 2:148–153, Apr. 1995.

[104] M.A. Rieffel. Von Neumann algebras associated with pairs of lattices in Lie groups. *Math. Ann.*, 257:403–418, Nov. 1981.

[105] A. D. Rizos, J. G. Proakis, and T. Q. Nguyen. Comparison of DFT and cosine modulated filter banks in multicarrier modulation. In *Globecom*, page 687C691, 1994.

[106] P. Robertson and S. Kaiser. Analysis of the loss of orthogonality through Doppler spread in OFDM system. In *Proc. IEEE Globecom*, Rio de Janeiro, Brazil, Dec. 1999.

[107] P. Robertson and S. Kaiser. The effects of Doppler spreads in OFDM(A) mobile radio systems. In *Proc. IEEE 50th Vehicular Technology Conference*, pages 329–333, Amsterdam, Netherlands, Sept. 1999.

[108] M. Rossi, J.Y. Zhang, and W. Steenaart. Iterative constrained least squares design of near perfect reconstruction pseudo QMF banks. In *CCECE'96*, Calgary, May 1996.

[109] B.R. Saltzberg. Performance of an efficient parallel data transmission system. *IEEE Trans. on Comm. Tech.*, 15(16):805–813, Jan. 1967.

[110] S.D. Sandberg and M.A. Tzannes. Overlapped discrete multitone modulation for high speed copper wire communications. *IEEE J. Select. Areas Commun.*, 9(13):1571C1585, Dec. 1995.

[111] S.D. Sandberg and M.A. Tzannes. Overlapped Discrete Multitone Modulation for High Speed Copper Wire Communications. *IEEE J. Sel. Area Comm.*, 13(9):1571–1585, Dec. 1995.

[112] J. L. Seoane, S. K. Wilson, and S. Gelfand. Analysis of Intertone and Interblock Interference in OFDM when the Length of the Cyclic Prefix is Shorter than the Length of the Impulse Response of the Channel. In *GLOBECOM*, Phoenix, Arizona USA, Nov. 1997.

[113] C. Siclet. *Application de de théorie des bancs de filtres à l'analyse et à la conception de modulations multiporteuses orthogonales et biorthogonales*. PhD thesis, Université de Rennes 1, Rennes, France, Nov. 2002.

[114] P. Siohan and C. Roche. Cosine modulated filterbanks based on Extended Gaussian Functions. *IEEE Transactions on Signal Processing*, 48(11):3052–3061, nov. 2000.

[115] P. Siohan, C. Siclet, and N. Lacaille. Analysis and design of OFDM/OQAM systems based on filterbank theory. *IEEE Transactions on Signal Processing*, 50(5):1170–1183, May 2002.

[116] D. P. Skinner. Pruning the decimation-in-time FFT algorithm. *IEEE Tans. on Acoust., Speech, Signal Processing*, ASSP-24:193–194, Apr. 1976.

[117] A. Skrzypczak, P. Siohan, and J-P. Javaudin. Application of the OFDM/OQAM Modulation to Power Line Communications. In *Proc. IEEE International Symposium on Power Line Communications and its Applications*, Pisa, Italy, Mar. 2007.

[118] H.V. Sorensen, D.L. Jones, M.T. Heideman, and C.S. Burrus. Real-Valued Fast Fourier Transform Algorithms. *IEEE Trans. on Acoust., Speech, and Signal Processing*, ASSP-35(6):849–862, Jun. 1987.

[119] T. Starr, J.M. Cioffi, and P.J. Silverman. *Understanding Digital Subscriber Line Technology*. Prentice-Hall, Englewood Cliffs, 1999.

[120] T.E. Sung, A. Scaglione, and S. Galli. Time-Varying Power Line Block Transmission Models over Doubly Selective Channels. In *Proc. IEEE International Symposium on Power Line Communications and its Applications*, Jeju, Korea, Apr. 2008.

[121] M. Tlich, A. Zeddam, F. Moulin, and F. Gauthier. Indoor Power-line Communications Channel Characterization Up to 100 MHz-Part I: One-Parameter Deterministic Model. *IEEE Trans. on Power Delivery*, 23:1392–1401, Jul. 2008.

[122] M. Tlich, A. Zeddam, F. Moulin, and F. Gauthier. Indoor Power-line Communications Channel Characterization Up to 100 MHz-Part II: Time-Frequency Analysis. *IEEE Trans. on Power Delivery*, 23:1402–1409, Jul. 2008.

[123] M. Tlich, A. Zeddam, F. Moulin, F. Gauthier, and G. Avril. A broadband Powerline Channel Generator. In *Proc. IEEE International Symposium on Power Line Communications and its Applications*, pages 59–64, Pisa, Italy, Mar. 2007.

[124] A. Tonello, S. D'Alessandro, and L. Lampe. Bit, Tone and Cyclic Prefix Allocation in OFDM with Application to In-Home PLC. In *IFIP Wireless Days - 2nd International Home Networking Conference (IHN 2008)*, Dubaï, Nov. 2008.

[125] D. Tse and P. Viswanath. *Fundamentals of Wireless Communication*. Cambridge, 2005.

[126] J.C. Tu. Optimum MMSE equalization for staggered modulation. In *Conf. Record of The Twenty-Seventh Asilomar Conf. on Signals, Systems and Computers*, pages 1401–1406, Pacific Grove, CA, Nov. 1993.

[127] P. Turcza. A New TMUX For xDSL Based On Linear Phase Modulated Filter Banks. In *EUSIPCO*, pages 1935–1938, Vienna, Austria, Sept. 2004.

[128] M.A. Tzannes, M.C. Tzannes, J.G. Proakis, and P.N. Heller. DMT systems, DWMT systems and digital filter banks. In *Proc. IEEE International Conference on Communications*, New Orleans, LA, May. 1994.

[129] M.A. Tzannes, M.C. Tzannes, and H.L. Resnikoff. The DWMT : a multicarrier transceiver for ADSL using M-band wavelets. In *ANSI TlEl.4 Committee Contribution*, number 93-067, Mar. 1993.

[130] P.P. Vaidyanathan. *Multirate systems and filter banks*. Prentice Hall, Englewood Cliffs, New-York, New Jersey, 1993.

[131] L. Vangelista and N. Laurenti. Efficient implementations and alternative architectures for OFDM-OQAM systems. *IEEE Trans. on Comm.*, 49(4):664–675, Apr. 2001.

[132] A. Viholainen, J. Alhava, and M. Renfors. Efficient Implementation of 2× Oversampled Exponentially Modulated Filter Banks. *IEEE Trans. on Circuits and Systems-II*, 53(10):1138–1142, Oct. 2006.

[133] A. Viholainen, T. Ihalainen, and M. Renfors. Performance of Time-Frequency Localized and Frequency Selective Filter Banks in Multicarrier Systems. In *International Symposium on Circuits and Systems*, Island of Kos, Greece, May 2006.

[134] D.S. Waldhauser and J.A. Nossek. MMSE equalization for bandwidth-efficient multicarrier systems. In *Proc. IEEE Int. Symp. Circuits Syst.*, pages 5391–5394, Island of Kos, Greece, May 2006.

[135] Z. Wang and G.B. Giannakis. Wireless multicarrier communications: Where Fourier meets Shannon. *IEEE Signal Processing Mag.*, 17(3):29–48, May 2000.

[136] M. Wax and T. Kailath. Detection of signals by information theoretic criteria. *IEEE Trans. on Acoust., Speech, and Signal Processing*, 33(2):387–392, Apr. 1985.

[137] S.B. Weinstein and P.M. Ebert. Data Transmission By Frequency Division Multiplexing Using the Discrete Fourier Transform. *IEEE Trans. Commun.*, COM-19(5):628–634, Oct. 1971.

[138] M. Zimmermann and K. Dostert. A Multi-Path Signal Propagation Model for the Power Line Channel in the High Frequency Range. In *Proc. IEEE International Symposium on Power Line Communications and its Applications*, Lancaster, UK, Mar. 1999.

[139] M. Zimmermann and K. Dostert. A multipath model for the powerline channel. *IEEE Trans. on communications*, 50(4):553–559, Apr. 2002.